MAGNETIC FIELD SIMULATION AND MAPPING BASED ON ZEEMAN-SPLIT LASER-INDUCED FLUORESCENCE SPECTRA OF XENON IN THE DISCHARGE CHANNEL OF 5-6 kW COAXIAL STATIONARY-PLASMA HALL THRUSTERS

by

Baïlo Bah Ngom

A dissertation submitted in partial fulfillment
of the requirements for the degree of
Doctor of Philosophy
(Aerospace Engineering)
in The University of Michigan
2009

Doctoral Committee:

Professor Alec D. Gallimore, Chair
Professor Yue Ying Lau
Associate Professor John Edison Foster
Lecturer Timothy B. Smith
Peter Y. Peterson, ElectroDynamic Applications, Inc.

© Baïlo Bah Ngom 2009

All Rights Reserved

I exclusively dedicate explanations, analyses, and results reported in this thesis and its entirety to those interested in promoting the betterment of the Human condition, in its exercise of free will—while respecting others' freedom—by any means other than the development of weapons with a potential to initiate an offense.

ACKNOWLEDGEMENTS

Thanks to everyone who motivated and offered their contribution to the initiation, evolution, and completion of this project whether directly or indirectly.

TABLE OF CONTENTS

CHAPTER

LIST OF FIGURES

Figure

LIST OF TABLES

Table

LIST OF APPENDICES

APPENDIX

ABSTRACT

We studied the effect of the Hall current's induced magnetic field on the vacuum field of coaxial Hall thrusters based on MagNet 6 simulation of a 5 kW thruster (P5) and laser-induced fluorescence spectra taken at the exit plane of a 6 kW thruster (H6).

MagNet 6 simulations were performed at power settings of 1.6 kW and 3 kW—each with a proper set coil currents and Hall current density distributions. The Hall current—simulated using a rectangular array of current-carrying coils —induced a significant reduction of the field strength . The radial component of the field strength shifted towards the anode by as much as 10 mm and its gradient lost its mononoticity as the Hall current's magnitude increased. Additionally, an increase in the concavity of streamlines along the axial direction was noted in the channel.

MagNet simulations were compared to non-intrusive radial field strength measurements at the exit of the 6 kW thruster from Zeeman-split laser-induced fluorescence spectra of neutral xenon ($6S'\,[1/2] \rightarrow 6P'\,[3/2]$ about 834.912 nm-vacuum) by fitting measured spectra with Lorentz and Doppler-broadened Zeeman-split fluorescence lineshapes.

Spectra were modeled using a linear Zeeman theory of fine structure splitting of isotopes with zero nuclear spin and a non-linear Zeman model of the splitting of hyperfine lineshape components of isotopes with non-zero nuclear spin. The resulting isotopes' line spectra were shifted, scaled (by natural abundance) and Lorentz- and Doppler-broadened (Voigt-profile) to yield neutrals' absorption spectrum.

A commercial non-linear least-squares solver was then used to compute radial components of the magnetic field strength and axial kinetic temperatures that minimize the fitting error between experimental and simulated spectra. The solver was applied to laser-induced fluorescence spectra measured at the exit plane of a 6 kW Hall thruster (H6). The resulting magnetic field strength calculations revealed, as in the MagNet 6 simulation study of the P5, that the plasma induces a reduction of the radial component of the field strength. Axial kinetic temperatures of neutral xenon particles remained fairly constant near the channel's centerline; closer to the inner wall, however, the temperature was found to be twice larger.

CHAPTER I

Introduction

A good literal translation of the world 'rocket' can be found in Chinese for 'Fire Arrow' [8]. Accounts of 'rockets' performing various functions date back as far as the turn of the first millennium [8]. Still, the first documented, revolutionary—in the source of inspiration and enthusiasm it triggered to future space engineers and scientists—and almost prophetic mention of it for space travel is owed to Jules Verne's 1865 science-fiction classic: *From the Earth to the Moon* .

Half a century later, theoretical foundations of space propulsion were beginning to take shape with the works of Konstantin Tsiolkovsky, who sketched the basic principles of rocket propulsion; these include the main design parameters associated with rocket engines and the identification of suitable propellants. Tsiolkovsky also initiated work related to the design of spacecrafts and mission planning [8]. Later, Herman Oberth continued along the same path; but his theoretical work had greater impact among many professionals and amateurs throughout the world, who began to put his ideas into practice [8].

It took, yet, another half-century before rocket technology reached the maturity required for space travel, as Mankind took a major step across Earth's atmosphere and marked its footsteps on the Moon's surface during the 1969 Appolo 11 mission.

Today, rocket technology has reached a level of sophistication that makes the launch, orbital positioning, and keeping of satellites and space-stations, routine activities. And more than ever before, Mankind is growing increasingly dependent on rocket technology. Nations around the globe rely on a complex communication grid, rendered possible by Earth-orbiting satellites, to perform vital activities in a wide range of sectors such as health, transportation, social, or financial. Research activities conducted in the weightless and isolated (from atmospheric perturbations or ground interferences) environment of space-stations have led to great progress in Medical and Material sciences and led to the emergence of a host of new technologies; and have broadened our knowledge of space and matter from the cosmologic scale to the subatomic scale. On a broader horizon, the development of rocket technology is an essential component in the exploration of the planetary systems, asteroids, and comets of the Solar system; these bodies may constitute alternative homes or transits to remote destinations for Mankind, which is beginning to realize the fragility of life in a home-planet exposed to apocalyptic menaces such as ozone layer depletion or meteorite impacts—to cite a few.

Whether in their proposal, development, or operational phase, several rocket propulsion concepts exist. Amongst operational rockets, different propulsion systems—namely chemical, electrothermal, and electrostatic and magnetic—present different advantages. For space missions of long duration and/or range, electrostatic/magnetic propulsion is more promising. Hall and ion thrusters, which belong to this latter category, have been the object of extensive study and testing. Hall thrusters have been applied to about a hundred space missions since the turn of the century [9, 8]. Among the many known variants of this class of magnetic thrusters, we focus our interest on xenon-propelled coaxial stationary-plasma Hall thrusters; these mainly consist of magnetic and electric circuits that are assembled in a remarkably simple structural design. Though operational, there is still room for improvement of the efficiency of Hall thrusters—currently within 50-60% efficiency [10]. A better understanding of the dynamics of particles in the discharge channel of Hall thrusters—in which most of the thrust is developped [1]—as well as their effect on the magnetic field induced by the circuitry of Hall thrusters could lead to such an increase [9].

The exhaust (or discharge) of a Hall thruster is a plasma consisting of neutrals, ions, and electrons whose motions result from magnetic and electric field effects and inter-particle and particle-to-wall collisions. The magnetic field topology is of primary importance in the design of Hall thrusters mainly because it approximates (to first order) the equipotential of electric field lines, whose optimal curvature ensures a collimated exhaust—key to an efficient propellant utilization for maximum thrust production [11, 12]. When coupled with an electric field, inherent to the discharge plasma, the magnetic field induces a circular closed-loop flow of electrons (Hall current) in an annular and opened channel of the thruster. The electron current manifests itself as a distinctive doughnut-shaped purplish cloud hovering about the thruster's exit plane—hence the name of 'Hall thruster'. In turn, the Hall current, induces a magnetic field. This latter field is not accounted for in the design of Hall thrusters' field structure, although the latter has been shown to be sensitive to minor modification of the thruster's magnetic components [11].

That is why, over the past decade, this topic has been the object of much inquiry; notable progress has been achieved at the Plasmadynamics and Electric Propulsion Laboratory (PEPL) of the University of Michigan [10, 13, 14, 11]. This thesis contributes to this quest by studying the effect of the magnetic topology on the discharge plasma and vice-versa in a 5 kW laboratory-class thruster (named P5). It improves on Haas' analysis [1] by considering a three-dimensional simulation of the Hall current's magnetic induction based on a magnetostatic commercial solver (MagNet 6) developed by Infolytica. The simulation is applied to the combined system of the thruster's magnetic circuit and a discretized Hall current as in Peterson's work [14]. However, the present study deviates from Peterson's in three major ways: firstly, the

Hall current used in this study results from planar probe measurements [1] rather than Hall parameter estimations; secondly, this study reports the effect of actual and scaled magnitudes of the Hall current on both radial and axial components of the magnetic field throughout the acceleration zone; lastly, the thrust vector field is estimated from the Hall current and field strength components based on a collisionless differential fluid-model of the momentum equation .

Aside from MagNet simulation, this thesis presents a non-intrusive method for mapping the magnetic topology of the P5 using a quantum-based numerical analysis of laser-induced fluorescence spectra measured in the plasma discharge plasma of the P5. The current analysis consists of solving for the radial magnetic field strength that externally acts on the plasma by fitting near-infrared absorption spectra of neutral xenon particles based on linear and non-linear Zeeman models—respectively applied to isotopes with zero spin (even-numbered isotopes) and non-zero spin (even-numbered isotopes). This method has successfully been validated using absorption spectra measured in the stationary plasma produced in an optogalvanic cell immersed in a magnetic field induced by a Helmholtz coil at various current settings [15].

CHAPTER II

Theoretical Foundations of Rocket Technology and its Development leading to Hall thruster propulsion

2.1 General concepts of space propulsion

2.1.1 Physics of rocket propulsion

The theory of rocket propulsion in space is simple though not necessarily intuitive. Turner [8] provides a good introduction on the topic, from which most of this chapter is built upon. We commonly perceive the motion of a body in a medium as the result of some reaction of the medium on the body as the latter exerts pressure against the former. A skater rides forward as it pushes against concrete. A boat moves forward when its rotor blade or its paddle presses against the water. A helicopter is propelled forward due to the pressure of air molecules on its rotor blades. Does the same apply to a jetliner or a spacecraft at take-off or in mid-air flight? Can one expect that the propulsion of these craft results from the reaction of the ambient medium (air)? As surprising as it might be the answer is not as intuitive as one might expect: though the atmosphere may contribute to the drag or lift of a jetliner, thrust is not due to the reaction of the atmosphere. According to classical physics, thrust within the atmosphere originates from the same principle that governs acceleration of a rigid body in what we common perceive as empty space with nothing to push against. We can determine the origin of thrust from the following conservation laws of motion:

- integral form of the conservation of momentum of a fluid
- Newton's laws of motion of a rigid body

In fluid mechanics, a useful recourse for studying the motion of a fluid-propelled device consists of applying the control-volume (CV) approach to some portion of the fluid interacting with the device. The way that such a volume is selected determines the ease with which one can extract the physics of the motion. The choice of the CV also depends on ones familiarity with physics of propulsion. Readers with a solid foundation in fluid mechanics are referred to John [16] who provides a short derivation of the thrust of a rocket. Turner [8] provides a longer but more insightful derivation that we elaborate on in this section for those who lack the appropriate background. Consider the sketch of Figure 2.1 showing a simplified view of the profile of the rocket structure (solid line) and its exhaust fluid (liquid, gas, or plasma) in the reference frame of the rocket at some time t. The rocket is traveling forward (negative x-direction) as the exhaust is expelled backward (positive x-direction). The CV approach consists of restricting one's interest to what happens at the boundaries of some region of space while traveling at the speed of the object. The Law of conservation of momentum of a fluid states that the net pressure that externally acts on the boundary of a control volume enclosing a fluid induces a net momentum of the fluid flowing across the boundaries as expressed below [16]:

$$-\oint_A p\,dA\,\widehat{n} = \oint_A \left(\rho\vec{V}\cdot\widehat{n}\,dA\right)\vec{V}; \tag{2.1.1}$$

in which, dA represents the area of an infinitesimally small surface element of A and the pressure force (left-hand side of the equation) is oriented along a direction that is opposite to a normal vector ($\widehat{n}$) pointing away from the infinitesimal patch; $\rho(t)$ is the local density in some infinitesimal fluid element at the boundary of the control-volume; and $\vec{V} = u\widehat{i} + v\widehat{j} + w\widehat{k}$ is the velocity of that fluid element in the reference of the rocket. As shown on Figure 2.1, the closed surface A can be split into an open control surface, A_r that separates the fluid from the walls of the rocket structure and the exit plane, A_e. A fluid pressure distribution function, p_f^r, acts on A_r from the reaction of the inner walls of the rocket structure while p_f^e acts on the exit plane of the rocket. Considering supersonic rockets (practical cases), p_f^e is distinct from the ambient pressure p_f^a. Based on the aforementioned facts and assuming that the exhaust speed remains constant and one-dimensional (along the x-direction) leads to:

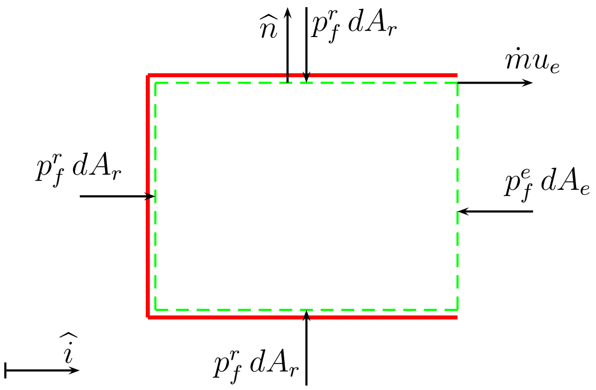

Fig. 2.1: Simplified sketch of the cross-section of a rocket exhausting its propellant; to which, a control-volume is applied at some arbitrary time

$$\int_{A_r} p_f^r dA_r - \int_{A_e} p_f^e dA_e = \dot{m}u_e \tag{2.1.2a}$$

$$\Rightarrow \int_{A_r} p_f^r \, dA_r - P_e A_e = \dot{m}u_e, \tag{2.1.2b}$$

where P_e denotes the mean fluid pressure at the exit plane .

Next, we consider the motion of the rocket. The thrust (R) acting on the rocket results from the reaction of the fluid pressure on the rocket structure. However, this action is reduced by a static atmospheric pressure acting on the overall rocket. The new control volume enclosing the overall rocket and ending on its exit plane (Figure 2.2) illustrates the gas and ambient pressures acting on the rocket structure (p_f^r and p_a^r respectively) to yield the following expression of thrust:

$$R = \int_{A_r} \left(p_r^f - p_a^r\right) \, dA_r. \tag{2.1.3}$$

From Newton's 3^{rd} Law of motion [1], it is evident that the pressure acting on the gas

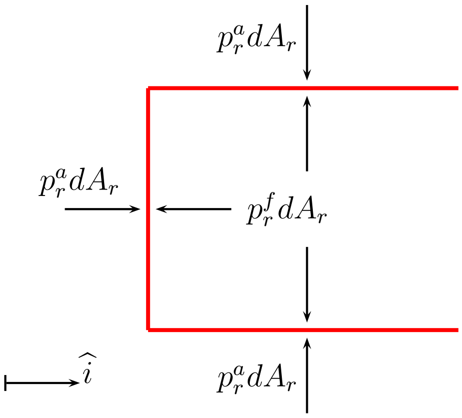

Fig. 2.2: Thrust generation as a result of pressure imbalance between ambient and propellant fluids on the rocket walls

must equal the latter's reaction so that $p_f^r = p_r^f$; from this (2.1.3) reduces to

$$R = \int_{A_r} \left(p_f^r - p_a^r\right) \, dA_r. \tag{2.1.4}$$

The retarding static pressure force (2^{nd} integral in eq. 2.1.4) is determined by applying the momentum equation to the control-volume that encloses the rocket structure in the absence of all influences, except from the ambient fluid (see Figure 2.3).

---

[1] According to Newton's 3^{rd} Law of motion, for every action there is a reaction of equal strength acting in the opposite direction

$$\int_A p_r dA_r = \int_{A_r} p_r^a dA_r - \int_{A_e} p_r^a dA_e = 0 \tag{2.1.5a}$$

$$\Rightarrow \int_{A_r} p_r^a dA_r = P_a A_e, \tag{2.1.5b}$$

where P_a is the mean ambient pressure acting on the exit plane.

Inserting (2.1.5b) into (2.1.4) and solving leads to:

$$\int_{A_r} p_r^f dA_r = R + P_a A_e. \tag{2.1.6}$$

Substituting the expression of the above integral into (2.1.2b) and solving for R yields the following expression of the magnitude of the rocket thrust based on the CV analysis:

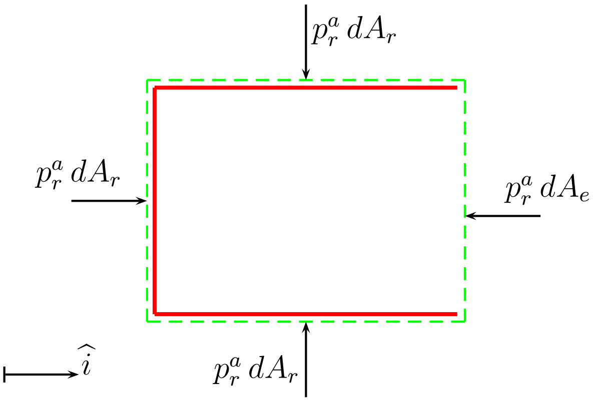

Fig. 2.3: Control volume applied to rocket in atmosphere in the absence of all influences except from the ambient fluid; that is, no propellant exhaust, no external forces

$$R = (P_f^e - P_a)A_e + \dot{m}u_e. \tag{2.1.7}$$

In the vacuum environment of space, the ambient pressure is nearly zero so that (2.1.7) reduces to

$$R = P_e A_e + \dot{m}u_e. \tag{2.1.8}$$

Since the exhaust pressure is proportional to the mass flow rate, eq. (2.1.8) can conveniently be re-expressed as

$$R = \dot{m}\overline{u}_e, \tag{2.1.9}$$

so that both pressure and inertial effects of the fluid can conveniently be combined into one inertial term owing to some pressure-less hypothetical fluid traveling at some 'effective exhaust' velocity $\overline{u}_e$.

As expressed in (2.1.9), the expression of thrust yields no direct information about the velocity gain of the rocket associated with its propellant expenditure. Such an insight can be gained by applying Newton's 2^{nd} Law [2] to the rocket at some arbitrary time, t, while its mass is $M(t)$ and its velocity is $\vec{V}(t)$ with respect to an inertial frame of reference (as viewed from a non-accelerating laboratory). Since the thrust must be the same in both moving and non-moving frames, the thrust from eq. (2.1.6) must be equal to the component of the following expression in the x-direction:

$$R = \frac{d}{dt}\left[M(t)\vec{V}(t)\right]. \tag{2.1.10}$$

Equating eqs. (2.1.10) and (2.1.7) and using the fact that the expression of the fluid's exhaust velocity in the rocket and inertial frames, u_e and $\overline{u}_{e,i}$ (respectively), relate to one another as $u_{e,i} = u_e - V$, we arrive at:

$$\dot{m}\left(\overline{u}_{e,i} + V\right) = \frac{d}{dt}\left[MV\right] \tag{2.1.11a}$$

$$= \dot{M}V + M\dot{V}. \tag{2.1.11b}$$

Assuming that the rocket-fluid system is isolated from the surroundings, the mass flow rate must be conserved as expressed in eq. (2.1.12); that is, the rate of mass loss

---

[2] Newton's 2^{nd} Law states that the sum of all forces externally applied to a point mass equals its time-rate of change of momentum in an inertial frame of reference.

of the rocket must balance the exhaust mass flow rate of the propellant:

$$\dot{M} + \dot{m} = 0 \Rightarrow \dot{M} = -\dot{m}; \tag{2.1.12}$$

which when applied to eq. (2.1.11b) yields after simplifications:

$$\overline{u}_{e,i}\dot{M} = M\dot{V} \;\Leftrightarrow\; \overline{u}_{e,i}\frac{dM}{dt} = -M\frac{dV}{dt}. \tag{2.1.13}$$

Discarding the time dependence in (2.1.13) and integrating the resulting equation between some initial state (at $t = t_o$) and some arbitrary state (at t) during the acceleration phase yields

$$-\overline{u}_{e,i}\int_{M(t_o)}^{M(t)} \frac{1}{M}dM = \int_{V(t_o)}^{V(t)} dV; \tag{2.1.14}$$

which upon evaluation leads to the Tsiolkovsky Rocket Equation relating the velocity increase of a rocket to its propellant expenditure and the effective exhaust velocity:

$$\Delta V = \overline{u}_e \; ln\left[\frac{M\left(t_o\right)}{M\left(t\right)}\right]; \tag{2.1.15}$$

for simplicity and because $u_{e,i} \approx u_e$ usually holds, the subscript associated with inertial frame of reference has been omitted in (2.1.15). The Tsiolkovsky Rocket Equation states that the greater the propellant expenditure at a constant exhaust speed, the greater the gain in speed but with logarithmically diminishing returns. It further states that larger gains are possible with higher propellant exhaust speeds. As mentioned earlier, the effective exhaust velocity is specific to a rocket design and is a useful parameter for comparing performances.

Another performance parameter of even greater importance is named ‘specific impulse’ or I_{sp} for short. I_{sp} can be defined as the amount of momentum imparted to a rocket per unit-weight of propellant expenditure within an infinitesimally small time-interval. From Newton's 2^{nd} Law, the thrust of a rocket results from the time rate of change of its linear momentum, p:

$$R = \frac{dp}{dt}; \tag{2.1.16}$$

hence the corresponding instantaneous momentum increase or impulse is:

$$I \equiv \lim_{\Delta t \to 0} \int_0^{\Delta t} R \; dt; \tag{2.1.17}$$

inserting the expression of thrust of (2.1.7) into the impulse function and integrating yields:

$$I = \left[\lim_{\Delta t \to 0} \int_0^{\Delta t} \dot{m} \; dt \right] \overline{u}_e = [\delta M] \;\; u_e \tag{2.1.18}$$

Since the equivalent weight of the propellant during that time is $\delta M g$ (g: acceleration of gravity), the impulse per unit propellant weight or 'specific impulse' is then:

$$I_{sp} = \frac{\overline{u}_e}{g} \text{ (seconds)}; \tag{2.1.19}$$

in which sea-level value ($\approx$ 10 m/s^2) of the acceleration of gravity, is conventionally used. From the expression of the I_{sp} given in (2.1.19), we can better appreciate its importance as a rocket parameter; not only does it indicate the amount of ΔV gained per unit weight of propellant burned, but it also yields the magnitude of the exhaust velocity (a quick yield resulting from its multiplication by 10 m/s in SI or 32 ft/s in English units). In short, I_{sp} can be thought of a compact description of Tsiolkovsky Rocket function for a specific design.

2.1.2 Rocket launch and space travel

Having explained how thrust is generated in a rocket and introduced important performance parameters such as ΔV (ref. Section 2.1.1), we illustrate their importance in this section. In space, every rigid body moves about along orbits; the Moon orbits the Earth; which, along with other neighboring planets, orbits the sun; and the solar system, along with nearby stars, all orbit the center the of the Milky-way galaxy. Similarly, spacecrafts, satellites, and even a stone thrown within the atmosphere are bound to orbits about the center of the Earth. The mechanics of orbital bodies are well understood. Orbits can be classified as circular, elliptical, parabolic, or hyperbolic. During an interplanetary mission, the trajectory of a spacecraft generally consists of patches of circular and/or elliptical orbits. Circular sections of the trajectory usually correspond to stationary phases of the mission (similar to taxi for an airplane) in preparation for a phase of acceleration towards a higher or lower orbit; as shown in eq. 2.1.20, the speed (V_c) of an object in circular orbit (2.1.20) about a body depends on the mass (M) of the latter body and the separation (r_c) between their respective centers of masses:

$$V_c = \sqrt{\frac{GM}{r_c}}. \tag{2.1.20}$$

Trajectories of transfers between the stationary states consist of elliptical sections. In order for a spacecraft to reach a higher elliptical orbit from some circular orbit, it must (instantaneously) add an increment ΔV to its original speed of V_c (2.1.21).

$$V_e = V_c + \Delta V = V_c\sqrt{1 + \frac{r_p - r_c}{r_p + r_c}} \tag{2.1.21}$$

The incremental change in velocity can be impulsive (in high thrust vehicles) or slow (in low thrust vehicles) [5]. The new speed V_e places the spacecraft in an elliptical

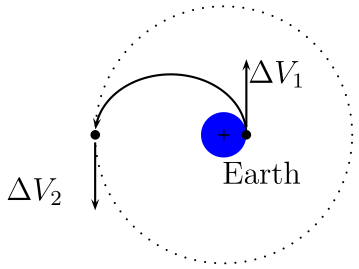

Fig. 2.4: Illustration of the acceleration process of a spacecraft from launch to its placement planetary orbit

trajectory whose periapsis and apogee are r_c and r_p, respectively. Equation (2.1.21) also applies to the opposite scenario; that is, a transfer from an elliptical orbit to a smaller circular orbit. In the latter case, the spacecraft would decelerate from V_e to V_c by firing its rocket in a direction that is opposite to its motion.

As a practical example, let's consider a one-way Earth-to-Mars trip; in the while, we ignore atmospheric effects during lauch and reentry and the orbital motion of any celestial body involved. At the start of the trip, the spacecraft is sitting on its Earth-based launch pad. The total ΔV required to elevate and keep the spacecraft at an altitude of about 500 km—where it can follow a stable orbit with negligible atmospheric perturbations—is: $\Delta V_E = |\Delta V_1| + |\Delta V_2|$, which states that two successive accelerations phases make up orbit-placement maneuver (Figure 2.4):

- a ΔV_1 to perform an elliptical transfer from the Earth surface to the stationary orbit
- a ΔV_2 performed from the stationary orbit mark to keep it there by thrusting against the spacecraft's direction of motion

From that transitionary orbit, the spacecraft performs a third velocity increment for an elliptical transfer for the longest strip of its journey towards a stationary orbit

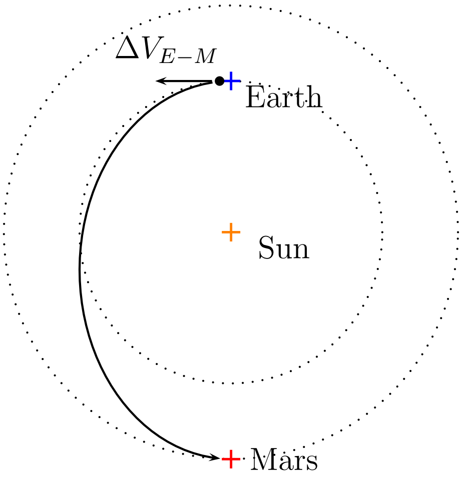

Fig. 2.5: Acceleration for Earth-to-Mars Hohmann transfer

about the destination planet—Mars, in our example. The ΔV-requirement for this elliptical transfer is minimal [17]—in which case, one speaks of a Hohmann transfer (see Figure 2.5). For this section of the Mars-mission, an increment ΔV_{E-M} transfers the spacecraft from the Earth orbit to a point outside the influence of the Martian atmosphere.

From that point, a reduction of speed by ΔV_M places the spacecraft into a stable stationary circular orbit (Figure 2.6); which is suitable for scientific probing of Mars or for stationing in preparation for descent on its soil.

When planning for a space mission, the financial budget limits the available energy or, equivalently, the available ΔV; which in turn, sets the trip duration. Once the ΔV-requirement is set, it becomes obvious from the Tsiolkovsky Rocket Equation (Section 2.1.1), that the trip will require more or less fuel expenditure; which, respectively translates into less or or more room for payload in the spacecraft depending on the magnitude of exhaust speed that the rocket is capable of achieving.

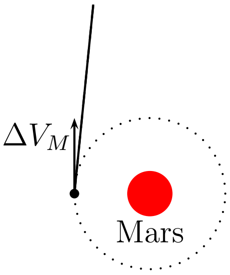

Fig. 2.6: Deceleration for stationary-orbit positionning around Mars

2.2 Overview of operational propulsion concepts

2.2.1 Chemical propulsion

Chemical propulsion is the first concept to be successfully applied to space travel and has reached a high level of maturity since the successful launch of satellites by the Soviet Union in the late 1950s. Figure 2.7 illustrates a chemical rocket consisting of a propellant storage system, a combustion chamber, and a convergent-divergent nozzle. A fuel and an oxidizer in liquid or solid form react to generate heat in the combustion chamber. Products of the chemical reaction form in this chamber at high pressure (P_c) and temperature (T_c). Due to a lower ambient pressure (P_e) at the exit plane of the thruster, the combustion products expand (accelerate) towards the thruster exit at some exhaust velocity (ref. Section 2.1.1). The expansion process is facilitated by the structure of the nozzle. Once produced in the combustion chamber, the subsonic exhaust ($Mach < 1$) accelerates in the convergent section of the nozzle until it reaches sonic speed ($Mach = 1$) at the 'throat'—where the waist-diameter of the nozzle is minimal. Beyond the throat, the exhaust speeds up beyond $Mach$ 1 owing to the divergence of the nozzle. By relating the loss of thermal energy of the combustion products to their kinetic energy gain from the moment of their creation to their emission across the exit plane at u_e and assuming that the gases are perfect and that the nozzle is shaped so to ensure an isentropic expansion (flow acceleration without energy loss to the environment) [16], one can show that the ‘ideal’ exhaust speed of a chemical rocket (with $P_e = 0$) is thermodynamically limited by the temperature of the combustion chamber (T_c), the ratio of the specific heat at constant pressure to that of the specific heat at constant volume (γ), and the molecular weight of the exhaust species (M):

$$u_{e,max} = \sqrt{\frac{2\gamma}{\gamma - 1}\frac{RT_c}{M}}; \tag{2.2.1}$$

in which R is the Universal Gas Constant. As evident from eq. (2.2.1), $u_{e,max}$ has no theoretical ceiling. In practice, however, $u_{e,max}$ is upper-bounded since $\gamma \approx 1.2$ for most propellants; $T_c < 3000\ K$ to prevent the melting of the chamber's structural components; and $M \approx 20\ g/mol$ for the exhaust products of the light propellants such as liquid hydrogen and liquid oxygen mixtures. Due to these constraints, the maximum achievable exhaust speed is on the order of 4 km/s for chemical rockets; many modern rockets are able to generate exhaust velocities of this magnitude: NASA's Space Shuttle main engine (SSME) with $u_e = 4550\, m/s$ is one such example.

Applying this exhaust speed to the one-way Mars mission, with a mission-ΔV of 6 km/s (recall Section 2.1.2), one finds via the Rocket equation (2.1.15) that about $4/5^{th}$ of the spacecraft mass must be propellant; which is viewed by many as an exorbitant expenditure to send scientific equipment—let alone humans to other planets. Ingenious ideas including the use of multi-stages and strap-on boosters have pushed the performance of chemical rockets a bit further than the aforementioned practical limit and are common recourses today for reducing fuel mass. Still, the consensus remains that chemical propulsion has reached the plateau of thermodynamic efficiency. The use of chemical propulsion during an entire interplanetary trip gets increasingly impractical as the mission-ΔV required for travel between the home and destination planets increases; but, for shorter trips such as propelling a craft across the Earth atmosphere (as in Figure 2.4), it remains the method of choice due to its large thrust capability.

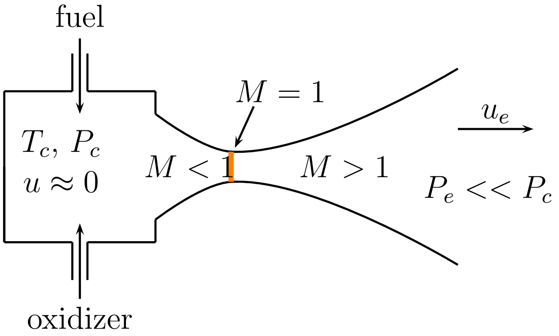

Fig. 2.7: A sketch of a chemical rocket

2.2.2 Electric propulsion

Higher exhaust velocities are needed to raise the payload capability and lower the fuel requirement of spacecrafts. One way to achieve this is to apply an external propulsive energy to the exhaust particles—instead of relying on the thermodynamically limited internal energy of the propellant. When using an electric power generator to supply propulsive energy to a rocket's propellant, one speaks of Electric Propulsion. The rocket equation eq. (2.1.15) still applies in this case; unlike in chemical propulsion, however, the exhaust speed is no longer a parameter that is set by the combustion, but depends on the weight of the power source and its electric-to-kinetic energy conversion efficiency via the following two respective parameters:

power-to-mass ratio: $\zeta = P_E/M_E$ defined as the ratio of electric power to the mass of the generator

thruster efficiency: $\eta = \frac{1}{2}\dot{m}u_e^2/P_E$; that is, the ratio of kinetic power in the exhaust stream to the electric power input

Based on these parameters, Turner [8] arrived at the following expression of the ΔV of an electric thruster at burnout:

$$\Delta V = u_e \, ln \left(1 + \frac{2\eta\zeta t}{2\eta\zeta t \frac{M_D}{M_P} + u_e^2} \right). \tag{2.2.2}$$

where M_P and M_D refer to the propellant mass and dry mass (structure, propellant tanks, payload) and t denotes the mean-time to burn all the propellant and is defined from $M_P = \dot{m}\, t$—where $\dot{m}$ denotes the constant mass flow rate (assumed constant).

2.2.2.1 Electrothermal Propulsion

An electrothermal propulsion system is similar to its chemical counter-part. The random kinetic energy of the particles making up a heated propellant in a high-pressure chamber is transformed into ordered kinetic energy as the bulk of the propellant expands along the axis of a convergent-divergent nozzle and is exhausted at high speed for thrust generation. Unlike chemical propulsion, however, the thermal energy of the propellant no longer originates from the bond-energy released during an exothermic reaction between a fuel and an oxidizer; rather, the propellant heat source consists of a metallic coil (resisto-jet) or an electric arc (arc-jet). Hence, in both cases, an oxidizer is no longer needed. This makes the choice of propellants with smaller molecular weights possible—-thereby yielding higher exhaust velocity (via eq. 2.2.1). As evident from the following, this translates to a lower thrust. From the definition of the thruster efficiency presented in the beginning of this section and that of the thrust (2.1.7), we note that $Tu_e = 2\eta P_E$; which means that the higher exhaust velocity capability of an electrothermal thruster yields a lower thrust than a chemical rocket of comparable jet power.

Resisto-jets (Figure 2.8) can generate exhaust speeds two times faster than chem-

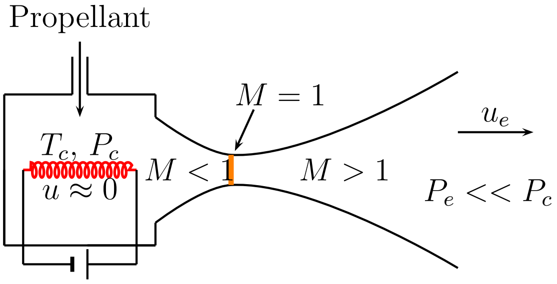

Fig. 2.8: A sketch of a resistojet

ical thrusters can with the same propellant; which allows for a greater payload capability (via eq. 2.1.15). But, their thrust is usually much smaller (up to one-millionth smaller) than chemical thrusters. A natural question might arise as to what good is such a thruster. The answer is none—at least and definitely not—in the neighborhood of the earth surface where such a thruster is barely good enough to lift 100 grams—and that, excluding atmospheric drag. In practically weightless and drag-free space, however, such low thrust capability is ideal for station-keeping of communication satellites for example; for, it allows them to overcome small drifts (due to slight upper-atmospheric drag) from their orbit during the long life-span of their missions (typically 10 years or more). A major limitation of resisto-jets is that the temperature of the gas is limited by the finite melting-point of the heater-wire, which restricts any further increase in the gas temperature and hence of the exhaust velocity (through eq. 2.2.1). Moreover, thermodynamic inefficiencies arise due to the inhomogeneous heating (heating is localized near the heater) and radiative losses; as a result, resistojets tend to have have high electric efficiencies on the order of 80% [18].

DC Arc-jets (Fig. 2.9) constitute another category of electrothermal thrusters. In this case, the electrical energy directly heats the propellant without any intermediate medium (like a heater wire in resisto-jets). The propellant is injected in a chamber, in which a static electric field acts due to the potential difference between two electrodes (anode and cathode). In this zone, the propellant is ohmically heated such that ionization and subsequent conduction of ions and electrons towards the electrodes occurs in a thin luminous region region called an arc (similar to lightning during a storm) within the bulk of the propellant. The high energy, concentrated within the arc, propagates through the propellant in the form of heat—a manifestation of the random motion of neutrals resulting from their collisions with electrons and ions. The arc is generated in a zone of minimal waist area downstream of the cathode (cylindrical) and upstream of the anode (hollow and nozzle-shaped); in this region, the plasma flow is sonic and involves complex acceleration, collisional, and recombination processes that are beyond the scope of this section. Beyond the region containing the arc, the waist-diameter of the anode increases; which, leads to further expansion of the sonic flow towards the exit, where the exhaust velocity can be as high as 20 km/s. The direct heating of the propellant (as opposed to contact heating by a metal) leads to higher temperatures than is possible in resisto-jets, which leads to a high exhaust speed (recall eq. 2.2.1). Further increase in the temperature to yield greater exhaust speeds is limited by the finite melting point of the metallic electrodes. The efficiency of thermal-to-kinetic energy conversion (thermodynamic efficiency) is not just affected by radiative heat losses as in resisto-jets, but also by process of ionization without which no arc would form in the first place! Ionization and dissociation (depending on the propellant choice) further adds to the complexity of arc-jets. These loss processes lead to a smaller electric efficiency (about 40%) in arc-jets than possible in resisto-jets. In spite of its low efficiency, complexity, and many engineering challenges it poses, the arc-jet remains the prefer

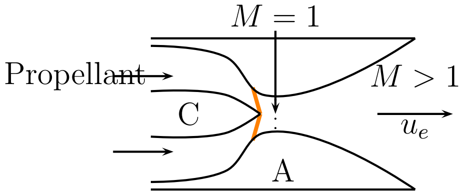

Fig. 2.9: A sketch of an arc-jet

2.2.2.2 Electrostatic/magnetic propulsion

To avoid any confusion with other authors' nomenclature, we start this section with the following clarification: we will use 'electromagnetic' as a generic adjective in reference to a class of propulsion systems relying on either electrostatic or magnetic forces or their combined effect for thrust generation.

Though electrothermal thrusters have higher exhaust velocities than their chemical counterparts, the temperature of the propellant or the thermal energy that can be imparted to it is limited by the melting point of the structural and/or electrical components in contact with it. This imposes a natural limit on the exhaust velocity, which we recall from (2.2.1) is inversely proportional to the temperature. So, to achieve higher exhaust velocities, alternative propulsion concepts that do not rely on thermal-to-electric energy conversion must be considered; that constitutes the main advantage of electromagnetic propulsion over chemical propulsion. In this propulsion concept, electric and magnetic energies are directly applied to the propellant for its ionization and acceleration; this leads to greater exhaust velocities than electrothermal rockets are capable of since the chemical nature of the propellant or melting of structural components are no longer relevant. Of the many known electrostatic and magnetic thruster concepts, two that have successfully been tested and are currently of use in space programs across the globe are ion and Hall thrusters [8].

Ion thrusters (Fig. 2.10) produce thrust by accelerating ions across a high-intensity electrostatic field between two parallel flat gridded electrodes (G_1 and G_2). Usually, the ions are produced in a cylindrical container (discharge chamber) by the impact of electrons with a non-reacting gaseous propellant (usually a noble gas), which is slowly metered into the discharge chamber. The electrons are thermionically emitted from a cylindrical cathode that is inserted in the upstream end (relative to the ionic flow) of the chamber. The chamber's inner wall, which acts as an anode at a slightly higher electrostatic potential (V_A) with respect to the cathode (V_C), attracts the electrons. Before they reach the anode, the electrons are trapped along helicoidal paths centered about magnetic field lines generated by O-ring shaped magnets that line the inner wall of discharge chamber. When electrons, with kinetic energies in excess of the first ionization potential, collide with neutrals, they become ionized. This initiates a plasma discharge in the chamber that is sustained by a steady stream of propellant and electron emission. In response to a higher density gradient of ions in the upstream region of the discharge chamber, ions diffuse downstream and reach the first grid (at cathode potential, i.e. $V_{G_1} = V_C$); at that location, a large electric field set up by the second grid (at a potential $V_{G_2} << V_{G_1}$) accelerates the ions, leading to until their emission from the second grid at high exhaust speeds. When the electrostatic energy is converted to kinetic energy without any losses and not accounting for the plasma potential, a simple balance between the two forms of energies reveals that the exhaust speed depends only on the charge-to-mass ratio of the propellant and the potential difference ($\Delta V_G = V_{G_2} - V_{G_1}$) between the grids:

$$u_e = \sqrt{2\frac{q}{m}\Delta V_G}. \tag{2.2.3}$$

Unlike in chemical and electrothermal propulsion where propellant temperature was found to be a limiting factor on the exhaust speed, no such ceiling exists in the case of ion propulsion as long as an external power supply provides the necessary 'quiescent' electrostatic field E_o for some inter-grid spacing d (since $E_o = \frac{\Delta V_G}{d}$). This capability for large exhaust speeds constitutes a major advantage of electromagnetic propulsion over electrothermal propulsion.

Still, ion thruster designers do not aim for the highest possible exhaust speed, for efficiency and performance parameters are weighted in heavily in its selection. As evident from both expressions of ΔV provided in eqs. 2.1.15 and 2.2.2, increasing the exhaust speed for some ΔV-requirement reduces the propellant requirement, and hence allows for greater payload mass; this constitutes no new information in that, as noted in the previous sections, the same remark was made in both chemical and electrothermal rockets. But a further non-dimensional analysis of eq. 2.2.2 by Sutton [3] by some characteristic velocity $U = 2\eta\zeta t$ yielding

$$\frac{\Delta V}{U} = \frac{u_e}{U} ln \left[1 + \frac{1}{\frac{M_D}{M_P} + \left(\frac{u_e}{U}\right)^2}\right]; \tag{2.2.4}$$

reveals that, for some parametric value of the ratio of payload to vehicle dry mass, the variation of ΔV with exhaust velocity is upper-bounded. The maximum value of ΔV occurs at some optimal value of the exhaust velocity—independently of thruster efficiency, η, and power-to-mass ratio, ζ. This concept can be understood from the fact that a large exhaust velocity requires a more massive power plant; moreover, with increasing exhaust velocity, the rate of increase of the power supply mass rises so much as to overcome any propellant savings accompanying that very velocity increase.

In sum, the optimal exhaust velocity can be thought of as that speed at which the payload mass saving is maximized for some mission ΔV-requirement. As we return to the non-dimensional form of the equation (2.2.2) and consider Turner's analysis, one finds—once the payload mass fraction is set to its optimal value—that there exists a critical power-to-mass ratio below which u_e deviates from its optimal value and above which the power supply source becomes unnecessarily high unless it is matched with a higher ΔV than the mission requires. From the aforementioned remark, one can appreciate why the highest possible exhaust speed is not systematically aimed for in ion thruster; rather, efforts are invested in lowering the speed to its optimal value via the common approach of using heavier propellants such as krypton, xenon [3], or mercury.

Aside from the aforementioned practical limit on the exhaust velocity, there is a theoretical limit on the mass flow rate due to a threshold on the current density commonly referred to as the 'space-charge limit'. This limit is due to a local decrease of the quiescent electric field downstream of the first grid due to a counter-acting opposing field generated by an accumulation of positive charges as ions flow through the gap. As the ionic mass flow rate—hence the current density, j, via the relationship $\dot{m} = MjA/q$ (A and M respectively denote area and particle mass)—increases, the strength of the opposing field progressively cancels the accelerating field immediately past the first grid until the ionic flow starts a reversal process; at which stage, the ionic current density becomes 'space-charge limited'. The threshold current associated with this state depends on the grids' voltages and their separation distance. Informative descriptions of the process including explicit derivations of the space charge limit can be found in Goebel [19], Turner [8], and Lieberman [20].

Based on (2.1.7), the combined effect of a limited exhaust velocity and mass flow

---

[3] Aside for its heavier mass, the use of xenon is even more prevalent as a propellant in ion thrusters due to its non-toxicity to the structural components of the thruster and ease of storage in liquid phase.

rate result in very small thrust density, which constitutes a distinct characteristic of ion thrusters[4].

Aside from a low thrust, ion thrusters suffer from a host of life-limiting and performance issues including: erosions of cathode and grid due to ionic bombardment; energy losses associated with the neutralization [5] of the exhaust beam; collisional losses induced by neutrals; and divergence of the exhaust ionic beam, which is detrimental to the already low thrust. Currently, these losses are overcome by providing electrons with energy much in excess of the first-ionization potential of neutrals (by emitting high-energy electrons from the cathode, for example). Still, provided that high enough energy is imparted to the electrons to ionize a vast majority (80-90%) of neutrals and that the exhaust velocty is high enough, ion thrusters constitute high-efficiency devices; currently efficiencies greater than 80% are achievable.

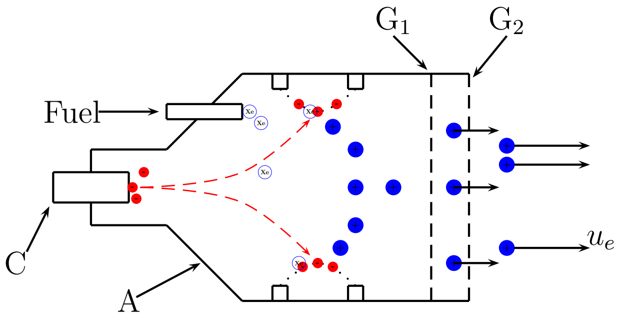

Fig. 2.10: A sketch of an ion thruster

Despite this high efficiency of ion thrusters, ions remain the sole contributor to

---

[4] for example, the NSTAR ion engine that propelled the Deep Space 1 probe on a fly-by mission to the asteroid Braille [21] had a maximum thrust of just 92 mN

[5] Neutralization consists of the emission of electrons from an auxiliary cathode that is mounted on the thruster to prevent an undesirable build-up of electrostatic charge.

the thrust; and as mentioned in the previous paragraph and as in arc-jets, they constitute a ‘nuisance’ to the thrust generation process [8]. This latter fact combined with a low thrust and a high degree of technical complexity[6] associated with this class of thrusters has shifted much preference to the Hall thruster, which relies on a simpler technological design and consists of fewer components. In Hall thrusters, both electrostatic and magnetic fields participate in the process of thrust generation. These devices operate in a somewhat similar fashion to ion thrusters in that a noble gas gets ionized by electrons, thermionically emitted from a cathode, and that ions are accelerated by an electrostatic field. However, they differ from ion thrusters in that the ionization occurs within an open annular discharge channel. Also, the accelerating electrostatic field exists between the anode and a static doughnut-shaped current of electrons (near cathode potential) concentrated near the exit-plane of the thruster along the center-line of the channel. This ‘Hall-current’, which owes its name from the Hall-effect [20] arises from the interaction between perpendicular components of the electrostatic and magnetic fields (refer to Chapter III.

The walls of the discharge channel usually consist of a metallic or ceramic material (non-conducting); the former case applies to the Thruster with Anode Layer (TAL) subclass [7] and the latter case applies to the Stationary Plasma Thruster (SPT) subclass [8]. In the case of the SPT, the discharge channel is deep and the ionization occurs very close to the anode. Moreover, the walls of its channel usually consist of Boron Nitride with a high-yield secondary electron coefficient which contributes to an increase in the density of electrons—upon ionic and electronic bombardment—near the anode and, hence, enhances the ionizing process. In comparison to the SPT, the TAL has a shallower discharge channel and metallic walls (at anode potential). This causes the action of the electrostatic field to begin downstream of exit plane. As a

---

[6] For example, the spacing between grids must be maintained below a certain sub-milliliter threshold and the holes of the gridded electrodes must be aligned

[7] The D-100 is an example Thruster with Anode Layer [8]

[8] The SP-100 is an example of an Stationary Plasma Thruster [8]

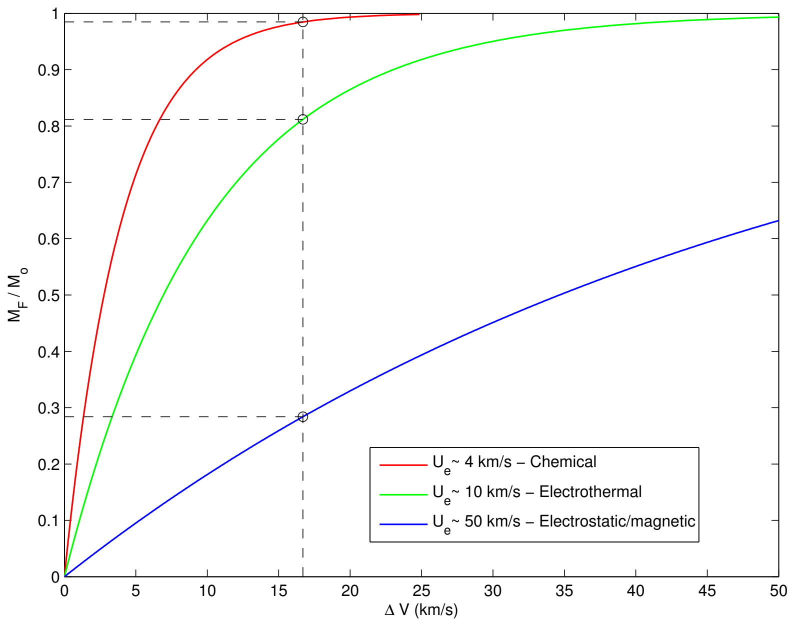

Fig. 2.11: Comparison of the variation of the fuel-to-dry mass ratio with mission-ΔV between chemical, eletrothermal, and electrostatic/magnetic propulsions

result, the Hall current region also lies further downstream (outside of the discharge channel); this further causes the ionization of neutrals and acceleration of resulting ions also starts outside of the channel.

In sum, for the Hohmann transfer involved in the Earth-to-Mars mission described in Section 2.1.2 (Figure 2.5), an electrostatic/magnetic rocket proves to be a better candiate than chemical and electro-thermal rockets considering the fuel-saving capability; this is demonstrated in Figure 2.11 illustrating the variation of fuel-to-dry mass ratio with ΔV at exhaust velocities representative of each propulsion system for a mission-ΔV of 16.7 km/s—based on Turner's estimation of a 9-month journey to Mars [8]. Though the low thrust capability would not permit the vehicle to reach a ΔV_{E-M} as quickly as a chemical rocket would; however, the former rocket could acquire the required ΔV over a longer period by accumulating small ΔVs after full cycles of a spiral orbit [3].

A comparative performance study by Fiehler [5] between ion and Hall thrusters reveals that the latter class is more advantageous when considering the Earth-to-

Mars transfer-mission during about 300 days: a Hall thruster, though functionning at a lower I_{sp} range (on average 2450 sec) could deliver the same payload mass using 50% less power (from 60 kW) than an ion thruster capable of higher I_{sp} (on average 3500 sec). While the aforementionned comparison demonstrates a clear advantage of Hall thrusters in interplanetary missions, it overlooks an important point: operating at such power levels and I_{sp} proves to be inefficient; optimal efficiencies are associated to each set of I_{sp} and power settings [5]. Furthermore, distributions of efficiency over I_{sp}, as well as varitions of I_{sp} with power, are discrete (1-10 kW range). Expanding these envolopes to higher power levels requires a better understanding of the magnetic field structure in Hall thrusters' discharge channel [10, 13, 14, 11].

As a summary, Table 2.1 lists performance parameters of the four most popular and operational electric thrusters as reported from various sources [3, 4, 5].

Thrusters	T (mN)	Isp (sec)	η (%)
Resito-jet	200-300	200-350	65-90
Arc-jet	200-1000	400-1000	30-50
Ion engine	up to 100	1500-5000	50-80
Hall thruster	10-250	1500-3500	30-65

Tab. 2.1: Performance parameters of various operational electric thrusters [3, 4, 5]

CHAPTER III

Structural and Functional Descriptions of the P5 Hall Thruster Revolving around the Magnetic Field

3.1 Structural components of the P5

The P5 is a laboratory-class 5 kW coaxial Hall thruster (of the SPT category) built in 1998 by the University of Michigan and the US Air Force for a better understanding of the physics of the physical mechanisms that govern the functioning of this type of electric thrusters—commonly used for orbit-maintenance of small satellites and orbit-transfer of spacecraft with a large payload requirement (recall Section 2.2.2.2). The broken 3D view in Figure 3.1 describes the simple symmetric geometry of the P5 and details its main components along with their material constituents. As shown in Figure (3.1), the thruster consists of a few components; most of which make up a magnetic circuit of primary importance to its proper functioning. These components can be categorized as follow:

- A set of nine magnets consisting of a wider central magnet (‘inner magnet’) and eight thinner peripheral magnets (‘outer magnets’). Each magnet is made of a central cast-iron core housed in a magnetic stainless steel bobbin, around which

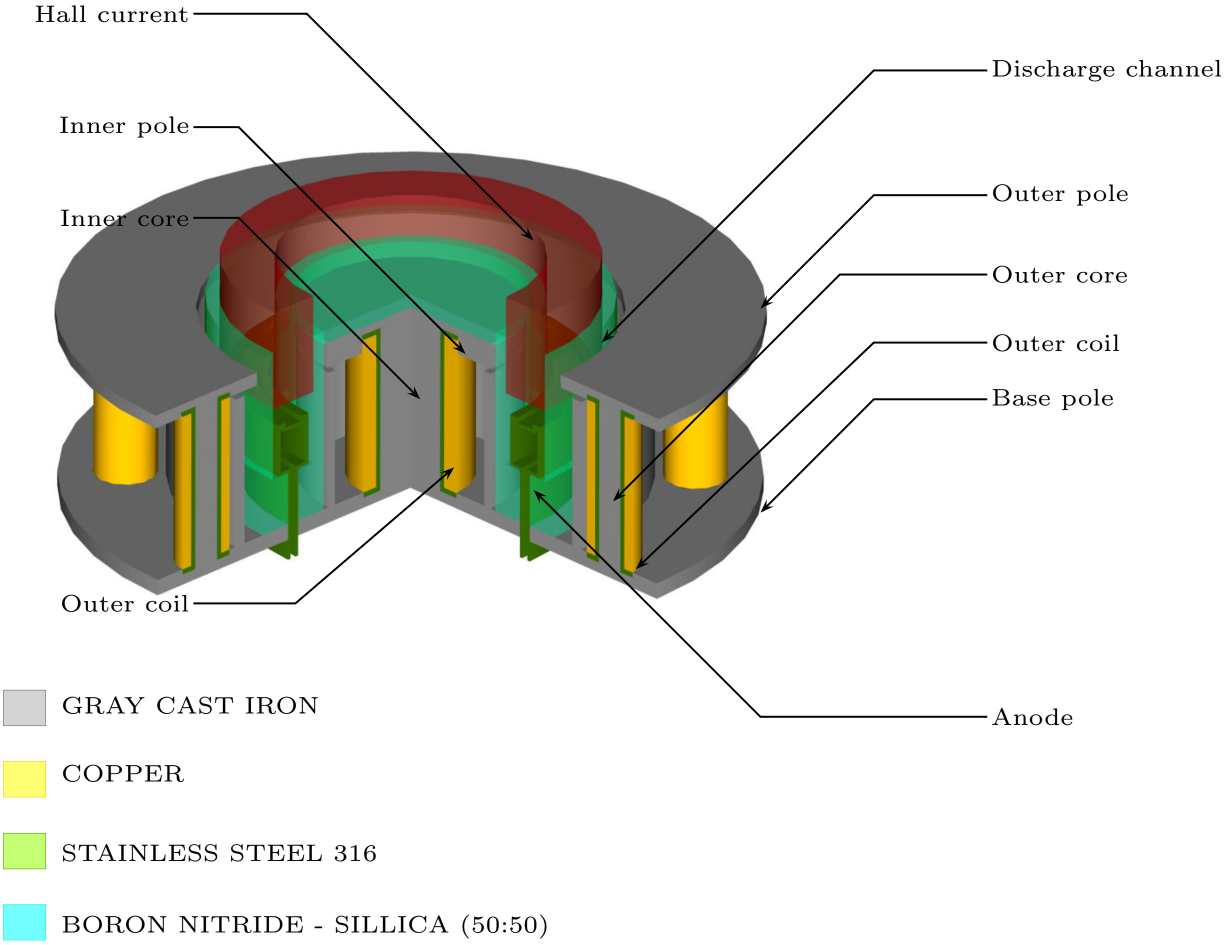

Fig. 3.1: Broken-view of the P5 illustrating its main structural components

Power (kW)	1.6		3.0	
Magnets	inner	outer	inner	outer
No. windings	240	120	240	120
Coil current (A)	2	1	3	2

Tab. 3.1: Coil settings of the P5's electromagnets at two nominal power levels

a copper wire is wound. At thruster power settings of 1.6 kW and 3.0 kW, the number of windings in each magnet is unchanged but different currents are run through inner and outer electromagnets. Coil settings at the two power settings are listed in Table 3.1. Note from the table that the currents through the inner and outer magnets flow in opposite directions; this ensures a predominantly radial magnetic flux density vector oriented from the inner to the outer magnets.

- Three cast-iron poles: a base pole, an inner pole, and an outer pole that channel the magnetic flux density ($\vec{B}$) as it emanates out of the inner magnet and sinks in the outer magnets.

- Two cast-iron screens consisting of an inner screen (closest to the central magnet) and an outer screen (closest to the peripheral magnets) that help guide the magnetic flux away from the anode and maximize the radial component of the magnetic field in the discharge channel for a better containment of the Hall current and optimal propellant acceleration.

- A discharge channel that houses a propellant feed-line at its base. The propellant feed-system emits gaseous neutral xenon into the annular region of the discharge channel (or annulus) and also functions as an anode. There are discrepancies in the literature as to the material constituent of the anode. Gulczinski [22] attributes magnetic stainless steel S 316 to it, while Haas [1] refers to its material composition as non-magnetic stainless steel 324. This may have prompted Haas [1] to not include the anode in their modelling of the P5's magnetic field topology. Regardless, we chose to assign steel S 316 to the anode because we found better agreement between vacuum experimental measurements and MagNet6 simulations of the field topology (as it will be demonstrated in Chapter IV).

- Other thruster parts include a ceramic guard disk that shields the inner pole from particle sputtering; and bolts that connect the various thruster parts.

Aside from a magnetic circuit, a Hall thruster also consists of an electric circuit. As shown in Figure 3.4, the electric circuit consists of two main constituents:

- a negatively biased cathode from which electrons are thermionically emitted
- a positively biased anode through which neutrals are injected into the discharge channel

3.2 Propellant utilization and plasma processes for thrust generation

In the previous chapter (Section 2.2.2.2), an overview of Hall thrusters is given, their advantage over other propulsion concepts is presented, and their ranges of applicability in diverse space missions is explored. In this section, we attempt to explain the main physical processes that lead to the generation of thrust in a coaxial SPT thruster such as the P5. As a preliminary, we begin by describing two important concepts:

- the plasma (Section 3.2.1), which is a state that the propellant assumes in all electromagnetic propulsion systems
- the Hall current (Section 3.2.2), which is a toroidal (doughnut-shaped) current of electrons that is specific to coaxial Hall thrusters

3.2.1 Description of the plasma discharge

The plasma discharge of a Hall thruster consists of electrons and ions interacting with applied and induced electric and magnetic fields. Though not as well-known as the other three states of matter (solid, liquid, and gas), plasma (or "fourth-state of matter") makes up 99% of the visible universe [23]. In nature, a plasma generally results from heating matter to temperatures much in excess of those that we experience on Earth. For example, in the environment of stars, temperatures can be as high as millions of degrees. The thermal motion of atoms in such an environment induces neutral-neutral and neutral-electron collisions. In some cases, the collisions might be inelastic and energetic enough to cause the atomic energy state to rise beyond the ionization potential; in which process, at least one electron gets stripped from the atoms and ions are formed. In other cases, neutral atoms get promoted to excited states and subsequently get de-excited to lower energy states and emit light. The resulting ions, electrons, and neutral atoms constitute a plasma, which sustains itself from the fields induced by its charged particles as well as the radiation emitted by some its excited atoms and ions.

However, not any high-temperature gas containing charged and radiating particles qualify as a plasma; in fact, no strict definition of a plasma is known to us. According to Chen [23], the agreement is simply widely spread among physicists that any system of particles exhibiting the following properties qualifies as a plasma:

1. Large length scale:

   The spatial extension of a plasma, L, must be much greater than some characteristic length scale, λ_D, defined as:

$$\lambda_D = \sqrt{\frac{kT_e}{4\pi n_e e^2}}, \tag{3.2.1}$$

   where T_e is the electron temperature and n_e is the electron number density (number of electrons per unit volume). λ_D can be interpreted as the minimum mean separation distance (sheath), beyond which a charged particle's thermal energy overcomes the local electrostatic attractive potential. Due to their low mass, highly mobile electrons tend to agglomerate within small spheres of radius λ_D, in which electric field gradients are significant. Near and away from these spheres, the electric field gradient decreases progressively until the motion of local electrons is no longer influenced by electrostatic effects but by random thermal effects. In fact, the electric field gradient becomes negligible throughout most of the extension of the plasma (assuming $\lambda_D << L$); resulting in a near-balance between electron and ion number densities [1] (n_e and ions n_i, respectively). This condition, termed quasineutrality, can be inferred from Poisson's equation [20, 23] by setting the electric field gradient to zero:

$$\epsilon \nabla \cdot \vec{E} = e \left(Z n_i - n_e \right) \approx 0, \tag{3.2.2}$$

where Z and e respectively denote ionic charge number electron charge. Quasineutrality is readily verified in the acceleration zone of the P5 by computing the electric field from known plasma potential (ϕ) measurements [1], which, when applied to the Poisson equation reveals that $\left| \frac{n_i - n_e}{n_e} \right| \approx 10^{-6}$.

2. Collective behavior:

   While $L >> \lambda_D$ must hold, the plasma density n (assuming quasi-neutrality: $n_e = n_i = n$) must be large enough for the plasma to exhibit collective behavior; that is, an ideal state in which the plasma sustains its charge content by setting up fields that control the motion of its constituent-particles so that they do not crowd within appreciably large zones or separate by generating distinct streams of opposite charges that would permanently depopulate the plasma.

---

[1] The number density, denoted n, stands for the number of particles per unit volume.

3. Low collision frequency:

   Collisions between charged particles must not be too frequent as to lead to a fluid-like behavior—characterized by a motion of particles dominated by diffusion and shear and pressure forces. Fewer collisions preserve the potential for long-range action of electric and magnetic forces within the plasma, which helps preserve the collective behavior of the plasma. According Goebel [19], a fluid-model can be used to describe the plasma in the discharge of Hall thrusters. The fact remains that there is no definite way categorization of the ionization level in a plasma (i.e. collisionless, weakly ionized, or highly ionized).

   A Hall Parameter (Ω), defined as the ratio of cyclotron frequency (ω_c) (refer to Section 3.2.2) to the collision frequency of electrons (ν), is commonly used to gauge the prevalence of collisions in Hall thrusters' discharge channel. Its aforementioned expression implies the mean number of turns (spirals) that electrons effectuate during their azimuthal ExB-drift in the Hall current (Section 3.2.2) before undergoing a collision. The Hall parameter is also defined as the ratio of the ExB-drift current (azimuthal) to axial current densities (J_H and J_z, respectively). This latter definition stems from the following fact: electrons become thermalized (that is, their motion becomes randomized and their mean directed kinetic energy is lost) after undergoing a collision, the electrostatic force momentarily takes over the lorentz force (until their velocity rises significantly enough to restore the Lorentz force) and the axial component of their flow rises. Hence, the following distinctions can be made [1]:

   - $\Omega << 1$ implies that collisions are very frequent and the electron flow is predominantly axial
   - $\Omega >> 1$ implies that collisions are very scarce and the electron flow is predominantly azimuthal around the discharge channel.

The above definition hints to the fact that a Hall parameter's order of magnitude, instead of its exact value, matters most. Using the second definition of the Hall parameter (based on current densities) Haas estimated its magnitude along the centerline of the P5's discharge channel at 1.6 kW and 3 kW to increase from about 1 (25 mm from the anode) to 1000 (from the exit plane to 60 mm from the anode). In the proximity of the anode, unaccounted pressure effects rendered his estimations unreliable [1].

3.2.2 Physical origin of the Hall current

The above definition of a plasma hints to the fact that—outside of sheaths—the motion of plasma particles depends on local fields resulting from the cumulative action of long-range fields. So, to understand the motion of charged particles in a plasma, it is natural to begin with a review of their individual interactions with magnetic and electric fields. We neglect relativistic effects and restrict our interest to the simple case of steady fields. Using these assumptions and considering the action of static electric and magnetic fields $\vec{E} = \vec{E}(x, y, z)$ and $\vec{B} = \vec{B}(x, y, z)$ acting on a particle of charge q and mass m, Newton's Second Law assumes the following form:

$$m\frac{d}{dt}\vec{V} = q\vec{E} + q\vec{V} \times \vec{B}. \tag{3.2.3}$$

As evident from eq. (3.2.3) and recalling our steady-field assumptions, we note that the electrostatic force is time-independent (first term on the right-hand side), while the Lorentz force (second term on the right-hand side) varies with time. Hence, one can anticipate a solution consisting of the superposition between a time-dependent component $\vec{V_L}(t)$ (homogeneous solution) and a time-independent component $\vec{V_E}$ (particular solution) as follow:

$$\vec{V} = \vec{V_L} + \vec{V_E}. \tag{3.2.4}$$

The homogeneous solution is found from solving the homogeneous part of eq. (3.2.3):

$$m\frac{d}{dt}\vec{V_L} = q\vec{V_L} \times \vec{B}. \tag{3.2.5}$$

Differentiating (3.2.5) with respect to time and multiplying both sides with m yields:

$$m^2\frac{d^2}{dt^2}\vec{V_L} = q\left(m\frac{d}{dt}\vec{V_L}\right) \times \vec{B}; \tag{3.2.6}$$

given that $\vec{B}$ does not vary with time. Substituting the time-derivative between parentheses in (3.2.6) by its expression given in (3.2.5), we get (after some algebra):

$$\frac{d^2}{dt^2}\vec{V_L} = \left(\frac{q}{m}\right)^2\left(\vec{V_L} \times \vec{B}\right) \times \vec{B} \tag{3.2.7a}$$

$$\Leftrightarrow \frac{d^2}{dt^2}\vec{V_L} = -\left(\frac{q}{m}\right)^2\left[\left\|\vec{B}\right\|^2\vec{V_L} + \left(\vec{V_L}\cdot\vec{B}\right)\vec{B}\right]. \tag{3.2.7b}$$

In equation (3.2.7b), the term $\vec{V_L}\cdot\vec{B}$ vanishes if we resolve $\vec{V_L}$ into components perpendicular ($V_{L,\perp}$) and parallel ($V_{L,//}$) to $\vec{B}$; this can be proved in the following analysis.

From the definition of a vector cross-product operation, we first note from (3.2.5) that $\frac{d}{dt}\vec{V_L} \perp \vec{B}$ must hold. From this latter fact, we find that a resolution of (3.2.6) along perpendicular and parallel directions to $\vec{B}$ result in the following respective expressions:

$$m\frac{d}{dt}\vec{V_{L,\perp}} = q\vec{V_{L,\perp}} \times \vec{B} \tag{3.2.8a}$$

$$m\frac{d}{dt}\vec{V_{L,//}} = q\vec{V_{L,//}} \times \vec{B} = 0; \tag{3.2.8b}$$

from the latter expression (3.2.8b), we deduce that $V_{L,//}$ is constant. So, if we assume that $V_{L,//} = 0$ at $t = 0$, the same must hold true at any time $t > 0$; hence, $\vec{V_L} = \vec{V}_{L,\perp}$, from which we further deduce:

$$\vec{V_L} \cdot \vec{B} = \vec{V_{L,\perp}} \cdot \vec{B} = 0. \tag{3.2.9}$$

A physical interpretation to (3.2.9) is that the motion of a charge possessing no initial velocity-component in a direction perpendicular to the local magnetic flux ($\vec{B}$) is constrained to move in a plane perpendicular to $\vec{B}$. Applying eq. (3.2.9) to eq. (3.2.7b), we arrive at the following equation:

$$\frac{d^2}{dt^2}\vec{V_L} = -\left(\frac{q}{m}\left\|\vec{B}\right\|\right)^2 \vec{V_L}, \tag{3.2.10}$$

which describes the motion of a harmonic oscillator function. Any arbitrary harmonic oscillator, $f(t)$, obeys:

$$\frac{d^2}{dt^2} f(t) = -\omega^2 f(t), \tag{3.2.11}$$

with a well known solution of the form:

$$f(t) = |\ f(0)|\ \ e^{\pm i\omega t+\delta}. \tag{3.2.12}$$

From the above general expression of a harmonic oscillator, we deduce that the solution, $\vec{V_L}$, to (3.2.10) can be resolved along the $\vec{i}$ and $\vec{j}$ directions as (the 'L' subscript will be omitted for clarity for the time-being):

$$V_x\,\widehat{i} + V_y\,\widehat{j} = |\ V_{x,t=0}|\ \ e^{\pm i\omega_c t}\widehat{i} + |\ V_{y,t=0}|\ \ e^{i(\pm\omega_c t+\delta)}\widehat{j}, \tag{3.2.13}$$

where the oscillation frequency, ω, has been subscripted by 'c' to denote the conventionally accepted terminology of "cyclotron frequency" defined as

$$\omega_c \equiv \frac{|q|}{m}\left\|\vec{B}\right\| \tag{3.2.14}$$

and the phase shift is taken relative to the x-component of the velocity for simplicity.

In its form, eq. (3.2.13) is ambiguous since the relative phase shift (δ) of $\vec{V}_y$ with respect to $\vec{V}_x$ is unknown as well as the sign of the exponential arguments. Knowledge of the sign is important because it reflects the orientation of the particle's motion in our right-handed coordinate system.

One can arrive at a more explicit form solution by applying conservation of energy to the motion during a small time-interval, Δt, during which the particle moves by $\Delta\vec{s} = \Delta\vec{x}\,\widehat{\imath} + \Delta\vec{y}\,\widehat{\jmath}$ as shown in the following equation, that expresses the equivalence between change in kinetic energy and work done by the Lorentz force during the particle's motion:

$$\Delta\left(\frac{1}{2}m\vec{V}\cdot\vec{V}\right) = \left(q\vec{V}\times\vec{B}\right)\cdot\vec{\Delta s}; \tag{3.2.15}$$

which, upon dividing through by Δt and taking the limit $t \longrightarrow 0$, leads to the following expression of the power lost by particle:

$$m\frac{d}{dt}\left(\vec{V}\cdot\vec{V}\right) = \left(q\vec{V}\times\vec{B}\right)\cdot\frac{d\vec{s}}{dt} \tag{3.2.16a}$$

$$= \left(q\vec{V}\times\vec{B}\right)\cdot\vec{V} = 0; \tag{3.2.16b}$$

We know that (3.2.16b) must hold from the fact that $\frac{d\vec{s}}{dt} = \vec{V}$ is perpendicular to $\left(\vec{V}\times\vec{B}\right)$. From the equivalence of (3.2.16a) and (3.2.16b), we deduce that the following must also hold:

$$\frac{d}{dt}\left(\vec{V}\cdot\vec{V}\right) = \frac{d}{dt}\left\|\vec{V}\right\|^2 = 0 \quad \text{or,} \tag{3.2.17a}$$

$$= 2\left(V_x\frac{d}{dt}V_x + V_y\frac{d}{dt}V_y\right) = 0. \tag{3.2.17b}$$

From (3.2.17a), we deduce that the norm of the particle's velocity is a constant of motion; that combined with the earlier statement that $\vec{V}_L = \vec{V}_{L,\perp}$ leads to:

$$\left\|\vec{V}\right\| = \left\|\vec{V}_\perp\right\| = \left\|\vec{V}_{\perp,t=0}\right\| = \left\|\vec{V}_{\perp,t>0}\right\| . \tag{3.2.18}$$

Also, substituting the expressions for the components V_x and V_y from eq. (3.2.13) into eq. (3.2.17b) shows (after some algebra) that eq. (3.2.16b) can only hold if the following two conditions are met:

1. The phase difference between V_x and V_y is $\frac{\pi}{2}$
2. $\left|V_{y,t=0}\right| = \left|V_{x,t=0}\right|$

From the latter expression, together with eq. (3.2.18), we can redefine the moduli of the component-velocities appearing in (3.2.13) as:

$$V_\perp \equiv \left|V_{\perp,t=0}\right| = \left|V_{y,t=0}\right| = \left|V_{x,t=0}\right| . \tag{3.2.19}$$

Applying the above definition, accounting for the proper phase shift, and substituting the result into the homogeneous equation (3.2.13), one finds:

$$\vec{V} = V_\perp e^{\pm i\omega_c t} \left(\widehat{\imath} + e^{i\frac{\pi}{2}}\widehat{\jmath}\right) , \tag{3.2.20}$$

which reveals that the velocity components are complex-valued. Restricting our interest to the real part of the solution (the physically realistic part), we find after some algebra that $\vec{V}$ assumes the form:

$$\vec{V} = V_\perp \left(\cos\left(\pm\omega_c t\right)\ \widehat{\imath} - \sin\left(\pm\omega_c t\right)\ \widehat{\jmath}\right) . \tag{3.2.21}$$

Recalling from (3.2.19) that $V_\perp$ is constant, (3.2.21) hints to a circular motion of the charged particle about $\widehat{k}$, whose orientation is defined by the sign of the arguments of the trigonometric functions; but so far, the orientation of the particle's orbit relative to the right-handed coordinate $(\widehat{i},\widehat{j},\widehat{k})$ is unknown. Such ambiguity comes about because the solution (3.2.21) was found after taking the derivative of the equation governing the motion of the charged-particle; thereby causing a "loss of physics." Substituting the solution (3.2.21) back into the governing equation of motion (3.2.3) and using the fact that $\frac{\|B\|q}{m} = \omega_c \frac{q}{|q|}$, we find that the ± 1 coefficients in the solution stand for $\frac{q}{|q|}$; hence, we arrive at the following final expression of the velocity of the particle due to the Lorentz force alone by rewriting (3.2.21) as:

$$\vec{V}_L = V_\perp \left[\cos\left(\frac{q}{|q|}\omega_c t\right)\widehat{i} - \sin\left(\frac{q}{|q|}\omega_c t\right)\widehat{j} \right] . \tag{3.2.22}$$

The above equation describes a clockwise (along $\widehat{k}$) circular motion for positive charges and a counter-clockwise (along $-\widehat{k}$) circular motion for negative charges.

We are now left with finding the particular part of the solution of eq. (3.2.4). Resolving eq. (3.2.3) into the three spatial components we find :

$$m\dot{V}_x = qE_x + \left(\vec{V} \times \vec{B}\right)_x \tag{3.2.23a}$$

$$m\dot{V}_y = qE_y - \left(\vec{V} \times \vec{B}\right)_y \tag{3.2.23b}$$

$$m\dot{V}_z = qE_z + \left(\vec{V} \times \vec{B}\right)_z , \tag{3.2.23c}$$

where the 'dot'-symbol denotes $\frac{d}{dt}$ for simplicity. For now, we consider one the components of eq. (3.2.3), say along the $\widehat{i}$ direction; which we differentiate by time and into which we substitute (3.2.23b) and (3.2.23c) to find (after some algebra):

$$m\ddot{V}_x = \frac{q}{m}\left[\left(\vec{E} \times \vec{B}\right) + \left(\vec{V} \times \vec{B}\right) \times \vec{B}\right]_x . \tag{3.2.24}$$

Applying the above analysis to the $\widehat{j}$ and $\widehat{k}$ components, one finds analogous expressions to (3.2.24) such that the following expression holds true in general:

$$m\ddot{\vec{V}} = \frac{q}{m}\left[\vec{E} + \left(\vec{V} \times \vec{B}\right)\right] \times \vec{B}, \tag{3.2.25}$$

so that unless the Lorentz force (term between brackets) is zero, the inertial term in (3.2.25) must remain perpendicular to $\vec{B}$ as expressed below:

$$m\ddot{\vec{V}} \perp \vec{B} \Rightarrow \frac{d^2}{dt^2}\left(m\vec{V}\right) \cdot \frac{1}{\left\|\vec{B}\right\|}\vec{B} = 0. \tag{3.2.26}$$

Substituting (3.2.4) into eq. (3.2.26) and recalling that $\vec{V}_E$ is independent of time, we find:

$$m\ddot{\vec{V}}_L = q\left[\vec{E} + \frac{1}{m}\left(\left(\vec{V}_E + \vec{V}_L\right) \times \vec{B}\right) \times \vec{B}\right]. \tag{3.2.27}$$

From (3.2.5), the following must hold true:

$$q\left(\vec{V}_L \times \vec{B}\right) \times \vec{B} = m\dot{\vec{V}}_L \times \vec{B} = 0 \tag{3.2.28}$$

given that $\vec{V}_L \perp \vec{B}$ (as mentioned earlier in eq. 3.2.9). Applying the simplification (3.2.28) to (3.2.27) leads to:

$$\vec{E} \times \vec{B} + \left(\vec{V}_E \times \vec{B}\right) \times \vec{B} = 0. \tag{3.2.29}$$

After expanding the triple cross-product in (3.2.29), applying (3.2.9), and solving for $\vec{V}_E$, we arrive at the following expression for the time-independent component of the particle's velocity; which is commonly termed 'ExB drift' (read 'E cross B'):

$$\vec{V}_E = \frac{1}{\left\|\vec{B}\right\|^2}\vec{E} \times \vec{B}. \tag{3.2.30}$$

Superposing real homogeneous (3.2.22) and particular (3.2.30) solutions of eq. 3.2.3

as prescribed by eq.3.2.4, we arrive at the following final expression of the particle's velocity:

$$\vec{V} = V_{\perp}\left[cos\left(\frac{q}{|q|}\omega_c t\right)\widehat{\imath} - sin\left(\frac{q}{|q|}\omega_c t\right)\widehat{\jmath}\right] + \frac{1}{\left\|\vec{B}\right\|^2}\vec{E}\times\vec{B}. \tag{3.2.31}$$

The particle's trajectory from some arbitrary initial location $\vec{s}_o$ at time t_o to $\vec{s}$ at a later time t becomes, after integrating eq. 3.2.31 with respect to time:

$$\vec{s}-\vec{s}_o = \frac{|q|}{q}\frac{V_{\perp}}{\omega_c}\left[sin\left(\frac{q}{|q|}\omega_c\left(t-t_o\right)\right)\widehat{\imath} + cos\left(\frac{q}{|q|}\omega_c\left(t-t_o\right)\right)\widehat{\jmath}\right] + \frac{1}{\left\|\vec{B}\right\|^2}\vec{E}\times\vec{B}\left(t-t_o\right). \tag{3.2.32}$$

Ignoring the last term of eq. 3.2.32, for the time being, its analysis reveals that the trajectory of the particle, possessing no initial velocity and travelling under the influence of an external magnetic field, consists of a circle of radius R_L whose direction depends on the sign of the charge and whose magnitude can directly be inferred from (3.2.32) as:

$$\|R_L\| = \frac{V_{\perp}}{\omega_c}; \tag{3.2.33}$$

such a trajectory is illustrated in Figure 3.2 for the case of an electron. The trajectory of the electron possessing an initial velocity-component along the direction of $\vec{B}$ is also plotted; in this case, the trajectory assumes the shape of a helix with an axis ('guiding-center') oriented along the direction of $\vec{B}$; for the sake of clarity, the figure only displays two orbits.

As a side-remark, it is interesting to note that the direction of a charge particle's gyration about its guiding-center is such that the induced local magnetic field opposes the local external field. This individual behavior of particles extends to a collective property of a plasma referred to as diamagnetism [23].

When an electric field is applied, eq. 3.2.32 describes the complete motion of the particle due to external electric and magnetic fields. In this case, too, the trajectory of

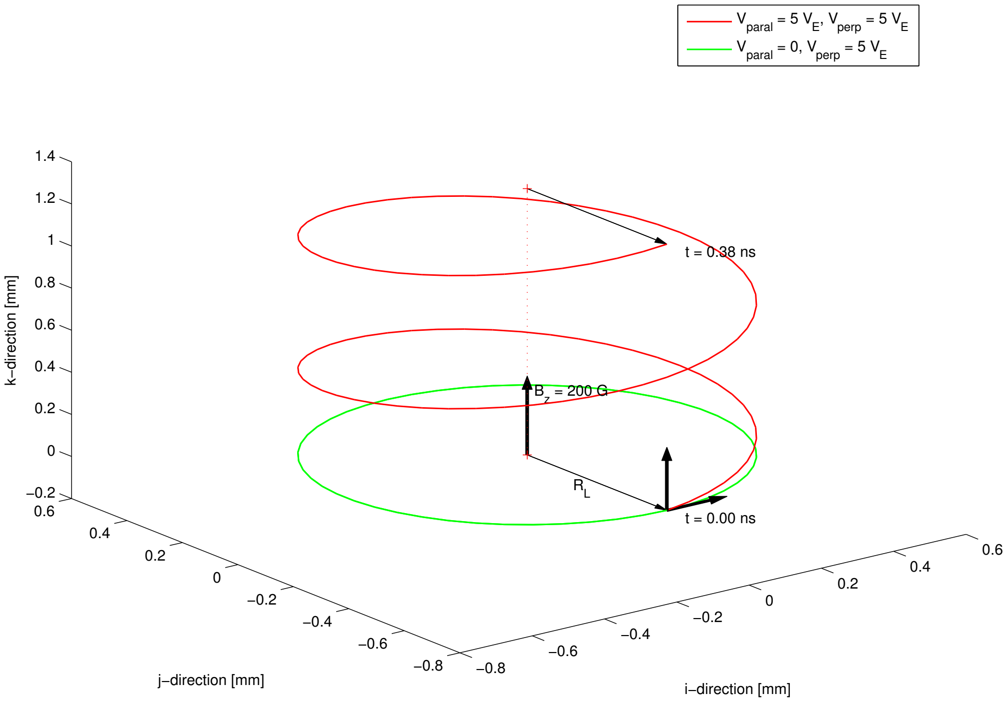

Fig. 3.2: Effect of an external magnetic field on the motion of an electron with and without initial velocity component along the direction of an externally applied local magnetic flux

a charged particle would be different depending on whether or not its initial velocity has a component along the direction of the magnetic flux density vector. Figure 3.3 depicts the trajectory of an electron in the two scenarios: $\vec{V}_{\|} = 0$ and $\vec{V}_{\|} \neq 0$; for the sake of comparison, a trajectory of the electron is overlaid to the plot when no electric is present and $\vec{V}_{\|} \neq 0$. In this case, the trajectory is a three-dimensional helix that gets increasingly slanted towards the direction of the drift velocity $(\vec{E} \times \vec{B})$ as $\vec{V}_{\|}$ approaches 0 until the limiting case where it remains confined to the $\left(\vec{E},\ \vec{V}_E\right)$ plane while maintaining its orientation along $\vec{V}_E$. This latter limiting case provides the following insight as to the physical origin of the ExB drift: Without any electric field, the electron only undergoes a centripetal acceleration that keeps its orbit circular about the direction of $\vec{B}$ (Figure 3.2); but, the application of $\vec{E}$ leads to the following two basic motions whose averaged effect leads to a net drift along the $\vec{E} \times \vec{B}$ direction:

1. Acceleration of the electron when its motion has a component along $-\vec{E}$, which leads to an elongation of the radius of its orbit along the $\vec{E} \times \vec{B}$ direction.

2. Deceleration of the electron when its motion has a component along $+\vec{E}$, which leads to a decrease of the radius of this orbit along the $-\vec{E} \times \vec{B}$ direction.

The trajectory of an ion deviates from the above description of an electron's motion in that the former particle would gyrate in the opposite direction and that its Larmor radius is $m_i/m_e \approx 100,000$ times larger than that of the electron—which, we infer from eq. 3.2.33 and the fact that the cyclotron frequency (3.2.14) is inversely proportional to a particle's mass. For better insight, we consider the following practical illustration. At the design coil settings listed in Table 3.1, the magnetic field strength in the discharge channel of the P5 does not exceed 200 G [1, 22] (value used in Fig. 3.2). Hence one can directly infer from the figure that Larmor radii are typically less than 0.5 mm for electrons, which implies that ions' Larmor radii are on the order of 50 m. These radii are 4 orders of magnitude greater than the dimensions

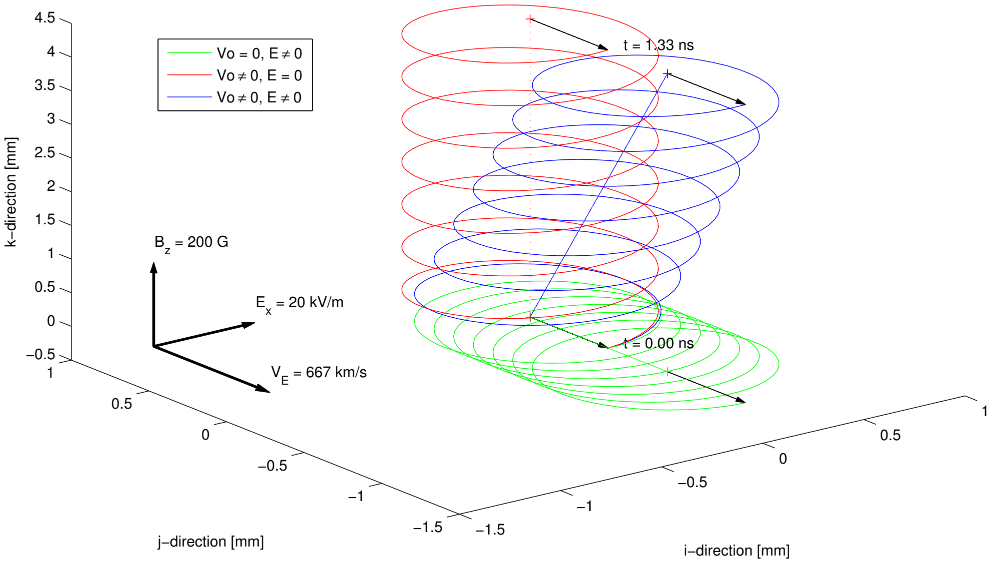

Fig. 3.3: Effects of external magnetic field and electric field on the motion of an electron with and without initial velocity along the direction of the local magnetic field

of discharge channel (see Fig. 3.5), which explains why the latter particles are said to be 'unmagnetized'; their Larmor radius is too large compared to the scale of the thruster for them to gyrate about magnetic field lines or exhibit ExB drift within the channel. Instead their motion is predominantly affected by the axial electric field within that small width.

Figure 3.4 provides a sketch of the in the discharge plasma of the P5.

3.2.3 The process of thrust generation

Having described plasma physics and explained the physical principles of the Hall current drift, we can now better appreciate how thrust is generated. Before we proceeding, however, we make note of the following important point. In a plasma, when referring to local 'macroscopic' properties of some specie (such as velocity, temperature, and density), reference is made to averaged quantities in some finite small characteristic (that is, in which the definition of a plasma still holds) volume-element enclosing a large number of particles whose property is probabilistically distributed about some mean. In the bulk of a Hall thruster's plasma, the distribution is safely assumed to be random; hence it is modeled as a Maxwellian variation over the number of particles within the small volume. A whole field, Kinetic Theory, is devoted to such study. Interested readers are referred to Gombosi [24]; for its treatment is beyond the scope of this thesis.

Based on the aforementionned discussion, any references made to properties apply to averaged local properties henceforth. An illustration of the main dynamics of particles in a Hall thruster's plasma discharge is shown in Figure 3.4 showing a broken view of the P5 (a Stationary Plasma Hall thruster) along with a depiction of the interaction of inter-particle and particle-to-field interactions in the discharge channel plasma. The process begins with the application of a radial magnetic flux ($\vec{B}$) that is maximal near the exit plane between the inner and the outer poles. Upon activation of the cathode, an electric field ($\vec{E}$) is setup between the anode and the cathode. This field accelerates electrons axially towards the anode after being emitted from the cathode. In a region of the discharge channel (acceleration zone) extending accross the exit plane of the thruster, the orthogonal configuration of electric and magnetic fields induces an large azimuthal component ($\vec{V}_D$ or ExB-drift velocity described in Section 3.2.2) to the local mean velocity of electrons; this azimuthal component largely exceeds their initially axial velocity. As a result, an azimuthal 'Hall' current cloud [23, 20, 19] propagating in a direction opposite to the electrons' drift is formed; the expression of the Hall current is:

$$\vec{J} = -en_e\vec{V}_D, \tag{3.2.34}$$

where n_e denotes the local number-density of electrons.

To this azimuthal current is superimposed an axial electron current arising from the electric field (recall eq. 3.2.32). After many revolutions in the discharge channel, some electrons eventually reach the anode. Other electrons collide with plasma particles and channel walls, get thermalized—that is, their initially oriented bulk motion becomes random—then diffuse to the anode [19]. The flow of electrons to the anode closes the thruster's electric circuit.

Continuous emission of electrons from the cathode (primary emission) prevents the Hall current's depletion; which, the axial component of electrons would have induced, were it to act alone. Aside from the primary source of electron emission (cathode emission), the high secondary-electron yield of the ceramic discharge channel walls of Stationary Plasma Hall thrusters increases the density of electrons in the channel as some energetic ions collide with discharge channel walls; this contributes to the ionization efficiency of the propellant.

As neutral atoms enter the discharge channel, some collide with the electrons

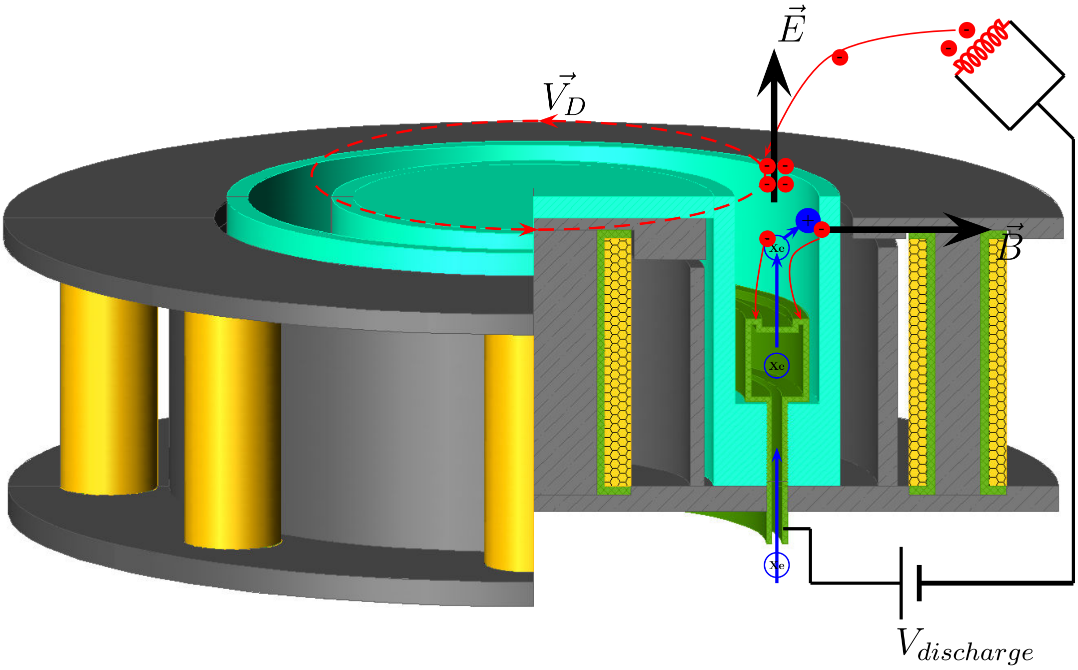

Fig. 3.4: Description of physical mechanisms leading to thrust in the Hall thruster

on their way to the anode while others collide with Hall current electrons. When the energy imparted to propellant particles during some collisional events exceeds their ionization potential, ions form. This process triggers a plasma discharge in the channel, which is sustained by the continuous feeding of propellant and electron emission in the discharge channel. As they accelerate due to local electric field effects, some ions cross the exit plane of the discharge channel. As they speed-up towards the exit, other ions collide with slower neutrals that diffused from the anode; these collisions induce an acceleration of neutrals as the faster ions transfer their kinetic energy to the former particles—a process commonly refered to as 'charge-exchange' or 'CEX' for short (readers interested in this processed are refered to Goebel who describes it in the BPT 4000 Hall thruster [19]). The flow of neutral and ionic particles accross the channel's exit both contribute to thrust in Hall thrusters [8].

Having completed a qualitative description of thrust generation, we now derive its expression based on Goebel's outline [19]. As mentionned earlier in Section 3.2.1, the plasma in Hall thruster discharges can be modeled as a fluid whose momentum equation in an infinitesimal volume element reads:

$$mn\frac{D\vec{V}}{Dt} = qn\left(\vec{E} + \vec{V} \times \vec{B}\right) - \nabla \cdot \vec{p} + \vec{F}_c. \tag{3.2.35}$$

where 'total' derivative on the left-hand-side accounts for temporal and convective derivatives; n, m, and q respectively denote the particle density, mass, and charge; $\vec{p}$ and $\vec{F}_c$ respectively account for the pressure and collisional effects. The fields are expressed in the cylindrical coordinate system (r, ϕ, z), with r, z, and ϕ respectively denoting the radial, axial, azimuthal directions centered along the thruster's centerline. Ignoring collisional and thermal effects, eq. 3.2.35 reduces:

$$mn\frac{D\vec{V}}{Dt} = qn\left(\vec{E} + \vec{V} \times \vec{B}\right), \tag{3.2.36}$$

Applying (3.2.36) to ions (of mass M)—whose motion neglibibly reflects the effect of the magnetic field since their Larmor radius is much larger than the length of the discharge channel—leads to the following expression of the force per unit volume acting on the ions:

$$\vec{f_i} = en_i\vec{E}, \tag{3.2.37}$$

which upon integration accross gives the total force acting on the ions in the discharge channel's cross-section:

$$\vec{F_i} = 2\pi \oint n_i\vec{E}rdrdz. \tag{3.2.38}$$

From Newton's 3^{rd} Law, we deduce that the thrust must be:

$$\vec{T} = -\vec{F_i}; \tag{3.2.39}$$

By analogy to (3.2.39) and using (3.2.37), we find that the thrust per unit volume (or specific thrust) is:

$$\vec{t} = -\vec{f_i} = -en_i\vec{E}. \tag{3.2.40}$$

Applying the quasi-neutrality approximation ($n_i \approx n_e$) to eq. 3.2.40 leads to the following expression of the specific thrust:

$$\vec{t} = -en_e\vec{E}. \tag{3.2.41}$$

Application of the momemtum equation to the electrons and neglecting inertial effects leads to:

$$0 = -en_e\left(\vec{E} + \vec{V_e} \times \vec{B}\right). \tag{3.2.42}$$

Substituting (3.2.41) into (3.2.42) and rearranging leads to the following approximation of the specific thrust in a coaxial Hall thruster:

$$\vec{t} = -en_e\vec{V_e} \times \vec{B}. \tag{3.2.43}$$

Assuming that the ExB-drift dominates electrons' bulk motion, we can assume:

$$\vec{V_e} \approx \vec{V_D}. \tag{3.2.44}$$

Substituting (3.2.44) into (3.2.43) and recalling the previous expression of the Hall current (3.2.34) leads to the following common form the specific thrust ('JxB-force'):

$$\vec{T} = -\vec{J} \times \vec{B} \tag{3.2.45}$$

3.3 Motivation for magnetic field mapping in the discharge channel of the P5

As mentionned in Section 2.2.2.2, for some required I_{sp} and available power, there is a corresponding optimal magnetic field structure, for which a Hall thruster operates at its peak efficiency. Up until the past couple decades, the use of Hall thrusters was limited to low-I_{sp} missions; station-keeping is one such example with I_{sp} values on the order of 1600 s. Thrusters operating at specific impulses exceeding this limit without magnetic field optimization experienced a reduction in efficiency [4]. The growing need to apply electric propulsion techology (due to its greater payload capability) to interplanetary transfer missions with higher I_{sp} requirements, prompted recent efforts to develop improve magnetic circuits; which, not only contributed to raising the limit of the distribution of efficiency over I_{sp}, but also promoted optimal thruster operation at maximum efficiency. Such interests motivated the development of the NASA-173Mv series and P5 Hall thrusters as well as studies to map their magnetic field and investigate how the latter's shape affects efficiency [4].

The gradient of the magnetic flux density along with the symmetry and concavity of magnetic field lines about the downstream direction of the discharge channel's centerline were found to strongly influence efficiency due to their effect on the focusing of ions along a Hall thruster's centerline [25, 4, 19]. In the following, we explain how the symmetry and concavity of magnetic field lines promotes the focusing of ions based on Morozov's derivation [25]. We begin by neglecting inertial and collisional effects to get:

$$0 = -en\left[\vec{E} + \left(\vec{V} \times \vec{B}\right)\right] - \nabla \vec{p}. \tag{3.3.1}$$

Next, we find the component of the resulting equation along the direction of the field by performing a dot-product operation with $\widehat{b} = \frac{\vec{B}}{B}$. This leads to:

$$E_b + \frac{1}{en}\frac{\partial p_b}{\partial b} = 0. \tag{3.3.2}$$

Defining ϕ as the plasma potential, the electric field reduces to:

$$E_b = \frac{\partial \phi}{\partial b}. \tag{3.3.3}$$

Assuming that the properties of electrons obey the ideal gas law and that their temperature is constant along $\widehat{b}$ (which makes sense since electrons move in plane normal to $\vec{B}$ when coupled to $\vec{E}$ in the discharge channel, eq. 3.3.2 reduces to:

$$\phi(b) - \frac{kT_e(b)}{e} ln \frac{n}{n(b_o)} = \phi(b_o) \tag{3.3.4}$$

Assuming that thermal effects are negligibly small next to electrostatic field effects leads to:

$$\phi(b_o) \approx \phi(b); \tag{3.3.5}$$

that is the electrostatic potential is can be assumed constant along a magnetic field line or, more simply, electric and magnetic field lines coincide to 'first-order' [25]. Hence, the acceleration of ions tends to be greater where the gradient of field lines is highest, which must coincide with zones of highest concavity. When symmetric about the channel's centerline, the ionic flow is predominantly centered about the centerline.

The dependence of the discharge channel length on the maximum magnetic field strength is another factor demonstrating the importance of the latter field. This results from the fact that the discharge channel's length scale (L_c) must be bounded above and below by the ion and electron Larmor radii [25] ($R_{L,i}$ and $R_{L,e}$ respectively) inversely proportional to the cyclotron frequency (via eq. 3.2.33); which, in turn, is proportional to the field strength (via eq. 3.2.14):

$$R_{L,i} > L_c >> R_{L,e}, \tag{3.3.6}$$

Since these radii were found to be inversely proportional to the magnetic field strength, one can infer from eq. 3.3.6 that the field strength must be upper-bounded for a proper sizing of the discharge channel. In addition to the aforementioned requirement, the magnetic field must ideally be radial and its gradient must remain positive along the axial direction of the discharge channel to prevent offsets of discharge current and voltage from design values [26].

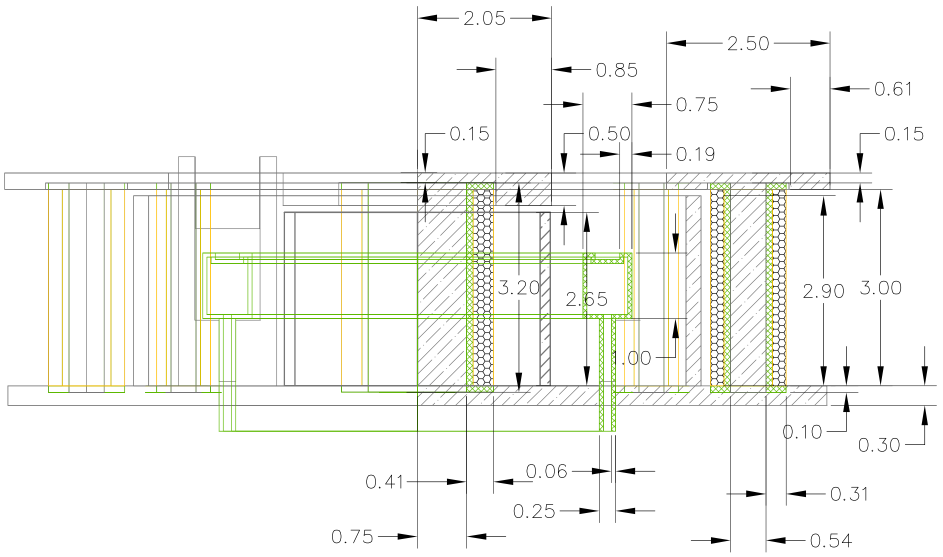

(a) Front view

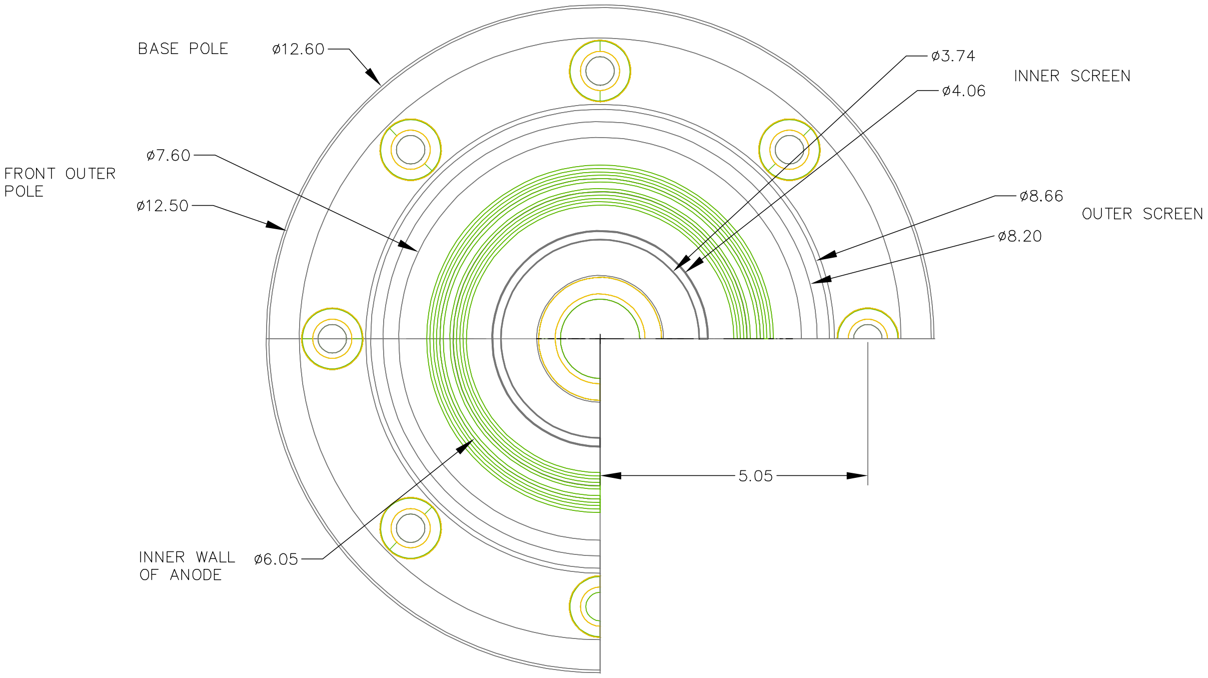

(b) Top view

Fig. 3.5: Major dimensions of the main components of the P5's magnetic circuit (INCHES)

CHAPTER IV

MagNet6 simulation of the P5 Magnetic Field Topology

Typically, the magnetic field of a commercial Hall thruster is optimally shaped and scaled for some I_{sp} in cold operation (recall Section 3.3); that is, in a vacuum, without any consideration of the fields that might be induced by currents in the plasma discharge. Based on Biot-Savart Law—according to which a looped flow of electric charges induces a magnetic field—one would expect the Hall current to induce a magnetic field, which would induce a deviation of the in vacuo field from its optimal structure.

4.1 Previous simulation attempts of magnetic field structure in the discharge channel of the P5

The effect of the Hall current's induction on the magnetic field of the P5 without discharge (in vacuo operation) has triggered much interest at PEPL. Based on a two-dimensional discretization of the Hall current of a 5 kW Hall thruster (named P5), Haas iteratively computed the induced magnetic field and reported its strength to be less than $1/50^{th}$ of the peak vacuum field (or circuit-induced field of the thruster operating without any discharge) strength throughout the discharge channel. His computations relied on an estimation of the spatial distribution of the Hall current (defined in Section 3.2.2) assuming strictly azimuthal conduction, quasi-neutrality ($n_i \approx n_e$), and neglecting the contribution of the magnetic field's axial component in the expression of the cuurrent density [27, 1]:

$$J = en_eV_D, \tag{4.1.1}$$

where e, n_e, and V_D respectively denote the charge of an electron, the number-density of electrons, and their mean drift-velocity. Haas estimated n_e using a double Langmir probe measurements of the number-density of ions and assuming quasi-neutrality. Neglecting the radial component of the electric field and the axial component of the magnetic field in the expression of the drift velocty (3.2.30) given in the previous chapter (III), yields the following approximation in the azimuthal direction as follow:

$$V_D \approx \frac{E_z}{B_r} \approx \frac{1}{B_r}\frac{\Delta\phi}{\Delta z}, \tag{4.1.2}$$

where $\frac{\Delta\phi}{\Delta z}$ denotes a first-order approximation of the partial derivative of the plasma potential distribution, $\left|\frac{\partial\phi}{\partial z}\right| \equiv E_z$, in the discharge channel of the thruster. Applying (4.1.2) to (4.1.1), the azimuthal component of the Hall current can be expressed as:

$$J \approx e\,n_e\,\frac{1}{B_r}\frac{\Delta\phi}{\Delta z}; \tag{4.1.3}$$

Haas estimated the distribution of the plasma potential from emissive probe measurements in the discharge channel of the P5 mounted on a High-Axial Reciprocating probe (HARP) [13]. The radial component of the magnetic field was in turn measured with a Hall probe with the thruster's plasma discharge shut-off. Based on his approach, he found the total Hall current at 1.6 kW and 3 kW power settings to be 25.1 A and 34.6 A, respectively [27].

Peterson followed a more complete approach to the problem. He not only simulated the Hall current's induction, but also the overall field using a three-dimensional simulation of the combined Hall current and magnetic circuit system on a commercial software (MagNet 6 by Infolytica). An in-depth description of the solver is beyond the scope of the current work; it suffices here to describe it as a finite-element solver of Maxwell's equations of classical electromagnetism in a volume (with specific boundary conditions) enclosing magnetic materials and electric currents [4]. In this case, the Hall current's spatial variation was inferred from previous estimations of the Hall parameter's spatial distribution in the discharge channel of the P5 [27, 1]. He based his estimation from the definition of the Hall parameter in terms of Hall current densities (Section 3.2)

$$\Omega = \frac{J_H}{J_z} \tag{4.1.4}$$

approximated as in terms of integral currents and azimuthal to cross-sectional area ratios (A_D and A_H respectively).

$$\Omega = \frac{I_H}{I_D}\frac{A_D}{A_H}. \tag{4.1.5}$$

Using (4.1.5), Peterson deduced the spatial distribution of the Hall current in a mesh of the rectangular current cells extending 10-60 mm from the anode (process later discussed in detail in Section 4.2.3). While his approach is sound, his estimations of the Hall current exceeded those of Haas by as much as an order of magnitude (156 A at 1.6 kW).

Peterson's report of the axial distribution of the field strength's radial component indicated a more pronounced effect of the Hall current's induction than previously reported by Haas; his results—limited to the discharge channel's centerline—revealed a deviation of the Hall current's field induction ranging from -20% to 10% of the peak vacuum field along an axial length probed (10-60 mm from the anode). In addition, Peterson attempted to validate his simulations based on miniature inductive loop probe measurements of the radial component of the magnetic field strength in the discharge channel of the P5 during a live firing of the P5 in the high vacuum environment of PEPL's Large Vacuum Test Facity (LVTF) [14]. Noise associated with the probe measurements and significant deviation of his estimation of the Hall current's magnitude from that of Haas' (by a factor of 7) prevented him from conclusively describing the effect of the Hall current's induction on the thruster's vacuum magnetic field [1].

4.2 Recent simulations of the magnetic field of the P5 using MagNet 6

In this chapter, we report results from three-dimensional MagNet 6 field simulations of the P5 Hall thruster accounting for the Hall current. Our simulation deviate from Peterson's [14] in that the Hall current was discretized based on experimental Hall current measurements based on a double probe [1]. In addition, our study applies to two power-level settings and considers various scalings of the Hall current. The scalings were chosen from a broad enough range (1-8) to account for uncertainties associated with double-probe measurements (15-43% off from vacuum and electric field-based calculations) and cover the large discrepancy between Hall current magnitudes originally reported by Haas [27] and Peterson [14].

As a preamble to presenting that study, the following important remarks must be taken into consideration by any reader interested in reproducing the work. Ceramic components (namely the discharge chamber, the anode, and the guard disk) were omitted since they are not magnetic. Also, screws and holes were not taken into account due to their relatively small dimensions. The major dimensions of the ferromagnetic parts used for modeling the magnetic field of the thruster are shown on the front and top views displayed in Figures 3.5. For a more complete description of the P5's dimensions, the interested reader is referred to Gulzinski [22].

The magnetic field topology of the P5 was simulated using a commercial software named MagNet 6 by Infolytica. Two sets of three-dimensional simulations were performed: a first one in 'cold' operation (partially active thruster with magnetic circuit switched on) and a second one in 'warm' operation (fully active thruster with a plasma discharge). Computations were performed at two thruster power levels: 1.6 kW and 3 kW.

The geometry used in the simulation was reported in Figure 3.5 of Chapter III. Owing to its azimuthal symmetry, only an eighth of the thruster was considered to minimize the computational load of the simulations (4.1(a)).

A listing of the materials constituting the diverse parts is provided in Section 3.1 of Chapter III; in which, reference was made to three materials used in the simulation. The magnetization curves [1] of Stainless Steel (SS) 316 and annealed iron were added to the software's database based on magnetization curves found in Baldan [29] and Hofer [10], respectively.

Field-tangential boundary conditions (i.e. normal component of the magnetic flux about a surface is zero) were imposed on all faces of the computational domain shown on Figure 4.1(b). This boundary condition is appropriate because the thruster is symmetric by reflection about the two slice-planes. On the remaining faces, this boundary condition enforces a zero normal component of the field at infinity; so to isolate the thruster from any external influences. Mesh generation was automatically handled by MagNet 6 (Figure 4.2). A greater degree of mesh refinement was specified

---

[1] A magnetization curve (also referred to as B-H curve) consists of the variation of magnetic flux density (B) with magnetic field strength (H). In a vacuum, the B-H curve is linear with a slope corresponding to the permeability of free space. In a medium, however, the B-H curve exhibits a non-linearity that depends on the medium's permeability to an external magnetic field; that is, the extent to which the spins (randomly oriented in the absence of an external field) of the particles that make up the material tends to realign themselves along the direction of the magnetic flux density vector ($\vec{B}$). [28]

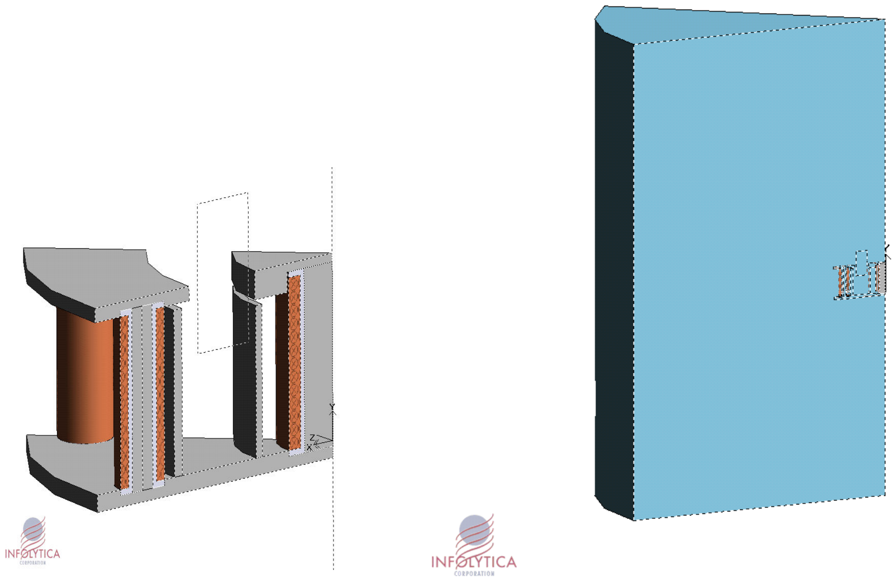
(a) Magnetic circuitry (b) Extent of the computational domain

Fig. 4.1: MagNet 6 Modeling of the P5 thruster's magnetic circuitry. An 8^{th} slice was considered with appropriate boundary conditions to minimize the computational load

in the acceleration zone, where higher magnetic field strength gradients were expected. The acceleration, which extends across the discharge channel and is defined by the region highlighted in red in Figure 3.1. This region, whose boundaries are presented in the following, was chosen to keep this work consistent with a previous study of the interaction between the Hall current and the vacuum magnetic field performed by Haas [1] (same reasonning goes with the choice of power settings: 1.6 kW and 3.0 kW) and due to the fact that 70% of the overall thrust is generated therein [27]:

- along the axial direction, the region extends 10 mm to 60 mm from the anode face plate
- along the radial direction, the region extends 2.5 mm to 22.5 mm from the inner wall of the discharge chamber

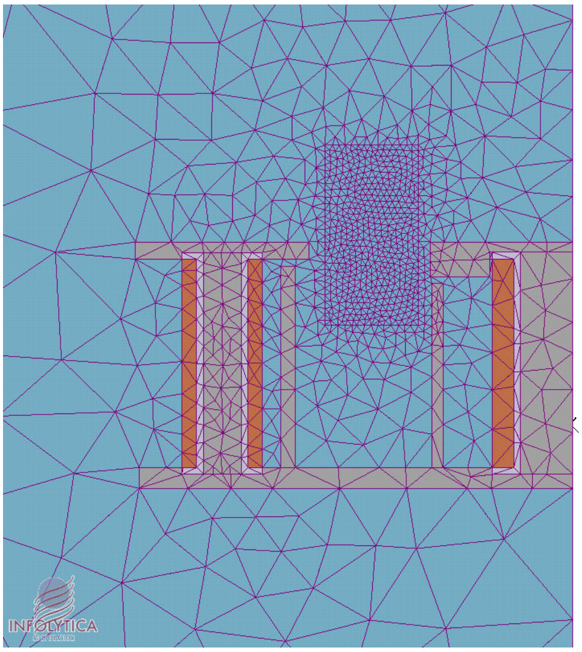

Fig. 4.2: Unstructured mesh of the P5 Hall thruster

4.2.1 Simulation of the P5's magnetic field structure without any discharge

Prior to simulating the effect of the Hall current on the P5's vacuum field structure, simulations were validated against Haas' measurements of the vacuum magnetic field structure based on a Hall sensor—whose variations in voltage induced by a local field were interpreted by a calibrated gaussmeter [1]. At each of the power levels investigated (1.6 kW and 3 kW), settings associated with outer and inner electromagnets (stranded coil wound about ferromagnetic cores) with specific number of turns and currents are listed in Table 3.1.

Results of the simulation are illustrated at the 1.6 kW level in the following figures showing streamlines of the magnetic field[2] (Figure 4.3) and filled contour-maps of the field's strength[3](Figure 4.4). Streamlines and contours of the field strength

---

[2] A streamline is an oriented line connecting neighboring points at which the slope of a local vector field—magnetic field strength, for our purposes—varies continuously

[3] Each line in a contour map connects points of constant magnetic field strength based on some arbitrary reference strength (could be taken at infinity, for example); the coloring between successive lines indicates the relative difference between these field strengths corresponding to the actual field

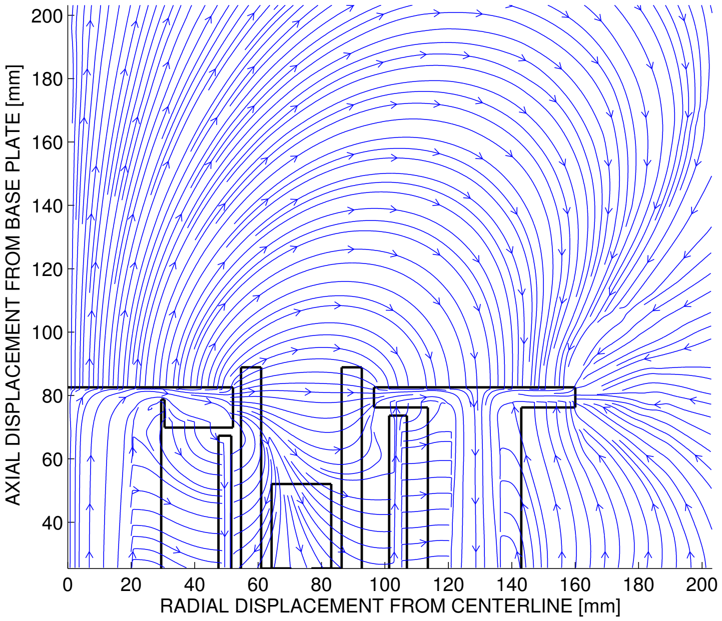

Fig. 4.3: Streamlines of the magnetic field strength's vector field generated by the magnetic circuit of the P5 operating without discharge plasma ('in vacuo' or 'cold operation') at electromagnets' coil settings at 1.6 kW

asssociated with the 3 kW level are reported in the Appendix.

We validated MagNet simulations of the magnetic field of the P5 in vacuo by comparing them to experimentally measured components (radial and axial) of the magnetic strength in the discharge channel (along its axial direction) at five equally spaced radial locations (from 2.5 mm to 22.5 mm in 5 mm increments) extending from the inner to the outer channel wall—this region corresponds to the acceleration zone described earlier. A validation of the simulated vacuum magnetic field strength along the centerline of the discharge channel is provided at each power setting in figures 4.5(a) and 4.5(b) reporting its radial components and in figures 4.6(a) and 4.6(a) reporting its axial components. Off-centerline radial and axial distributions are plotted in figures A.3 through A.6 and figures A.7 through A.10 of Appendix A, respectively at both power settings.

Overall, considering shape-similarity alone, MagNet 6 simulations predict the vari-

---

strength and based on a color map

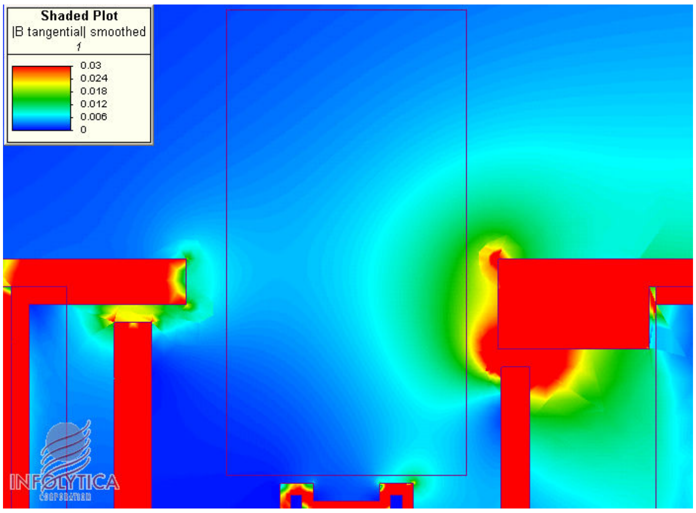

Fig. 4.4: Contour map of the magnetic field strength of the P5 operating without discharge plasma ('in vacuo' or 'cold operation') at electromagnets' at 1.6 kW Field strengths are expressed in Tesla (equivalent to 10^5 Gauss)

ation of axial and radial components of the field well. The largest discrepancies occur closer to the anode and near the inner wall. These discrepancies may be attribuable to the fact that the mesh was not fine enough in this region; Further attempts at improving the solution in these regions were inhibited by limited computer memory. Probe misalignment might also have led to the errors; in fact, MagNet 6 has been shown to be more reliable (to within 10%) than experimental measurements of the magnetic field in a vacuum [4].

Aside from mismatches in shape-similarity, the figures exhibit disagreements in the magnitudes of experimental and simulated field strengths. These were underestimated by about 20 % in the radial direction and by as much as 50 % in the axial direction. These disagreements were more important at the lower 2 kW power-setting.

It is worthwhile noting that the radial component of the magnetic field is up to five times larger than its axial component the closer one gets to the outer wall. Near the inner wall and closer to the anode, however, radial and axial components are of the same order of magnitude.

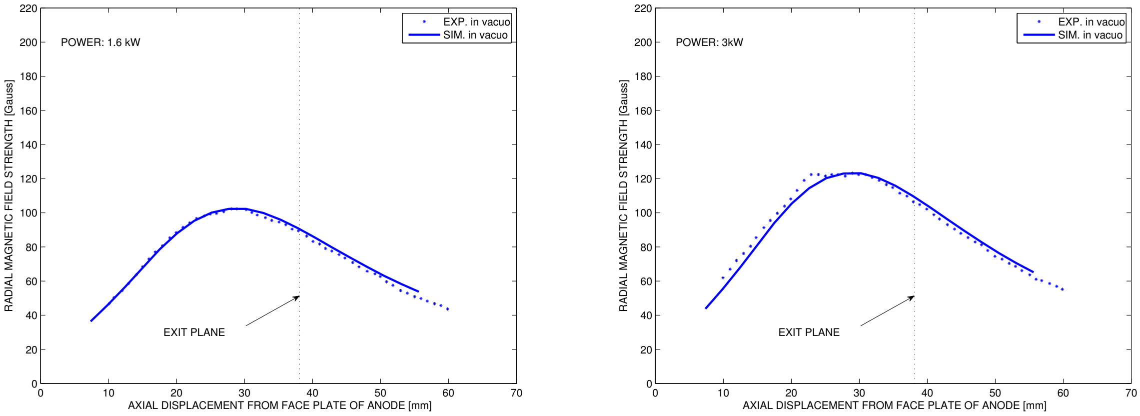

(a) 1.6 kW

(b) 3.0 kW

Fig. 4.5: Validations of MagNet 6 simulation of the radial component of the P5's magnetic field strength at 12.5 mm from the inner wall at 1.6 kW and 3 kW

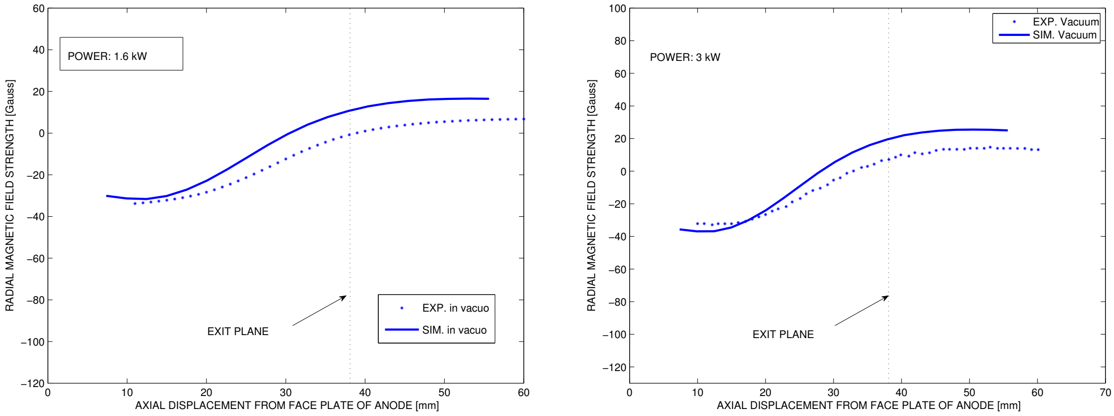

(a) 1.6 kW

(b) 3.0 kW

Fig. 4.6: Validations of MagNet 6 simulation of the axial component of the P5's magnetic field strength at 12.5 mm from the inner wall at 1.6 kW and 3 kW

4.2.2 Experimental measurement of the Hall current in the discharge channel of the P5

The Hall current was measured in the discharge channel of the P5 by Haas using a floating double-probe mounted on a High-speed Axial Reciprocating Probe system (HARP) [1]. The experiment was conducted in a large vacuum tank facility at PEPL at a pressure of about 10^{-5} Torr. The thruster was operated at a discharge voltage of 300 V and discharge currents of 5.5 A (1.6 kW) and 10 A (3 kW). The cathode flow rate was maintained at 6 sccmwhile the anode flow rates were respectively set at 58 sccm (1.6 kW) and 105 sccm[4] (3 kW). The double-probe consists of cylindrical and planar electrodes respectively oriented along the radial and azimuthal directions of the discharge channel. The cylindrical electrode collects ion saturation current so to bias the planar electrode for electron collection. Owing to a low-residence time (about 100 ms) in the discharge channel plasma, the HARP permitted measurements to be performed with little perturbation from the surrounding plasma. The following figures (4.7) summarize Hall-current density measurements at 1.6 kW and 3 kW as reported in Haas [1].

4.2.3 MagNet 6 simulation of the Hall current in the acceleration zone of the P5

Haas [1] performed a two-dimensional study of the effect of the Hall current on the vacuum field of the P5 by discretizing the Hall current into cells—each corresponding to the profile of an infinite wire carrying a current computed from distributions similar to those shown in Figure 4.7. The resulting ‘self-field’ induced by the wires was computed from the Biot-Savart Law using an iterative approach. His study revealed that the Hall current has a negligible effect on the magnitude of the vacuum magnetic

---

[4] sccm is a unit of gas flow rate standing for Stantard Cubic Centimeter and equivalent to 9.76 x 10^{-2} mg/s in xenon [1]

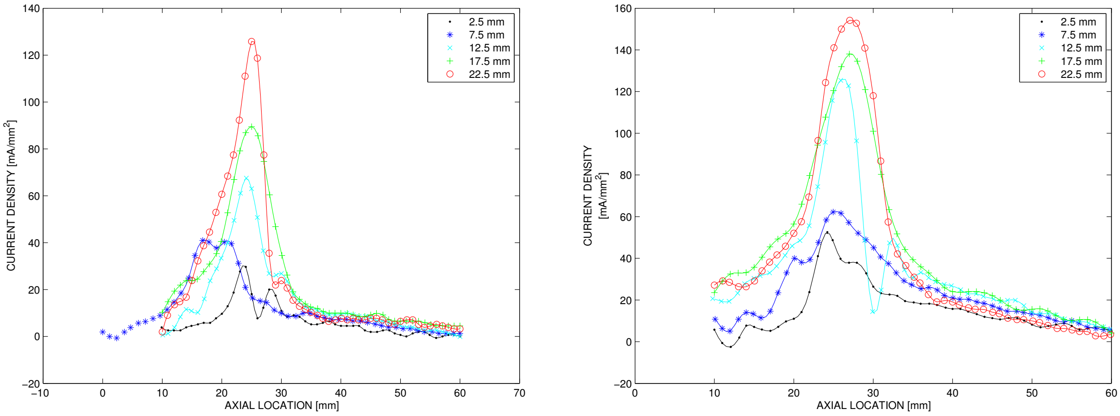

(a) 1.6 kW

(b) 3 kW

Fig. 4.7: Hall current density distributions measured by a floating double probe at various radial locations in the discharge channel of the P5 at 1.6 kW and 3 kW [1]

field as he reported self-field strengths that are one to two orders smaller than vacuum field strengths [1].

In this work, we followed Haas' approach of discretizing the Hall current into separate current-carrying wires. Our simulation of the Hall current deviates from his in that our approach was three-dimensional. Additionally, we not only used MagNet 6 to simulate the Hall current, but also ensured that each cell (of rectangular profile) carried its own integral current; an illustration of this process is described in Figure 4.8 at a radial displacement of 12.5 mm from the inner wall at 1.6 kW.

As a first step, the axial variation is smoothed through cubic interpolation. In a second step, the area below the resulting distribution is computed within very narrow intervals (100 in this case) so that their sums add-up to a value close to the theoretical total current per unit radial length. In a third and final step, sets of small intervals are merged and scaled by the unit radial separation length of the experimental distributions (Figure 4.7(a)) to yield an integral Hall current in each rectangular cell of the 5x20 mesh. Application of the discretization to the remaining four radial locations resulted in the 5x20 rectangular[5] mesh shown on Figure 4.9(a)

---

[5] To optimize the solver's performance, rectangular cells of smaller cross-sectional areas were

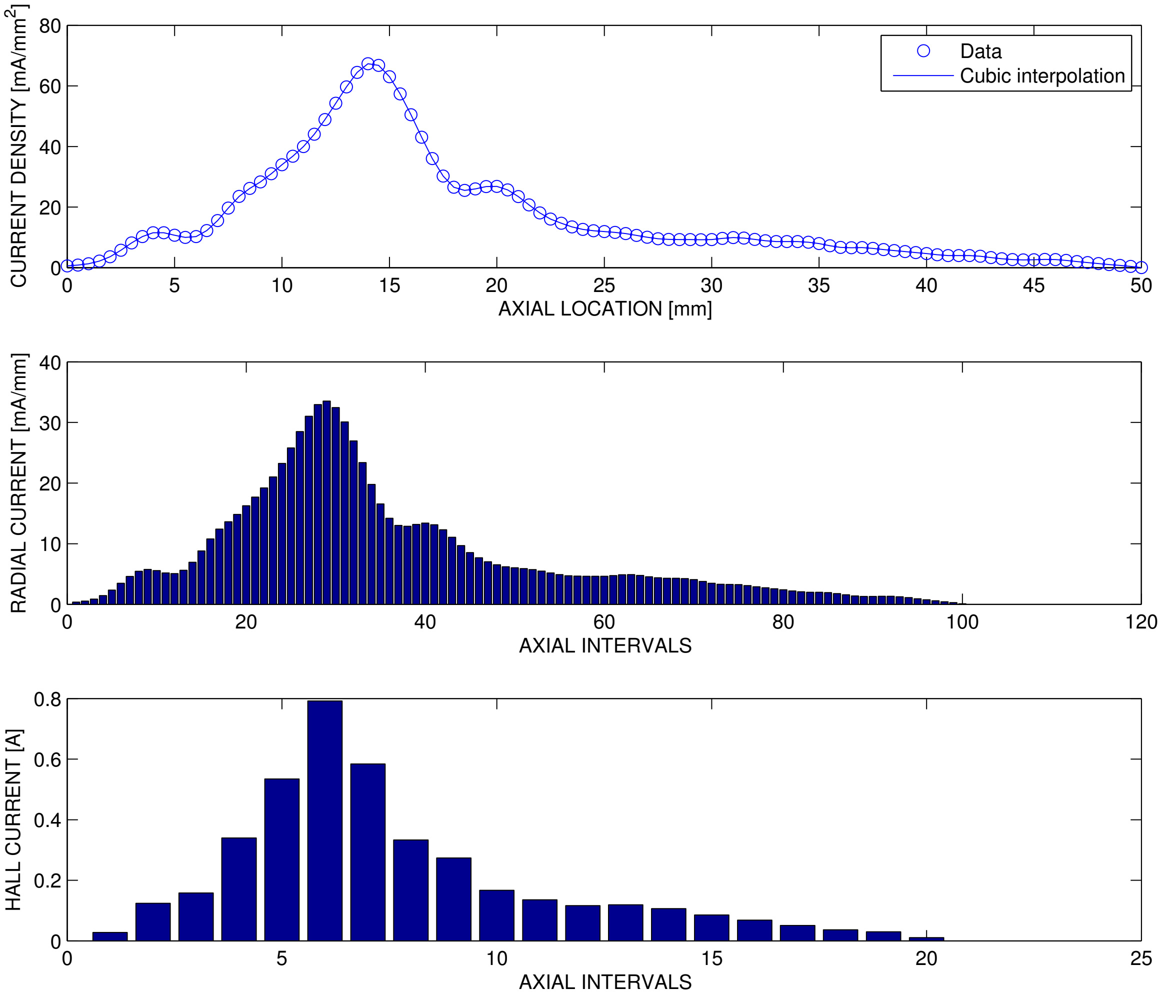

Fig. 4.8: Procedure used for the discretization of the Hall current into cells from an experimental axial variation of the Hall current at a radial displacement of 12.5 mm from the inner wall

within an area extending axially from 30 mm upstream to 20 mm downstream of the exit-plane (acceleration zone, recall Section 4.2.1). Each Hall current cell was treated as a metallic conductor and modeled as a stranded coil in MagNet 6. This discretization yielded a total current of 22 A accross the acceleration zone. The resulting MagNet 6 simulation of the magnetic field structure induced by the Hall current alone (or self-field) is reported in Figure 4.9(b).

The discretization process was applied to the 3 kW power-setting with different Hall current distributions (Figure 4.7(b)) to yield the mesh and self-field respectively displayed in figures 4.10(a) and 4.10(b).

Note from figures 4.9(b) (1.6 kW) and 4.10(b) (3 kW) that the magnitude of the self-field's strength peaks to about 70-80 G and is concentrated in zones whose extents and location vary with power. At 1.6 kW, the self-field is significant in a small area extending about 10 mm along the radial and axial directions and is located by the outer wall near the exit plane. At 3 kW, however, the self-field is predominant in a wider region extending over 25 mm and 40 mm along the radial and axial directions, respectively. Comparing the latter magnitudes to vacuum field strengths reported in figures A.3 through A.6, we deduce that peak vacuum field strengths along the various radial locations investigated are no more than an order of magnitude larger than the Hall-current's induced field within the acceleration zone; this conclusion substantially deviates from his report that the former is nearly two orders of magnitude smaller than the latter [1].

---

investigated as well as circular profiles prior to adopting the current cell shapes.

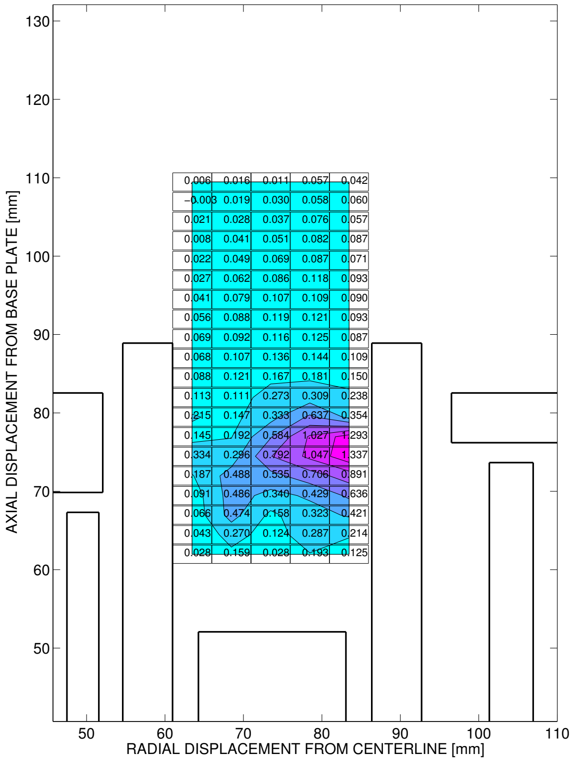

(a) Current discretization

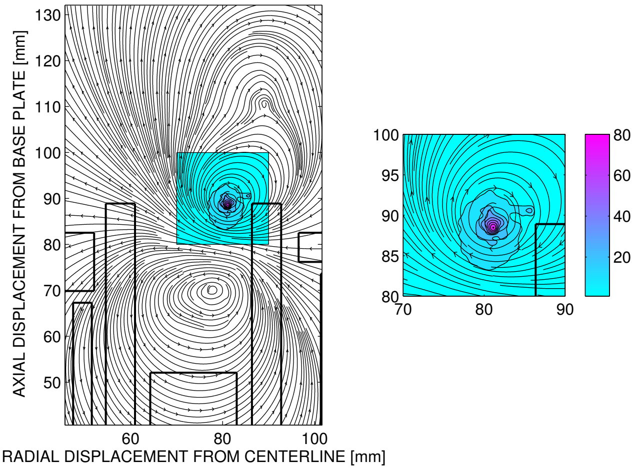

(b) Magnetic field induction

Fig. 4.9: Computational mesh and magnetic field induced by the Hall current at 1.6 kW. Each cell corresponds to the profile of a current-carrying wire (current specified in Ampere)

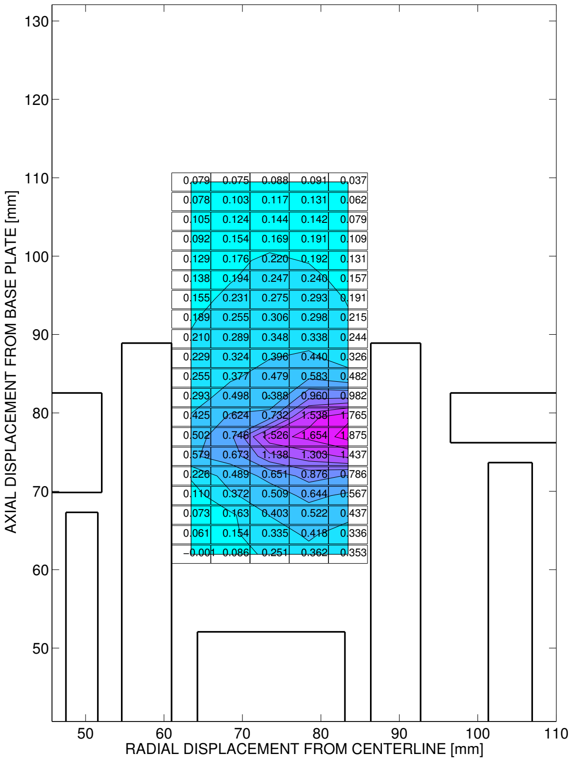

(a) Current discretization

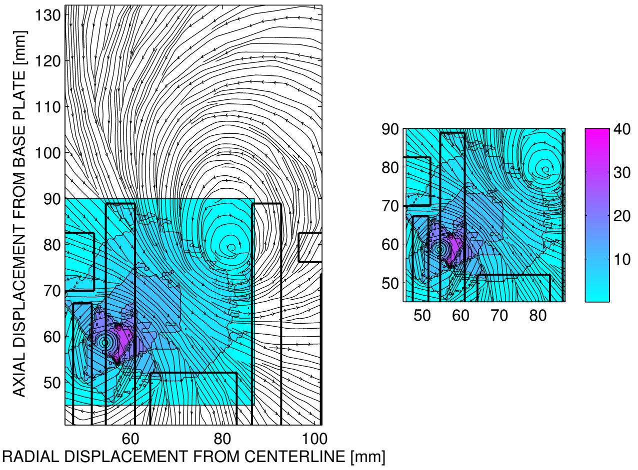

(b) Magnetic field induction

Fig. 4.10: Computational mesh and magnetic field induced by the Hall current at 3 kW. Each cell corresponds to the profile of a current-carrying wire (current specified in Ampere)

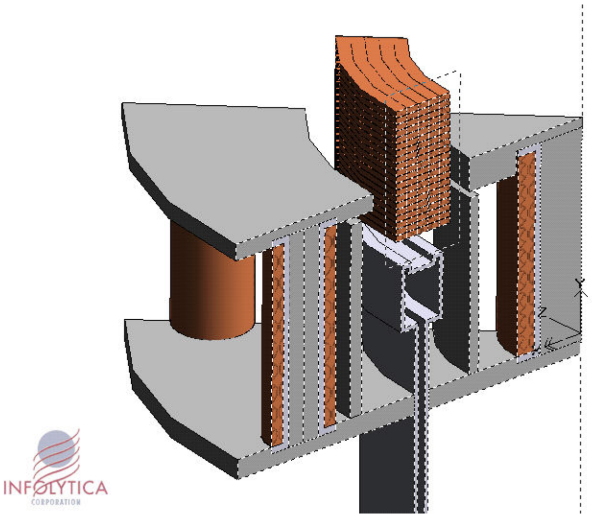

Fig. 4.11: Geometry used to simulate the effect of the Hall current on the vacuum field of the P5

4.2.4 Effect of the Hall current on the vacuum magnetic field

In Sections 4.2.1 and 4.2.3, we respectively, reported simulated topologies of the magnetic field of the P5 in vacuum and that of the field induced by the Hall-current at 1.6 kW and 3 kW. We now focus on how the two fields interact. For that purpose, we used MagNet 6 to generate a model that combines the $1/8^{th}$ slice of the P5 geometry and the coils simulating the Hall current. Figure 4.11 depicts the overall geometry of the model combining the magnetic circuit of the P5 and the coils simulating the Hall current.

Axial distributions found from the simulation are reported in figures 4.12 and 4.13 showing radial and axial components of the field strength at both power settings. The '22 A' and '41 A' labels refer to the integral of the Hall current distributions at 1.6 kW and 3.0 kW, respectively, in the area where its profile has been simulated. A striking remark from the figures is that the Hall current does not affect the strength of the vacuum magnetic field much at the power levels investigated. The mean reduction in magnetic field strength is on the order of 5-8% as the power rises from 1.6 kW to 3 kW. We present the following argument to explain the relatively small effect of the

Hall current's induction on vacuum field. Because the current density distributions are smooth (recall Figure 4.7)—that is, the profiles exhibit no sudden jumps—the current between neighboring cells are relatively close in magnitude (obvious from 4.9(a) and 4.10(a)). Based on Biot-Savart law, one can deduce that magnetic field strengths between any two neighboring cells are opposite in sign; this induces a mutually canceling effect of field strengths induced by the Hall current cells; which, in turn, results in a much smaller net contribution of the cells on the vacuum field than it would be the case were one to consider the sum of the absolute of field strengths induced by each cell.

Having discussed the effect of the Hall current's induction on the strength of the vacuum field, we now switch our interest on the field topology. The effect of the Hall current on the field can be infered from the streamlines plotted in figures 4.14(a) and 4.15(a) throughout a region encompassing the symmetric half of the thruster's profile. Comparison of the figures reveals very similar field features at the two power levels. This can be better appreciated by considering the zone highlighed with dashed lines extending from the anode to about 20 mm downstream of the exit plane. Close-ups of these regions are provided in figures 4.14(b) and 4.15(b) at 1.6 kW and 3.0 kW, respectively showing streamline plots and vector plots of the magnetic field strength. The latter vector plots are included, for completeness, to give an idea on the relative magnitude of the field strength; however, we are mainly interested in the plots of the streamlines. The figures reveal that the Hall current leads to an increase in the concavity of streamlines in the discharge channel. Such a feature is beneficial in SPT Hall thrusters because it ensures a better focusing of ions along the axis of the discharge channel; hence, it reduces the likelihood of their collision with the walls, which would negatively impact thrust. The effect of the concavity of the magnetic streamlines along the axial direction on plasma focusing is discussed in Morozov [25] and Zhurin [9]. The idea stems from an integration of the momentum equation of

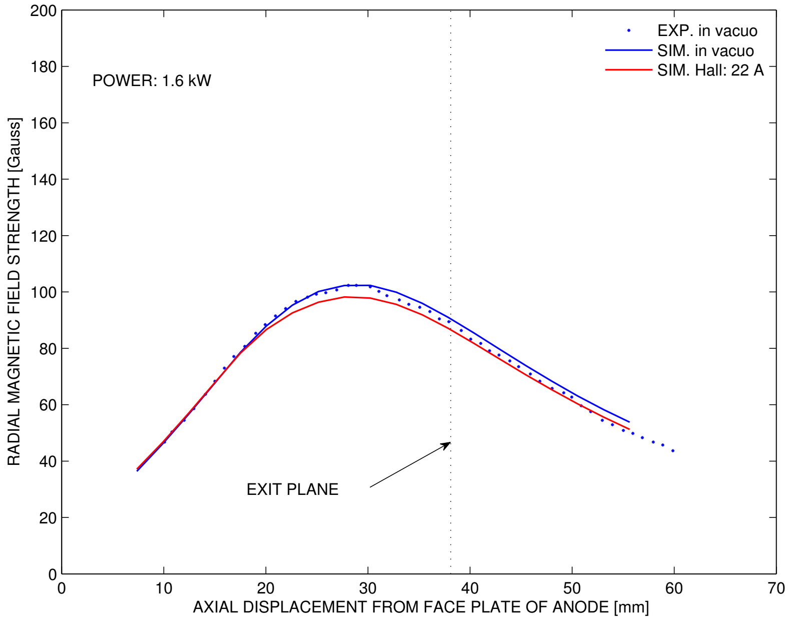

(a) 1.6 kW

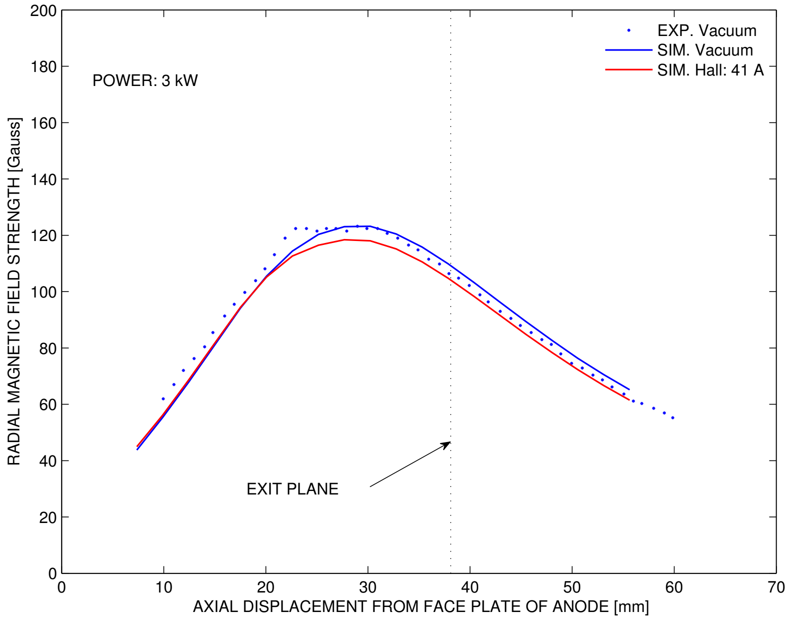

(b) 3.0 kW

Fig. 4.12: Effect of the Hall current on the variation of in vacuo radial magnetic field strength in the discharge channel of the P5 at 12.5 mm (centerline of channel) from the inner wall. The variations are normalized by the maxima of experimental field strengths. The ‘22 A’ and ‘41 A’ labels refer to the integral of the Hall current distributions at 1.6 kW and 3.0 kW, respectively, in the area where its profile has been simulated. Experimental distributions in vacuo [1] are displayed in the figures for the sake of completeness.

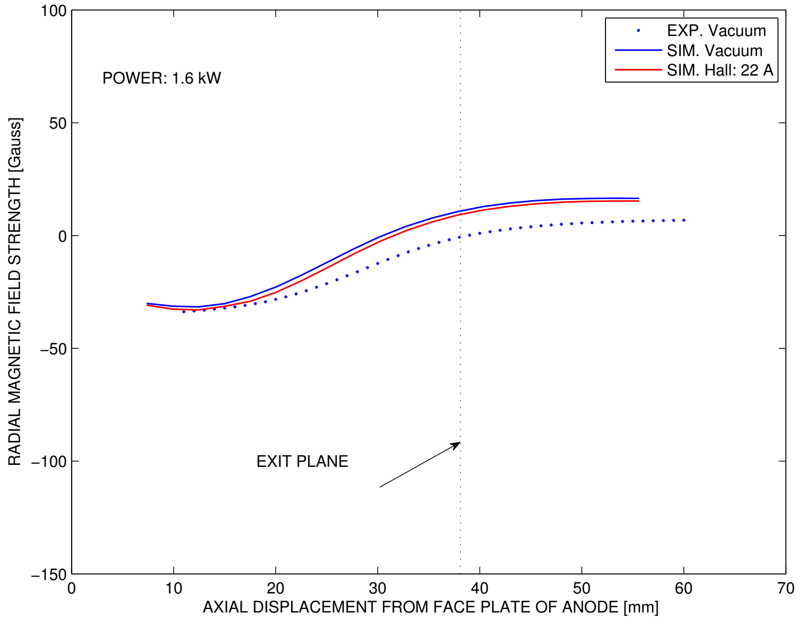

(a) 1.6 kW

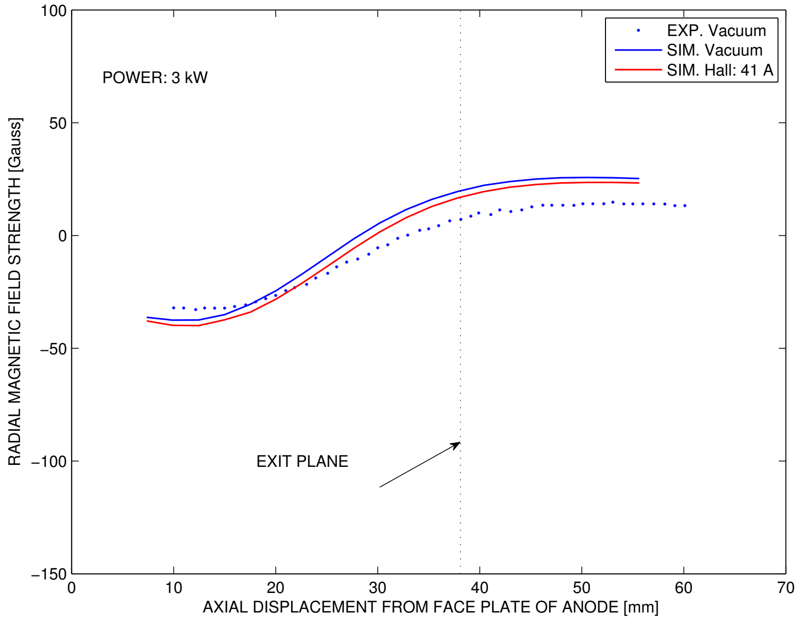

(b) 3.0 kW

Fig. 4.13: Effect of the Hall current on the variation of in vacuo axial magnetic field strength in the discharge channel of the P5 at 12.5 mm (centerline of channel) from the inner wall. The variations are normalized by the maxima of experimental field strengths. The '22 A' and '41 A' labels refer to the integral of the Hall current distributions at 1.6 kW and 3.0 kW, respectively, in the area where its profile has been simulated. Experimental distributions in vacuo [1] are displayed in the figures for the sake of completeness.

electrons along magnetic stremline that reveals that magnetic field lines correspond, to a first-order approximation, to 'thermal potential' lines or equipotentials of the electric field. Since ions travel in a direction opposite to the field, equipotentials with a positive curvature (concave) along the radial direction focus ions as well as neutrals (produced from charge-exchange) along channel's axis.

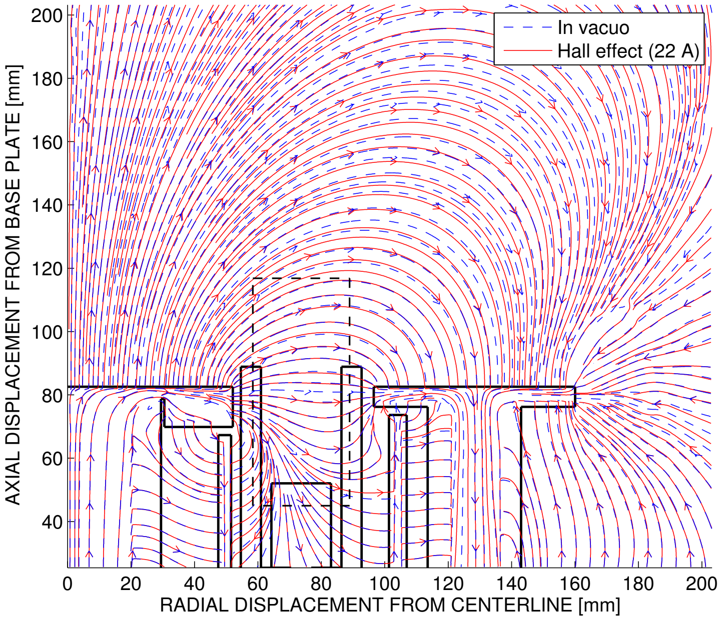

(a) Streamlines of the magnetic field

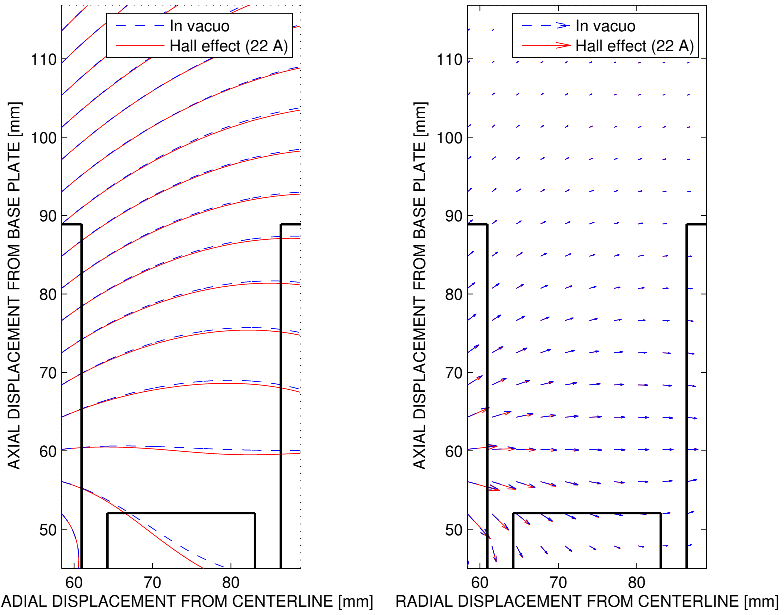

(b) Close-up at the exit plane

Fig. 4.14: Effect of the Hall current on vacuum field topology of the P5 in the acceleration zone at 1.6 kW

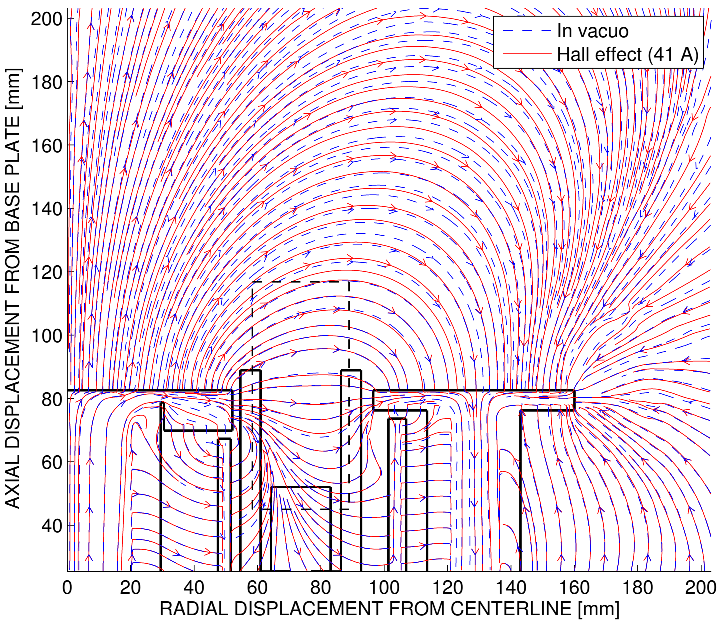

(a) Streamlines of the magnetic field

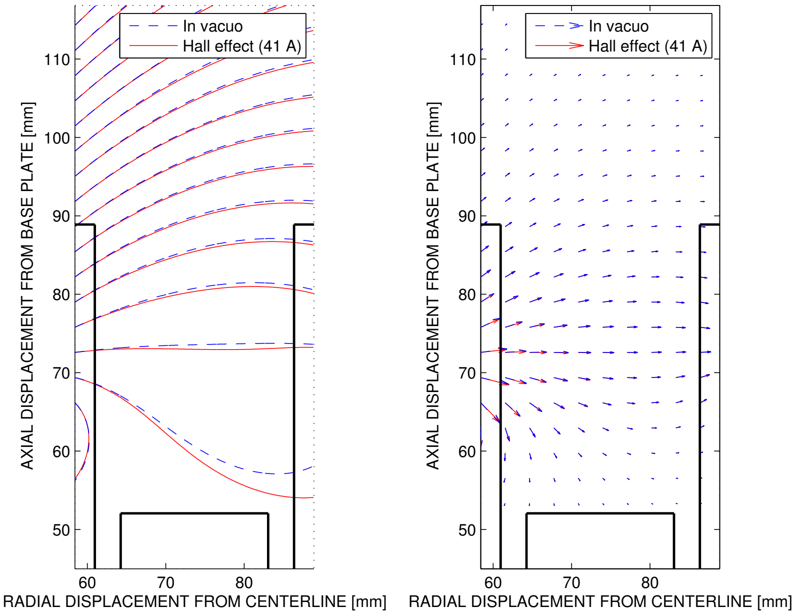

(b) Close-up at the exit plane

Fig. 4.15: Effect of the Hall current on vacuum field topology of the P5 in the acceleration zone at 3 kW

4.3 Effect of varying the Hall current's magnitude on the vacuum magnetic field of the P5

4.3.1 Effect of the Hall current on magnetic field strength

The above analysis is based on Hall current distributions whose integral value is on the same order as Haas' estimations at 1.6 kW and 3 kW. However, as mentionned in Section 4.1, these proved to be considerably smaller than previous estimations of the Hall current at similar power levels and discharge parameters.

Such discrepancies prompted us to consider other magnitudes of the Hall current in the study of the Hall current's effect on the thruster's magnetic field. In the analysis reported in the current Section, the Hall current was uniformly scaled accross its spatial distribution by factors varying from 1 to 8—while preserving its spatial variation—which, in practice, can be achieved by varying the electron density via changes in the cathode flow rate, for example. Figures 4.16(a) and 4.16(b) respectively report the variation of the magnetic field strength's radial component along the channel's centerline at 1.6 kW and 3.0 kW. At the 1.6 kW setting, the Hall current's integral was scaled from 22 A to 88 A; while at the 3 kW setting, the integral of the total Hall current ranged from 41 A to 168 A. When scaled by a factor as large as 8, the Hall current current induced a reduction of the radial magnetic field strength by as much as 25% from the circuit-induced field strength; the reduction gets more important with increasing power.

The effect of the Hall current on the radial field strength at off-centerline radial locations are listed in Appendix A. At each of those radial locations, the peak of the radial component of the field strength shifts towards the anode as the integrated current density increases. This is undesirable based on Morozov's finding that the gradient of the magnetic strength must be positive within the discharge chamber [25] (refer to the discussion at the beginning of this chapter).

Corresponding axial distributions are reported in figures 4.17(a) and 4.17(b) at both power settings along the channel's centerline. When scaled by a factor as large as 8, the Hall current current induced a reduction of the magnetic field strength by as much as 85% from the circuit-induced field strength; as in the previous case, the reduction becomes more important with increasing power. The effect of the Hall current on the axial field strength at off-centerline radial locations are listed in Appendix A. The axial distributions exhibit evidence of a positive contribution of the Hall current's induction on the vacuum field strength upstream of the centroid of the Hall current (centered about 15 mm from anode's face plate at both power settings as shown in figures 4.9(a) and 4.10(a)) magnetic field strength is evident along the radial and axial directions with increased integrated current. The variation of the axial component of the magnetic field strength along the channel's centerline exhibits a decrease of the vacuum field (or increase in its absolute value) when exposed to the Hall current; which, in this case persists along the channel's length since the centroid is located to the right of the centerline.

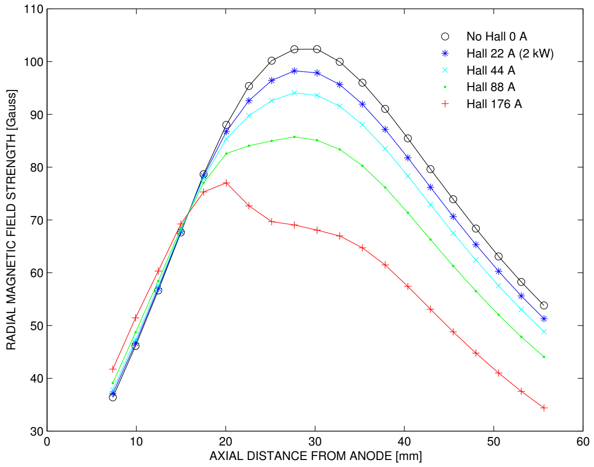

(a) 1.6 kW

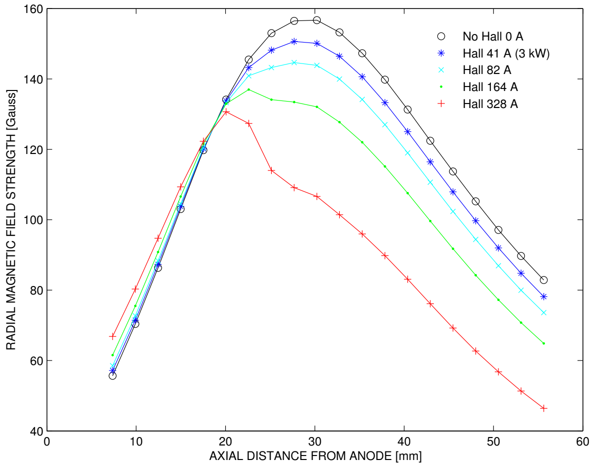

(b) 3.0 kW

Fig. 4.16: Effect of the Hall current on the variation of in vacuo radial magnetic field strength in the discharge channel of the P5 at 12.5 mm (centerline of channel) from the inner wall. The variations are normalized by the maxima of experimental field strengths. Five different Hall current settings are considered: each results from scaling the Hall current distribution associated with the 1.6 kW (22 A) and 3 kW (41 A) power settings by 1, 2, 4, and 8. Experimental distributions in vacuo [1] are displayed on the figure for the sake of completeness.

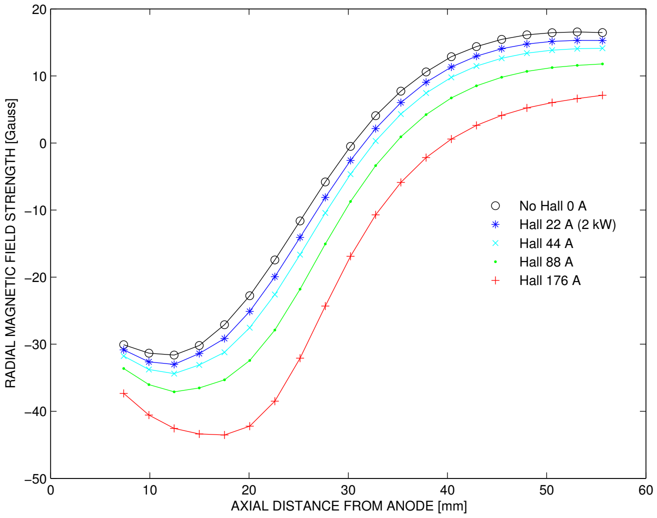

(a) 1.6 kW

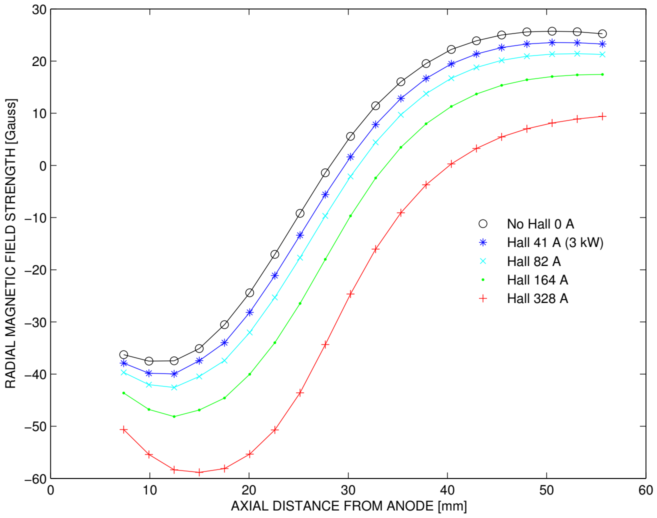

(b) 3.0 kW

Fig. 4.17: Effect of the Hall current on the variation of in vacuo axial magnetic field strength in the discharge channel of the P5 at 12.5 mm (centerline of channel) from the inner wall. The variations are normalized by the maxima of experimental field strengths. Five different Hall current settings are considered: each results from scaling the Hall current distribution associated with the 1.6 kW (22 A) and 3 kW (41 A) power settings by 1, 2, 4, and 8. Experimental distributions in vacuo [1] are displayed on the figure for the sake of completeness.

4.3.2 Effect of varying the Hall current on magnetic field shape

Varying the magnitude of the Hall current not only significantly affects the strength of the magnetic field in the discharge channel of the P5, but also substantially affects its shape. Figures 4.18 and 4.19 respectively report streamlines of the magnetic field with and without the effect of the Hall current in the discharge channel of the P5 at Hall current integrals of 176 A and 328 A, respectively associated with scalings of the total current by a factor of 8 from its actual value at 1.6 kW and 3 kW. Note that these contours differ from field lines (resulting in no scaling of the Hall current) plotted in figures 4.14 and 4.15 of Section 4.2.4. At each power setting, a comparison of the streamlines indicates that the larger integral current, the greater the concavity of field lines. Moreover, this effect is more pronounced with increasing power.

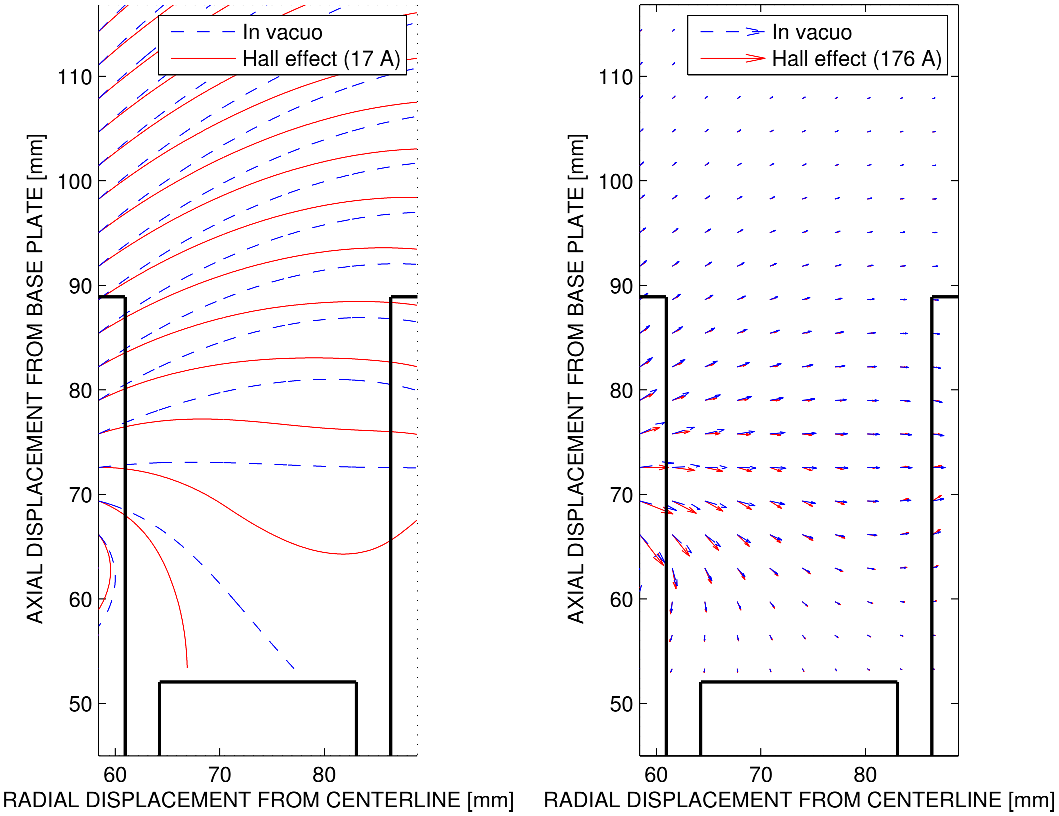

Fig. 4.18: Effect of changing the integral of the Hall current's magnitude on the structure of the circuit-induced magnetic field in the discharge channel of the P5. The plotted field results from a uniform scaling of the Hall current by a factor of 8; that is, 176 A at 1.6 kW. The corresponding spatial distribution of the Hall current remains unchanged from Haas' probe measurements at the 1.6 kW (22 A) [1].

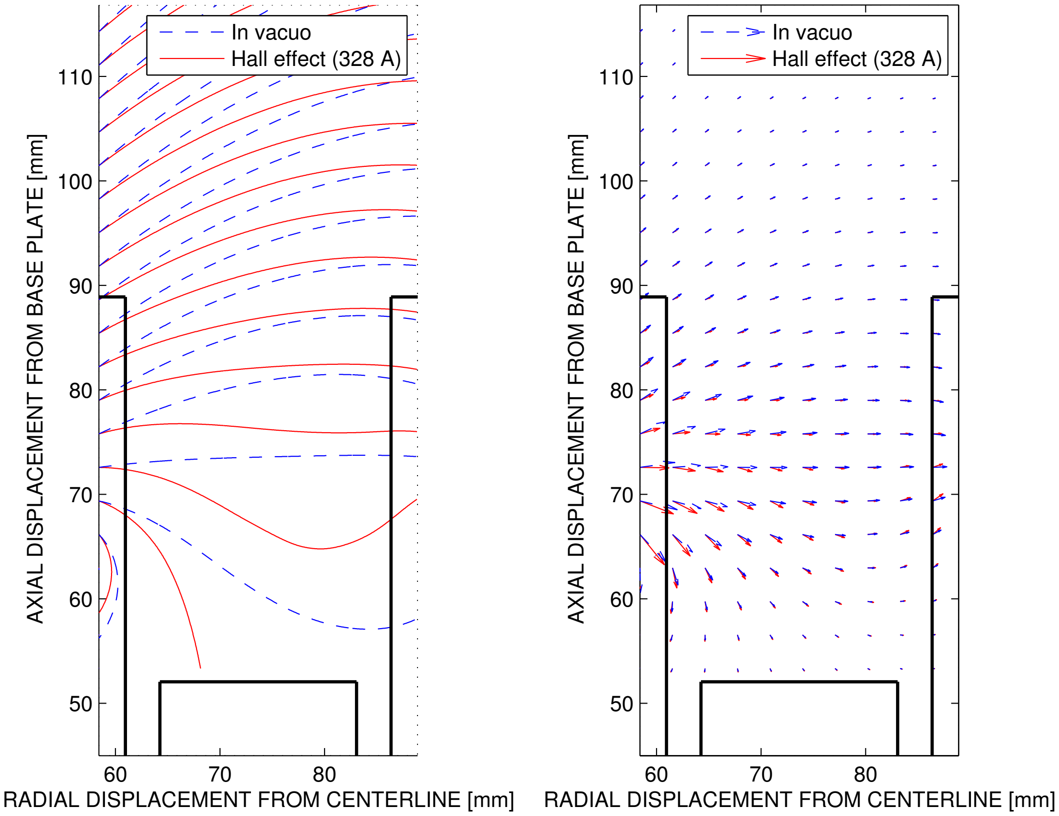

Fig. 4.19: Effect of changing the integral of the Hall current's magnitude on the structure of the circuit-induced magnetic field in the discharge channel of the P5. The plotted field results from a uniform scaling of the Hall current by a factor of 8; that is, 328 A at 3 kW. The corresponding spatial distribution of the Hall current remains unchanged from Haas' probe measurements at the 3 kW (41 A) [1].

4.4 Estimation of the thrust vector field the discharge channel of the P5

MagNet 6 is not only useful in studying the effect of the Hall current on the vacuum magnetic field but also allows an easy deduction of the thrust per unit volume per particle via equation 4.4.1 (recall Section 3.2.3 of Chapter III):

$$\vec{T} = \vec{J} \times \vec{B} \tag{4.4.1}$$

The resulting thrust fields are presented in the arrow plots of figures 4.14 and 4.15 for the 1.6 kW and 3 kW settings, respectively. The vector fields, which are similar at the two design power settings investigated, are predominantly axial; except near the inner wall of the discharge chamber where they exhibit some substantial radial component, which may reflect the fact that the axial component of the magnetic field strength is significant in this region (recall Section 4.2.1). We also note that the acceleration zone is primarily concentrated in a region extending axially from the middle of the discharge channel to the exit plane. It is interesting to note that large acceleration zones coincide with regions where the curvature of magnetic field streamlines is negative the most; this further confirms Morozov [25] and Zhurin's [9] claims reported earlier in 4.2.4.

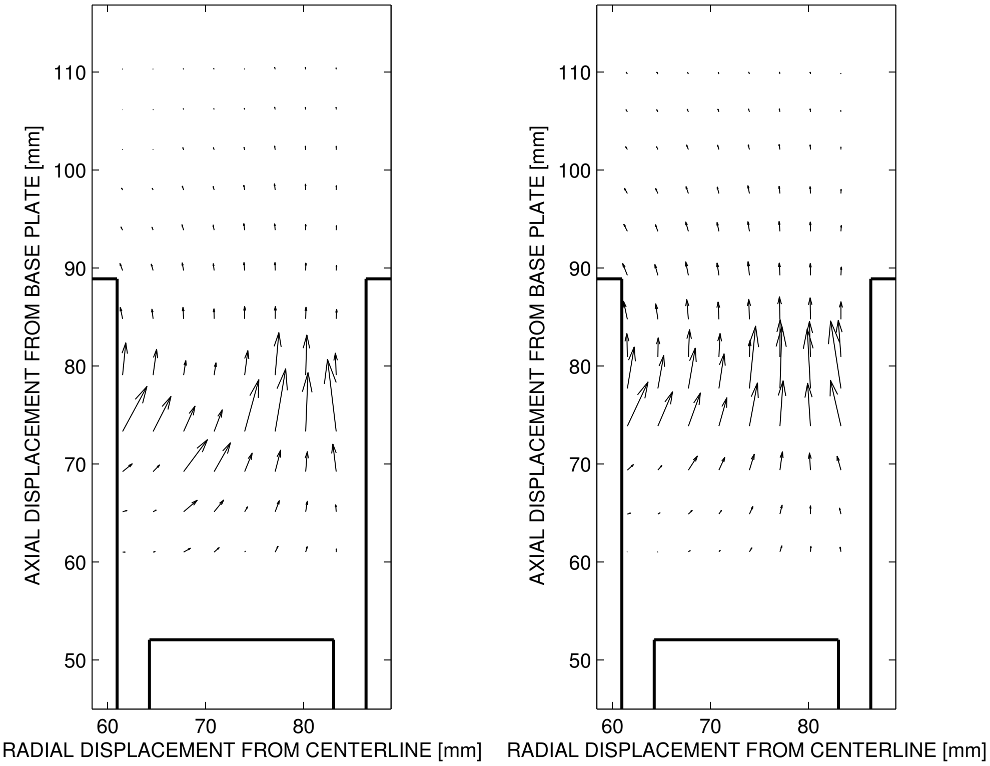

(a) Power: 1.6 kW

(b) Power: 3.0 kW

Fig. 4.20: JxB vector-field in the acceleration zone of the P5 estimated from MagNet simulations of the Hall current and magnetic field at two power levels

CHAPTER V

Absorption spectrum modeling of neutral xenon undergoing Zeeman effect in an optogalvanic cell exposed to an external magnetic field

As demonstrated in the previous chapter, MagNet 6 is a reliable tool for simulating the magnetic field structure of the P5 Hall thruster in vacuo (magnetic circuit switched on without any plasma discharge). As it was then demonstrated, simulated field variations exhibited shape-similarity with experimental measurements along both radial and axial directions while their magnitudes were underestimated. We also attempted to simulate the effect of the plasma on the magnetic field by modelling the Hall current with current conducting wires based on current density measurements extracted from the discharge channel.

Experimental errors associated with magnetic field measurements were found by Haas to be small in vacuo (less than 1 % error) [1]; hence, making it possible to reliably validate our simulations. When plasma is present however, no experimental field measurements are available to validate our 'warm' simulations of the field topology; finite-sized probes are unattractive for such task since they tend to contaminate the plasma. Perturbations from physical probe insertion include Hall current blockage, secondary electron emission, and sputtering of exposed metals and ceramics [1, 30].

This makes probe-size reduction to sub-millimeter magnitudes the main recourse to reducing intrusiveness; this, however, comes at the expense of higher sensitivity to failure.

As a result, there has been growing interest in laser-induced fluorescence (LIF); the non-intrusive nature of this optical technique makes it attractive for sketching the magnetic field topology in thruster discharges through spectral analysis. When subject to the external effect of field-generating thruster-magnets, energy levels of plasma-discharge particles split, thereby affecting LIF spectra. While non-intrusive, the LIF-approach may be inconvenient to the novice in quantum physics, for analyses of measured spectra tend to be computationally tedious. Unlike physical probe-based measurements, whose results easily yield sought field magnitudes via an auxiliary device (such as a Hall probe), the optical approach relies on a complex computational analysis of measured spectra based on the quantum mechanics of light matter interaction in the environment of an external magnetic field. The splitting of atomic spectra under the influence of an external magnetic field was first observed by Pieter Zeeman in 1896 while studying the spectrum of sodium light emission in the neighborhood of an electromagnet [31]. All elements of the periodic table exhibit such an effect to varying degrees of complexity depending on the wavelength probed.

As mentioned earlier the magnetic field topology of the P5 is not known when in warm operation; hence, we could not reliably validate our computational model based from LIF measurements in the discharge channel of the thruster. LIF experiments in Hall thruster discharges involve a great deal of preparation, are costly (due to tank pump-down and propellant cost), and involve tedious data reduction (e.g. spectral deconvolution, noise filtering, etc...) before any absorption spectra can be extracted for analysis. To avoid any potential waste of time and resources in validating our computational model, we used xenon spectra measured in the plasma discharge of an optogalvanic cell—a small plasma tube that requires a simpler experimental setup and data acquisition process.

5.1 Near-infrared neutral xenon spectroscopy in an optogalvanic cell exposed to an external magnetic field

Smith et. al [32] performed absorption spectroscopy of neutral xenon using an optogalvanic sensor exposed to an external magnetic field. A sketch of the optogalvanic sensor or 'laser galvatron' used in their experiment is shown on Figure 5.1. A sketch of the optical setup is shown in Figure 5.2 while an illustration of optical, analog, and digital signal flows are reported in Figure 5.3. The laser galvatron consists of a glass tube filled with a gas and containing two oppositely charged hollow electrodes (a negative cathode and a positive anode). The type of gas and the material constitution of the cathode may vary. The experiment was conducted with an L2783-42x NE-MO galvatron (manufactured by Hamamatsu Photonics) filled with xenon and neon (non-reacting gas used as a filler) and whose cathode is made of molybdenum.

The principle of operation of the galvatron is simple [33]. An external power source generates a potential difference between the electrodes to initiate and sustain a plasma discharge in the glass tube. Smith et. al used a Stanford Research Systems, Inc. power supply (model P5310 capable of delivering 1250 V at 25 W) and maintained the discharge voltage and current to 250 V and 4.0 mA (respectively) during the experiment. The device has a wide range of applications in optics: from calibration and stabilization of lasers to communication and spectroscopy. In its latter application, it allows the measurement of absorption spectra of plasma species—xenon, for our purposes. A laser beam is sent in a direction parallel to the axis of the glass tube (Figure 5.1) across the inclined input windows through the hollow electrodes. The input and output windows are inclined at 10^o (Brewster angle) with respect to the vertical to minimize refractive losses. Xenon particles contained within the path length of the laser absorb light and assume higher energy levels when the energy spectrum of the incident photons matches the transition's lineshape spectrum. When the laser is properly aligned with the axis of the electrodes and its wavelength is tuned at the absorption line of xenon (e.g. 834.912 nm-vacuum line of neutral xenon) within a small detuning interval (10 GHz or 0.02 nm about a center-wavelength), the conductivity of the plasma changes substantially (resonance); which, in turn affects the voltage difference between electrodes. The corresponding electric signal, which varies with the strength of the transition, is relayed to an RC circuit. This circuit filters out high-frequency components of the galvatron's signal output with a time constant of $t_c = RC \approx 15\ s$. In this experiment, the laser beam was segmented at a frequency of roughly 1700 kHz by a chopper (C) so to induce an AC optogalvanic voltage that can detected and amplified by a lock-in amplifier (phase-sensitive detector) before being relayed to a PC running a LabVIEW interface.

The measurements of absorption spectra were performed on neutral xenon and were restricted in the near-infrared because of the narrow coarse-tuning range (820-836 nm) of the source of our optical diagnostic system consisting of a tunable single-mode diode-laser (manufactured by TOPTICA Photonics Inc.) with a 10 GHz-mode-hop-free frequency detuning range [34]. Such a laser offers many advantages (e.g. compactness and ease of operation) over traditional dye lasers in spite of the latter devices' much wider coarse detuning ranges. A scan-controller (SC) varied the voltage input to a piezoelectric diffraction-grating element over a 10 V span so as to induce a detuning of 10 GHz about the center-frequency of the sought spectrum. Both the scan-controller (SC) and the grating element are part of the diode-laser system (DL). A beam-splitter (BS) and a set of reflecting mirrors (RM) guided the laser beam atop a vibration-isolated table toward the various optical devices. A WA-1000 wavemeter (WA) permitted live monitoring of the laser wavelength during the detuning process while its digital output was sent to a LabVIEW interface. A neutral density filter

(NF) was used to attenuate the input beam to the wavemeter (WA).

A magnetic field produced by a pair of Helmholtz coils or, simply put, electromagnets (EM) on either side of the galvatron, produced field lines oriented perpendicularly to the galvatron's axis and of maximum intensity at its center. To excite σ-transitions, the polarization axis of the laser beam was rotated until perpendicular to the magnetic field inside the galvatron. A cubic polarizing-beam splitter (P) was used for that purpose. A diaphragm or iris (I) reduced the diffusion of the light input to the galvatron so to reduce its scattering by electrodes, which tends to distort the optogalvanic signal. For safety purposes, a beam dump (BD) intercepted the laser-beam exiting the galvatron's window.

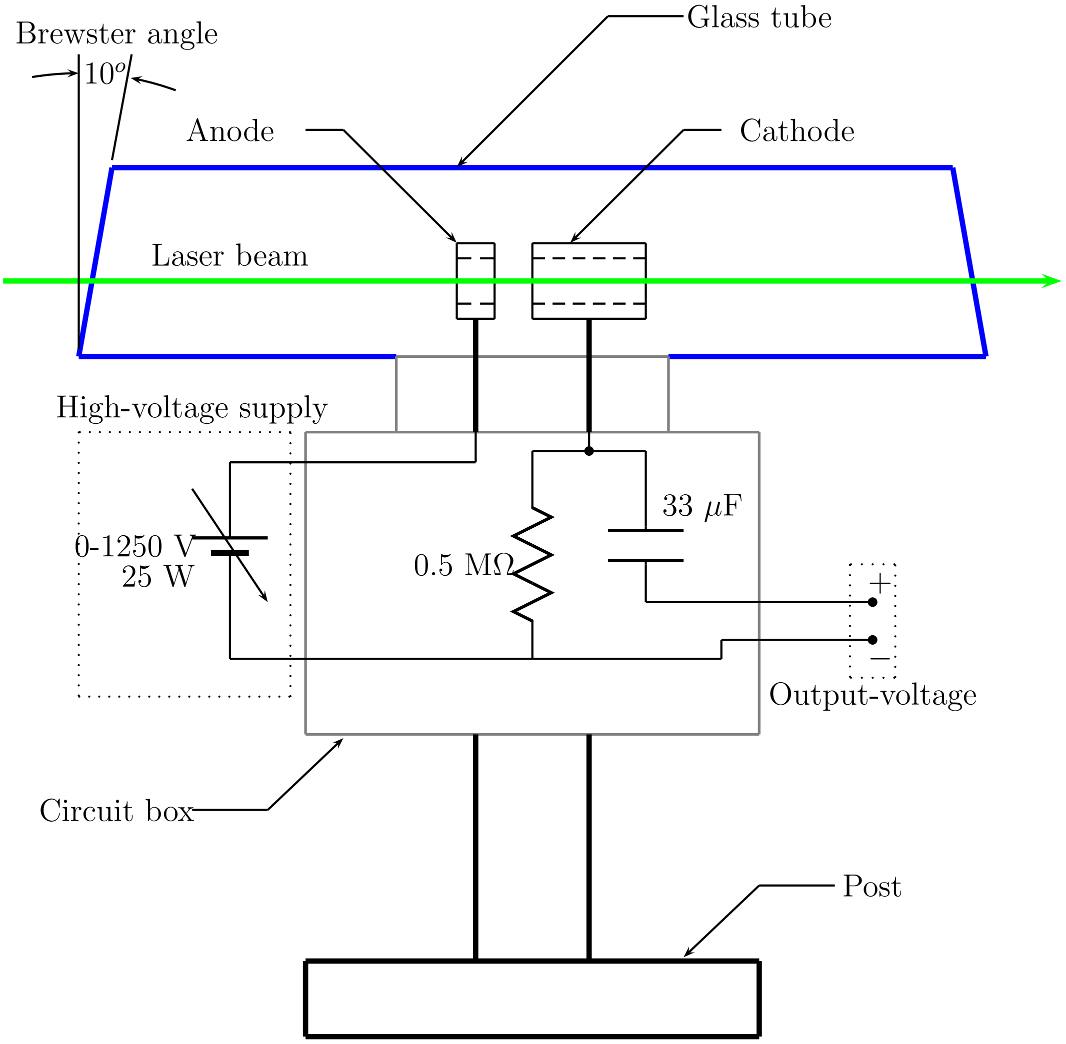

Fig. 5.1: Description of a laser-galvatron for xenon spectroscopy

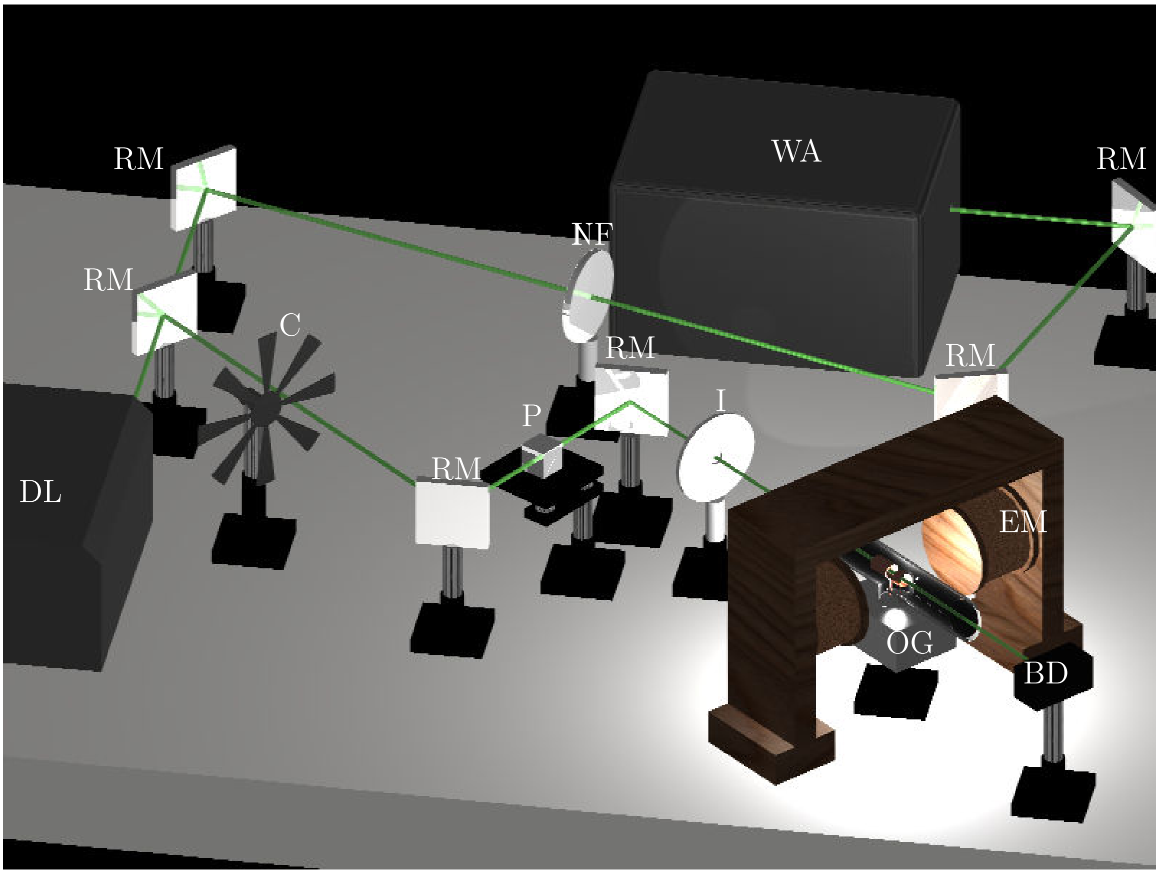

Fig. 5.2: Optical setup for xenon spectroscopy using a laser galvatron exposed to an external magnetic field

5.2 Introduction to theories of the Zeeman effect on fine and hyperfine structure

As mentioned earlier, the spectrum of plasma particles undergo the Zeeman effect when subject to an external magnetic field. Hence, in the remainder of this chapter, we will:

- introduce background needed for a basic understanding of the Zeeman theory;
- present a practical example, demonstrate how the theory can be applied to the determination of xenon's line spectra (discrete spectra);
- simulate xenon absorption spectra (continuous spectra) by Doppler-broadening

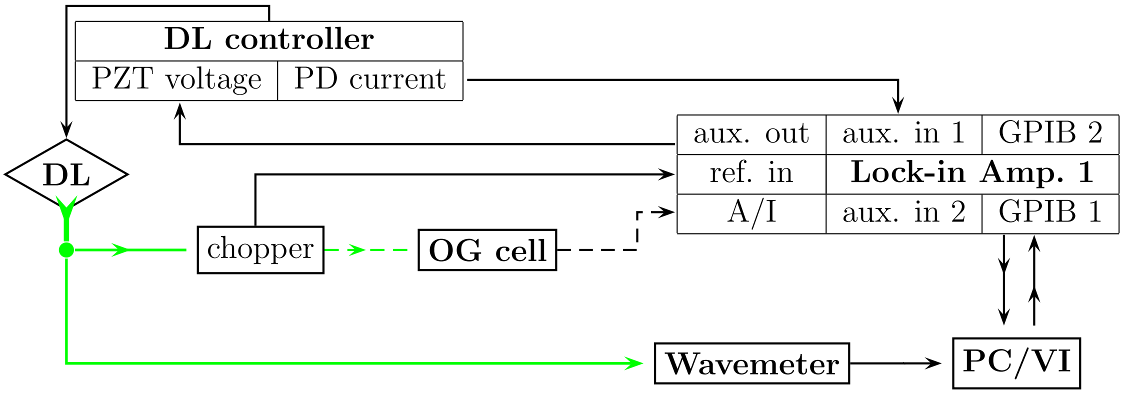

Fig. 5.3: Flow diagram illustrating optical, electric, and digital signals in spectroscopy of xenon in an optogalvanic sensor

line spectra and validate the former spectra against experimental measurements at a few magnetic field settings;

- and test the capability of a non-linear least-squares solver for the extraction of magnetic field strengths and kinetic temperatures that best minimize the error between measured and simulated spectra.

5.2.1 The Anomalous Zeeman effect

We start our theoretical introduction with the simplest Zeeman effect described by the Anomalous Zeeman theory [35]. This theory applies to atoms that possess no nuclear spin and are subject to an external magnetic field of strength H. Based on the vector model, the application of such a field leads to a precession of an outer-electron's resultant momentum vector ($\vec{J}$) about the direction of propagation of the field lines ($\vec{H}$). To each $\vec{J}$ is associated a discrete 'J-level' of the atom denoting the energy of a valence electron arising from the interaction between the particle's orbital angular momentum ($\vec{L}$) and its spin ($\vec{S}$). This interaction results in a total angular momentum vector $\vec{J} = \vec{L} + \vec{S}$, whose magnitude is proportional to a quantum number J (integer-valued). The angle between $\vec{J}$ and $\vec{H}$ can only assume discrete values. To each possible orientation of $\vec{J}$ is associated a specific magnetic moment $\vec{\mu_J}$, whose magnitude is proportional to a quantum number M_J that can only assume discrete values given by:

$$-J \leq M_J \leq +J \text{ with } \Delta M_J = \pm 1, \text{or } 0. \tag{5.2.1}$$

This quantization of the magnetic moment leads to quantized M_J-levels symmetrically distributed about each parent J-level. Possible energy displacements about some parent J-level vary linearly with M_J and H according to the following equation for each M_J state:

$$\Delta E = g_J M_J H, \tag{5.2.2}$$

where g_J is the Landé factor associated with the total electronic angular momentum J. The splittings of the J-level can be interpreted as the various possible projections of $\vec{J}$ about $\vec{H}$ is restricted to vary discretely.

The transition between energy levels varies depending on the orientation of the polarization vector of the exciting radiation (perpendicular or parallel) with respect to the direction of the magnetic flux density vector. Parallely polarized light excites π-transitions such that $\Delta M_J = 0$ (also labeled as $M_J \rightarrow M_J$). Perpendicularly polarized light, on the other hand, excites $\sigma^{\pm}$-transitions such that $\Delta M_J = \pm 1$ (also labeled as $M_J \rightarrow M_J \pm 1$). In this work, we will limit our interest to σ-transitions whose intensities are expressed in the following equations:

$$I_{M_J \rightarrow M_J - 1} = \quad K\,(J - M_J + 1)\,(J - M_J + 2) \tag{5.2.3a}$$

$$I_{M_J \rightarrow M_J + 1} = \quad K\,(J + M_J + 1)\,(J + M_J + 2) \tag{5.2.3b}$$

where K is an arbitrary normalization factor and all quantum numbers are associated with lower (or initial) states.

5.2.2 The Zeeman effect of hyperfine structure

The Zeeman effect on species having a non-zero nuclear spin (denoted I and not to be confused with transition intensity)—hence, exhibiting hyperfine structure [36]—is more complex than the previously described linear Zeeman model. The complexity arises from coupled interactions of the magnetic field with momenta associated with the nucleus and an outer electron. A matrix-based non-linear theory [37] by Sommerfeld, Heisenberg, Lande, and Pauli dating back to the 1930s accurately models the Zeeman effect on a spinning spherical charged body orbiting a central force field while subject to an external magnetic field. A relatively more thorough accessible formulation of the theory can be found in Darwin's simpler wave-mechanics treatment [37, 38]. Bacher [39] applied the theory to thallium and bismuth hyperfine lines in the 300-500 nm wavelength range and validated it to good approximation against observed spectra. Though useful, the theory has been, for the most part, ignored among the engineering community probably because of the complex nature of computations involved—especially when applied to elements with high momentum quantum numbers. As a recourse, a common trend has been to use approximate methods suited for low and high magnetic field intensities; low-field linear Zeeman and high-field Paschen-Back models are two such common recourses.

With modern days' advances in computing capabilities, modeling the non-linear Zeeman effect on hyperfine structure (ZHFS) is becoming increasingly attractive. Before describing the ZHFS theory, we begin a brief introduction of the approximate Zeeman models.

5.2.2.1 Linear approximation of the Zeeman effect of hyperfine structure in weak and strong-field strength regimes

Low and high-field approximations of the Zeeman effect on hyperfine structure are linear theories, more thoroughly discussed by Haken and Wolf[35] and Sobelman[40].

In this chapter, we only report essentials of the theories needed for an introduction of the non-linear Zeeman theory. The weak-field Zeeman theory of hyperfine structure applies when the mean separation of energy levels due to hyperfine structure alone (ΔE_{hfs} as $H \rightarrow 0\ G$) is much smaller than their mean splitting due to the Zeeman effect ΔE_{mag}. In the vector representation, the model predicts a precession of the total angular momentum ($\vec{F}$ resulting from IJ-coupling denoting the interaction between nuclear-spin and angular momentum) of an atomic system about $\vec{H}$. This precessive motion only occurs at discrete angles and leads to a quantized magnetic moment μ_M proportional to a quantum number M. The following selection rules dictate permissible values of F and M.

$$|I - J| \leq F \leq I + J \;\text{ with }\; \Delta F = 0, \pm 1; \tag{5.2.4}$$

where I and J respectively denote nuclear spin and total electronic angular momentum.

$$-F \leq M \leq +F \;\text{ with }\; \Delta M = 0, \pm 1. \tag{5.2.5}$$

Energy displacements about some parent F-level due to an external field of strength H are given by:

$$\Delta E = \mu_M H = (g_{F} \mu_B M) H, \tag{5.2.6}$$

where the Landé-factor, g_{F}, linearly varies with electronic and nucleic Landé g-factors $g_{J}$and g_{I}, as expressed below:

$$g_{F} = g_{J} \frac{F\left(F+1\right) + J\left(J+1\right) - I\left(I+1\right)}{2F\left(F+1\right)} - g_{I} \frac{\left(\frac{\mu_N}{\mu_B}\right)\left[F\left(F+1\right) - J\left(J+1\right) + I\left(I+1\right)\right]}{2\frac{F}{F1+1}} \tag{5.2.7}$$

In equation (5.2.7), μ_B and μ_N respectively denote the Bohr magneton and the nuclear moment (refer to Section 5.3.1 for a discussion on the latter variable).

In the weak-field approximation, intensities of perpendicularly polarized transitions associated with parent levels $J \rightarrow J+1$ are of the same form as those of the Anomalous Zeeman theory (refer to equation 5.2.3) and are found by replacing J by F and M_J by M; this is based on Sobelman's argument that F components split in a similar fashion as J components in a weak field [40].

In the strong-field limit—when $\Delta E_{mag} \gg \Delta E_{hfs}$[35, 39]—the Pashen-Back effect on hyperfine structure applies. In this case, H is so large as to cause a decoupling of $\vec{I}$ and $\vec{J}$; hence, leading to independent precessions of the latter momenta about $\vec{H}$. The precessions lead to separate quantized magnetic moment vectors $\mu_{\vec{M_J}}$ and $\mu_{\vec{M_I}}$ of magnitudes respectively proportional to moment quantum numbers M_J and M_I and whose selection rules are respectively given in (5.2.1) and:

$$-I \leq M_I \leq +I \;\text{ with }\; \Delta M_I = 0, \pm 1. \tag{5.2.8}$$

5.2.2.2 Non-linear Zeeman effect of hyperfine structure

The non-linear theory of the Zeeman effect of hyperfine structure is based upon a simple two-particle model. A spinning particle induces a central force field on a spinning spherical particle in orbit about the former as a magnetic field externally acts upon the overall system[37, 39]. The theory is exact over an arbitrarily broad range of field strengths when applied to one-electron atoms, whose nuclei exert a spherically symmetric electric potential on their respective electrons. Based on this model, the system's wave-function $\Psi = \Psi(\lambda, \chi, \mu, r, \theta, \varphi)$ is respectively separable into nuclear and outer-electron components ($\Psi_N = \Psi_N(\lambda, \chi, \mu)$) and ($\Psi_E = \Psi_E(r, \theta, \varphi)$), respectively; whose separate motions are described in independent Eulerian polar coordinate systems[39]. Under these assumptions, the time-independent form of the

Schrödinger wave-equation assumes the form [41]:

$$\left(V_{KE} + V_E + V_{LS} + V_{IJ} + V_{H^1} + V_{H^2}\right)\Psi = E\Psi, \tag{5.2.9}$$

where the left-hand side of the equation consists of a Hamiltonian operator acting upon the wave-function and accounting for (from left to right):

- the free particles' kinetic energy, coulombic interaction (V_E), and electronic spin-to-angular momentum interactions—both are inherent to the atomic system and lead to the fine structure of its spectrum;
- nuclear spin and outer-electron's resultant momentum interaction (V_{IJ}), which is responsible for hyperfine structure;
- and independent and coupled interactions of $\vec{I}$ and $\vec{J}$ with $\vec{H}$, responsible for linear (through V_{H^1}) and non-linear (through V_{H^2}) Zeeman effects on the hyperfine structure.

Solving (5.2.9) results in the following exact form of the wave-function [39]:

$$\Psi^{M_J,M_I}\left(\lambda,\chi,\mu,r,\theta,\varphi\right) = \sum_{M_J,M_I} X_{M_J,M_I}\Psi_E^{M_J}\left(r,\theta,\varphi\right)\Psi_N^{M_I}\left(\lambda,\chi,\mu\right), \tag{5.2.10}$$

in which the separate wave-functions associated with the electron and nucleus respectively assume the following forms:

$$\Psi_E^{M_J}\left(r,\theta,\varphi\right) = f(r)P_J^{M_J}(\cos\theta)e^{iM_J\varphi} \tag{5.2.11a}$$

$$\Psi_N^{M_I}\left(\lambda,\chi,\mu\right) = P_I^{M_I}(\cos\chi)e^{i(M_I\lambda+\tau\mu)}. \tag{5.2.11b}$$

Substitution of (5.2.11a) and (5.2.11b) into (5.2.10), then into the Schrödinger equation (5.2.9); and integration over the space enclosing outer-electron and nucleus subspaces leads to the following characteristic equation (5.2.12) relating energy levels to a set of probability amplitudes (X) associated with each quantum state:

$$\begin{aligned}
&-\left[\frac{a}{2}\left(J-M_J+1\right)\left(I+M_I+1\right)\right]X_{M_J-1,M_I+1}\\
&-\left[\frac{a}{2}\left(J+M_J+1\right)\left(I-M_I+1\right)\right]X_{M_J+1,M_I-1}\\
+&\left[E_{M_J,M_I}-a\,M_J\,M_I-\left(M_Jg_J+M_Ig_I\right)\,o\,H\right]X_{M_J,M_I}=0,
\end{aligned} \tag{5.2.12}$$

In the above characteristic equation,

- H denotes the magnetic field strength;
- $o = e/\left(4\pi mc^2\right)$ is the Larmor precession frequency;
- g_J and g_I denote Landé g-factors, respectively associated with the outer-electron and the nucleus;
- a denotes the hyperfine unit interval;
- and M_J and M_I are moment quantum numbers associated with the precessive motion of the outer-electron's orbital momentum and the nucleus' spin about $\vec{H}$.

In conjunction with the sum rule ($M = M_J + M_I$), the selection rules given in equations (5.2.1) and (5.2.8) yield all permissible sets (M_J,M_I). While M is a quantum number in the weak-field approximation[1] (recall to 5.2.2.1), it is not considered a quantum number in the non-linear ZHFS model [39]; hence, the set $\left|JFM_JM_I\right\rangle$ is sufficient and necessary to fully describe a single quantum state. To each such set, corresponds a single sub-equation of (5.2.12). Considering n possible energy states, one can conveniently express the characteristic equation (5.2.12) in the following matrix form:

$$[\mathrm{X}]_{n\times n}[\mathrm{E}]_{n\times n} = [\mathrm{C}]_{n\times n}[\mathrm{X}]_{n\times n}, \text{where} \tag{5.2.13}$$

---

[1] While M is a valid quantum number in the low-field approximation, it is not considered one in the non-linear Zeeman theory on hyperfine structure. Its use in the latter theory is exclusively limited to denote possible sums of $M_J$and $M_I$and to insure conservation of angular momentum.

- [E] is a diagonal matrix whose diagonal entries consist of all possible energy displacements about some parent J-level of interest;
- [X] is a square matrix whose columns represent vectors whose components consist of a set of mode-shape amplitudes $X^{J,F}_{M_J,M_I}$ associated with each state;
- and [C] is a matrix of factors multiplying each mode-shape amplitude in equation (5.2.12)

Depending on the polarization of the exciting radiation, transitions may obey one of the following rules: $\Delta M = 0$ for parallel (π-) or ± 1 for perpendicular ($\sigma^{\pm}$) polarizations, respectively. In this paper, we restrict our interest to the latter type of polarization and for the particular class of $J \rightarrow J-1$ transitions for which, intensity formulas read:

$$I = \frac{\left[\sum_{M} X^{J,F}_{M_J,M_I} X^{J-1,F'}_{M'_J\pm 1,M_I}(I+M_I)!(I-M_I)!(J+M_J)!(J-M_J)!\right]^2}{N^{J,F}_{M} N^{J-1,F}_{M\pm 1}}, \qquad (5.2.14)$$

where upper- and lower-state normalization constants ($N^{J,F}_{M}$ and $N^{J-1,F}_{M\pm 1}$, respectively) are found from the following equation:

$$N^{J,F}_{M} = \sum_{M} (X^{J,F}_{M_J,M_I})^2 (I+M_I)!(I-M_I)!(J+M_J)!(J-M_J)!. \qquad (5.2.15)$$

The summations (5.2.14) and (5.2.15) are performed over all possible sets (M_J, M_I) satisfying the conservation of momentum condition (or sum-rule): $M = M_J + M_I$. For a better grasp of the implementation of the above intensity formulas, we recommend consultation of publications by Bacher [39] and Darwin [38]; which, contain several examples of their application worked out in great detail.

5.3 Application of the Zeeman theories of fine and hyperfine structure to the simulation of the absorption spectrum of neutral xenon (Xe I) about 834.912 nm

We applied linear and non-linear models to respectively simulate Zeeman effects on fine and hyperfine structures of neutral xenon (Xe I) at 834.682 nm (vacuum wavelength), which corresponds to the excitation wavelength of a particle transiting from lower energy level $6S'\,[1/2]$ to upper energy level $6P'\,[3/2]$. Owing to the fact that the nine stable isotopes of xenon are grouped into sets of atoms with and without nuclear spin, modeling the 834.682 nm absorption spectrum of Xe I, required separate analyses for each set. We validated our Zeeman model using spectral measurements of a xenon plasma produced in an optogalvanic cell immersed in a magnetic field generated by Helmholtz coils.

5.3.1 Transition line spectra modeling of isotopes with non-zero nuclear spin

As we noted in Section 5.2.2.2, the non-linear Zeeman theory was developed for hydrogen-like elements. However as it can be inferred from the ground state configuration of neutral xenon, $[Kr]\,4d^{10}5s^25p^6$), this atom has many electrons. So, before applying the non-linear ZHFS model to the two isotopes of non-zero spin (^{129}Xe and ^{131}Xe), we first ensure that our approach is reasonable. The 834.682 nm line of Xe I results from the interaction of two excited upper and lower states: $5p^5(^2P_{1/2})6s$ and $5p^5(^2P_{1/2})6p$. In this transition, a single electron from the outer $6s$ subshell assumes a higher orbital angular momentum state $6p$. The term $5p^5$ means that the outermost subshell of the ground state is vacant by one electron (since a p-subshell may contain no more than six electrons). This leaves the atomic system with an inner core: $[Kr]\,4d^{10}5s^25p^5$ [42].

The electron outside this inner core (termed 'outer-electron') undergoes LK coupling [42] (also termed LS_1). In this electronic configuration scheme, L accounts for the coupling of the orbital angular momentum of the core electrons with that of the outer-electron. The interaction of L with the overall spin of core electrons leads to a total angular momentum K. The interaction of K and the spin of the outer-electron (S) results in an effective resultant momentum quantum number, J, associated with the outer-electron. The nomenclature in LK coupling is of the form ${}^{2S+1}[K]_J$, which is analogous to the nomenclature of hydrogen-like atoms: nl^2L_J [42]. Based on this analogy, we can approximate our multi-electron atomic system as a hypothetical one-electron atomic system of angular momentum K, multiplicity $2S+1$, and total angular momentum J.

Next, we verify that the assumption of a spherically symmetric potential (or central field assumption) on the nucleus, mentioned at the beginning of this section, is reasonable for the $6\mathrm{S}'[1/2] \rightarrow 6\mathrm{P}'[3/2]$ transition of Xe I. Aside from the main Coulomb potential that acts upon all nuclei, there exists a differential electrostatic potential, which acts upon nuclei exhibiting an asymmetric structure. Such an asymmetry causes a variation of the gradient of the electric potential within the space occupied by the nucleus that leads to an electric quadrupole interaction moment Q. Positive and negative values of Q correspond to prolate ('cigar-like') and oblate ('disc-like') structures of the nucleus, respectively. The effect of this interaction on each hyperfine structure line component is a specific shift proportional to an electric quadrupole interaction constant [36] given by:

$$B = \frac{e^2}{4\pi\epsilon_0} q_J Q, \tag{5.3.1}$$

where the quantity q_J linearly depends on the electric field gradient. All nuclei of Xe I isotopes are symmetric except that of ^{131}Xe, whose nucleus exhibits a prolate structure

($Q > 0$). Suzuki [6] provides upper and lower state values of B for the latter isotope. When accounted for, this parameter induces a shift of hyperfine line components smaller than 5% based on transition energy formulae given by Svanberg [36]—who also reports hyperfine transition intensity formulae. This is illustrated in Figure 5.4(a), which compares cold spectra of ^{131}Xe for $B = 0$ and $B \neq 0$. Furthermore, these deviations are much less noticeable on the combined cold spectra of all isotopes (refer to Figure 5.4(b)). These facts validate the spherically symmetric potential assumption necessary for the application of the nonlinear ZHFS theory in modeling the Zeeman effect on the 6S′ [1/2] → 6P′ [3/2] transition of Xe I.

The application of the ZHFS theory to the 6S′ [1/2] → 6P′ [3/2] transition of neutral isotopes ^{129}Xe (nuclear spin 1/2) and ^{131}Xe (nuclear spin 3/2) begins with the determination of lower and upper energy levels and mode-shape amplitudes based on characteristic equation (5.2.12). The fortunate fact that all physical parameters associated with the two isotopes are known for this transition renders any numerical evaluation of the characteristic equation trivial:

- electronic Landé factors, g_J are given by Saloman [43]
- nuclear Landé factors, g_I, can be deduced for each isotope from nuclear moments, μ_N, reported by Emsley [44] based on the relationship $g_I = (m_e/m_p) \times (\mu_N/I)$ [35]
- upper and lower level hyperfine constants, a, are listed in Suzuki et al. [6] and Jackson et al. [45]

As a practical illustration of the determination of energy levels from the nonlinear ZHFS theory, we will consider the simpler case of 6S′ [1/2] of ^{129}Xe for which $J = 1$ and $I = 1/2$ [46]. Starting with selection rules (5.2.4), (5.2.1), and (5.2.8), we respectively find:

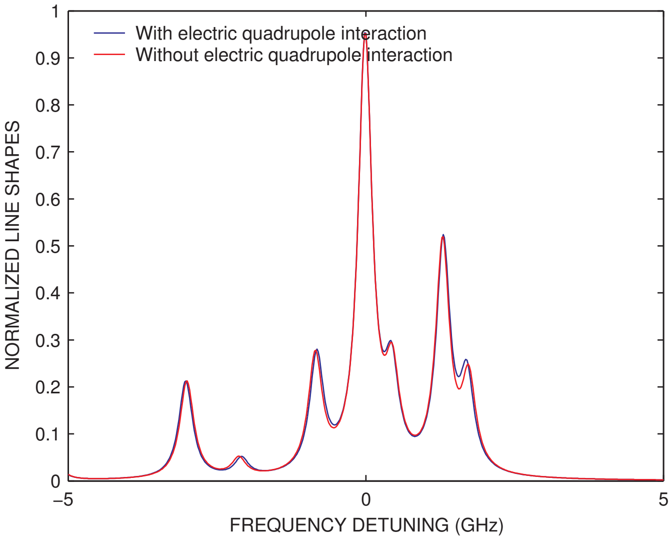

(a) Effect on ^{131}Xe spectrum

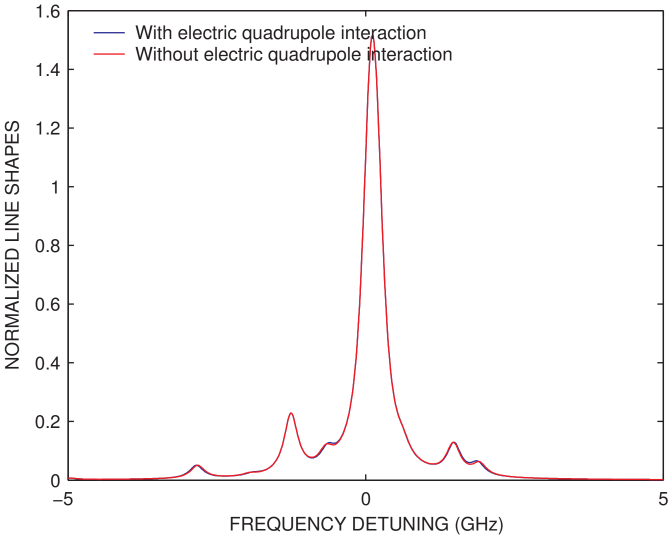

(b) Effect on combined spectra of ^{129}Xe and ^{131}Xe

Fig. 5.4: Illustration of the negligible effect of the electric quadrupole interaction on the spectrum of Xe I

F		M_J			M_I	
$\frac{1}{2}$	$\frac{3}{2}$	-1	0	1	-$\frac{1}{2}$	$\frac{1}{2}$

Tab. 5.1: Possible F, M_J, and $M_I$values for state 6S′ [1/2] of ^{129}Xe

Next, we find all permissible combinations of M_J and M_I satisfying the rule $M = M_J + M_I$, where M sums are given by (5.2.5). The simple process, illustrated below, leads to six possible states for 6S′ [1/2]:

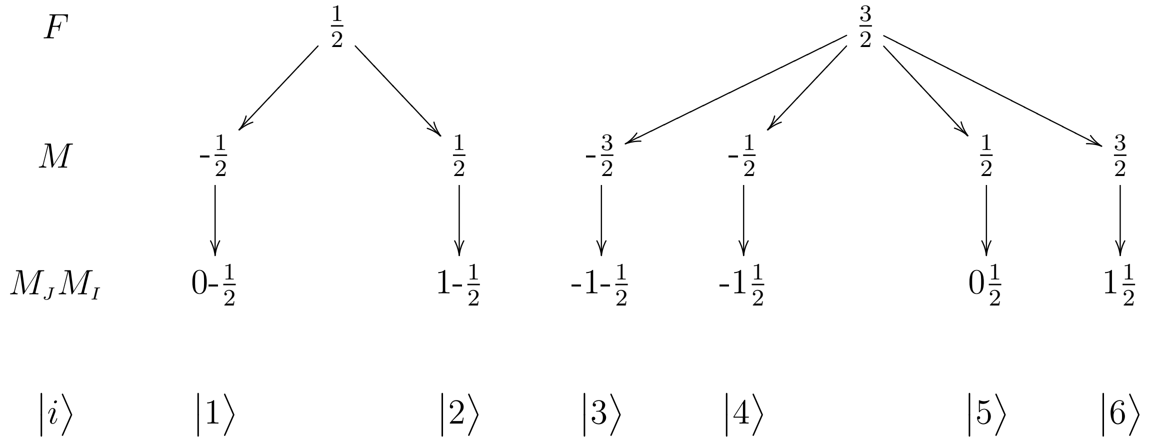

Successively applying each possible set (M_J,M_I) associated with some state $|i\rangle$ and physical parameters[2] listed in Table 5.2 to equation (5.2.12), we arrive at the following eigenvalue problem (5.3.2) expressed in terms of a corresponding i^{th} eigenvector when $H = 312\ G$.

$$\left\{ E^{|i\rangle}[\mathrm{I}] - \begin{bmatrix} -2.35 & 0 & 0 & 0 & 0 & 0 \\ 0 & -1.78\cdot 10^{-4} & -5.80 & 0 & 0 & 0 \\ 0 & -2.90 & 3.46 & 0 & 0 & 0 \\ 0 & 0 & 0 & 2.35 & -2.90 & 0 \\ 0 & 0 & 0 & -5.80 & 1.78\cdot 10^{-4} & 0 \\ 0 & 0 & 0 & 0 & 0 & -3.46 \end{bmatrix} \right\} \begin{bmatrix} X^{1,3/2}_{1,1/2} \\ X^{1,3/2}_{0,1/2} \\ X^{1,1/2}_{1,-1/2} \\ X^{1,3/2}_{-1,1/2} \\ X^{1,1/2}_{0,-1/2} \\ X^{1,3/2}_{\text{-1,-1/2}} \end{bmatrix}^{|i\rangle} = [0]. \tag{5.3.2}$$

The resulting eigenvalues (energy levels) and eigenvectors (mode-shape ampli-

---

[2] The physical parameters (e.g. hyperfine structure constant and Landé g-factors) used to write the eigenvalue problem slightly differ from nominal published values. These values are optimal within their associated ranges of uncertainty as described by the optimization process described in Chapter VI

Mass Number	129	131	Ref.
I	$\frac{1}{2}$	$\frac{3}{2}$	[7]
μ_N $[\left(\frac{m_e}{m_p}\right)]$	-0.7768(0.0001)	0.700(0.05)	[44]
A [GHz]	-5801.1(12.8)	1713.7(6)	[6]
	-2892.4(6.9)	858.9(3.1)	[45]
g_J	1.321	1.321	[43]
	1.190(0.001)	1.190(0.001)	[47]

Tab. 5.2: Physical parameters associated with stable isotopes ^{129}Xe and ^{131}Xe having hyperfine structure. Upper and lower sub-rows are respectively associated with initial and final states. From μ_N and I, we deduced Landé-$g_I$factor using: $g_I = (\frac{m_p}{m_e})^{-1}\frac{\mu_N}{I}$, where the proton-to-electron mass ratio $\frac{m_p}{m_e} = 1836$. The numbers between parentheses are uncertainty widths (e.g. 1.190(0.001) is equivalent to 1.190 ± 0.001) that, in some cases, incorporate widths by other authors cited within listed sources.

tudes) are reported in Table 5.3. For the lower state (6P$'$ [3/2]), the eigenvalue problem is more complex in that the coefficient matrix is of dimension 10×10; the resulting energy levels are listed in Table 5.4. The degree of complexity increases for ^{131}Xe due to a higher nuclear spin for this isotope ($I = 3/2$). the resulting twelve upper states and twenty lower states are reported in tables 5.5 and 5.6, respectively.

The next step in modeling the full spectrum consists of determining all allowed transitions and corresponding normalized line strengths associated with isotopes ^{129}Xe and ^{131}Xe using transition rules along with intensity and normalization formulas of equations (5.2.14) and (5.2.15), respectively[3]. Table 5.7 illustrates details of the calculation of line intensities for the eleven $M \rightarrow M{-}1$ transitions (or 'σ^- transitions') of ^{129}Xe at $H = 312\ G$; expressions of unnormalized intensities (numerator of equation (5.2.14))[4] and and normalization factors from equation (5.2.15) are listed therein in

---

[3] The physical parameters (e.g. hyperfine structure constant and Landé g-factors) used to write the eigenvalue problem slightly differ from nominal published values. These values are optimal within their associated ranges of uncertainty (refer to Table 5.9 and Section 5.4 showing how they were found.

[4] Bacher[39] only reports intensity formulas for $J \rightarrow J-1$ transitions. However, for the 834.682 nm line, respective upper and lower J-values are 1 and 2; hence, falling in the class of to $J \rightarrow J+1$ transitions. To appropriately account for this class of transitions, one simply need to switch upper

terms of mode shape amplitudes. The resulting normalized intensities are also listed along with corresponding transition energies. The complete σ line spectra of the two isotopes are reported in figures 5.5 and 5.6.

Tab. 5.3: ^{129}Xe upper state's (6S′ [1/2]) energy levels along with corresponding mode-shape amplitudes

State	Energy [GHz]	Mode-shape amplitudes $X^{1,3/2}_{1,1/2}$	$X^{1,3/2}_{0,1/2}$	$X^{1,1/2}_{1,-1/2}$	$X^{1,3/2}_{-1,1/2}$	$X^{1,1/2}_{0,-1/2}$	$X^{1,3/2}_{-1,-1/2}$
$\left\|1\frac{3}{2}1\frac{1}{2}\right\rangle$	-2.33	0.707	-	-	-	-	-
$\left\|1\frac{3}{2}0\frac{1}{2}\right\rangle$	-2.72	-	-0.834	0.552	-	-	-
$\left\|1\frac{1}{2}1\text{-}\frac{1}{2}\right\rangle$	6.20	-	-0.390	-0.590	-	-	-
$\left\|1\frac{3}{2}\text{-}1\frac{1}{2}\right\rangle$	-3.10	-	-	-	0.426	0.564	-
$\left\|1\frac{1}{2}0\text{-}\frac{1}{2}\right\rangle$	5.43	-	-	-	0.798	-0.603	-
$\left\|1\frac{3}{2}\text{-}1\text{-}\frac{1}{2}\right\rangle$	-3.50	-	-	-	-	-	0.577

Tab. 5.4: ^{129}Xe lower state's (6P′ [3/2]) energy levels

State	$\left\|2\frac{5}{2}2\frac{1}{2}\right\rangle$	$\left\|2\frac{5}{2}1\frac{1}{2}\right\rangle$	$\left\|2\frac{3}{2}2\text{-}\frac{1}{2}\right\rangle$	$\left\|2\frac{5}{2}0\frac{1}{2}\right\rangle$	$\left\|2\frac{3}{2}1\text{-}\frac{1}{2}\right\rangle$	$\left\|2\frac{5}{2}\text{-}1\frac{1}{2}\right\rangle$	$\left\|2\frac{3}{2}0\text{-}\frac{1}{2}\right\rangle$	$\left\|2\frac{5}{2}\text{-}2\frac{1}{2}\right\rangle$	$\left\|2\frac{3}{2}\text{-}1\text{-}\frac{1}{2}\right\rangle$	$\left\|2\frac{5}{2}\text{-}2\text{-}\frac{1}{2}\right\rangle$
Label	$\left\|1\right\rangle$	$\left\|2\right\rangle$	$\left\|3\right\rangle$	$\left\|4\right\rangle$	$\left\|5\right\rangle$	$\left\|6\right\rangle$	$\left\|7\right\rangle$	$\left\|8\right\rangle$	$\left\|9\right\rangle$	$\left\|10\right\rangle$
Energy (GHz)	-1.85	-2.28	-5.28	-2.69	4.66	-3.11	4.04	-3.52	3.41	-3.93

---

by lower states in the intensity formulas as suggested by Bacher.

Tab. 5.5: ^{131}Xe upper state's (6S′ [1/2]) energy levels

State	$\lvert 1\frac{5}{2}1\frac{3}{2}\rangle$	$\lvert 1\frac{5}{2}0\frac{3}{2}\rangle$	$\lvert 1\frac{3}{2}1\frac{1}{2}\rangle$	$\lvert 1\frac{5}{2}\text{-}1\frac{3}{2}\rangle$	$\lvert 1\frac{3}{2}0\frac{1}{2}\rangle$	$\lvert 1\frac{1}{2}1\text{-}\frac{1}{2}\rangle$	$\lvert 1\frac{5}{2}\text{-}1\frac{1}{2}\rangle$	$\lvert 1\frac{3}{2}0\text{-}\frac{1}{2}\rangle$	$\lvert 1\frac{1}{2}1\text{-}\frac{3}{2}\rangle$	$\lvert 1\frac{5}{2}\text{-}1\text{-}\frac{1}{2}\rangle$	$\lvert 1\frac{3}{2}0\text{-}\frac{3}{2}\rangle$	$\lvert 1\frac{5}{2}\text{-}1\text{-}\frac{3}{2}\rangle$
Label	$\lvert 1\rangle$	$\lvert 2\rangle$	$\lvert 3\rangle$	$\lvert 4\rangle$	$\lvert 5\rangle$	$\lvert 6\rangle$	$\lvert 7\rangle$	$\lvert 8\rangle$	$\lvert 9\rangle$	$\lvert 10\rangle$	$\lvert 11\rangle$	$\lvert 12\rangle$
Energy (GHz)	3.15	-1.50	2.94	-4.55	-1.60	2.72	-4.18	-1.75	2.49	-1.97	2.25	2.00

Tab. 5.6: ^{131}Xe lower state's (6P′ [3/2]) energy levels

State	$\lvert 2\frac{7}{2}2\frac{3}{2}\rangle$	$\lvert 2\frac{7}{2}1\frac{3}{2}\rangle$	$\lvert 2\frac{5}{2}2\frac{1}{2}\rangle$	$\lvert 2\frac{7}{2}0\frac{3}{2}\rangle$	$\lvert 2\frac{5}{2}1\frac{1}{2}\rangle$	$\lvert 2\frac{3}{2}2\text{-}\frac{1}{2}\rangle$	$\lvert 2\frac{7}{2}\text{-}1\frac{3}{2}\rangle$	$\lvert 2\frac{5}{2}0\frac{1}{2}\rangle$	$\lvert 2\frac{5}{2}\text{-}1\frac{1}{2}\rangle$	$\lvert 2\frac{3}{2}0\text{-}\frac{1}{2}\rangle$	$\lvert 2\frac{1}{2}1\text{-}\frac{3}{2}\rangle$	$\lvert 2\frac{7}{2}\text{-}2\frac{1}{2}\rangle$	$\lvert 2\frac{5}{2}\text{-}1\text{-}\frac{1}{2}\rangle$	$\lvert 2\frac{3}{2}0\text{-}\frac{3}{2}\rangle$	$\lvert 2\frac{7}{2}\text{-}2\text{-}\frac{1}{2}\rangle$	$\lvert 2\frac{5}{2}\text{-}1\text{-}\frac{3}{2}\rangle$	$\lvert 2\frac{7}{2}\text{-}2\text{-}\frac{3}{2}\rangle$	$\lvert 2\frac{5}{2}0\frac{1}{2}\rangle$	$\lvert 2\frac{3}{2}1\text{-}\frac{1}{2}\rangle$	$\lvert 2\frac{1}{2}2\text{-}\frac{3}{2}\rangle$
Label	$\lvert 1\rangle$	$\lvert 2\rangle$	$\lvert 3\rangle$	$\lvert 4\rangle$	$\lvert 5\rangle$	$\lvert 6\rangle$	$\lvert 7\rangle$	$\lvert 8\rangle$	$\lvert 9\rangle$	$\lvert 10\rangle$	$\lvert 11\rangle$	$\lvert 12\rangle$	$\lvert 13\rangle$	$\lvert 14\rangle$	$\lvert 15\rangle$	$\lvert 16\rangle$	$\lvert 17\rangle$	$\lvert 18\rangle$	$\lvert 19\rangle$	$\lvert 20\rangle$
Energy (GHz)	-2.23	3.60	0.364	3.33	-2.02	0.0970	3.05	-3.57	-0.201	2.76	-4.53	-2.72	-0.532	2.46	-3.25	-0.888	2.16	-1.27	1.85	1.53

Once line intensity is known, we account for relative frequency shifts [6] and natural abundances [7] associated with each isotope. Each set of energy splittings associated with each isotope undergoes a particular shift due to two effects: a mass effect caused by differences in the number of nucleons and a volume effect due to differences in the shape of the charge distribution of protons. The resulting 'isotopic shift'; which, Firestone et al. [7] elaborate on in greater depth, depends on wavelength. For the 834.682 nm line of Xe I (6S$'$ [1/2]$\rightarrow$ 6P$'$ [3/2]), Suzuki et al. [6] provides all shifts associated with its stable isotopes; their study also reports shifts associated with several other lines ranging from 820.6 to 904.5 nm-air. Additionally, xenon isotopes vary in their relative preponderances in nature [7]. We account for this effect by normalizing each set of isotope lines by unity prior to scaling by the corresponding natural abundance ratio. Figure 5.7 illustrates frequency shifting of σ^- lines ($M \rightarrow M-1$ transitions)for ^{129}Xe and ^{131}Xe. For the sake of completeness, we also report the full σ^+ spectrum ($M \rightarrow M+1$) of the two isotopes in Figure 5.8.

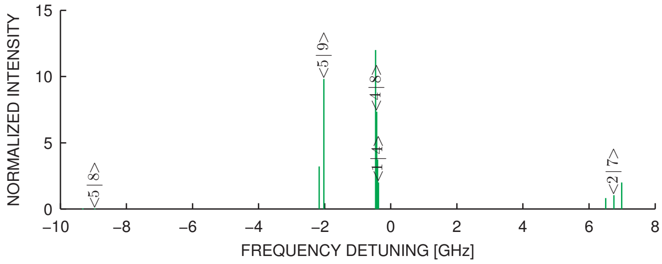

(a) ^{129}Xe line spectrum

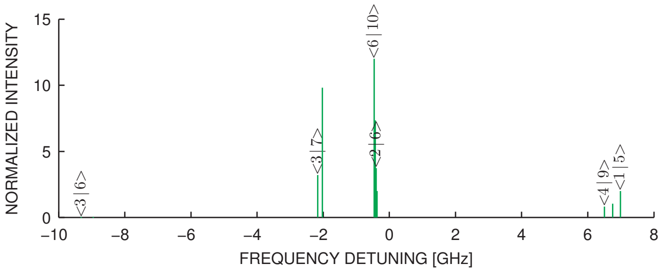

(b) ^{129}Xe line spectrum

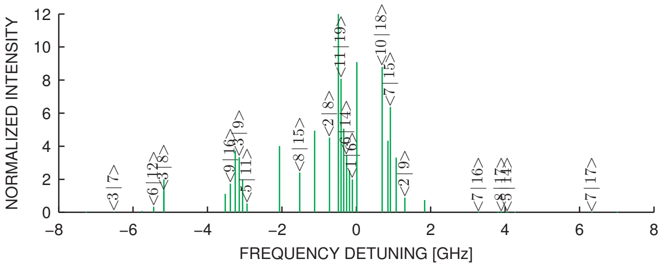

(c) ^{131}Xe line spectrum

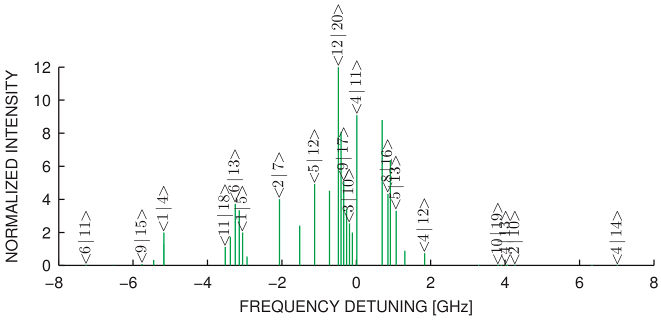

(d) ^{131}Xe line spectrum

Fig. 5.5: σ^- transition line spectra of ^{129}Xe and ^{131}Xe for an external field strength of 312 G. For the sake of clarity, annotations are applied to every other line and those of intensity below 0.1 are omitted.

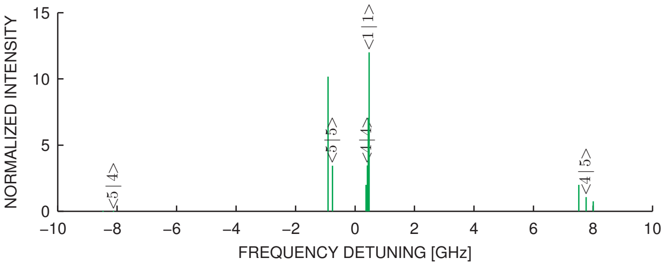

(a) ^{129}Xe line spectrum

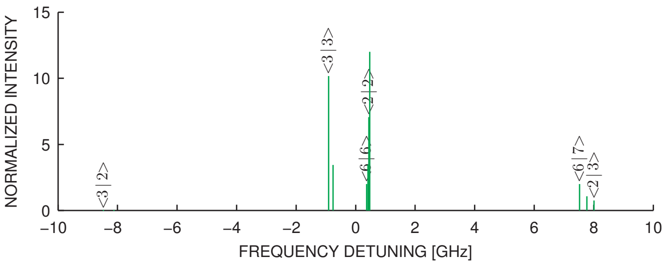

(b) ^{129}Xe line spectrum

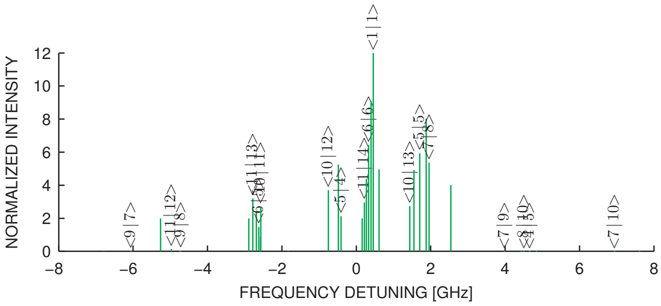

(c) ^{131}Xe line spectrum

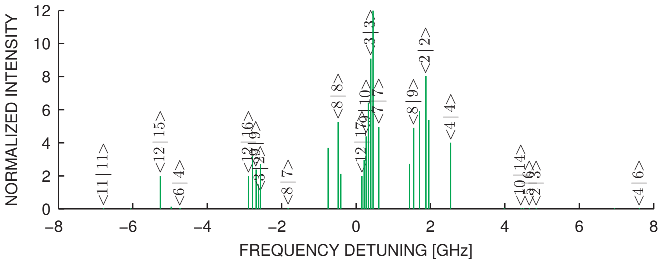

(d) ^{131}Xe line spectrum

Fig. 5.6: σ^+ transition line spectra of ^{129}Xe and ^{131}Xe for an external field strength of 312 G.For the sake of clarity, annotations are applied to every other line and those of intensity below 0.1 are omitted.

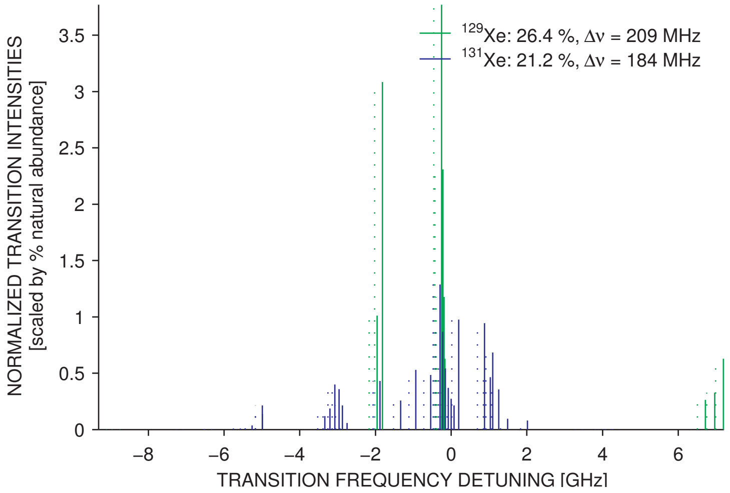

Fig. 5.7: $\sigma-$ transition line strengths of ^{129}Xe and ^{131}Xe for an external field strength of 312 Gauss. The figure further illustrates frequency shifting associated with each isotope (unshifted lines appear dashed).

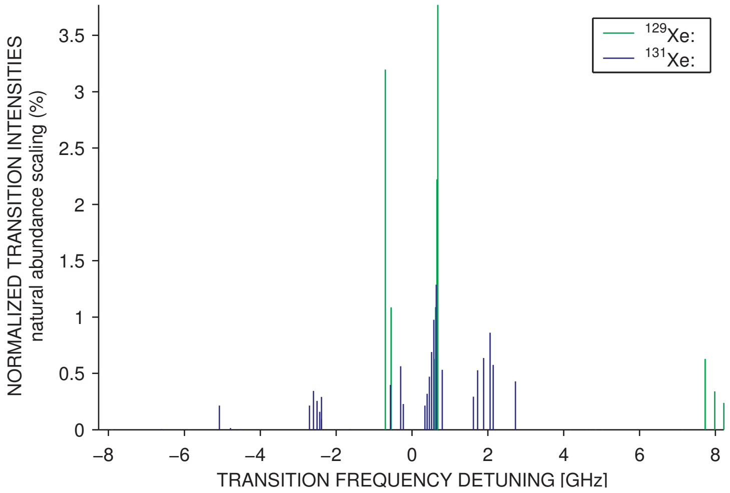

Fig. 5.8: σ^{+} transition line strengths of ^{129}Xe and ^{131}Xe.

5.3.2 Transition line spectra modeling of isotopes with zero nuclear spin

For the treatment of the remaining seven isotopes (^{124}Xe, ^{126}Xe, ^{128}Xe, ^{130}Xe, ^{132}Xe, ^{134}Xe, and ^{136}Xe with $I = 0$), we use the simpler Anomalous Zeeman theory.Once all possible M_J values are generated from equation (5.2.1), transition energies are determined from equation (5.2.3). Owing to the dependence of energy displacements on H and M_J alone, line components of all these isotopes have equal transition energies. Intensity formulas given in equation (5.2.3) are applied prior to isotope shifting and scaling based on shifts and percent natural abundances provided by Suzuki [6] and Firestone [7] (respectively) and reported in Table 5.8. The resulting transition lines are plotted in Figure 5.9; this latter step is identical to the treatment of ^{129}Xe and ^{131}Xe outlined at the end of Section 5.3.1.

Tab. 5.7: Illustration of the calculation of transition intensities based on σ^- components of ^{129}Xe 6S′ [1/2]→ 6P′ [3/2] when $H = 312\,Gauss$.

Transition	Energy [GHz]	I_N	I	$N_M^{J,F}$	$N_{M'}^{J+1,F'}$
$\langle 1\|4\rangle$	-0.374	2	$(4X^{1,3/2}_{1,1/2}Y^{2,5/2}_{0,1/2})^2$	$2(X^{1,3/2}_{1,1/2})^2$	$4(Y^{1,5/2}_{0,1/2})^2$
$\langle 1\|5\rangle$	6.99	2	$(4X^{1,3/2}_{1,1/2}Y^{2,3/2}_{0,1/2})^2$	$2(X^{1,3/2}_{1,1/2})^2$	$4(Y^{2,3/2}_{0,1/2})^2$
$\langle 2\|6\rangle$	-0.398	3.74	$(6X^{1,3/2}_{0,1/2}Y^{2,5/2}_{-1,1/2}+4X^{1,3/2}_{1,-1/2}Y^{2,5/2}_{0,-1/2})^2$	$(X^{1,3/2}_{0,1/2})^2+2(X^{1,3/2}_{1,-1/2})^2$	$6(Y^{2,5/2}_{-1,1/2})^2+4(Y^{2,5/2}_{0,-1/2})^2$
$\langle 2\|7\rangle$	6.75	1.04	$(6X^{1,3/2}_{0,1/2}Y^{2,3/2}_{-1,1/2}+4X^{1,3/2}_{1,-1/2}Y^{2,3/2}_{0,-1/2})^2$	$(X^{1,3/2}_{0,1/2})^2+2(X^{1,3/2}_{1,-1/2})^2$	$6(Y^{2,3/2}_{-1,1/2})^2+4(Y^{2,3/2}_{0,-1/2})^2$
$\langle 3\|6\rangle$	-9.32	3.77 10^{-5}	$(6X^{1,1/2}_{0,1/2}Y^{2,5/2}_{-1,1/2}+4X^{1,1/2}_{1,-1/2}Y^{2,5/2}_{0,-1/2})^2$	$(X^{1,1/2}_{0,1/2})^2+2(X^{1,1/2}_{1,-1/2})^2$	$6(Y^{2,5/2}_{-1,1/2})^2+4(Y^{2,5/2}_{0,-1/2})^2$
$\langle 3\|7\rangle$	-2.17	3.22	$(6X^{1,1/2}_{0,1/2}Y^{2,3/2}_{-1,1/2}+4X^{1,1/2}_{1,-1/2}Y^{2,3/2}_{0,-1/2})^2$	$(X^{1,1/2}_{0,1/2})^2+2(X^{1,1/2}_{1,-1/2})^2$	$6(Y^{2,3/2}_{-1,1/2})^2+4(Y^{2,3/2}_{0,-1/2})^2$
$\langle 4\|8\rangle$	-0.426	7.35	$(24X^{1,3/2}_{-1,1/2}Y^{2,5/2}_{-2,1/2}+6X^{1,3/2}_{0,-1/2}Y^{2,5/2}_{-1,-1/2})^2$	$2(X^{1,3/2}_{-1,1/2})^2+(X^{1,3/2}_{0,-1/2})^2$	$24(Y^{2,5/2}_{-2,1/2})^2+6(Y^{2,5/2}_{-1,-1/2})^2$
$\langle 4\|9\rangle$	6.51	0.836	$(24X^{1,3/2}_{-1,1/2}Y^{2,3/2}_{-2,1/2}+6X^{1,3/2}_{0,-1/2}Y^{2,3/2}_{-1,-1/2})^2$	$2(X^{1,3/2}_{-1,1/2})^2+(X^{1,3/2}_{0,-1/2})^2$	$24(Y^{2,3/2}_{-2,1/2})^2+6(Y^{2,5/2}_{-1,-1/2})^2$
$\langle 5\|8\rangle$	-8.96	7.27$10^{-5}$	$(24X^{1,1/2}_{-1,1/2}Y^{2,5/2}_{-2,1/2}+6X^{1,1/2}_{0,-1/2}Y^{2,5/2}_{-1,-1/2})^2$	$2(X^{1,1/2}_{-1,1/2})^2+(X^{1,1/2}_{0,-1/2})^2$	$24(Y^{2,5/2}_{-2,1/2})^2+6(Y^{2,5/2}_{-1,-1/2})^2$
$\langle 5\|9\rangle$	-2.02	9.82	$(24X^{1,1/2}_{-1,1/2}Y^{2,3/2}_{-2,1/2}+6X^{1,1/2}_{0,-1/2}Y^{2,3/2}_{-1,-1/2})^2$	$2(X^{1,1/2}_{-1,1/2})^2+(X^{1,1/2}_{0,-1/2})^2$	$24(Y^{2,3/2}_{-2,1/2})^2+6(Y^{2,3/2}_{-1,-1/2})^2$
$\langle 6\|10\rangle$	-0.460	12	$(24X^{1,3/2}_{-1,1/2}Y^{2,5/2}_{-2,-1/2}$	$2(X^{1,3/2}_{-1,-1/2})^2$	$24(Y^{2,5/2}_{-2,-1/2})^2$

Mass number	124	126	128	130	132	134	136
Abundance [%]	0.1	0.09	1.91	4.1	26.9	10.4	8.9
Shift [MHz]	279.8(30)	238.6(30)	197.45(30)	151.7(21.3)	110.1(11.3)	74.0(11.1)	0

Tab. 5.8: Isotopic shifts [6] and natural abundances [7] of stable xenon species with no nuclear spin

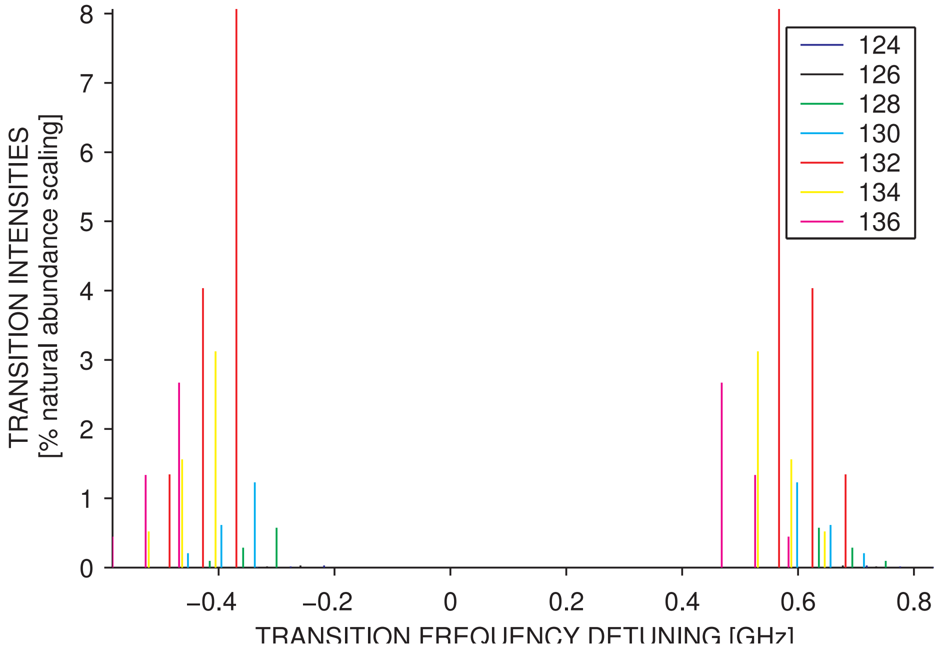

Fig. 5.9: Line spectrum of xenon isotopes with no nuclear-spin

5.3.3 Natural and Doppler broadening of line spectra

Lastly, we apply a Voigt profile [35] to the overall spectrum combining line components of each isotope. It suffices, here, to briefly describe such a profile as the product of a two-step process [48, 49]. In the first, a cold spectrum is generated by Lorentz-broadening the lines. This is achieved through a Lorentz distribution simulating spontaneous emission of light through a rate $\Delta\nu = A_{ij}/(2\pi)$, which represents the width at half-maximum of the distribution and is proportional to a transition constant A_{ij}, whose value is reported in the work Miller et al. [50] for the 834.682 nm Xe I line. In the second, the 'cold spectrum' is convolved with a Doppler distribution to generate a 'warm spectrum' that simulates the absorption spectrum of Xe I for a particular external magnetic field strength and plasma kinetic temperature. An illustration of the broadening process is shown in Figure 5.10; in which, line, cold, and warm spectra are overlaid.

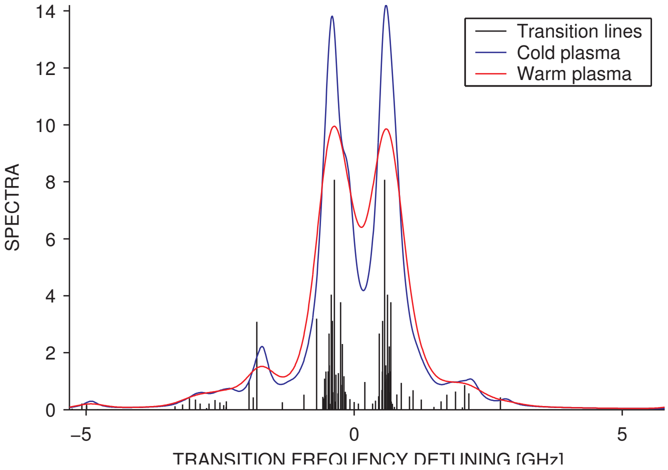

Fig. 5.10: Voigt profile generation from the spectrum of transition lines. The cold and warm spectra shown are based on Lorentz and Doppler broadenings of transition lines. The external field strength is 312 G in this plot.

5.4 Computing magnetic field strengths and kinetic temperatures from optogalvanic spectra

5.4.1 Description of the non-linear least-squares solver

We applied Matlab's built-in non-linear least-squares solver (LSQNONLIN)[5] to our optimization problem. It finds optimal design paramaters $\boldsymbol{p^*} = \boldsymbol{p^*}(p_1^*, p_2^*, \ldots p_k^* \ldots p_n^*)$ that minimize the fitting error (5.4.1) between a theoretical model, $T_i(\boldsymbol{p})$ and an experimental distribution, E_i (with i denoting an i^{th} datapoint) as expressed below:

$$\epsilon(\boldsymbol{p}) = \frac{1}{2}\sum_i (T_i(\boldsymbol{p}) - E_i)^2. \tag{5.4.1}$$

The minimization process starts with the definition of a set of guessed solutions $\boldsymbol{p^o} = \boldsymbol{p^o}(p_1^o, p_2^o, \ldots p_k^o \ldots p_n^o)$ as well as lower and upper bounds (p_{min} and p_{max} respectively) defining some finite interval $\Delta p = p_{max} - p_{min}$ or 'feasible region'. From these initial inputs, LSQNONLIN computes $\epsilon(\boldsymbol{p})$ by iterative steps of optimal lengths along steepest descent search-directions, $\nabla\epsilon$, successively applied to successive points until the coordinate $\epsilon(\boldsymbol{p^*})$ of the error functions' minimum is located. Convergence of the solver to an optimal point or solution is achieved when the change in the norm of the residual[6] falls below a pre-set tolerance level. This novel non-linear method [51], which is suited for large scale problems of many variables is more efficient than traditional linear optimization techniques in its interior-reflective Newton line-search technique that allows a quadratic decay of the residual norm and insures global minimization of the error function. The efficiency stems primarily from the fact that $\boldsymbol{p}$ progresses towards $\boldsymbol{p*}$ within some 'bounded path' (the feasible region defined above), constrained within bound intervals within which $\boldsymbol{p}$ progresses. An affine transforma-

---

[5] We used LSQNONLIN from MATLAB Version 6.5, Release 13

[6] the residual, which is not to be confused with the error between fit and experiment, is related to the gradient of the error function at some point of the iteration path leading to the point of convergence

tion of the vector space defined by $\boldsymbol{p_k}(k = 1, 2, \ldots, n)$ and successive reflections of steepest descent directions with respect to prior ones about the normal of the feasible region at each point (in a piece-wise fashion) generates a search path that remains well centered[7] between the boudaries—key to fast and robust convergence.

5.4.2 Continuity of transition energies and smooth distribution of absorption spectra

Successful application of LSQNONLIN requires a smooth and continuous input error function. We checked for continuity of the energy levels by studying their evolution with magnetic field intensity. With machine tolerance being the only constraint, we found the range of magnetic field strengths recoverable with this technique to extend from 0.01 to 50,000 Gauss; we stress, however, that the 'Zeeman-split Hyperfine Structure' (ZHFS) model is theoretically applicable to an arbitrarily wide range of field strengths. Figures 5.11 illustrates continuous variations of transition energies from 0.01 to 1000 Gauss for ^{129}Xe and ^{131}Xe. Energy level continuity led to smooth variations of cold and warm spectra with magnetic field intensity as shown in the surface plot of the cold spectrum Xe I in Figure 5.12.

---

[7] The interior-reflective Newton method deviates from lesser efficient traditional methods like the Simplex method, which for example, causes a marching of the iterated solutions along the boundaries of the feasible region [51]

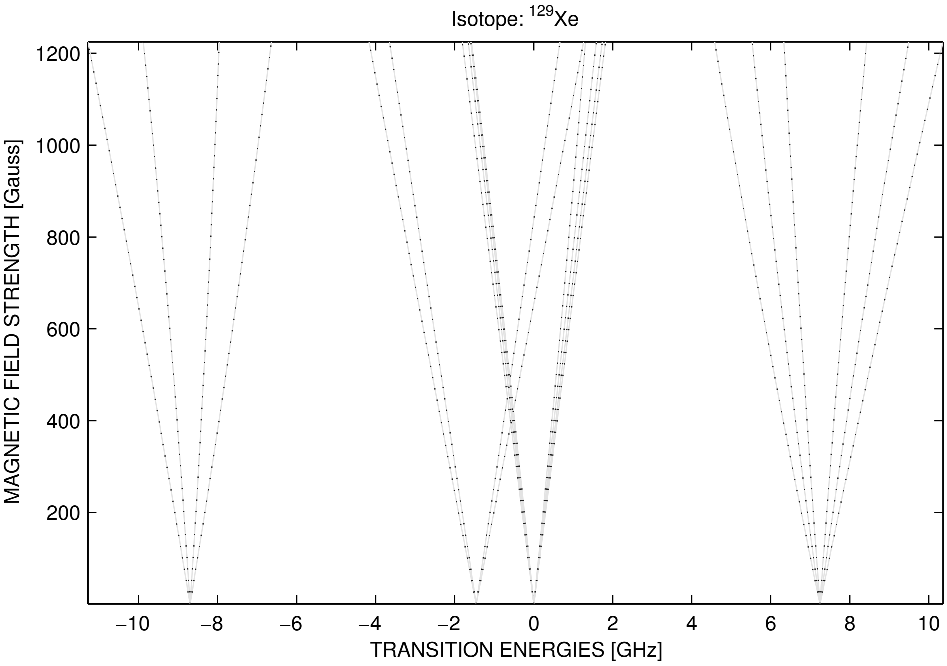

(a) ^{129}Xe energy levels

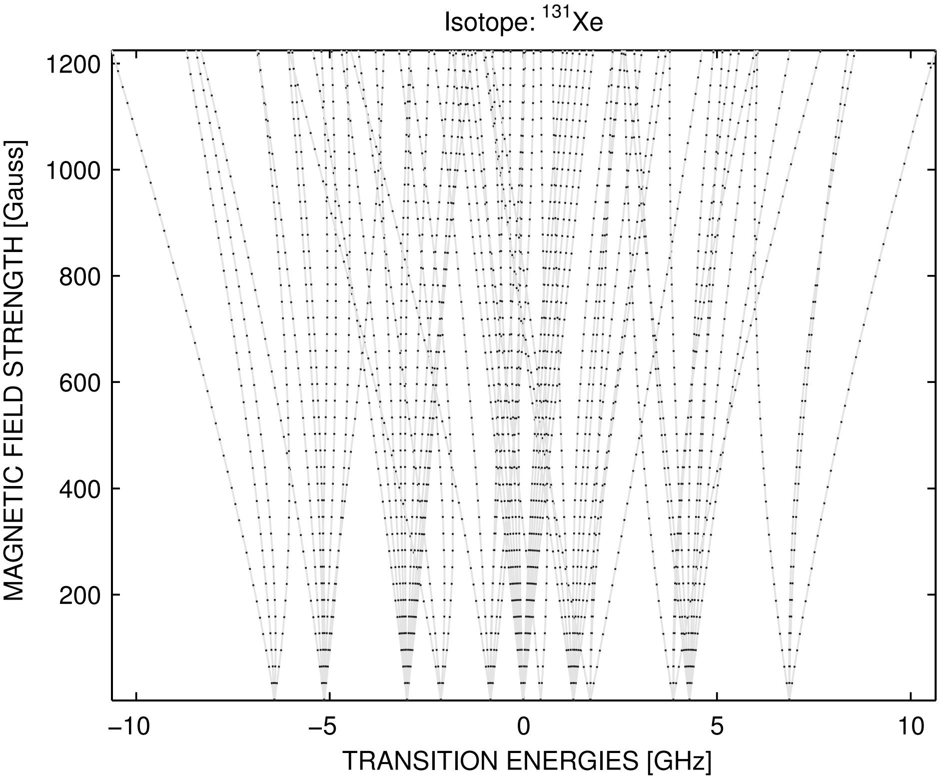

(b) ^{131}Xe energy levels

Fig. 5.11: Variation of transition energies of ^{131}Xe with magnetic field strength

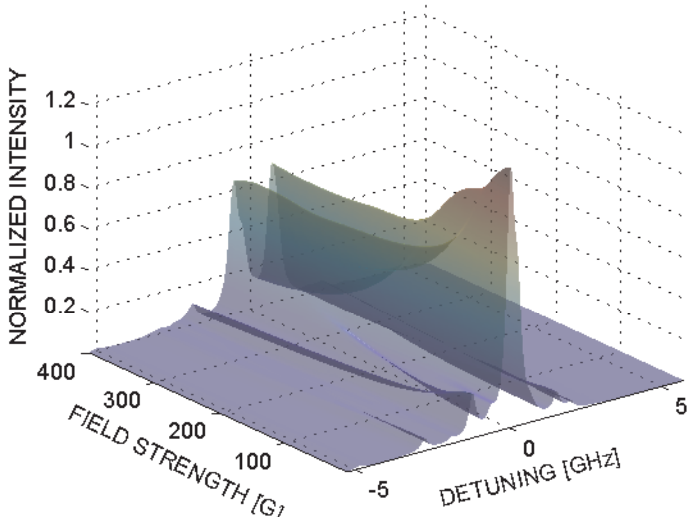

Fig. 5.12: Smooth surface distribution of cold spectra with respect to magnetic field intensity.

5.4.3 Validation of a Non-linear Least-squares solver for the determination of magnetic field strengths and kinetic temperatures of Xe I from fitted optogalvanic spectra exhibiting a Zeeman effect

5.4.3.1 Pre-optimization: defining target solutions and optimal physical parameters within their uncertainty intervals

Prior to applying LSQNONLIN to solve for external field strengths and its kinetic temperatures from measured spectra, we first set out to determine; which 'target' magnetic field strengths and kinetic temperatures and 'optimal' physical parameters best model the 834.682 nm absorption line within their respective uncertainty intervals; these variables were simultaneously solved for.

By 'target', we mean our best estimates of experimental settings within reported uncertainty bounds. To account for any potential contamination of the external magnetic field by devices surrounding the galvatron and the plasma-induced magnetic field as well as any possible errors associated with Hall probe measurements, we solved for the actual (effective or 'target') field strengths felt by xenon neutrals at the various experimental settings. Center field strength values (recall Section 5.1) were used as starting guesses and error bounds were set arbitrarily wide at ±100% about them. As for target temperatures, they were computed based on a starting guess of 700 K and an error bound interval of 300 K. We infered this width by correlating our galvatron's discharge voltage setting with that of a previous optogalvanic study [52], which reported a kinetic temperature of 800 K at a 440 V discharge voltage setting.

Due to uncertainties associated with physical parameters[8] involved in modeling the 834.682 nm line, we also needed to determine what 'optimal' values would best minimize ϵ within their respective published error bounds. Published mean values served as initial guesses to the pre-optimization solver described in appendices E and F.

A summary of target magnetic field strengths and kinetic temperatures as well as optimal physical parameters found at each of the ten Helmholtz coil field settings is presented in Table 5.9. Since the discharge current and voltage of the galvatron were kept constant throughout the experiment, the plasma kinetic temperature can safely be assumed constant; hence, one can deduce a target temperature corresponding to the averaged solution output listed at the last column of the temperatures' row-entry. Averages of the optimal physical parameters are also listed in the last column. It is interesting to note that these latter variables—intrinsic to the probed absorption line of Xe I—deviate to a lesser extent than the temperature of xenon particles; this is to be expected since the state of the plasma likely fluctuates over the duration (a few hours) of the experiment.

---

[8] Some physical parameters were published with rather substantial uncertainties. For example the published value of the spontaneous emission coefficient involved in the 834.682 nm transition of neutral xenon is only accurate to within 40 %.

5.4.3.2 Determination of magnetic field strengths and plasma kinetic temperatures from measured optogalvanic spectra

The averaged optimal physical variables (Table 5.9) were used as input in a modified version of the magnetic field strength and kinetic temperature solver described in appendices D and E; which, when applied to the ten optogalvanic spectra yielded the fits reported in figures 5.13 through 5.22. The good fits indicate that LSQNONLIN was successful in simultaneously recovering, to a fair approximation, the actual strengths of the external magnetic field and the plasma kinetic temperature. The fits reveal convergences to within 10% of target temperatures and field intensities even when starting guesses deviated by as much as 100% from expected targets. Values for the starting guesses B_o and T_o, solutions B^* and T^*, and deviations Δ_B and Δ_T are listed above each fit. The latter two parameters are deviations of solutions from target parameters that indicate the quality of the convergence; the smaller the deviations, the better the match between solutions and respective targets. Starting guesses and center-field and target field strengths are also included for comparison. While field strength solutions remain consistently close to target values at all settings, they significantly deviate from center-field values by nearly 50%. An illustration of the minimization is shown on the three-dimensional distribution of the error-function plotted in Figure 5.23 with respect to magnetic field strength and kinetic temperature, which displays an initial guess and resulting minimum at the 270 Gauss setting.

In the event that the level of field contamination and Hall probe calibration error were insignificant; that is, if center-field strengths effectively acted upon xenon species, the previously mentioned mismatch would be indicative of a weakness of the spectral model at low field settings (below 100 Gauss), which may be due to two reasons. Firstly, the Zeeman HFS theory does not account for the electric quadrupole interaction between nuclei and associated electron clouds arising from the former particles' non-spherical charge distributions [53, 54]. Secondly, the magnitudes of the

Zeeman splitting of some hyperfine energy levels approach our solver's numerical tolerance levels as the field strength drops below 100 Gauss. Doppler broadening further amplifies the problem by causing a blurring of line spectra.

Kinetic temperature solutions, on the other hand, remained close to targets independently of the magnetic field strength. The relatively flat distribution of solutions shown in Figure 5.24(b) illustrates this fact and validate the solver's reliability in computing plasma kinetic temperature given that the galvatron's discharge voltage was kept constant throughout the data acquisition process.

Tab. 5.9: Computed solutions from the application LSQNONLIN to the determination of optimal physical parameters and target magnetic field strengths and kinetic temperatures based on Xe I absorption spectra about 834.682 nm at ten external magnetic field settings

		Magnetic field strengths (Gauss)										
Center		33.19	65.6	99.01	131.9	164.8	197.8	230.8	263.7	296.7	329.7	
Optimal		16.59	33.68	49.51	112.1	148.1	174.6	216	240.8	277	315.6	
States	Isotopes	Optimal variables										**averages**
		Galvatron temperatures (K)										
		450	510.8	563.9	540.9	464.2	450.7	474.3	452.2	453.5	499.1	**486**
		Isotope shifts (MHz) - relative to 136										
	124	250.3	250.2	250.2	250.2	250.2	250.2	250.2	250.2	250.2	250.2	**250.2**
	126	209.1	209.1	209.1	209.1	209.1	209.1	209.1	209.1	209.1	209.1	**209.1**
	128	167.9	167.9	167.9	167.9	167.9	167.9	167.9	167.9	167.9	167.9	**167.9**
	129	208.7	208.7	208.7	208.7	208.7	208.7	208.7	208.7	208.7	208.7	**208.7**
	130	130.4	130.4	130.4	130.4	130.4	130.4	130.4	130.4	130.4	130.4	**130.4**
	131	183.6	183.6	183.6	183.6	183.6	183.6	183.6	183.6	183.6	183.6	**183.6**
	132	98.9	98.9	98.9	98.9	98.9	98.9	98.9	98.9	98.9	98.9	**98.9**
	134	62.9	62.9	62.9	62.9	62.9	62.9	62.9	62.9	62.9	62.9	**62.9**
		Hyperfine constants (MHz)										
$6S'$ [1/2]	129	-5811	-5811	-5786	-5811	-5797	-5786	-5811	-5811	-5811	-5811	**-5805**
	131	-2893	-2899	-2899	-2898	-2899	-2899	-2889	-2899	-2886	-2886	**-2895**
$6P'$ [3/2]	129	1718	1718	1718	1718	1718	1718	1718	1718	1718	1718	**1718**
	131	855.8	855.8	855.8	855.8	855.8	855.8	855.8	855.8	855.8	855.8	**855.8**
		Electron Landé-g factors: g_J										
$6S'$ [1/2]		1.321	1.321	1.321	1.321	1.321	1.321	1.321	1.321	1.321	1.321	**1.321**
$6P'$ [3/2]		1.189	1.189	1.189	1.191	1.191	1.191	1.191	1.191	1.191	1.191	**1.19**
		Nuclear moments: μ_N										
	129	-0.7767	-0.7767	-0.7767	-0.7767	-0.7767	-0.7767	-0.7767	-0.7767	-0.7769	-0.7769	**-0.7767**
	131	0.7498	0.7498	0.7498	0.7498	0.7498	0.7498	0.7498	0.7498	0.7498	0.7498	**0.7498**
		Spontaneous emission probability (10^{-9} sec)										
		0.8743	0.8904	0.8904	0.8904	0.8904	0.8904	0.8904	0.8904	0.8904	0.8904	**0.8888**

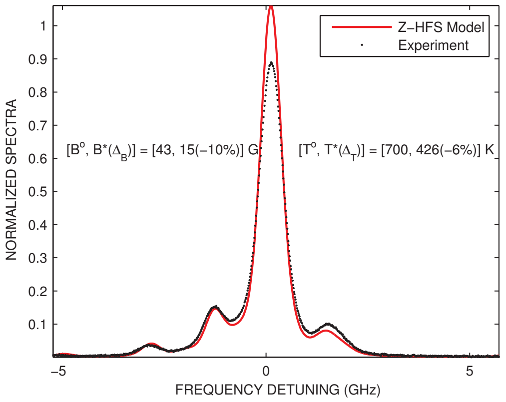

Fig. 5.13: Least-squares fitting of neutral xenon absorption spectra at 834.682 nm in an optogalvanic cell at 30 G. The fitting is based on optimal magnetic field intensity and plasma kinetic temperature outputted by Matlab's LSQNONLIN solver.

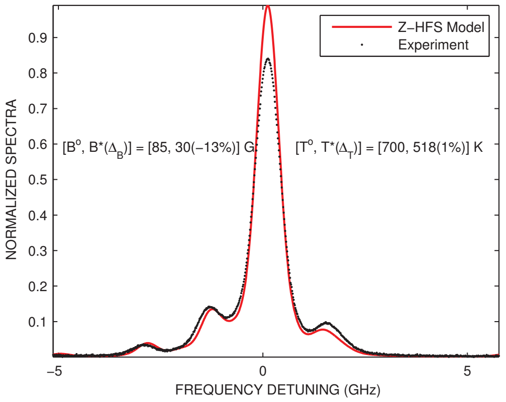

Fig. 5.14: Least-squares fitting of neutral xenon absorption spectra at 834.682 nm in an optogalvanic cell at 60 G. The fitting is based on optimal magnetic field intensity and plasma kinetic temperature outputted by Matlab's LSQNONLIN solver.

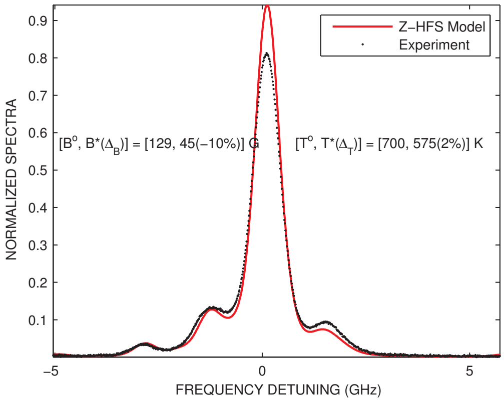

Fig. 5.15: Least-squares fitting of neutral xenon absorption spectra at 834.682 nm in an optogalvanic cell at 90 G. The fitting is based on optimal magnetic field intensity and plasma kinetic temperature outputted by Matlab's LSQNONLIN solver.

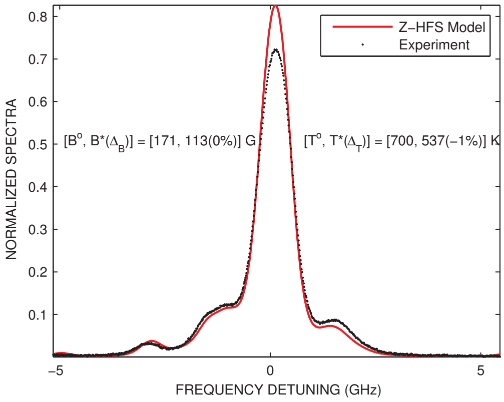

Fig. 5.16: Least-squares fitting of neutral xenon absorption spectra at 834.682 nm in an optogalvanic cell at 120 G. The fitting is based on optimal magnetic field intensity and plasma kinetic temperature outputted by Matlab's LSQNONLIN solver.

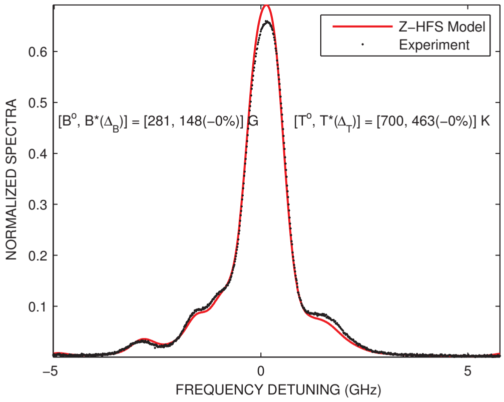

Fig. 5.17: Least-squares fitting of neutral xenon absorption spectra at 834.682 nm in an optogalvanic cell at 150 G. The fitting is based on optimal magnetic field intensity and plasma kinetic temperature outputted by Matlab's LSQNONLIN solver.

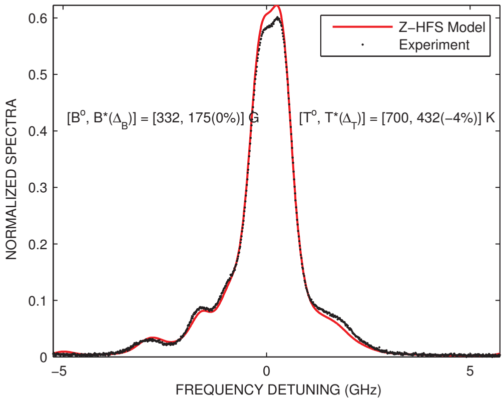

Fig. 5.18: Least-squares fitting of neutral xenon absorption spectra at 834.682 nm in an optogalvanic cell at 180 G. The fitting is based on optimal magnetic field intensity and plasma kinetic temperature outputted by Matlab's LSQNONLIN solver.

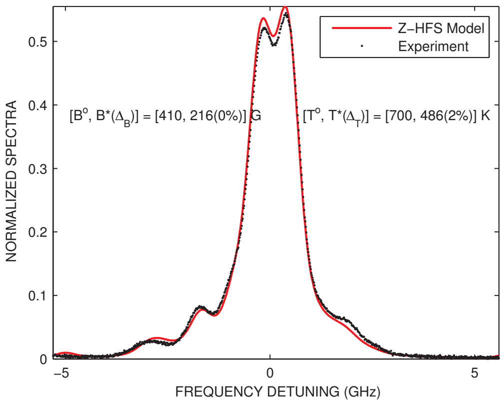

Fig. 5.19: Least-squares fitting of neutral xenon absorption spectra at 834.682 nm in an optogalvanic cell at 210 G. The fitting is based on optimal magnetic field intensity and plasma kinetic temperature outputted by Matlab's LSQNONLIN solver.

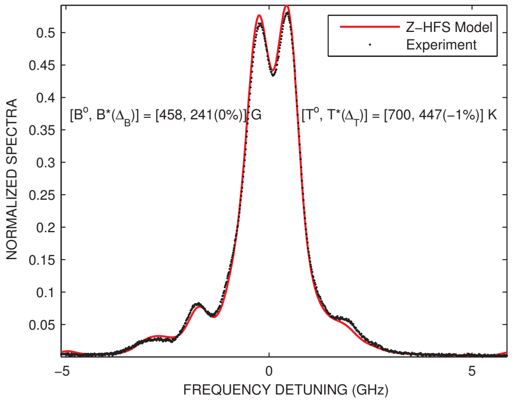

Fig. 5.20: Least-squares fitting of neutral xenon absorption spectra at 834.682 nm in an optogalvanic cell at 240 G. The fitting is based on optimal magnetic field intensity and plasma kinetic temperature outputted by Matlab's LSQNONLIN solver.

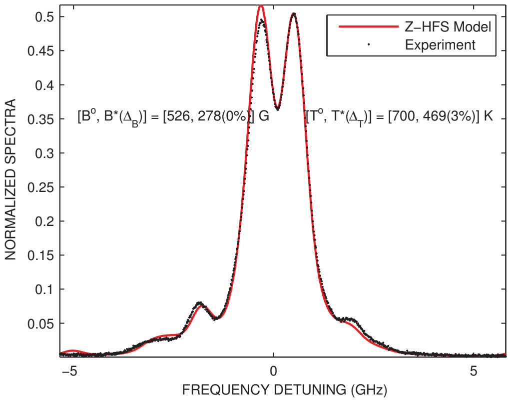

Fig. 5.21: Least-squares fitting of neutral xenon absorption spectra at 834.682 nm in an optogalvanic cell at 270 G. The fitting is based on optimal magnetic field intensity and plasma kinetic temperature outputted by Matlab's LSQNONLIN solver.

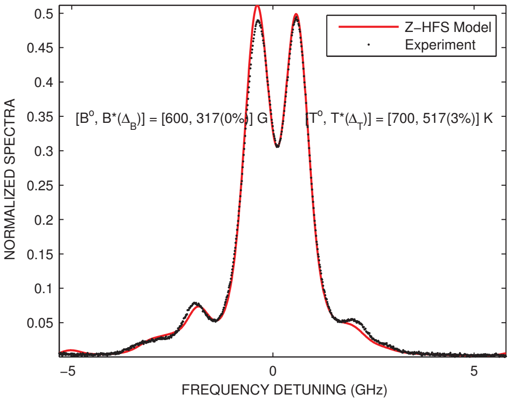

Fig. 5.22: Least-squares fitting of neutral xenon absorption spectra at 834.682 nm in an optogalvanic cell at 300 G. The fitting is based on optimal magnetic field intensity and plasma kinetic temperature outputted by Matlab's LSQNONLIN solver.

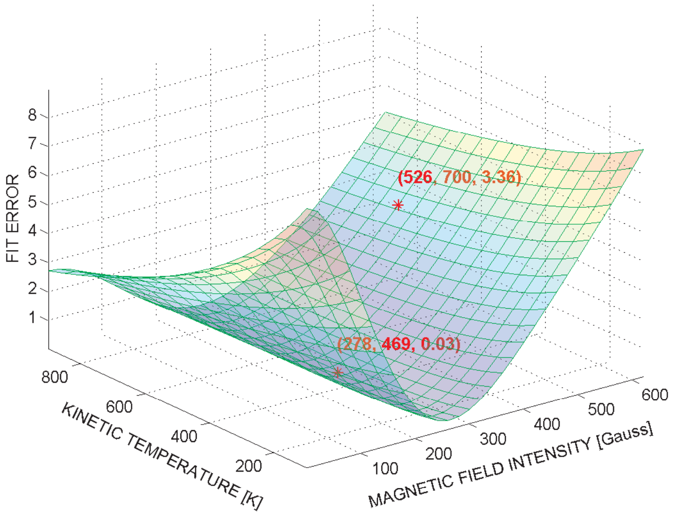

Fig. 5.23: Graphical illustration of the error function's distribution with respect to magnetic field strength and kinetic temperature in the neighborhood of the minimum. The relative displacement of the initial guess is also displayed

5.4.4 Sensitivity of LSQNONLIN to signal-to-noise ratio (SNR)

Though the above analysis dealt with optogalvanic spectra, the primary purpose of the solver is to resolve magnetic field intensities and kinetic temperatures from laser-induced fluorescence spectra (from future work) of electric thruster discharges. The latter spectra are typically noisier with SNR on the order of 100[48]. Hence, to further validate the H and T solver, we studied the effect of noise on convergence. Gaussian noise, at various SNR levels, was added to optogalvanic spectra. This study revealed little impact of noise on the quality of convergence for SNR levels above 200. At lower SNR levels, deviations of optimal values from expected target solutions still remained below 80%. Figures 5.25(a) and 5.25(b) illustrate the evolution of the deviations with decreasing SNR.

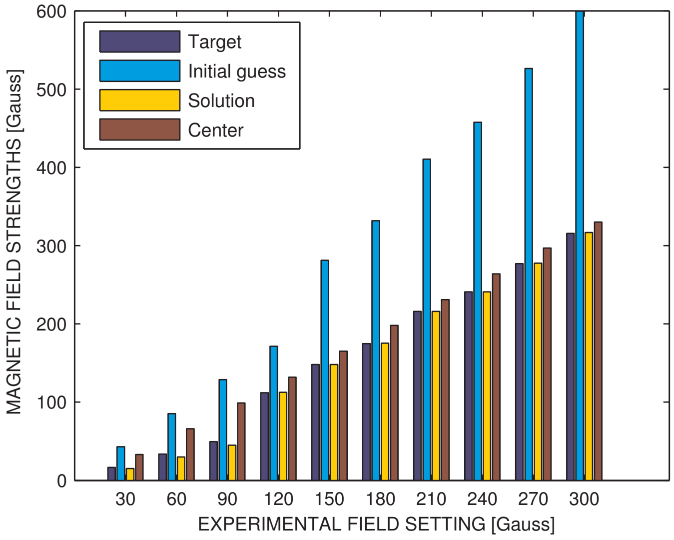

(a) Magnetic field strength parameters

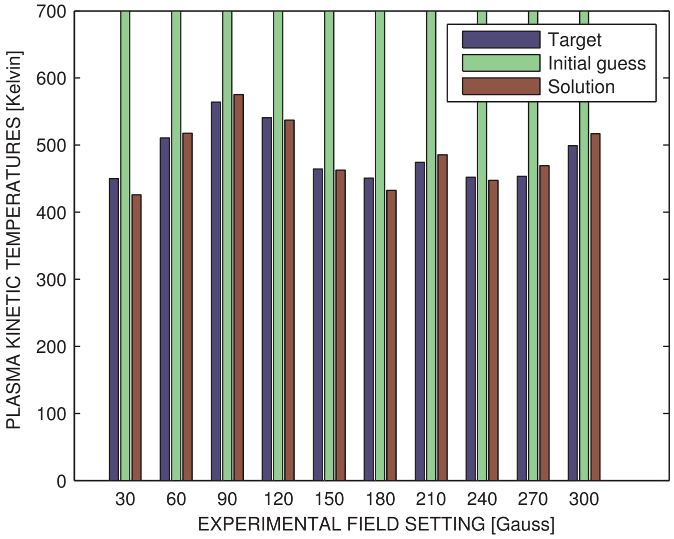

(b) Kinetic temperature parameters

Fig. 5.24: Comparison of solver solutions with target values, center-field values (applicable to magnetic field only), and initial guesses.

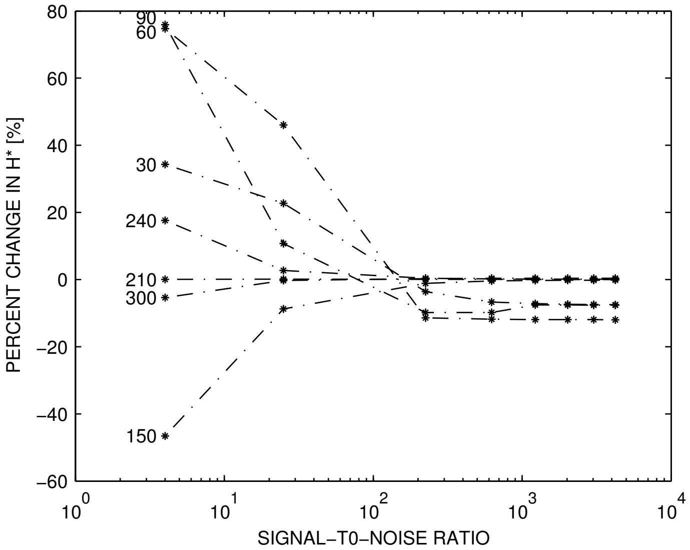

(a) Effect of SNR on H convergence

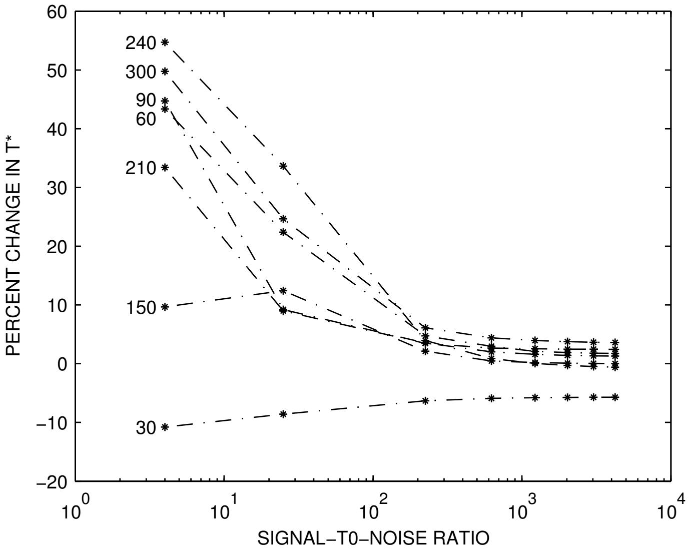

(b) Effect of SNR on T convergence

Fig. 5.25: Effect of signal-to-noise ratio (SNR) on the optimization of external magnetic field intensity (H) and plasma kinetic temperature (T) of an optogalvanic cell based on non-linear least-squares fitting of neutral xenon absorption spectra at 834.682 nm (in air). Gaussian noise was added to experimental spectra.

5.4.5 Necessity of the non-linear Zeeman theory on hyperfine structure for Xe I lineshape modeling

For the sake of completeness, we compare the performance of the non-linear ZHFS theory with its weak-field linear counter-part. In our analysis, we pay particular interest to the range of field strengths investigated (0 to 300 G) by comparing the variations of transition energies with magnetic field strength as predicted by the two theories for the two xenon isotope with non-zero nuclear spins. From Figure 5.26(a), we find that, for the case of ^{129}Xe with a small nuclear spin, both theories agree well beyond the upper bound of our range of interest. But, for the case of ^{131}Xe whose nuclear spin is higher—implying a more complex hyperfine structure—Figure 5.26(a) reveals a greater non-linearity of transition energies with field strength leading to larger disparities between the predictions of the two models. The differences becomes noticeable from 100 G and intensify from 0.1 GHz to 1 GHz as the field strength increases from 300 G to 900 G (refer to line components centered about -6.5 GHz and -2 GHz for example).

The above analysis suggests that the weak-field approximation is reliable for locating energies of Xe I transition lines about 834.682 nm provided the field strength does not exceed 300 G. Is it so for line intensities? For the sake of clarity, we chose to answer this question using cold spectra instead of cluttered transition line plots; we note from Figure 5.27, clear differences between cold spectra modeled from the two theories for an external field setting as low as 17 Gauss. Furthermore, we tested the performance of a magnetic field strength solver using a low-field linear modeler; figures 5.28(a) and 5.28(b) compare the latter solver's solutions with those reported in Section 5.4. An implementation of LSQNONLIN to the calculation of field strengths based on the linear model revealed a good match of field strength solutions only below 90 G (see Figure 5.28(a)). Above 90 G, the solutions deviate by as much as 30% from those outputted by the non-linear ZHFS solver. Worse, a comparison of plasma kinetic temperature solutions shown in figure 5.28(b) reveals no match throughout the range of field strengths investigated. Assuming that the mean of temperature solutions (on the order of 500 K) obtained from the non-linear ZHFS theory is accurate, we conclude that the weak field theory is not a reliable model for predicting kinetic temperature from Xe I spectra.

This comparative analysis omits the strong-field linear approximation because its range of validity spanning 10 to 20 KGauss [41] falls far beyond the range investigated in this study.

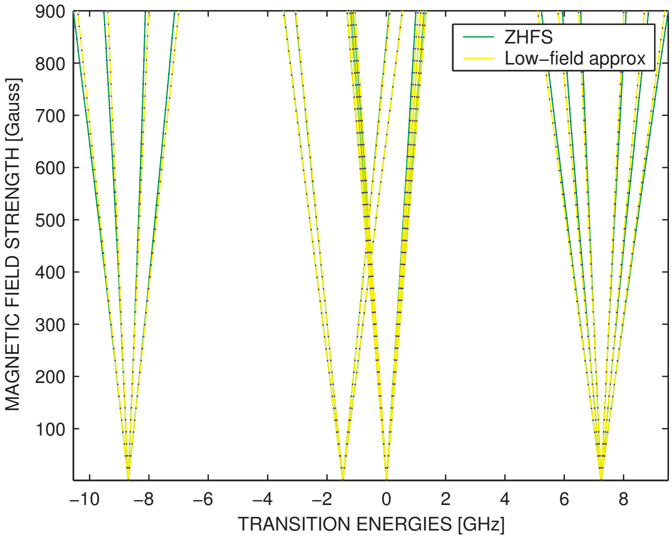

(a) Transition energies of ^{129}Xe

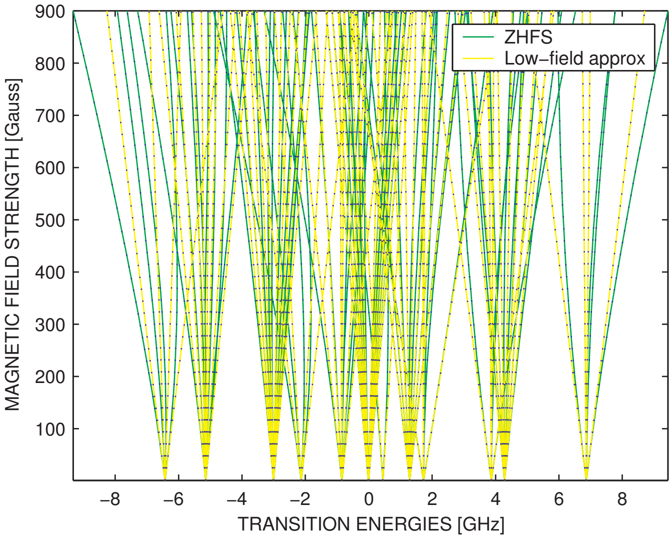

(b) Transition energies of ^{131}Xe

Fig. 5.26: Variation of transition energies of ^{129}Xe and ^{131}Xe as predicted by the weak-field linear and non-linear theories of the Zeeman effect on hyperfine structure.

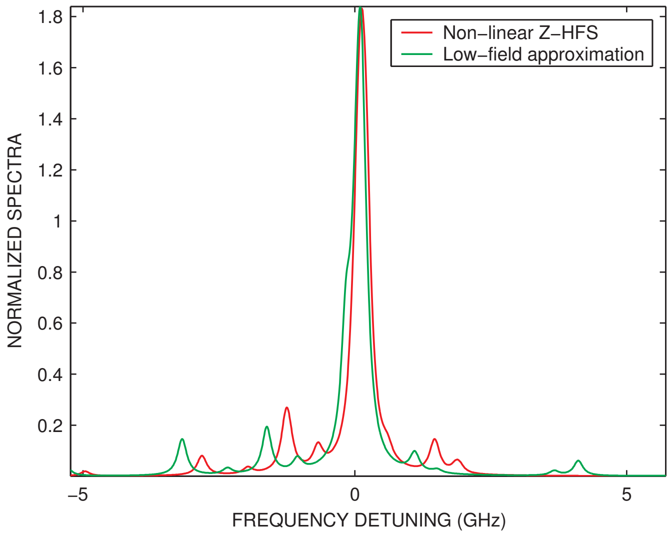

Fig. 5.27: Comparison of cold spectra as computed by the non-linear and weak-field Zeeman effects of hyperfine structure at 30 G.

5.5 Chapter summary

The non-linear Zeeman effect on the hyperfine structure is to date the most accurate theory for modeling hydrogen-like atomic spectra. We successfully used this theory to model neutral xenon absorption spectra in the plasma environment of an optogalvanic cell to which an external magnetic field was applied. The reliability of the model prompted us to use it as an input function to a non-linear solver of magnetic intensity and kinetic plasma temperature based on a best fit of experimental spectra. We noted good convergence of the solver in both variables even in the presence of Gaussian noise. The results reported in this study prove that our solver can be a reliable computational tool for the study of the interaction between an external magnetic field and a xenon plasma and the determination of Maxwellian velocity distributions in Hall thruster plumes.

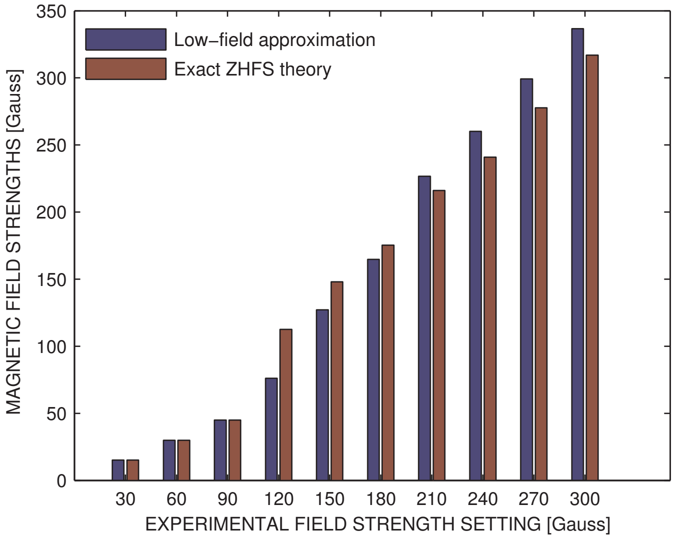

(a) External magnetic field strength solutions

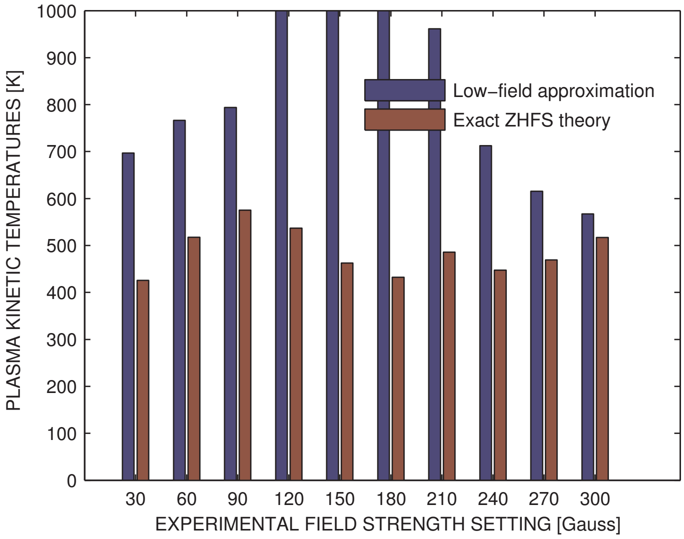

(b) Plasma kinetic temperature solutions

Fig. 5.28: Comparison of solver's solutions based on the weak-field linear and non-linear theories of the Zeeman effect on hyperfine structure.

CHAPTER VI

Magnetic Field Mapping in the Discharge Channel of the H6 from LIF of Xe I

6.1 Basics of Laser-induced Fluorescence

Based on the semi-classical quantum description of the interaction between light and matter, fluorescence can be defined as the emission of light accompanying the decay of a bound electron to a lower energy level during some finite time after some external physical process promoted it to a higher energy level. In spectroscopy, the excitation source is usually a laser; in which case, one speaks to Laser-induced Fluorescence (LIF). The de-excitation of the electron is mainly due to three physical processes, listed as follow in order of predominance:

- Spontaneous emission: intrinsic property of an excited atom, causing it to decay to a lower energy level without the effect of any external disturbances
- Stimulated emission: amplification of light subsequent to its interaction with a bound electron—basis for laser operation.
- Radiative collisional quenching: loss of kinetic energy of an atom in the form of emitted radiation subsequent to its collision with another atom. Owing to

the previously assumed state of a collisionless plasma[1], we will neglect this contribution to the fluorescence lineshape.

For the sake of simplicity and to limit our focus to understanding LIF, we limit our interest to a one-electron atom possessing no nuclear spin. From this simple picture, we will then show that the basic principles of LIF remain, in essence, the same even when the technique is extended to atoms possessing a non-zero nuclear spin and are under the influence of an external magnetic field.

6.1.1 Semi-classical description of light absorption by an atom

The semi-classical approach has been found to accurately model an atom's absorption of light in most cases of practical interest such as plasma diagnostics. The approach is classical in its wave-description of light and in its description of the atom as an electric dipole. Demtröder [55] and a few other authors (to be named as the need arises) provide a good analysis of the process that we outline in this section.

6.1.1.1 Harmonic wave description of light

As Maxwell demonstrated, light can be modeled as two mutually self-sustaining magnetic and electric waves. For now, we focus on the electric component of the wave. In the reference frame of the electron (see Fig. 6.1), the incoming light can be modeled as a planar wave in the same manner as water ripples (say, from a stone dropped on the water surface) appear less curved and more planar the further away an observer is located from their source; the temporal and spatial dependence of the wave is

$$\vec{E} = \vec{A}(\omega)\ \cos(\omega t - \vec{k}\cdot\vec{r}); \tag{6.1.1}$$

where, $\vec{r}$ represents the displacement of the electron from the nucleus (in the reference frame of the nucleus), $\vec{A}(\omega)$ is a frequency-dependent wave-amplitude, and ω

---

[1] a commonly made assumption in partially ionized plasmas as we recall from Chapter III

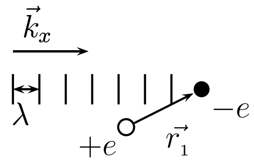

Fig. 6.1: Dipole approximation of a one-electron atom interacting with with a planar wave

and $\vec{k}$ respectively denote circular frequency and wave-number vector; the latter two variables are related as follow:

$$k = \frac{\omega}{c}, \tag{6.1.2}$$

where c is the speed of light in vacuum. The wave-number k can be interpreted as the number of periods per unit length that can be fitted around the perimeter of a circle of radius unit as expressed below:

$$k = \frac{2\pi}{\lambda}. \tag{6.1.3}$$

Because laser wavelengths ($\approx 10^3$ nm) are typically much larger than the size of atoms (≈ 1 nm), the relationship $r << \lambda$ must hold at any arbitrary time t; that fact combined with eq. 6.1.3 leads to

$$\vec{k} \cdot \vec{r} << 1. \tag{6.1.4}$$

Applying the relationship (6.1.4) to eq. 6.1.1, one finds that the spatial dependence of the electrostatic wave vector is negligibly small compared to its temporal dependence so that the expression of the electrostatic field simplifies to:

$$\vec{E} = \vec{A}\, cos(\omega t). \tag{6.1.5}$$

6.1.1.2 Classical dipole approximation of an atom

As shown in Figure 6.1, an atom can be modeled as an electric dipole whose negative pole of charge $-e$ lies at some equilibrium position $\vec{r}_1$ from the center-of-mass of the nucleus (of charge e). Upon application of an external electric field ($\vec{E}$) to the system, the electron is displaced to a new position $\vec{r}_2$ as it and the nucleus feel electrostatic forces $-e\vec{E}$ and $e\vec{E}$, respectively. These opposite forces lead to a torque $\vec{T}$ expressed in eq. 6.1.6, which when rearranged reveals an important property of the atom called dipole moment ($\vec{M}_d$):

$$\vec{T} = \vec{r} \times e\vec{E} = e\vec{r} \times \vec{E} = \vec{M}_d \times \vec{E}, \tag{6.1.6}$$

such that:

$$\vec{M}_d \equiv e\vec{r}. \tag{6.1.7}$$

6.1.1.3 Quantum mechanical description of the absorption of light

Up to this point, classical models were used to describe the atom and the exciting radiation, respectively. Based on these models, the classical expression of the potential energy associated with the interaction between light and atom yields:

$$V_{ext} = \vec{M}_d \cdot \vec{E} = -e\vec{r} \cdot \vec{A}(\omega)\cos(\omega t), \tag{6.1.8}$$

which results from inserting eqs. 6.1.7 and 6.1.5 into eq. 6.1.8.

We now use quantum mechanics to characterize the absorption of light. The derivation reported in this section mainly consists of highlights from Demtroder [55]; clarifications will be made throughout based on other authors when necessary. We begin the procedure with the Schrödinger wave-equation—a statement of conservation of energy in the atomic system

$$\widehat{H}\psi(\vec{r},t) = i\hbar\frac{\partial}{\partial t}\psi(\vec{r},t), \tag{6.1.9}$$

where:

- $\psi(\vec{r},t)$ denotes the wavefunction of the overall system and represents the probability density of finding the electron at some arbitrary location (relative to the center-of mass of the nucleus) and time
- $\widehat{H}$ is the Hamiltonian of the system representing an energy operator that summarizes all physical processes that a system might may undergo

In most cases (including spectroscopic applications), the electrostatic field interaction between nucleus and electron is much stronger than the exciting light. Hence, the external electrostatic field can be considered a small disturbance on the initial atomic state. The Method of Variation of Constants, described in Bohm's treatment of Perturbation Theory [56], is suitable for such problems. The method is applicable when an exact solution of the unperturbed Schrödinger equation (SE for short) (6.1.13b) exists and is known. So, we begin by expressing the Hamiltonian, $\widehat{H}$, as the sum of operators $\widehat{H_o}$ and $\widehat{\widehat{H}}$; which are respectively associated with unperturbed and perturbed states of the atom. From this, eq. (6.1.9) becomes:

$$\left(\widehat{H_o} + \widehat{\widehat{H}}\right)\psi(\vec{r},t) = i\hbar\frac{\partial}{\partial t}\psi(\vec{r},t), \tag{6.1.10}$$

where the perturbation term corresponds to the potential associated with the dipole moment (defined in eq. 6.1.7)

$$\widehat{\widehat{H}} \equiv V_{ext} \rightarrow -e\vec{r}\cdot\vec{A}(\omega)cos(\omega t). \tag{6.1.11}$$

Based on this superposition of Hamiltonians, the wave function can be separated into decoupled wavefunction c_n and ϕ_n that respectively account for the perturbed and unperturbed states of the atom as expressed in the following infinite series:

$$\psi(\vec{r},t) = \sum_n c_n(t)\phi_n(\vec{r},t), \tag{6.1.12}$$

To determine ϕ_n, we begin by noting that the unperturbed atom should only consist of kinetic and internal potential energies; hence, the Hamiltonian acting on ϕ can be expressed as: $\widehat{H_o} = -\frac{\widehat{\boldsymbol{p}^2}}{2m} + \widehat{V}_{int}$. In this expression, the first term in the summation denotes a kinetic energy operator in terms of the momentum operator ($\widehat{p}$ defined as $-i\hbar\nabla$). The term V_{int}, denotes an internal potential energy of the atomic system and corresponds to the potential energy operator associated with the linear harmonic oscillator model of the atom described earlier; interested readers are referred to Yariv [57] who provides its full expression that we omit here for simplicity. Based on the aforementioned definitions, the SE of the unperturbed systems assumes the form:

$$\widehat{H_o}\phi(\vec{r},t) = i\hbar\frac{\partial}{\partial t}\phi(\vec{r},t) \quad \Leftrightarrow \tag{6.1.13a}$$

$$-\frac{\hbar^2}{2m}\nabla^2\phi(\vec{r},t) + V_{int}\phi(\vec{r},t) = i\hbar\frac{\partial}{\partial t}\phi(\vec{r},t) \tag{6.1.13b}$$

Equation (6.1.13b) can be solved by separating spatial from temporal variables: $\phi(\vec{r},t) = u(\vec{r})g(t)$; which when substituted into eq. 6.1.13b and upon dividing both sides by $u(\vec{r})g(t)$, yields

$$\frac{1}{u(\vec{r})}\left(-\frac{\hbar^2}{2m}\nabla^2 u + V_{int}u\right) = i\hbar\frac{\dot{g}}{g} \tag{6.1.14}$$

in which the ‘dot’-operator denotes the time-derivative. Since the left-hand side of eq. (6.1.14) is strictly space-dependent while its right-hand side is strictly time-dependent, they must equal to some constant energy. And recalling from eq. (6.1.12) that there are many possibles modes associated with ϕ, we conclude that the constant must correspond to a discrete energy level (one among an infinite number), E_n, of the unperturbed atom. So, for some arbitrary mode n, eq. (6.1.14) can be re-expressed as

$$\begin{aligned} \frac{1}{u_n(\vec{r})}\left(-\frac{\hbar^2}{2m}\nabla^2 u_n + V_{int}u_n\right) &= E_n \quad = constant && (6.1.15a)\\ i\hbar\frac{1}{g_n(t)}\frac{\partial}{\partial t}g_n(t) &= E_n \quad . && (6.1.15b)\end{aligned}$$

When the potential is that of a dipole (recall that the corresponding operator was given in eq. 6.1.8), the solutions to eq. (6.1.15a) are a set of Hermite polynomials whose full expressions are of no use in this chapter (interested readers are referred to Yariv [57]). We will only make use of the important property that they form a complete set of orthonormal (i.e. normalized by unity and mutually orthogonal) mode shapes satisfying:

$$\int_{-\infty}^{+\infty} u_i(\vec{r})^* u_k(\vec{r}) d\vec{r} = \delta_{ik}, \tag{6.1.16}$$

where the '$*$' denotes a complex-conjugate operator applied to $u_i(\vec{r})$. The second equation (6.1.15b) is a first-order homogeneous linear differential equation of the simple closed-form solution $g(t) = e^{-iE_n t}$. Hence, an n^{th} arbitrary mode of the unperturbed wave-function can be expressed as

$$\phi_n(\vec{r}, t) = u_n(\vec{r})e^{-iE_n t/\hbar}. \tag{6.1.17}$$

We now return to the original problem of characterizing the absorption of light by the atom. Using eq. (6.1.8), we rewrite (6.1.10) explicitly:

$$\left[\widehat{H_o} - e\vec{r}\cdot\vec{A}(\omega)cos(\omega t)\right]\psi(\vec{r}, t) = i\hbar\frac{\partial}{\partial t}\psi(\vec{r}, t) \tag{6.1.18}$$

Restricting our interest to the interaction between two arbitrary energy levels i and k (such that $E_i < E_k$), we substitute eq. (6.1.17) into the expression of the overall wave-function associated with the perturbed system (6.1.12) and insert the result into the main SE (6.1.10); apply the simplifying relationship[2] $\widehat{H_o} u_n = E_n u_n$; and multiply the resultant equation by u_i^* before integrating with respect to r from $-\infty$ to $+\infty$. Then, applying the orthonormality relationship (6.1.16) to the result leads to following simple set of first-order linear homogeneous partial differential equations:

$$\dot{c}_i(t) \quad = -i\tfrac{e}{2\hbar}\vec{R}_{ik}\vec{A}(\omega)\left[e^{i(\omega_{ik}-\omega)t} + e^{i(\omega_{ik}+\omega)t}\right] c_k(t) \tag{6.1.19a}$$

$$\dot{c}_k(t) \quad = -i\tfrac{e}{2\hbar}\vec{R}_{ik}\vec{A}(\omega)\left[e^{-i(\omega_{ik}-\omega)t} + e^{-i(\omega_{ik}+\omega)t}\right] c_i(t) \tag{6.1.19b}$$

in which:

$$\vec{R}_{ik} \equiv \int_{-\infty}^{+\infty} u_i^* \, \vec{r} \, u_k d^3 r = R_{ki} \tag{6.1.19ca}$$

$$\omega_{ik} \equiv \frac{E_k - E_i}{\hbar} = -\omega_{ki}, \tag{6.1.19cb}$$

where:

- $\vec{R}_{ik}$ denotes the ‘matrix dipole element’
- ω_{ik} denotes the ‘center-frequency’; that is the frequency about which detuning is to be performed[3].

In eq. (6.1.19), $c_n(t)$ represents the probability density of finding the electron in some state n at time t; so for a $|i\rangle \rightarrow |k\rangle$transition[4], the initial conditions ($c_i(0) = 1$ and $\dot{c}_i(0) = 0$ are appropriate; which makes sense when $t = 0$ is taken as the time immediately before the interaction between the light and the electron. Solving eq.

---

[2] One can easily verify this result by back-substituting eqs. (6.1.17) into (6.1.13a)

[3] In Chapter V for example, this center-frequency was set to 0 and corresponded to the 834.682 nm (air-wavelength) absorption wavelength of Xe I.

[4] ‘$|\rangle$’ is the Dirac representation of a state

(6.1.19) for these initial conditions and noting that[5] $|\omega_{ik} - \omega| << \omega$, we arrive at an expression of the variation of the probability (per unit detuning frequency) with frequency-detuning of the exciting light that the electron assumes a higher energy-level $\big|k\big\rangle$ at some arbitrary time t.

$$|c_k(t)|^2 \propto \left\{ \vec{R}_{ik}\vec{A}(\omega)\frac{sin\left[\left(\omega_{ik} + \omega\right)t\right]}{\omega_{ik} + \omega} \right\}^2 \tag{6.1.4}$$

Integrating (6.1.4) over an infinitely wide detuning range yields the variation per unit-time of the probability that the transition $\big|i\big\rangle \rightarrow \big|k\big\rangle$ occurs; which, when differentiated with respect to time yields the rate of atomic absorption of radiation:

$$\frac{d}{dt}P_{ik} \propto \left\|\vec{R}_{ik}\right\|^2 \tag{6.1.5}$$

Note that the result in (6.1.5) is only valid when $A(\omega)$ is nearly constant—this 'Rotating wave approximation' a valid assumption in LIF since detuning ranges are small. Under this condition and the aforementioned dipole approximation, equation (6.1.5) leads to an important conclusion: **for LIF purposes the rate of absorption of light is negligibly dependent on the amplitude of the incident radiation** without which no absorption would occur in the first place! This rate is more commonly associated with the Einstein coefficient of induced absorption:

$$B_{ik} = \frac{\pi e^2}{3\epsilon_o \hbar^2}\left\|\vec{R}_{ik}\right\|^2 \tag{6.1.6}$$

6.1.2 The fluorescence lineshape: an intrinsic property of the atom

Once excited through a $\big|i\big\rangle \rightarrow \big|k\big\rangle$ transition, the atom re-emits the radiation it absorbed as it returns to the lower level $\big|k\big\rangle$ during a finite interval of time on the

---

[5] This 'rotating-wave approximation' [55] is realistic for LIF where detuning ranges are on the order of 0.03 nm (10 GHz) << 834.682 nm (absorption wavelength of Xe I)

order of 10^{-8} s [58]. For now, we assume that the atom is isolated from any other external influences (other than electromagnetic field effects) and restrict our interest to a two-level interaction. In this simple picture, the emitted radiation is monochromatic (hypothetical state of the radiation exhibiting a single mode of oscillation) and appears as a line on the emission frequency spectrum. Owing to its discreteness, this spectrum is commonly referred to as 'fluorescence lineshape'.

6.1.2.1 Spontaneous emission

Two main processes might affect the fluorescence lineshape. Of the two, spontaneous emission, the most important contribution, is an intrinsic property of the atom that can be described as a natural tendency of the electron to decay to a lower energy level. During this decay, energy is lost in the form of a photon of energy $\hbar\omega$ and carried in an electromagnetic wave oscillating at a frequency ω along some arbitrary direction. Spontaneous emission is not a definite process; a finite probability is associated with it that depends on the spacing between energy levels. The probability per unit time of spontaneous emission occurring is given in eq. (6.1.7) as follow:

$$\frac{d}{dt}P_{ki}^{spont} = A_{ki}, \tag{6.1.7}$$

where A_{ki} denotes the Einstein coefficient of spontaneous emission.

6.1.2.2 Stimulated emission

The other effect, which typically contributes to a much lesser extent to the fluorescence lineshape[6], is termed stimulated emission. In this case, a 'perturbing' photon induces the return of the electron to its initial (lower) energy state $|i\rangle$. Energy is, as in the previous case, lost in the form of an emitted electromagnetic wave in the

---

[6] Demtroder [55] shows that at room temperature the stimulated emission rate is nearly 10^{-10} smaller than the rate of spontaneous emission

same mode of vibration as the stimulating radiation. In this process, a single photon induces the emission of two photons[7]. This process amplifies the exciting light; in fact, it forms the basis of operation of lasers [57]. The rate of stimulated emission is

$$\frac{d}{dt}P_{ki}^{simul} = \rho(\omega)B_{ki}, \tag{6.1.8}$$

where $\rho(\omega)$ denotes Planck's spectral energy density of a black-body. Assuming that the laser cavity is that of a black body, ρ can be interpreted as the number of electromagnetic modes per unit frequency detuning interval. Recalling the rotating-wave approximation in LIF, $\rho(\omega) \approx constant$ (assuming that the laser cavity is a black-body). Under these circumstances, eq. (6.1.8) can be rewritten as:

$$\frac{d}{dt}P_{ki}^{simul} \propto B_{ki}, \tag{6.1.9}$$

where B_{ki} denotes the Einstein coefficient of induced absorption.

6.1.2.3 The fluorescence lineshape

For spectroscopic purposes, the fluorescence emitted is usually guided by a set of optics towards a detector that converts the intensity of the light across some frequency detuning range to an analog or digital signal that can be interpreted by a computer. The intensity of the fluorescence increases with the number, N_i, of atoms in the interrogation volume (region where fluorescence is being collected from). Assuming that the atoms are at thermal equilibrium, one can expect that the same probabilities of absorption and emission (P_{ik}^{absorp} and P_{ik}^{emiss}, respectively) remain associated with each atom. Hence, the probability of fluorescence occurring must be: $P_{ik} = P_{ik}^{absorp} \times P_{ik}^{emiss}$, which factors in the collected intensity. One can also expect the fluorescence

---

[7] This is analogous to a billiard ball resting at the edge of the table and being ejected from it by another ball.

intensity to depend on the number of oscillators in the laser cavity, $\rho(\omega)$ which we know to vary little due to the rotating-wave approximation. Lastly, the intensity of the fluorescence is reduced by the overall efficiency, $K(\omega)$ of the laser-guiding optics and the detector; and, again from the rotating-wave approximation, it is reasonable to treat this latter variable for LIF purposes. From these definitions, one can express the fluorescence intensity emitted subsequent to some excitation $\big|i\big\rangle \rightarrow \big|k\big\rangle$ as [55]:

$$I = K(\omega)\rho(\omega)N_i B_{ik} A_{ki}. \tag{6.1.10}$$

The the coefficients B_{ik}, A_{ki}, and B_{ki} relate to one another as [55]:

$$B_{ik} = \frac{g_2}{g_1} B_{ki} \tag{6.1.11a}$$

$$A_{ki} = \frac{8\pi h \nu^3}{c^3} B_{ki}, \tag{6.1.11b}$$

where h denotes the Planck constant and ν is another expression of the frequency of light that relates to ω as $\omega = \frac{\nu}{2\pi}$, and c is the vacuum speed of light. Inserting eqs. (6.1.11a) and (6.1.11b) into eq. (6.1.10) shows that fluorescence intensity only varies with the probability of absorption (as expressed in the following) which, recalling 6.1.1, was found to be an intrinsic property of the atom.

$$I \propto (B_{ik})^2 \propto P_{ik}^{absorp}. \tag{6.1.12}$$

From eq. (6.1.12), we make the important deduction that within the assumptions permissible in LIF, **fluorescence is also an intrinsic property of the atom**; that is, independent of the exciting radiation or any other external influences. Though eq. (6.1.12) was derived from the dipole model, one can generalize it to the spherically symmetric atom used to describe the Zeeman effect in Chapter V, in which the absorption probability in the transition $|i\rangle \rightarrow |k\rangle$ was found to be:

$$I_{ik} \propto {}_k\langle JFM_jM_i | JFM_jM_i\rangle_i^2. \tag{6.1.13}$$

Ideally, when conducting LIF of Xe I in the plume of a Hall thruster, one would expect to detect a fluorescence lineshape consisting of a set of discrete lines each representing the likelihood (or probability, I_{ik}) of a transition induced by light with a frequency ω_{ik}.

6.1.3 Broadening of the fluorescence lineshape

In practice, however, the detected fluorescence emanating from a plasma is not discrete. As it were briefly mentioned in Chapter V, the fluorescence exhibits a Voigt profile resulting from two dominant broadening mechanisms: Lorentz and Doppler broadening. The former process is inherent to plasma particles while the latter process depends on the particles' kinetic temperature. In the partially ionized discharges that we are interested in, many other broadening mechanisms might occur to a lesser extent. Amongst these, two are frequently cited in literature: collision-induced broadening arising from the interaction between plasma species and saturation broadening arising from the interaction between the exciting light and plasma particles.

6.1.3.1 Lorentz broadening

As mentioned in Section 6.1.2, spontaneous emission is the predominant emission mechanism leading to the LIF lineshape. This emission transforms a line spectrum into a continuous function commonly referred to as a Lorentzian profile (bell-shape like). This broadening mechanism is natural or intrinsic—an inherent property of the atom that is independent of the exciting radiation field. The breadth or width[8] of a

---

[8] conventionally defined as the wavelength or frequency width of a spectral distribution at half the peak intensity

Lorentz distribution assumes a theoretical value of 0.00116 nm (thousands of times smaller than the radius of the hydrogen atom); which is believed to be a constant that does not dependent on the wavelength probed or type of atom [53].

Due to the small width of the breadth of natural broadening, its accurate measurement is limited to the resolving power of spectrographs which, to date, remains too low; hence no direct experimental proof of this width can be made for the time being. Still, it has been a well accepted fact ever since the turn of the 20^{th} Century that atoms in plasma discharges spontaneously would emit radiation even when they do not interact and even when they are isolated from all external influences disturbances [53]. Allen's analysis of spectral lines in copper discharges using a spectrograph seems to confirm this fact [59]. He showed that below a certain level, the breath of certain lines was unaffected by a further decrease in pressure as one would expect (due to collision broadening); rather their breath remained appreciably wide even in the cold environment of a vacuum. Other potential causes of the broadening that were investigated such as electric field effects or the resolving power of the spectrograph could not be attributed to the broadening. These observations along with his remark that the intensity distribution exhibited a Lorentz profile[9] prompted Allen to conclude 'that the breath is an inner property of the copper atom, i.e., not due to external disturbances.' [59]

Good derivations of the expression of the Lorentz profile can be found in various sources [55, 58, 53, 36], from which we extract essential points to provide good insight on this important broadening process. Due to the spontaneity of the process—occurring without energy input in the atomic system—it constitutes an energy loss mechanism. Returning to the dipole approximation of an electron oscillating (as it absorbs and re-emits light) about some position of rest $\vec{r}_1$ from the nucleus, this loss

---

[9] By the time Allen performed his experiment, natural broadening had already been predicted through 'radiative damping' theory—a name, then, associated with the energy loss accompanying spontaneous light emission

manifests itself as a damping of the oscillations. In Classical Physics, the equation of motion of a damped oscillator results from Newton's second Law of motion stating that the sum, F, of external forces on a particle of mass m equals the time-derivative of its momentum (for simplicity we consider a one-dimensional motion):

$$F_x = m\frac{d^2}{dt^2}x. \tag{6.1.14}$$

Assuming a displacement $\vec{r}_2 - \vec{r}_1$ from the rest position of the electron, the external forces are:

- a restoring coulombic force from the nucleus modeled as a spring exerting a force $-kx$, where $k = \omega_o^2 m_e$ denotes the spring constant, m_e denotes the electron mass, and ω_o the frequency of oscillations at resonance.
- a frictional force $-\gamma\frac{d}{dt}x$ where γ denotes some a-priori damping constant, whose physical origin will come clear later in this section.

In term of the aforementioned expressions, eq. (6.1.14) assumes the form of a linear ordinary 2^{nd} order linear differential equation

$$\ddot{x} + \gamma\dot{x} + \omega_o^2 = 0, \tag{6.1.15}$$

whose solution, assuming small oscillations, is expressed in Demtroder [55] as:

$$X(t) = X_o(\omega)(\omega)e^{-\frac{\gamma}{2}t}cos\left(\omega t\right), \tag{6.1.16}$$

where $\omega = \sqrt{\omega_o^2 - \frac{\gamma^2}{4}}$.

The oscillations of the electron are related to the atom's spontaneous emission of light. To understand this, let us first consider the hypothetical condition of no damping ($\gamma = 0$); in this case, eq. (6.1.16) reduces to a harmonic wave solution

$Y = Y_o(\omega_{ik})cos(\omega_{ik}t)$ and each oscillation of the electron corresponds to a spontaneous switch of its energy from an upper level E_k to a lower level E_i. This energy is lost in the form of a monochromatic light wave undulating at a frequency $\omega_{ik} = (E_k - E_i)/\hbar$. On the frequency spectrum, the emission appears as a single line centered at ω_{ik} and of intensity (or probability of light emission) corresponding to the square of the amplitude of the oscillation at that frequency: $|Y_o(\omega_{ik})|^2 = Y_o(\omega_{ik})^* Y_o(\omega_{ik}) =$ constant (again, '$*$' denotes 'complex-conjugate').

Returning to our damped oscillator, we note from eq. (6.1.16) that the amplitude, $X_o(\omega)e^{-\frac{\gamma}{2}t}$, of the oscillations decreases over time with a time-constant $\tau = \frac{2}{\gamma}$. Hence, at the end of the each cycle, a light wave is emitted at a different frequency, ω and amplitude $X_o(\omega)$

$$X_o(\omega) = \frac{1}{\sqrt{2\pi}} \int_{-\infty}^{+\infty} X(t) e^{-i\omega t}; \tag{6.1.17}$$

from which, we deduce that the intensity of the light $|X_o(\omega)|^2$ is no longer constant but distributed over the frequency spectrum as evident from the following analysis.

Substituting the wave solution (6.1.16) into (6.1.17) leads to the following expression of the wave amplitude:

$$X(t) = \frac{X_o(\omega)}{\sqrt{8\pi}} \left[\frac{1}{i(\omega - \omega_{ik}) + \frac{\gamma}{2}} + \frac{1}{i(\omega + \omega_{ik}) + \frac{\gamma}{2}} \right]. \tag{6.1.18}$$

From eq. (6.1.18) and using the approximation $|\omega - \omega_{ik}| << \omega_{ik}$, the intensity of spontaneous emission assumes the following normalized distribution of the intensity of spontaneous radiation [55]:

$$|A(\omega)|^2_{normalized} = \frac{1}{2\pi} \frac{\gamma}{(\omega - \omega_{ik})^2 + \left(\frac{\gamma}{2}\right)^2}. \tag{6.1.19}$$

Noting from eq. (6.1.17) that the amplitude of the wave decays with a time-constant of

$$\tau \approx \frac{1}{\gamma} \tag{6.1.20}$$

and using the fact that its variance is on the order of τ^2, Svanberg [36] showed that the uncertainty $\Delta\tau$ must be on the order of τ; that, combined with the Heisenberg Uncertainty principle [56], $\Delta E \Delta\tau \geq \hbar \Leftrightarrow \frac{\Delta E}{\Delta\omega} \geq \hbar$, led him to deduce that there is some 'natural width'[10] associated with the profile:

$$\Delta\omega_N = \frac{1}{\tau}. \tag{6.1.21}$$

Returning to the Lorentz distribution (6.1.19), one can easily verify that the full-width at half-maximum of the distribution is:

$$\Delta\omega_{1/2} = \gamma. \tag{6.1.22}$$

Since $\Delta\omega_{1/2}$ is a unique feature of a particular Lorentz profile, Svanberg identified it as $\Delta\omega_N$, from which he deduced that $\gamma = A_{ik}$; a relationship which, when applied to eq. (6.1.19) leads to a 'natural broadening' of the fluorescence lineshape:

$$L(\omega - \omega_{ik}) = \frac{1}{2\pi} \frac{A_{ki}}{(\omega - \omega_{ik})^2 + \left(\frac{A_{ki}}{2}\right)^2}. \tag{6.1.23}$$

6.1.4 A practical example: the interaction between light and an atom with an external magnetic field

In Section 6.1.1, an attempt was made to explain how light and matter interacted in a generic sense based on the dipole model of an atom while only considering a single excitation between two atomic energy levels for simplicity. We now set out to link these basic principles to LIF of an atom upon which acts an external magnetic

---

[10] The attribution of 'natural' to the width makes sense given that it corresponds to the minimum uncertainty on the energy based on the Heisenberg Uncertainty relation [36]

field. Since the Zeeman effect had already been described in Chapter V in detail, we will only consider atoms possessing no nuclear spin but having the same J-values as the upper and lower states of Xe I in its 834.687 nm transition (for the sake of illustration).

These processes can be summarized in the sketches of the following figures. In fig. 6.2, an atom is in its rest state (before being perturbed by light) as the total angular momentum of its electron is precessing about the direction of the magnetic field and induces a magnetic moment μ_{j_1}; the various possible orientations of the angular momentum vector with respect to the direction of the field lead to different values of μ_{j_1}; which, in turn, is proportional to a quantum number $M_j = -J, -J+1, \ldots,$ or $+J$. So when $J_1 = 1$, three possible energy levels $\left|\alpha_1\ J_1\ M_{j_2}\right\rangle_i$ are possible as shown on fig. 6.2.

The light excites the atom in fig. 6.3 and causes its angular momentum to rise ($J_2 = 2$) as the electron oscillates about the rest electron-to-nucleus spacing. The electron now transitions (stimulated absorption) to an excited level corresponding to one of five possible energy states $\left|\alpha_2\ J_2\ M_{j_2}\right\rangle_k$ shown on fig. 6.3.

About a nanosecond later, the electron returns to its rest state by spontaneous emission (dominant mechanism), stimulated emission (neglected, since likelihood is $1/10^{10}$), or by collisional de-excitation (neglected in our partially ionized plasma) as fluorescence light is emitted.

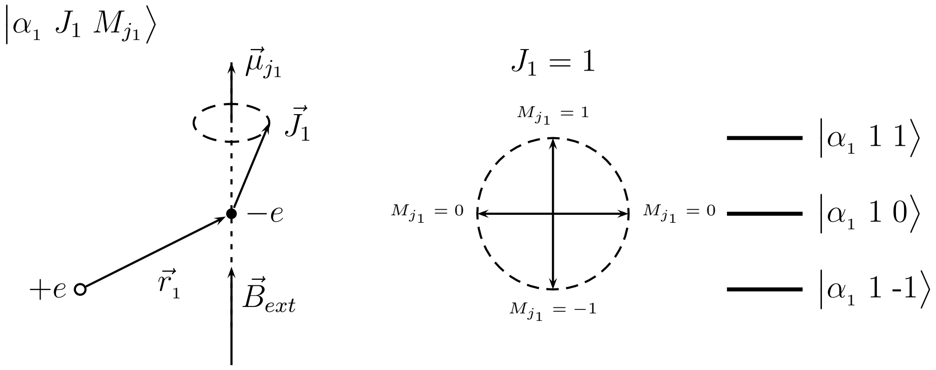

Fig. 6.2: Atom at rest before interacting with light

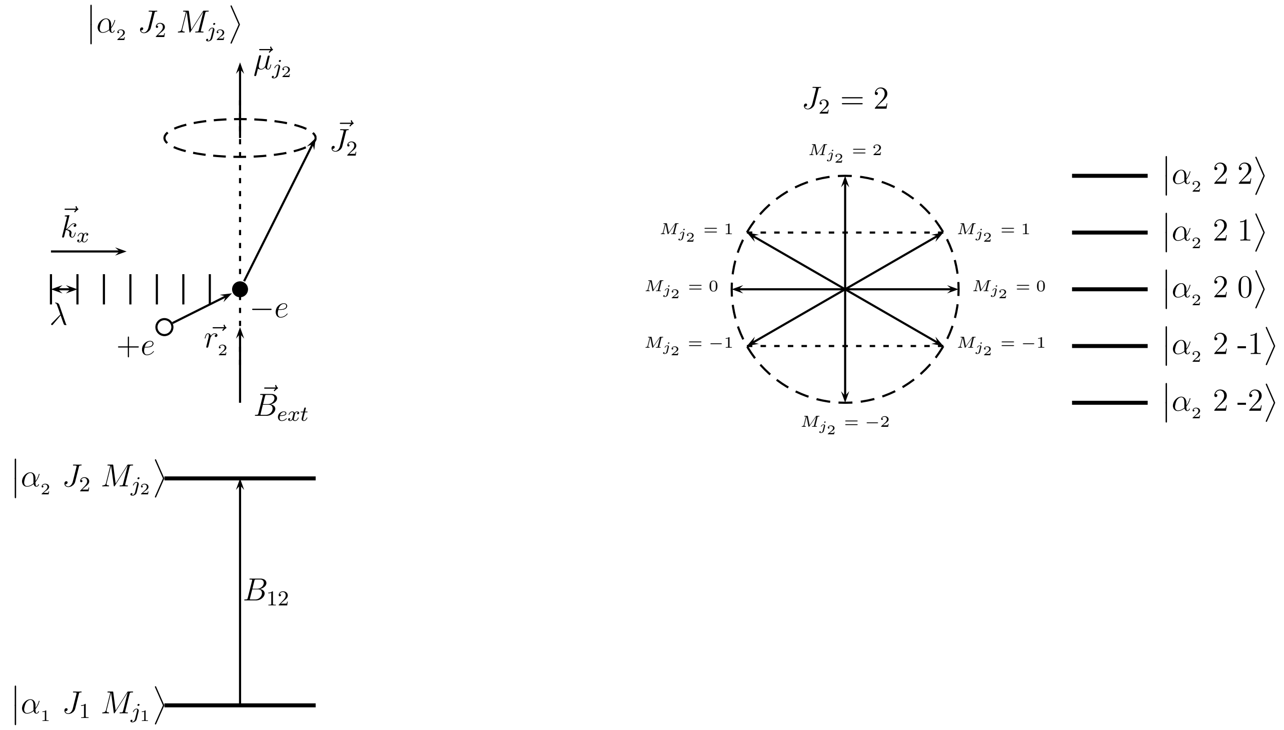

Fig. 6.3: Excitation of the atom

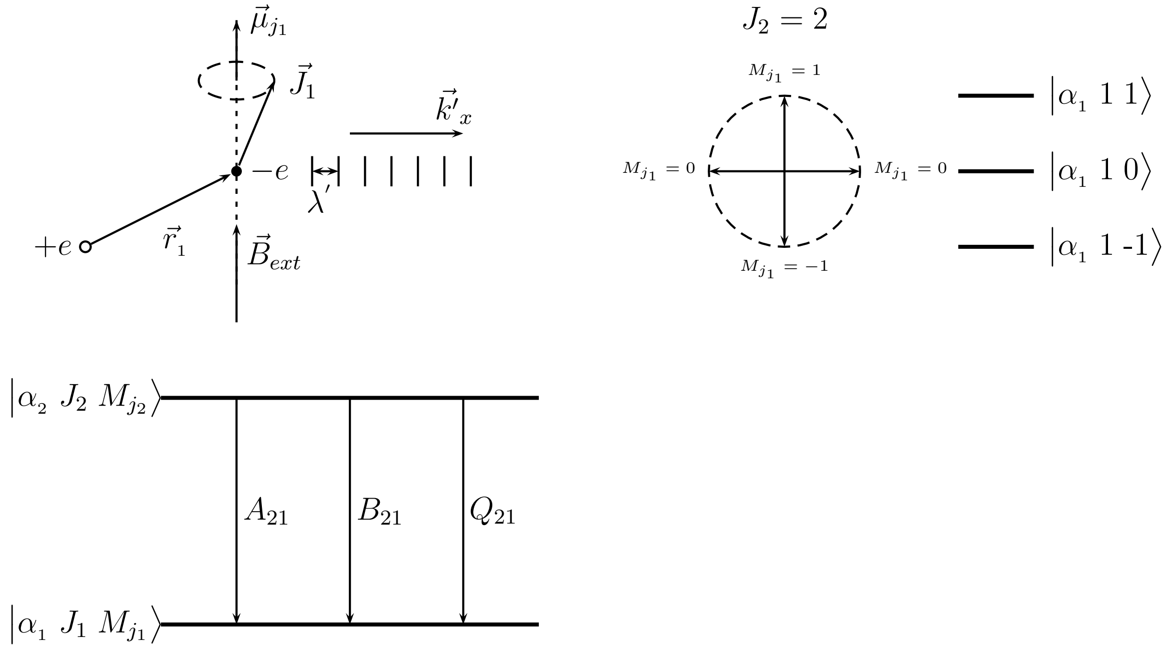

Fig. 6.4: Fluorescence emission from atom

6.1.4.1 Doppler broadening

In practice, the fluorescence spectrum does not exhibit Lorentz broadening alone unless the probed sample is at absolute zero temperature ($T = 0\ K$). In plasmas, thermal effects are important and lead to another broadening mechanism: Doppler broadening [36, 55]. Unlike Lorentz broadening, this mechanism is not intrinsic to atoms but depends on the temperature of the gas that contains them. We note however that the mechanism described in what follows applies to ideal gases—a safe assumption for the partially ionized plasma of our interest [58]. Considering N_i plasma particles in some initial energy state E_i and at thermal equilibrium, their velocity distribution is Maxwellian. Such a distribution is expressed below as the number of particles per volume having velocities $[v, v + dv]$ [55]:

$$n(v)dv = \frac{N_i}{v_{th}\sqrt{\pi}} exp\left[-\left(\frac{v}{v_{th}}\right)^2\right] dv, \tag{6.1.24}$$

where $v_{th} = \sqrt{\frac{2kT}{m}}$ is the most probable speed of the particles, which we will refer here on as the 'mean thermal speed'. As expressed in velocity-space, eq. (6.1.24) is of no direct use for LIF purposes. We are interested in its analog in frequency space. Such a distribution can be found by assuming that the line-components of the fluorescence lineshape have a center of gravity ω_o corresponding to some hypothetical radiation inducing some transition $\left|u\right\rangle \rightarrow \left|v\right\rangle$; that is, we assume that all gas particles are excited by some monochromatic light at the frequency ω_o in some inertial frame of reference (such as a laboratory).

Owing to the Doppler effect, each particle traveling at a velocity $\vec{v}$ no longer perceives the light to oscillate at ω_o, but to some other frequency ω whose magnitude depends on the orientation of wave-vector $\vec{k}_o$ relative to $\vec{v}$ as seen in the following equation:

$$\omega = \omega_o - \vec{k}_o \cdot \vec{v}. \tag{6.1.25}$$

In LIF of Hall thrusters, the angle exciting light beam is usually directed along a direction opposite to the direction of propagation of the discharge particles (except in particle velocimetry). In this case, the angle between $\vec{k}_o$ and $\vec{v}$ is close to 180^o; also, recalling $\left|\vec{k}_o\right| = \frac{\omega_o}{c}$, eq. (6.1.25) can be solved for $|\vec{v}|$ to yield the following expression:

$$v = \frac{|\omega - \omega_o|}{\left|\vec{k}_o\right|} = \frac{|\omega - \omega_o|}{\omega_o} c, \tag{6.1.26a}$$

$$\Rightarrow \qquad dv = c\frac{d\omega}{\omega_o}. \tag{6.1.26b}$$

Since the radiation power absorbed by the atoms is proportional to their number-density within $[v,\ v + dv]$ or rather its analog $[\omega,\ \omega + d\omega]$ in frequency space, one obtains after replacing v and dv in the Maxwellian distribution (6.1.24) by their respective analogs given in eq. (6.1.26a) and (6.1.26b), at the Doppler-broadening distribution per unit frequency interval about the center-frequency, ω_o, of the fluorescence lineshape spectrum

$$D(\omega) \propto exp\left[-\frac{(\omega-\omega_o)c}{v_{th}\omega_o}\right]^2, \tag{6.1.27}$$

such that the radiated power radiated within $[\omega,\ \omega+d\omega]$ is $P(\omega) = D(\omega)d\omega$.

6.1.4.2 Saturation broadening

Unlike natural and Doppler broadenings (homogeneous), saturation broadening does not depend on frequency; hence, it falls in the class of inhomogeneous broadening mechanisms. This type of broadening depends on the flux density or intensity of the exciting radiation [55], $I(\omega)$ in W/m^2, defined as:

$$I \equiv c\rho(\omega_{ik}), \tag{6.1.28}$$

in which, c denotes the speed of light in a vacuum and the spectral energy density about the center-frequency, ω_{ik}, can be assumed independent of frequency over the small detuning ranges considered in LIF (recall rotating-wave approximation in Section 6.1.2.2); hence, I only depends on the power of the laser and its cross-sectional area (the latter is assumed constant).

The origin of saturation broadening can be quantitatively described following an approach found in Demtröder based on absorption from some level i to k respectively populated by N_i and N_k atoms. Assuming that no other process is involved, the rates of increase and decrease of N_k and N_i must be balanced as expressed in the following equation:

$$\frac{dN_i}{dt} + \frac{dN_k}{dt} = 0 \Rightarrow \frac{dN_i}{dt} = -\frac{dN_k}{dt}. \tag{6.1.29}$$

While stimulated absorption promotes the depopulation of i, spontaneous and stimulated emissions promotes the population of k; hence, (6.1.29) can further be expressed in terms of the rate coefficients as:

$$\frac{dN_i}{dt} = -\frac{dN_k}{dt} = -B_{ik}\rho(\omega_{ik})N_i + B_{ki}\rho(\omega_{ik})N_k + A_{ki}N_k. \tag{6.1.30}$$

Stimulated absorption and emission coefficients depend on the degeneracies associated with each level [55]:

$$B_{ik} = \frac{g_k}{g_i}B_{ki}. \tag{6.1.31}$$

Furthermore, assuming that the system is isolated from its surroundings, the overall population (N) of species must be preserved; that is,

$$N = N_i + N_k \tag{6.1.32}$$

must hold at all times. Applying (6.1.31) and (6.1.32) to (6.1.30) at steady state (that is, no changes over time or $\frac{dN_i}{dt} = \frac{dN_k}{dt} = 0$), leads, after some algebraic manipulations, to the following expression of the ratio of upper level to total population:

$$\frac{N_i}{N_k} = \frac{\frac{B_{ki}\rho}{A_{ki}} + 1}{\left(\frac{g_k}{g_i} + 1\right)\frac{B_{ki}\rho}{A_{ki}} + 1}. \tag{6.1.33}$$

Defining a 'saturation parameter' [55] as:

$$S \equiv \rho\frac{B_{ki}}{A_{ki}}, \tag{6.1.34}$$

which we re-express in terms of laser power—owing to the dependence of the flux density (6.1.28) on laser power (P)—leads to the following dependence assuming all else constant:

$$S \propto P. \tag{6.1.35}$$

Applying (6.1.34) to the expression for the ratio of upper and lower levels (6.1.33) leads to:

$$\frac{N_i}{N_k} = \frac{S+1}{\left(\frac{g_k}{g_i}+1\right)S+1}. \tag{6.1.36}$$

As the laser power rises in the limit $P \to \infty$ or equivalently $S \to \infty$ (from 6.1.35) on finds that (6.1.36) reduces to:

$$\frac{N_i}{N_k} = \frac{1}{\frac{g_k}{g_i}+1}; \tag{6.1.37}$$

that is, when levels i and k have the same statistical weight for example (say $g_i = g_k = 1$), the relative population ratio of levels i and k tends to half. As a result, the fluorescence spectrum becomes progressively blurred or indiscernible until the plasma volume being probed becomes completely transparent to the exciting radiation.

To avoid saturation of the spectrum, the laser power input to the sample is chosen in the linear range of the variation of its integral with laser power. The attenuation of the laser power can conveniently be controlled with a neutral density filter while monitoring the integral of the fluorescence spectrum [60, 54, 61].

6.1.4.3 Collision broadening

Collisions between atoms in a plasma can induce shifting and broadening of a spectrum. We first consider elastic collisions during which no internal energy is transferred between interacting particles. The interacting particles may similar or dissimilar; in the former case, Lorentz broadening applies, while in the latter case Holtsmark broadening applies [62]. Despite the different nomenclature, Mitchell [62] considers both broadenings to be similar and refers to them as ‘pressure broadening’. Figure 6.5 depicts the process. Here we are interested in the effect that some particle B has on the fluorescence emitted by particle A undergoing a transition from energy levels E_i to E_k as the former particle approaches the latter with some mean velocity $\overline{v}$. At some initial time t_1, particle B is in the zone of influence of A or impact parameter (D_1). At a latter time t_2, particle A emits light and the separation between the particles is now D_2. When the process of fluorescence occurs during a time-interval much smaller than the mean collision time ($\tau_c \approx \frac{D_1}{\bar{v}}$), the energy levels of A exhibit small shifts in response to the approach of B. These shifts are affected by the distance between the particles; hence $E_i = E_i(D)$ and $E_k = E_k(R)$, which in turn implies that the transition frequency $\omega_{ik} = \left| E_i(D) - E_k(D) \right| / \bar{h}$ depends on D. Given that temperature (T) and pressure (P) affect plasma density, which to a good approximation is Maxwellian, D must then be randomly distributed about some mean value $\overline{D} = \overline{D}(T, P)$.

The random distribution of D about $\overline{D}(T, P)$ induces a Lorentzian distribution of the fluorescence spectrum about some corresponding mean absorption frequency $\overline{\omega}_{ik}$; this can be proved from an analysis similar to the one used in describing natural broadening (Section 6.1.3.1) by modelling the atomic dipole as an harmonic oscillator and collisions as a damping mechanism [55] leading to a constant $\gamma_c \approx 1\tau_c$. Superposition of collision and natural damping mechanisms lead to an effective damping constant $\gamma = \gamma_c + \gamma_n$, which when applied to the harmonic oscillators' equation 6.1.15, leads to a more general form of the Lorentz distribution 6.1.23 with an effective absorption coefficient $A_{eff} = \gamma_c + \gamma_n$. So, at low enough pressures ($\gamma_n >> \gamma_c$) only natural broadening needs be to accounted for, while at high pressures ($\gamma_c >> \gamma_n$) a pressure-induced collision broadening (hence the term 'pressure broadening') must be accounted for citemarr.

Aside from broadening, the effect of the plasma pressure leads to a shift $\Delta\omega_{ik}$ of the fluorescence spectrum from some unperturbed center-frequency ω_{ik}^{unpert} (would-be frequency in a nearly collisions-free plasma such that $\overline{D} >> D_1$) to $\overline{\omega}_{ik}$ resulting from the difference $\Delta\omega_{ik}(D_2) - \Delta\omega_{ik}(D_1)$ associated with a finite $\overline{D}$ such that $\overline{D} < D_1$.

Besides from elastic collisions, inelastic collisions might also occur during which, some or all of the excitation energy of A (from light absorption) is transferred into the internal energy of B. This process is illustrated in Figure 6.6 showing a return of A to the energy level that it assumed before the collision. When considering a large number of particles, this effect manifests itself as a depopulation of level E_i—hence its name collisional quenching. The rate (probability per unit time: $\frac{dP}{dt}$) of collisional quenching induced by B particles depends on their flux within some collisional cross-section (σ_{ik}) related to the energy difference between E_i and E_k as shown in the equation below:

$$\frac{dP}{dt} = \frac{1}{\tau_c} = n_B \sigma ik \overline{V} = \frac{P_B}{kT} \sigma ik \overline{V}, \tag{6.1.38}$$

where $\overline{V}$ is the mean relative velocity in a Maxwellian distribution of perturbing particles [63]. This inelastic collision rate (6.1.38) corresponds to a damping coefficient γ_c analogous to the one associated with elastic collisions. Hence, inelastic collisions also induce a Lorentz broadening of the transition line. Inelastic collisions, however, do not induce any shifting of the fluorescence spectrum.

Demtröder [55] estimates the collision broadening width at half-maximum and shift of the spectrum of Cs in xenon (used as a filler) to be about 0.2-0.7 cm^{-1} and 0.2-0.7 cm^{-1}, respectively at 1 atm (or 760 Torr) and 15^{o}C. Assuming that a broadening of the same of order of magnitude apply to xenon particles colliding with each other, one would expect widths on the order of $10^{-7}\mathrm{cm}^{-1}$ (or roughly 1 kHz) at the lower pressures (10^{-5} Torr) at which Hall thruster experiments were conducted based on the following linear dependence of spectral frequency width on pressure [36, 62]:

$$\Delta\nu(P,T) = \Delta\nu(P_o,T_o)\frac{P}{P_o}\sqrt{\frac{P}{P_o}} \tag{6.1.39}$$

; hence, in comparison to the linewidths of xenon spectra on order of 1 GHz, on can deduce that pressure broadening is negligible. The same deduction applies to pressure-induced line shifting; in fact, were it not the case, the shift would still not matter in our study of the Zeeman effect.

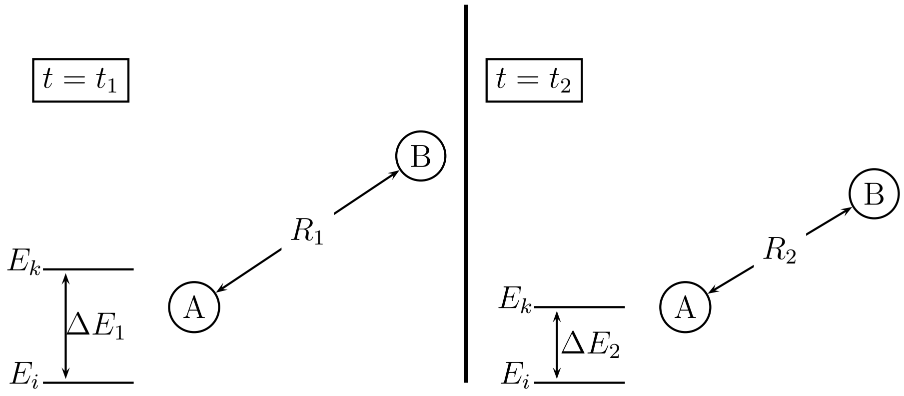

Fig. 6.5: Effect of an elastic collision on the transition energy between two quantum levels

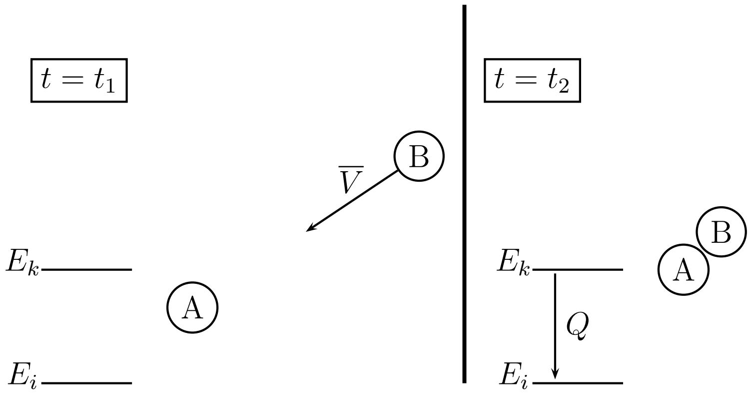

Fig. 6.6: Effect of inelastic collisions on the spacing of atomic energy levels

6.1.4.4 Stark broadening

Stark broadening applies to charged particles; therefore, neutral xenon spectra are not expected to exhibit such an effect. Still, for the sake of completeness, we will briefly describe it. Stark broadening results from the interaction of charged plasma particles with electric fields that are externally applied to the plasma or internally induced by the particles [64]. A local E-field disrupts the symmetry of the spatial distribution of an atom's electron-cloud about its nucleus; as a result, a dipole is formed and its interaction with the E-field affects the atoms potential energy, which manifests itself as a shift of J-energy levels. In hydrogen, this shift has a linear dependence on the magnitude of the E-field ($|E|$); in other elements however, the shift varies (quadratically) with $|E|^2$. When considering a large number of plasma particles, each undergoing a quadratic Stark shifting of energy levels, the overall effect on the spectrum is reflected by an asymmetric distribution on the latter.

A study of the Stark broadening on the spectrum of xenon ions is beyond the scope of this thesis; however, the interested reader might find the following work useful for first-order estimations. Accounting for quadratic Stark broadening alone, Thorne [64] estimated the broadening of a spectral lineshape to be on the order of 10^-1cm^-1 (about 3 GHz) for electric fields on the order of 10^3 to 10^4 kV. Mitchell [62] reported Stark shifts of line spectra of Sodium at various electric field settings spanning 10-16 MV.

6.2 Experimental setup for Hall thruster LIF

6.2.1 Optical setup and instrumentation

Figure 6.7 shows the basic setup for LIF spectroscopy of xenon in the plume of a Hall thruster as performed by Huang et al. [61]. The LIF results reported in this thesis correspond to a power level of 6 kW, discharge voltage of 300 V, and propellant flow rate of 20 mg/s of the thruster. The experiment can be summarized in the following four main processes from the moment the laser is emitted and splitted in three beams (labeled A, B, and C in 6.7)

- **Monitoring of frequency detuning.** As mentioned in Chapter V, the 834.657 nm absorption line (reference wavelength) undergoes various isotopic shifts, Zeeman splitting, and Lorentz and Doppler broadenings. Hence, to capture the overall spectrum one has to sweep the laser wavelength within a wide-enough frequency range centered about the reference wavelength. For this experiment, a taper-amplified diode laser (DL/TA) with a 12 GHz mode-hop free range (MHFR) was used. This MHFR is ample enough to cover the 10 GHz (≈ 0.02 nm) frequency span typically used in LIF of plasmas. For coarse monitoring of the laser wavelength, a fraction of the laser output beam (Beam A) was guided to the input aperture of a wavemeter (1 pm resolving power). Part of this beam was further split and sent to the input aperture of a Fabry-Perot interferometer for fine-tuning.

- **Reference xenon absorption spectroscopy.** An optogalvanic cell (OG) with a plasma discharge of 250 V was used to measure the absorption spectrum of stationary Xe I particles. For that purpose, another fraction of the laser beam (Beam B) was intermittently blocked by a chopper (C_1) before being fed through the cell. Beam chopping was necessary to because the OG outputs an AC voltage to simulate the spectrum. Past the exit aperture of the OG the beam was sent to a beam dump (BD) for safety.

- **Excitation of Xe I particles.** A third fraction (beam C) of the laser beam was polarized until its magnetic flux density vector was made perpendicular to the radial magnetic field of the thruster. The beam was then elevated by a set of mirrors (in a periscopic configuration) until it was at the height of the input aperture of the Large Vacuum Test Facility (LVTF). A second chopper (C_2) chopped the beam before it was sent in the LVTF through an optical window (OW). Once in the LVTF the beam propagated through a periscope that housed mirrors and a convergent lens and redirected it along a direction parallel to the axis of the thruster (T). At the output aperture of the periscope a convergent lens (CL_1) ensured a minimal beam waist (sub-millimeter) at some desired interrogation point (IP) in the plume (P) of the thruster. To probe various points in the plume, the thruster was moved with respect to the IP using a translational and rotational stage assembly (T/R S)—this and vibration-isolated supports (VIS) guaranteed a stable optical setup.

- **Fluorescence collection.** Part of the isotropic fluorescence emitted after resonant excitation of Xe I particles was collected at right-angle from the exciting beam using a divergent lens to collimate it, so to minimize any diffraction losses as the beam makes it out of the LVTF across a second optical window. Once out of the LVTF, the fluorescence beam was concentrated to a small waist diameter ($\approx$ 1 mm) as a set of two reflecting-mirrors steered it to the input aperture of a monochromator, which converted the fluorescence signal to an AC output current.

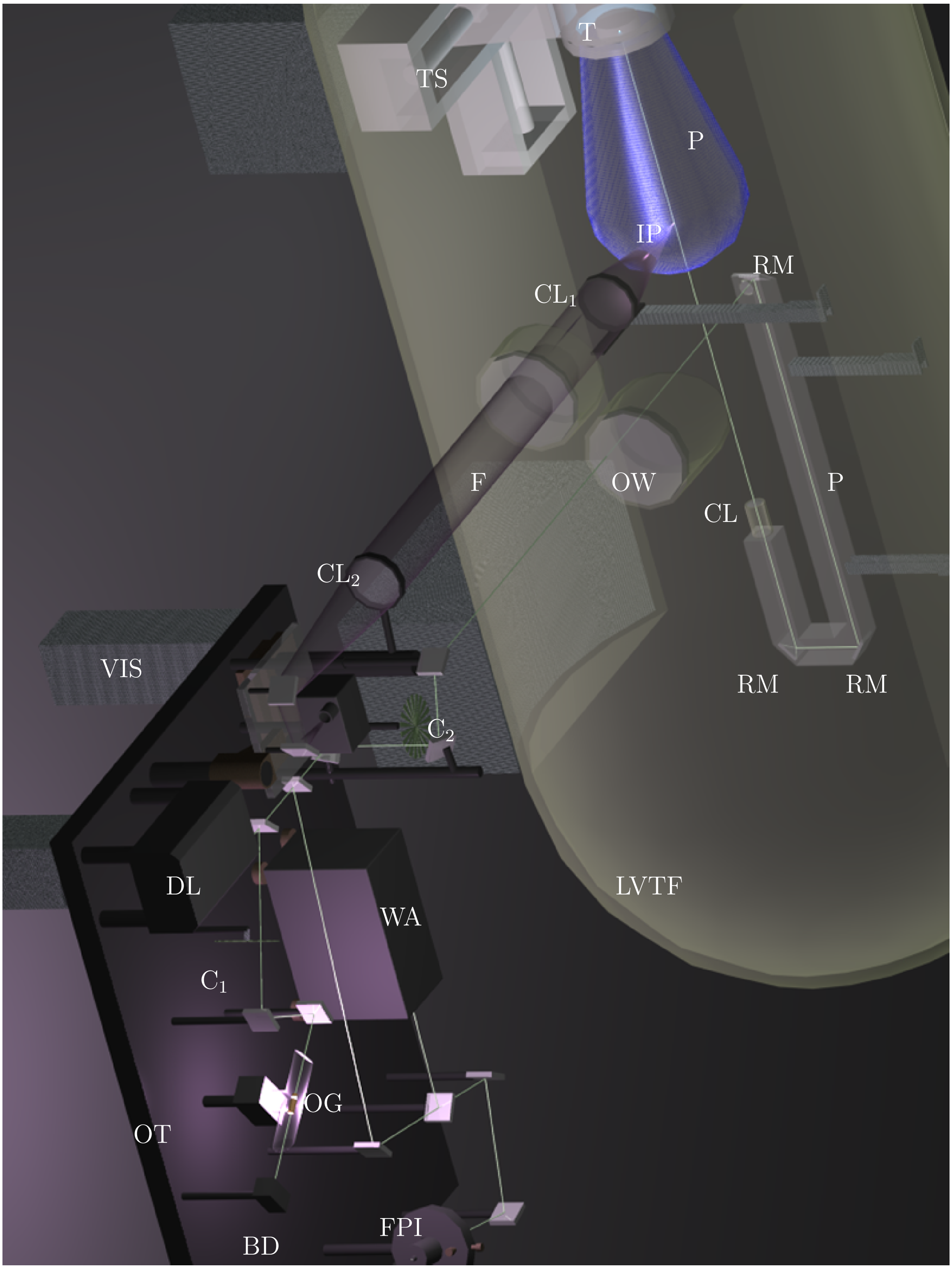

Fig. 6.7: A basic experimental setup for LIF spectroscopy in the plume of a Hall thruster

6.2.2 Signal processing

The process starts with the laser emission from a 12 GHz mode-hop free taper-amplified diode laser. The flow diagram in Fig. 6.8 describes the excitation process of the Xe I particles and resulting LIF signal flow from detection to digitization for data processing.

In this section, we concentrate on the data acquisition process, which was mainly performed using two lock-in amplifiers connected in series: one processed the reference OG cell's AC voltage output while the other processed the monochromator's AC current output. The analog signals from these devices were relayed to a computer (PC) running a Virtual Instrument (VI) processing software. Lock-in amplifiers isolate the weak signals from noise and amplify them. Reference frequencies from the two choppers —operating at different frequencies to prevent undesirable interferences—described earlier are sent to the reference inputs of the devices. OG cell and monochromator signals are then fed in the analog input bus of each lock-in amplifier, which detects and amplifies each Fourier component of the same frequency and phase as the corresponding chopper's signal. The resulting signals are sent to a PC/VI (connected to GPIB buses of the lock-in amplifiers) that plots both LIF and OG spectra.

One of the lock-in amplifier (No. 1) is used to detune the laser wavelength about the reference-wavelength as it varies the voltage of a piezo-electric device that rotates a grating element within the DL/TA assembly. The VI interface is used to set the voltage input to the piezo-electric device via an auxiliary output bus (aux. out.).

Lock-in amplifier 1 also serves as a data transmitter to the VI. It reads the photodiode current and relays it to the VI so the laser power can be monitored. It also reads the DC signal from the FPI via its built-in detector amplifier (DA) before relaying it to the VI which plots the laser's modal distribution for high-resolution frequency detuning.

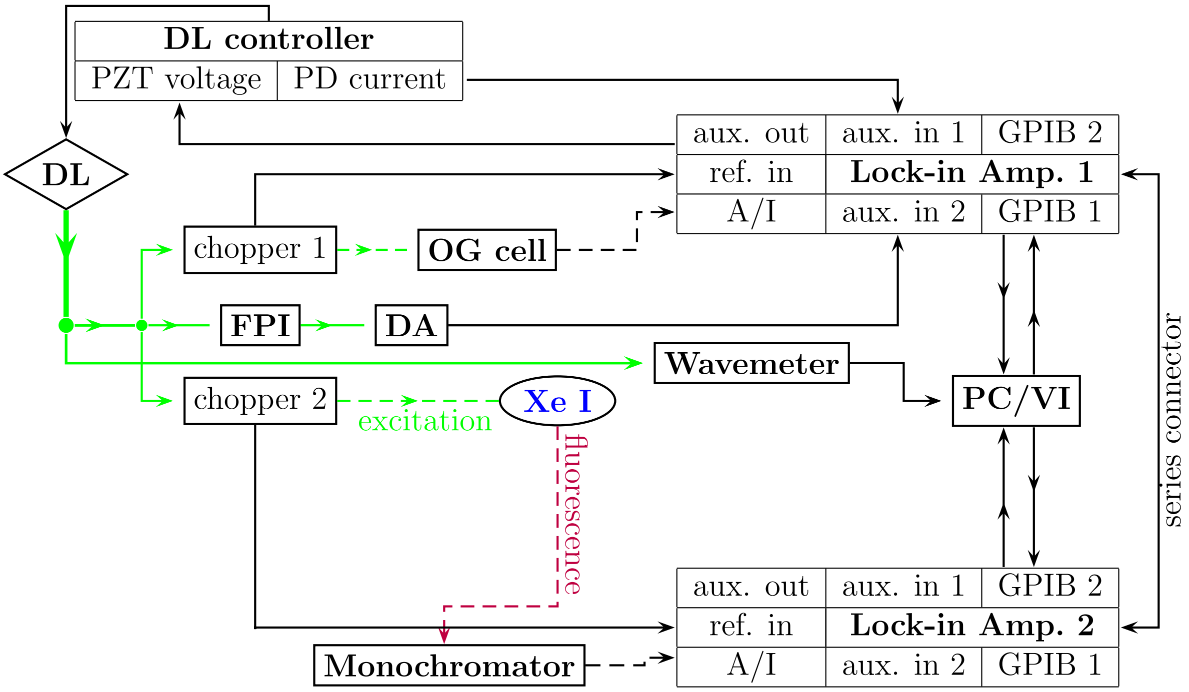

Fig. 6.8: Description of the flow of optical, analog, and digital signals in LIF spectroscopy of Xe I

Lastly, the wavelength signal from the wavemeter is directly interpreted by the computer, which VI directly plots.

6.3 Determination of magnetic field topology and kinetic temperature of Xe I particles from measured LIF spectra

The description of the experimental setup in Section 6.2 constitutes the first LIF attempt in the Large Vacuum Tank Facility (LVTF) of the Plasma Electric Propulsion Laboratory (PEPL) using a diode-laser. But the configuration described herein failed to yield LIF spectra in the discharge of a 6 kW Hall-thruster (H6) due to a defective monochromator (offset from design calibration). David Huang, a Doctoral-candidate at PEPL successfully performed the experiment using a new monochromator. He also improved on the technique by replacing the periscopic axial injection and fluorescence collection systems with optical fibers. But, instead of a Fabry-Perot interferometer, he relied on the lower resolving power of a wavemeter; which actually proved to be a reliable device for resolving the frequency scale of diode-LIF spectra—at least for the strong Xe I line investigated.

From this latest experimental setup, LIF spectra were successfully generated at the exit plane of the H6 thruster at five radial locations extending from the inner wall the the thruster to its outer wall. The tests were performed with the thruster operating at a power of 6 kW, discharge voltage of 300 V, and a mass flow rate of 20 mg/s. Due to International Traffic in Arms Regulations (ITAR) restrictions, no depiction of the thruster can be presented in this thesis. Still, the H6 has a design that is, in essence, similar to that of the P5 considering the fact that both thrusters are co-axial SPT-types and that their maximum power outputs are close (P5 and H6 operate at 5 kW and 6 kW respectively).

Application of the Non-linear least-square solver to the LIF data yielded the fits shown on figures 6.9 through 6.16. The computed radial magnetic field strengths and kinetic temperatures of Xe I are listed therein.

Computed neutral xenon temperature solutions are plotted on Fig.6.18. The distribution reveals higher temperatures closer to the walls than along the mid-section of the channel, where the faster flow of heavy particles is expected to induce a lower pressure and, hence, a lower temperature of neutrals and ions. Notice that the temperatures are about half smaller than optogalvanic cell temperatures computed in Chapter V. Moreover, throughout most of the exit plane, the temperature of neutral xenon particles approaches its boiling point (162 ^oK)) [65], which deviates from ion temperatures in plasmas—typically at room temperature [20].

According to Goldfinch [66], such low temperatures can arise in plasmas jets with anisotropic temperature distributions. Unlike in a closed sphere, in which the equilibrium temperature is the same in all directions, temperatures can differ in plasma jets depending on the direction being considered. Temperatures are cooler along a direction parallel to the bulk flow or expansion of the plasma than along perpendicular directions. Since LIF spectra correspond to velocity distribution along the axial direction of the thruster, the temperatures outputted by the solver should be interpreted as axial temperatures rather than overall temperatures. Assuming that the perpendicular temperature components are isotropic (that is, radial and azimuthal temperature components respectively obey $T_r = T_\phi = T_\perp$), the overall temperature assumes the following form in fully ionized plasmas:

$$T = \frac{T_{//} + 2T_\perp}{3}, \tag{6.3.1}$$

which implies that the parallel temperature component remains smaller than the effective temperature for some finite perpendicular temperature; this is exacerbated by the fact that the temperature of ions (hence, neutrals assuming that the two species are in thermal equilibrium with each other) are smaller in partially ionized plasma (applicable to the P5's discharge) at the same separation distance from the source of a plasma jet [66].

Hence, a more complete description of the distribution of temperature along the exit plane, should include other temperature components as well; whose estimation requires application of the solver to LIF spectra taken along the radial and/or azimuthal directions of the thruster. Assuming that the discharge exhaust is predominantly axial (1D flow), the gradient of the latter temperature components may be assumed negligible so that the reported axial varitions reasonably reflect the variation of the actual temperature of neutrals.

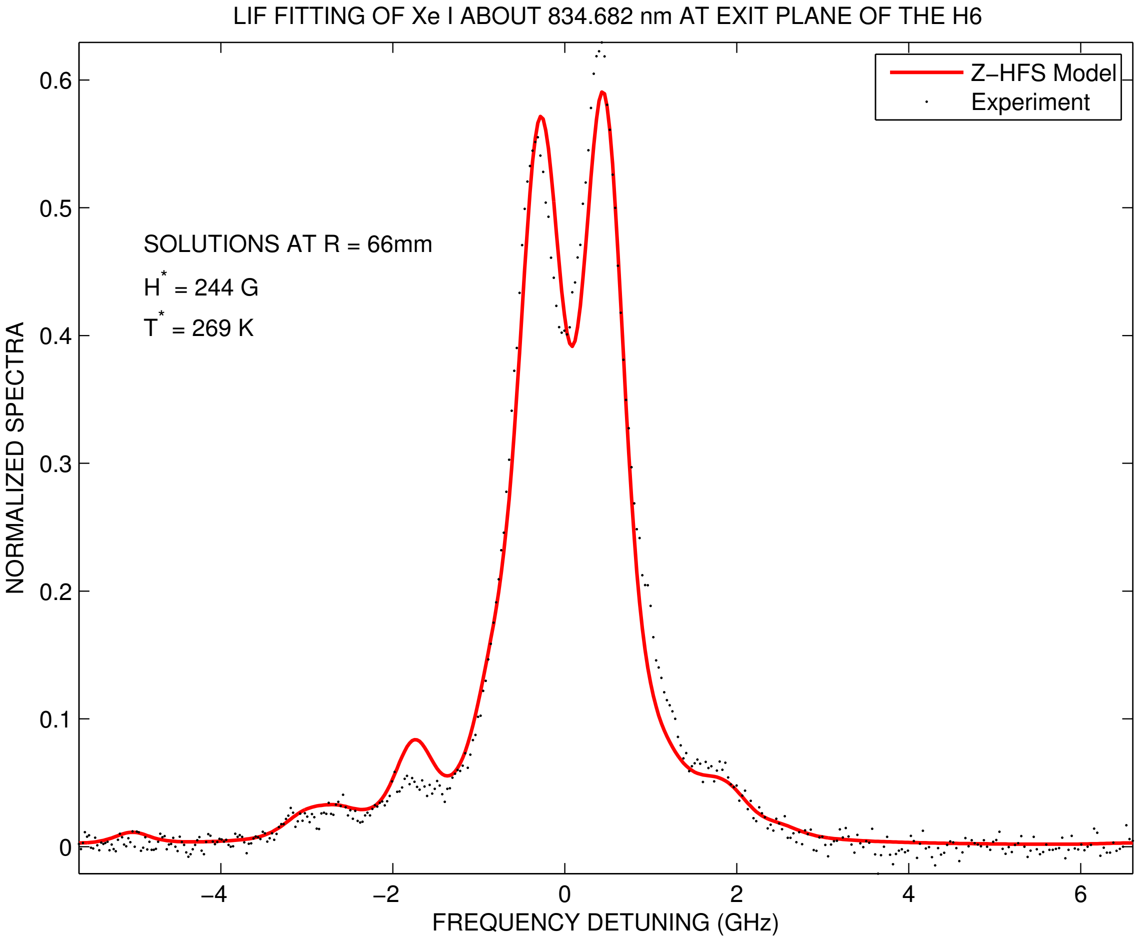

Fig. 6.9: Least-squares fitting of non-resonant LIF spectra of neutral xenon about 834.682 nm at the exit plane of the H6 thruster at 66 mm from its centerline. A commercial non-linear least-squares solver computes local magnetic field strengths and plasma kinetic temperatures for which the fit is optimal.

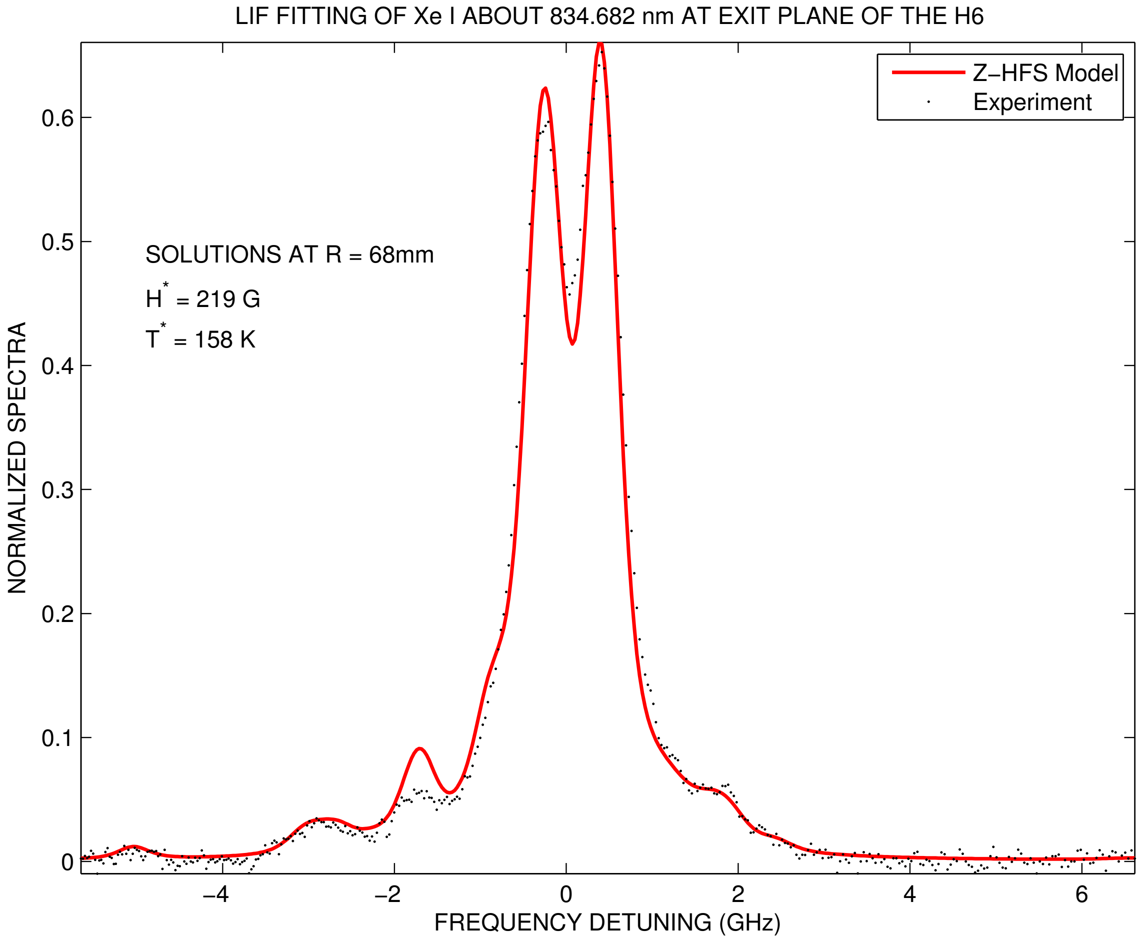

Fig. 6.10: Least-squares fitting of non-resonant LIF spectra of neutral xenon about 834.682 nm at the exit plane of the H6 thruster at 68 mm from its centerline. A commercial non-linear least-squares solver computes local magnetic field strengths and plasma kinetic temperatures for which the fit is optimal.

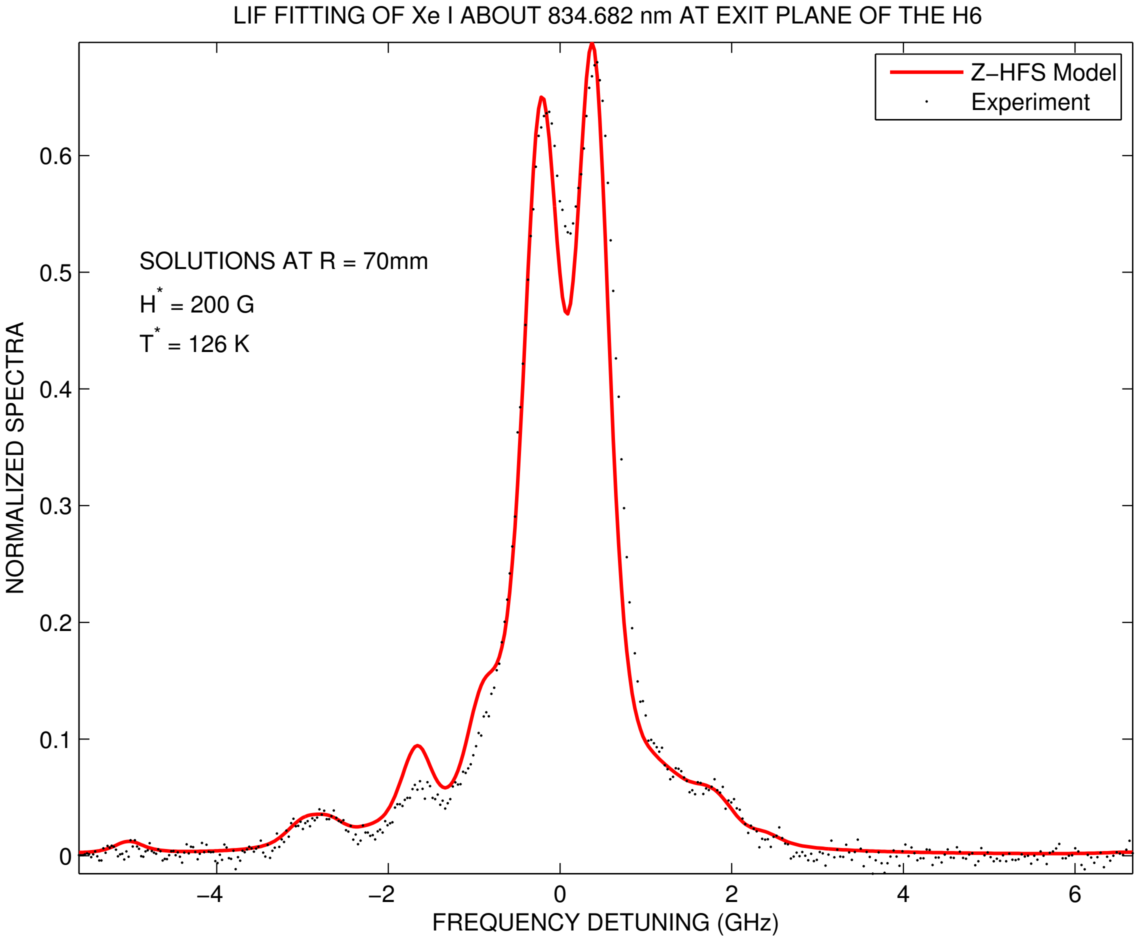

Fig. 6.11: Least-squares fitting of non-resonant LIF spectra of neutral xenon about 834.682 nm at the exit plane of the H6 thruster at 70 mm from its centerline. A commercial non-linear least-squares solver computes local magnetic field strengths and plasma kinetic temperatures for which the fit is optimal.

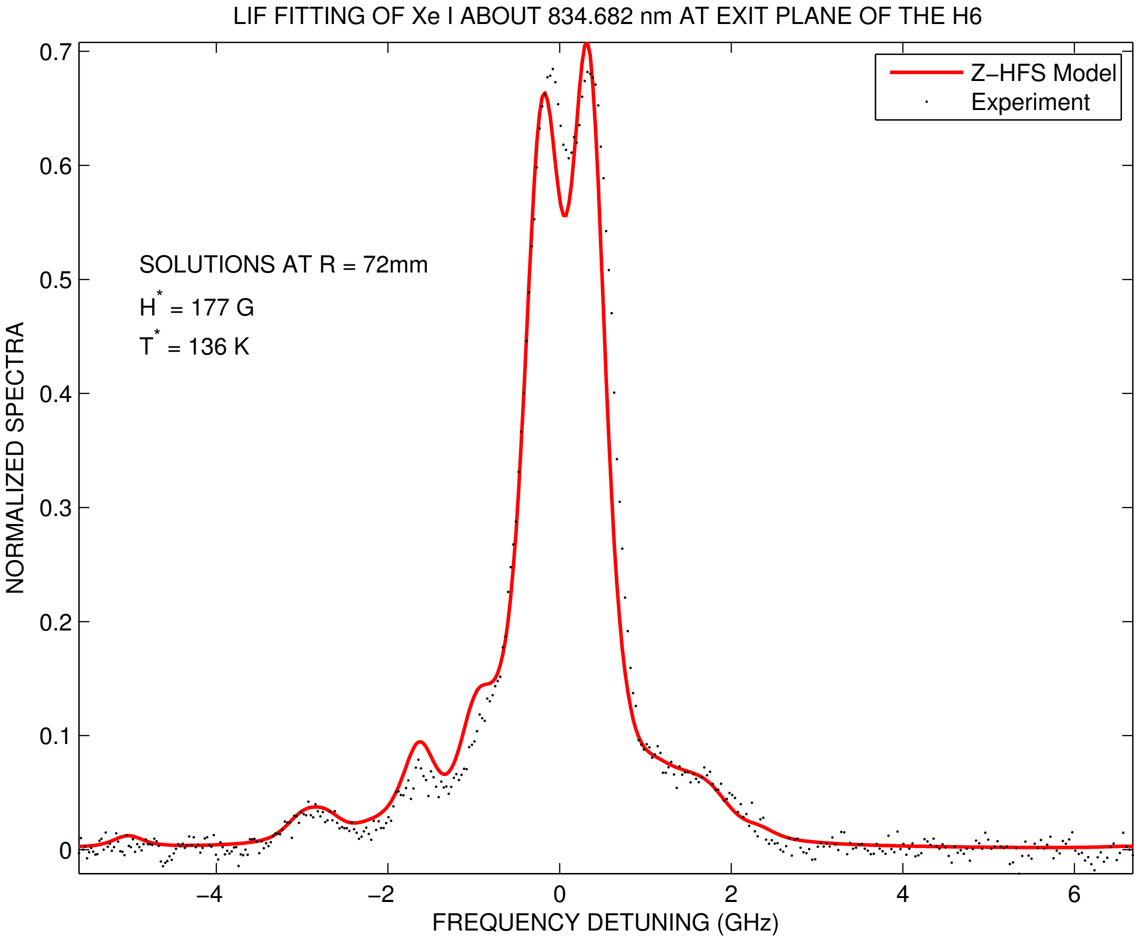

Fig. 6.12: Least-squares fitting of non-resonant LIF spectra of neutral xenon about 834.682 nm at the exit plane of the H6 thruster at 72 mm from its centerline. A commercial non-linear least-squares solver computes local magnetic field strengths and plasma kinetic temperatures for which the fit is optimal.

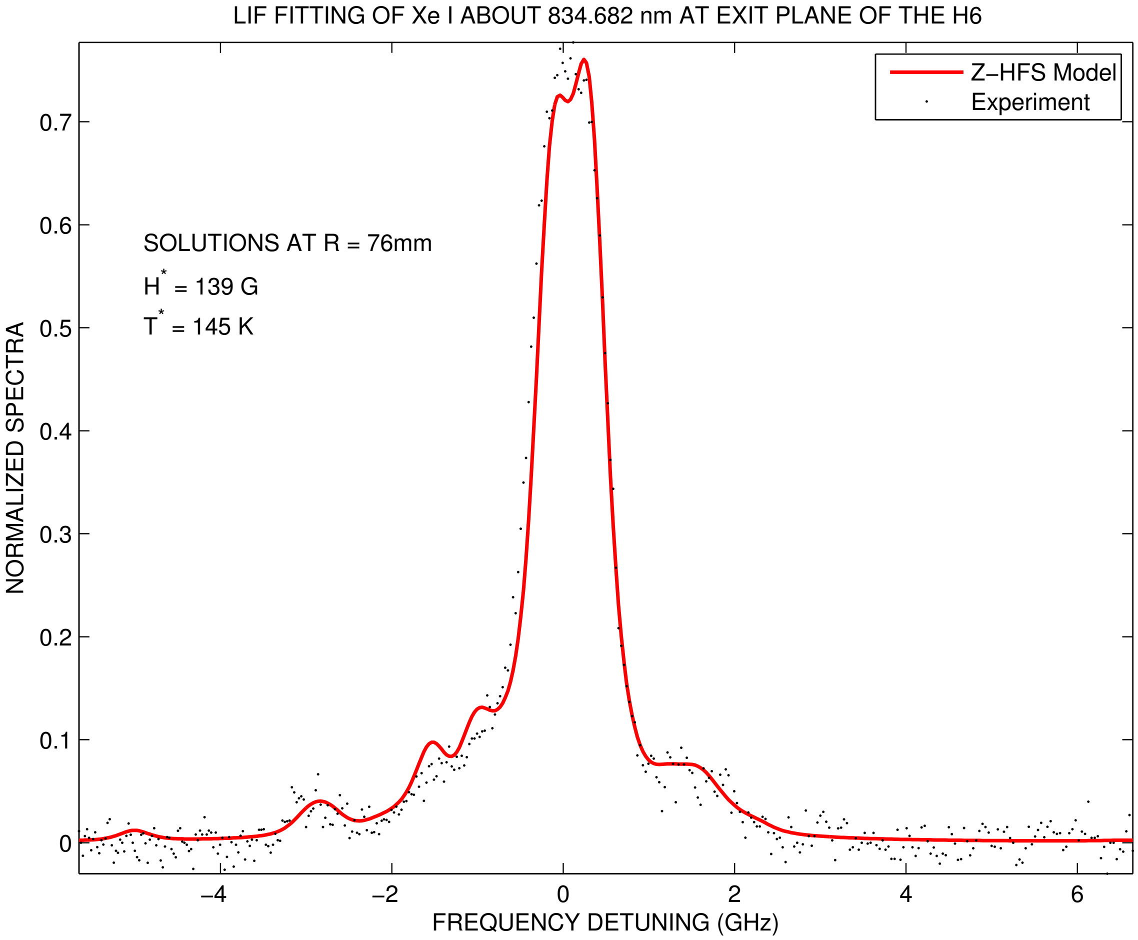

Fig. 6.13: Least-squares fitting of non-resonant LIF spectra of neutral xenon about 834.682 nm at the exit plane of the H6 thruster at 76 mm from its centerline. A commercial non-linear least-squares solver computes local magnetic field strengths and plasma kinetic temperatures for which the fit is optimal.

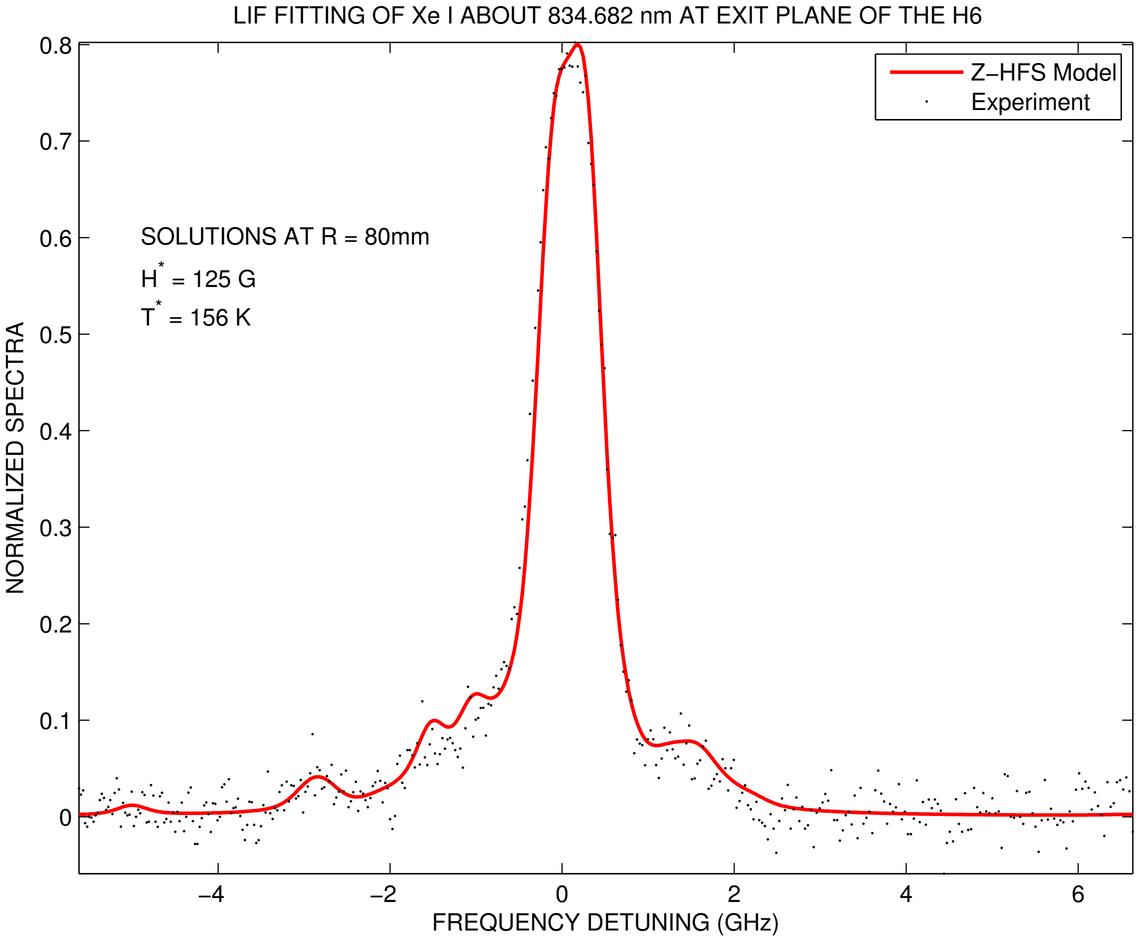

Fig. 6.14: Least-squares fitting of non-resonant LIF spectra of neutral xenon about 834.682 nm at the exit plane of the H6 thruster at 80 mm from its centerline. A commercial non-linear least-squares solver computes local magnetic field strengths and plasma kinetic temperatures for which the fit is optimal.

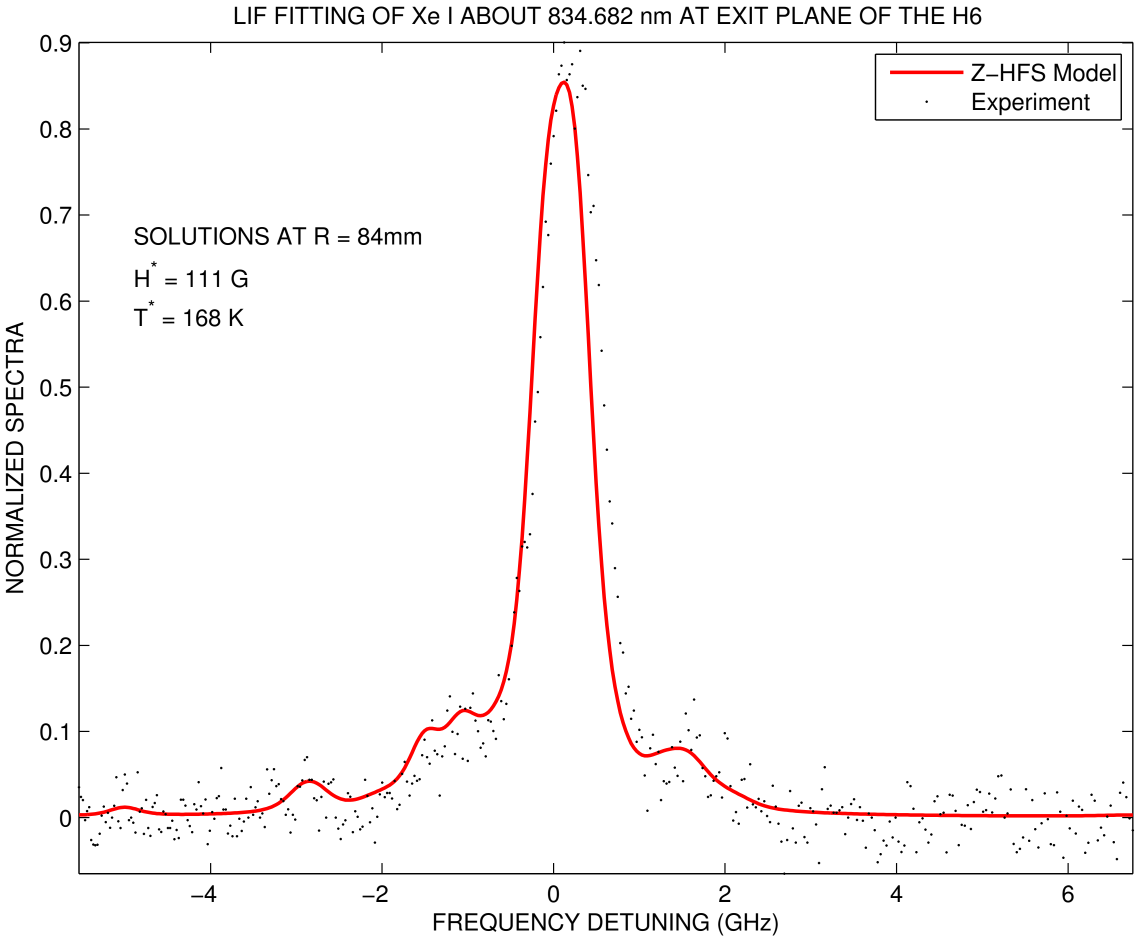

Fig. 6.15: Least-squares fitting of non-resonant LIF spectra of neutral xenon about 834.682 nm at the exit plane of the H6 thruster at 84 mm from its centerline. A commercial non-linear least-squares solver computes local magnetic field strengths and plasma kinetic temperatures for which the fit is optimal.

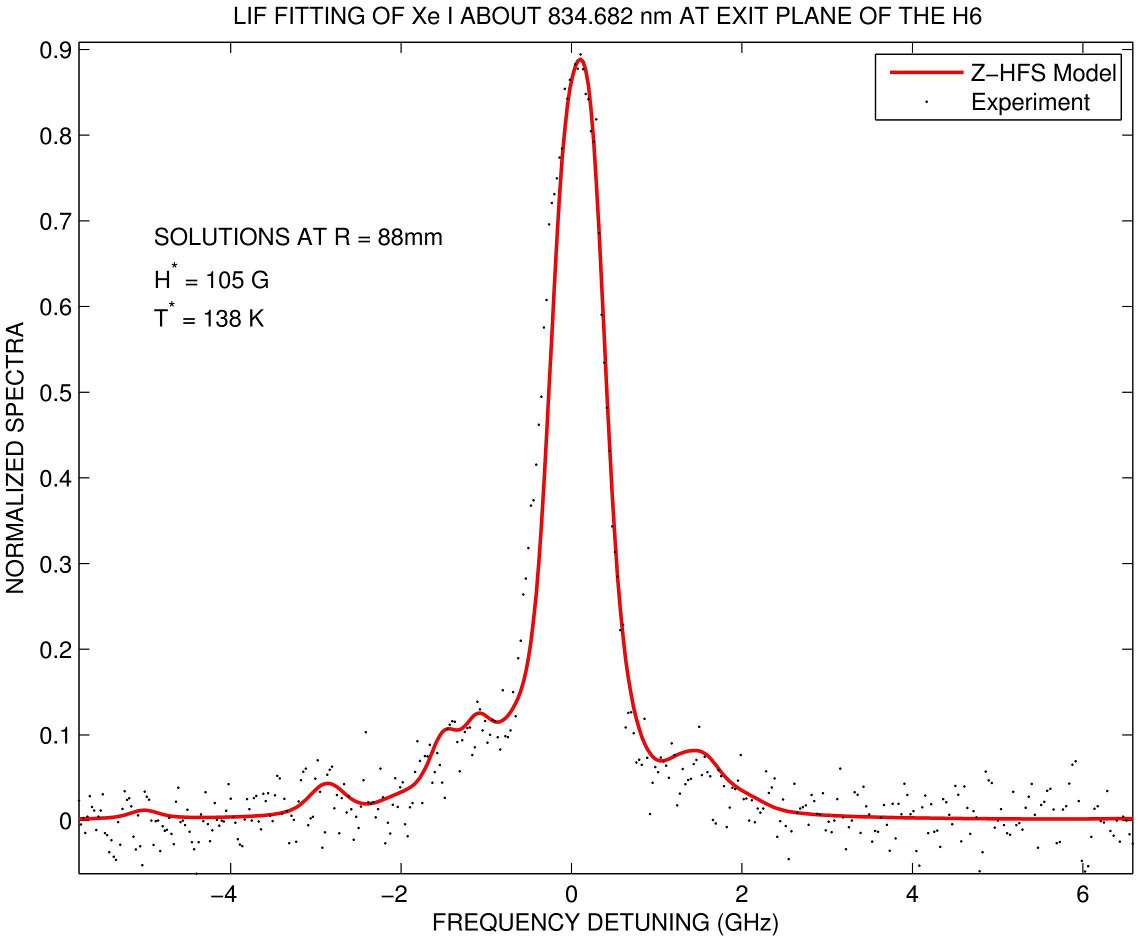

Fig. 6.16: Least-squares fitting of non-resonant LIF spectra of neutral xenon about 834.682 nm at the exit plane of the H6 thruster at 88 mm from its centerline. A commercial non-linear least-squares solver computes local magnetic field strengths and plasma kinetic temperatures for which the fit is optimal.

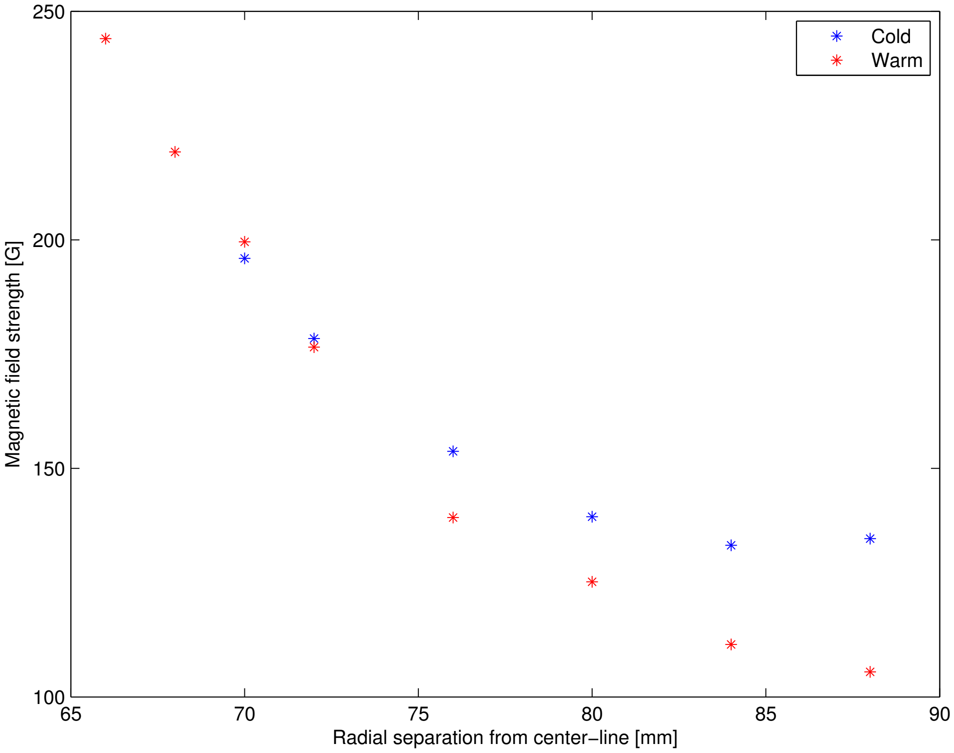

Fig. 6.17: Comparison between magnetic field strength distributions determined from LIF spectra of neutral xenon and MagNet 6 simulation (performed by Raymond Liang, PEPL Graduate Research assistant) at the exit-plane of the H6 thruster

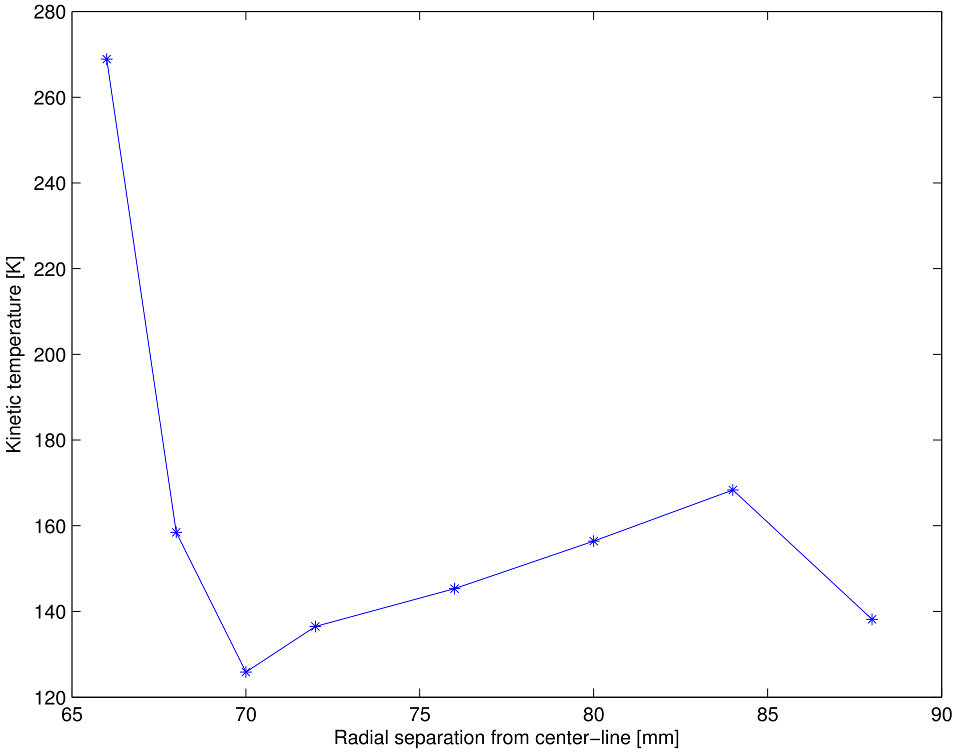

Fig. 6.18: Kinetic temperature distribution of neutral xenon in the plasma discharge of the H6 thruster computed from LIF spectra taken at the thruster's exit plane

6.4 Comparison between magnetic field strength distributions at the P5 and H6's exit planes

Results from MagNet 6 simulations of the P5's magnetic field strength are reported in detail in Chapter IV. In the present Section, we report magnetic field strengths at the exit-plane of the P5 thruster (Figure 6.19) to further validate our calculations of the field strengths at the exit plane of the H6 from measured LIF spectra. Figures 6.19(a) and 6.19(b) show the variations of the magnetic field strengths at 1.6 kW and 3 kW found from MagNet 6 simulations of the P5 in vacuo and in the presence of plasma. Both distributions exhibit shape-similarity with the variation of the H6's magnetic field strength reported in Figure 6.17; the gradient of the magnetic field increases from the outer to the inner wall.

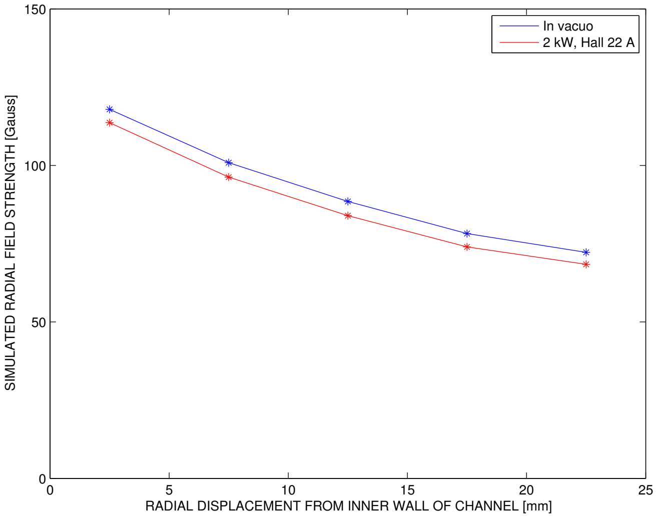

(a) Exit-plane magnetic field at 1.6 kW

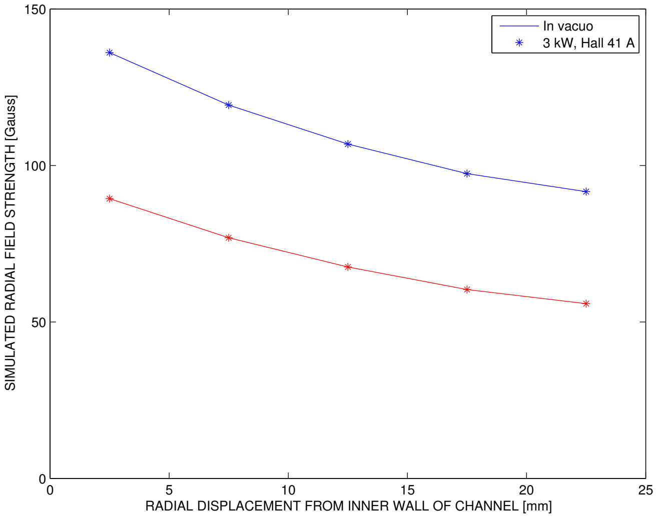

(b) Exit-plane magnetic field at 3 kW

Fig. 6.19: Variations of the magnetic field strength at the exit plane of the P5 Hall thruster MagNet 6 simulations

CHAPTER VII

Conclusion

We studied the effect of the Hall current's induced magnetic field on the vacuum field of coaxial Stationary Plasma Hall thrusters based on MagNet 6 simulation of a 5 kW thruster (P5) and laser-induced fluorescence spectra taken at the exit plane of a 6 kW thruster (H6). MagNet 6 simulations were performed at power settings of 1.6 kW and 3 kW. Simulations of the field topology due to the thruster's electromagnets operating in vacuo agreed well previous studies [1] performed on the same thruster. An investigation of the effect of the Hall current on the vacuum field revealed a reduction of the magnetic field strength as expected from the diamagnetic nature of plasmas. The reductions from vacuum field strengths were found to be more significant closer to the outer wall. Axial components of the magnetic field exhibited a negligible sensitivity to the Hall-current's self field. Aside from its effect on the field strength, the Hall current was found to enhance the concavity of field lines in the discharge along the axial direction; which promotes focusing of the exhaust plasma.

An increase of the integral value of the Hall current up to twice its value at each power level investigated—while maintaining its spatial variation, say by increasing the cathode flow rate—revealed larger reductions of the peak magnetic field strength; more interestingly, this study also revealed that the peak of the field strength shifts closer to the anode with increased Hall current density. Moreover, it was found that the gradient of the magnetic field strength loses its monotonicity at higher integrated currents. We learned from this study that increasing the magnitude of the integral of the Hall current beyond design levels, say, by raising the density of electrons—in order to enhance ionization for example—is undesirable because it causes a deviation of the magnetic field strength's variation from that of an ideal positive gradient distribution in the discharge channel.

From near-infrared laser-induced fluorescence spectroscopy of neutral xenon performed at the exit plane of the H6 thruster (extending from the inner wall to the outer wall), we computed actual magnetic field strengths and kinetic temperatures by fitting measured spectra with natural and Doppler-broadened Zeeman-split fluorescence lineshapes. A commercial non-linear least-squares solver was used to compute radial magnetic field strengths and plasma kinetic temperatures that best minimize the fitting error between experimental and simulated spectra. As a preliminary step, the solver was validated using spectra measured from an optogalvanic cell with known plasma temperature and exposed to an external field of known strength. Application of the solver to LIF data of the H6 revealed, as in the MagNet 6 simulation study of the P5, that the plasma induces a reduction of the radial magnetic field strength. This reduction was also found to be more important closer to the outer wall. The distribution of the kinetic temperature remained fairly constant with respect to the centerline temperature value in most of the discharge channel. Closer to the inner wall, however, the temperature was found to increase by as much as twice as the that of the centerline temperature. These results confirm that neutrals are faster—that is, their kinetic energy is less random and their temperature is smaller—around the center-line of the channel where the magnetic field peaks. We attribute the abrupt temperature rise near the inner wall to a greater collision frequency between neutrals and the hot wall. Extending the data collection zone closer to the outer wall would likely have revealed a similar trend in the temperature distribution.

This thesis reveals that both MagNet 6 and LIF are reliable non-intrusive tools for probing the magnetic field topology in the plasma environment of a Hall thruster. This study is encouraging: with more complete LIF probing, a full mapping of the magnetic field topology and temperature distribution in the discharge channel of a Hall thruster is possible; which is key to a better understanding of the interaction between plasma and magnetic field in the acceleration zone of Hall thrusters. With the development of Hall thrusters with higher power, one can expect this interaction to be more important.

The following projects might constitute useful validation and extensions to this thesis:

- A more complete mapping of the discharge channel's magnetic field from Zeeman split LIF spectra upstream and downstream of the exit plane and a subsequent validation of MagNet 6 simulations reported in this study.
- An estimation of the Hall current's magnetic field induction by substracting the field in the presence of plasma (computed from LIF specra in the discharge channel) to the circuit-induced field; then, using a computational approach, estimate the associated Hall current. Such a study could prove to be a reliable non-intrusive way of determining the Hall currentl, and hence, a definite means for non-intrusively finding the spatial distribution of the Hall current. Combined with the latter distribution and magnetic and electric fields—the latter, which can be computed from available high-accuracy measurements of Haas [13]—would yield a reliable estimation of electrons' and ions' number density (assuming quasi-neutrality).
- A validation of the thermal potential approximation of magnetic field lines may reveal a valuable means of non-intrusively estimating the plasma potential from computations of the magnetic field based on LIF. Such a study would, however,

require two-components LIF in the thruster's discharge channel. Computing the gradient of the electric potential would lead to a spatial distribution of the electric, which may be validated against available data.

APPENDICES

APPENDIX A

Additional results from MagNet simulation of the P5's magnetic circuitry

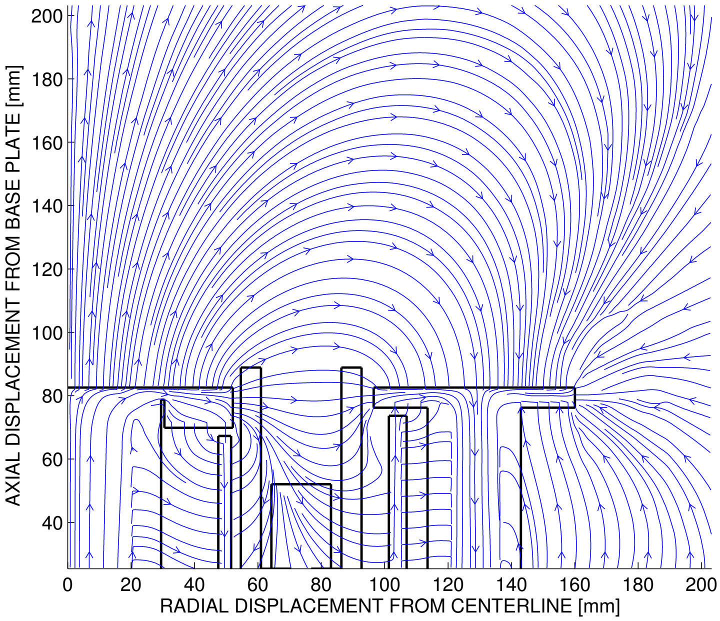

Fig. A.1: Streamlines of the magnetic field strength's vector field generated by the magnetic circuit of the P5 operating without discharge plasma ('in vacuo' or 'cold operation') at electromagnets' coil settings at 3 kW

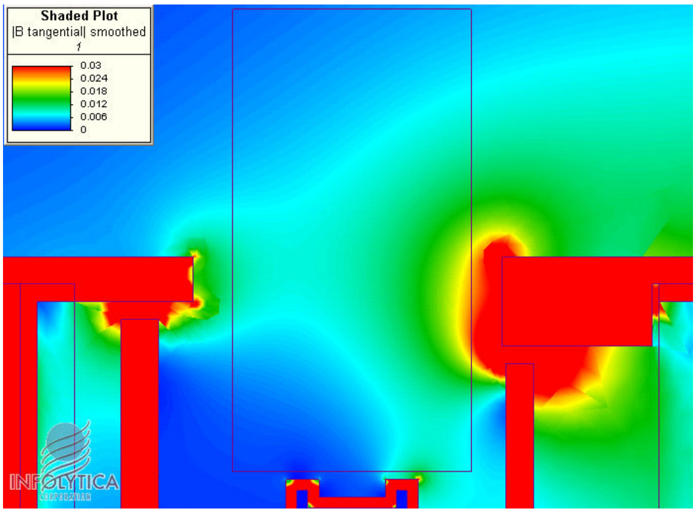

Fig. A.2: Contour map of the magnetic field strength of the P5 operating without discharge plasma ('in vacuo' or 'cold operation') at electromagnets' at 3 kW Field strengths are expressed in Tesla (equivalent to 10^5 Gauss)

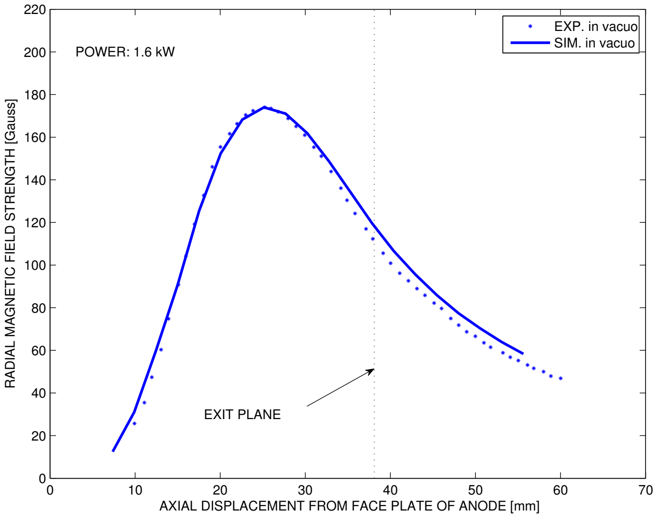

(a) 1.6 kW

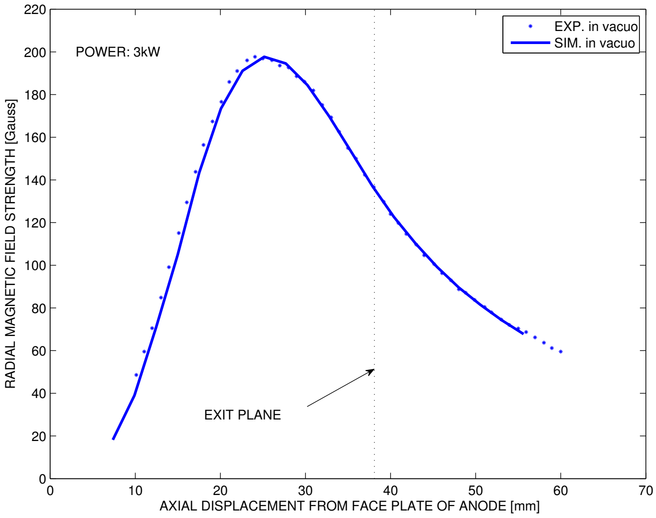

(b) 3.0 kW

Fig. A.3: Validation of MagNet 6 simulation of the radial component of the P5's magnetic field strength at 2.5 mm from the inner wall at 1.6 kW and 3 kW

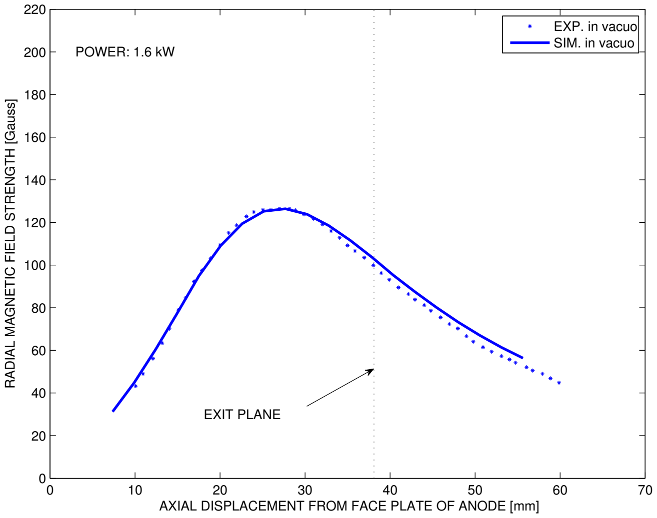

(a) 1.6 kW

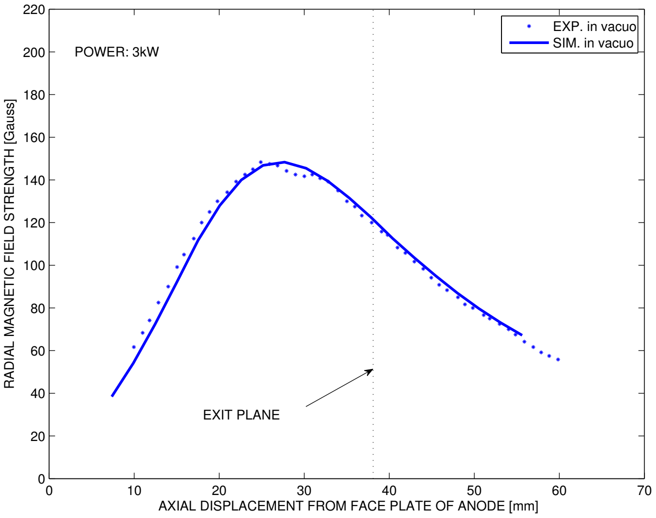

(b) 3.0 kW

Fig. A.4: Validation of MagNet 6 simulation of the radial component of the P5's magnetic field strength at 7.5 mm from the inner wall at 1.6 kW and 3 kW

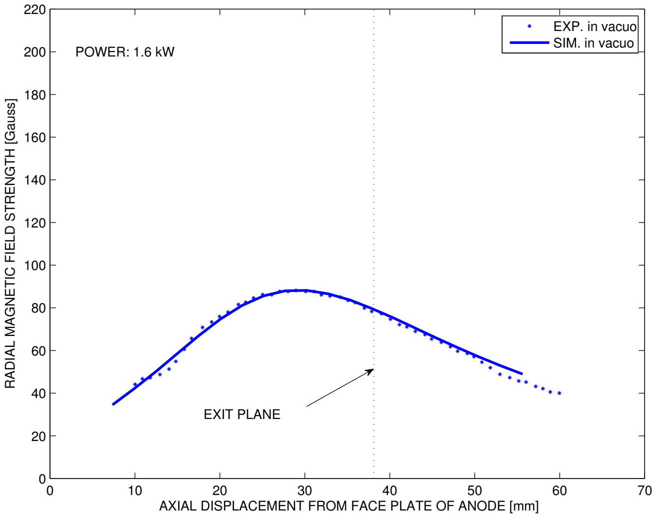

(a) 1.6 kW

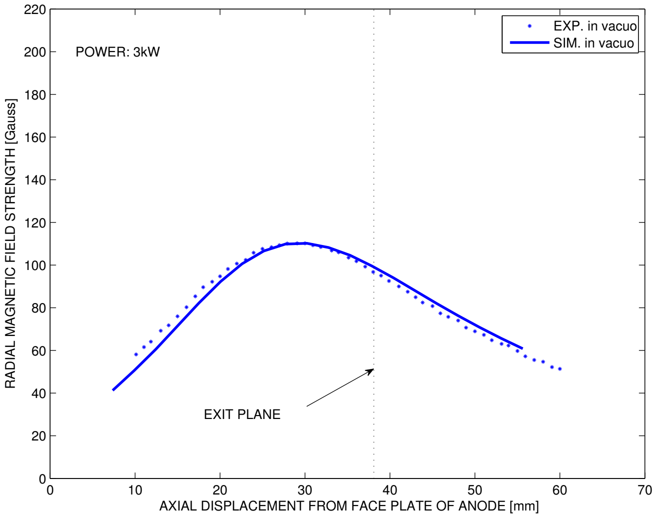

(b) 3.0 kW

Fig. A.5: Validation of MagNet 6 simulation of the radial component of the P5's magnetic field strength at 17.5 mm from the inner wall at 1.6 kW and 3 kW

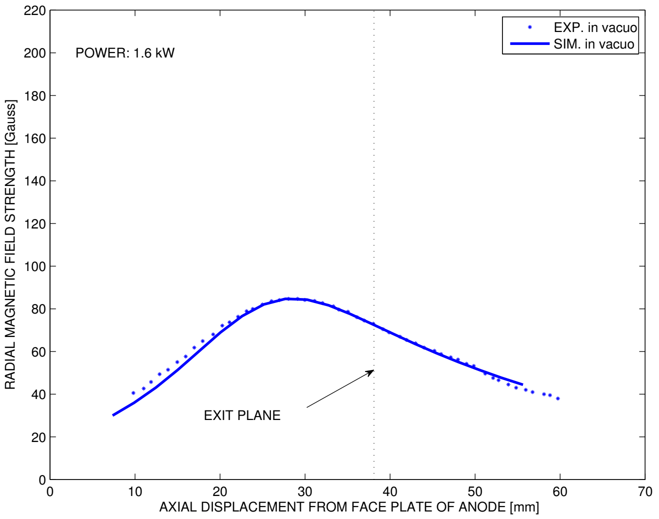

(a) 1.6 kW

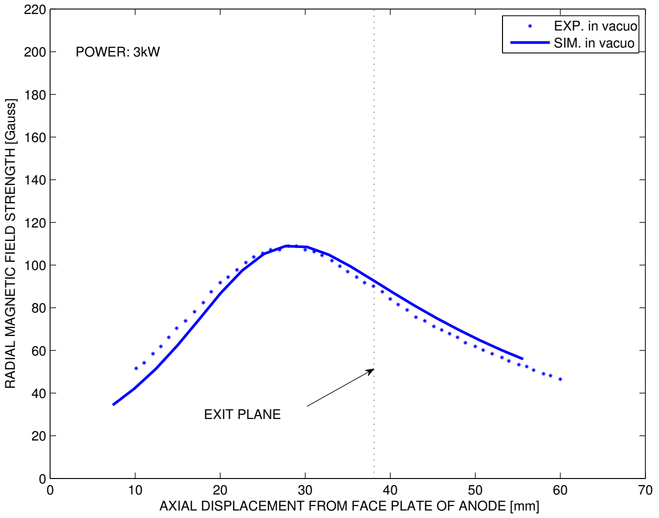

(b) 3.0 kW

Fig. A.6: Validation of MagNet 6 simulation of the radial component of the P5's magnetic field strength at 22.5 mm from the inner wall at 1.6 kW and 3 kW

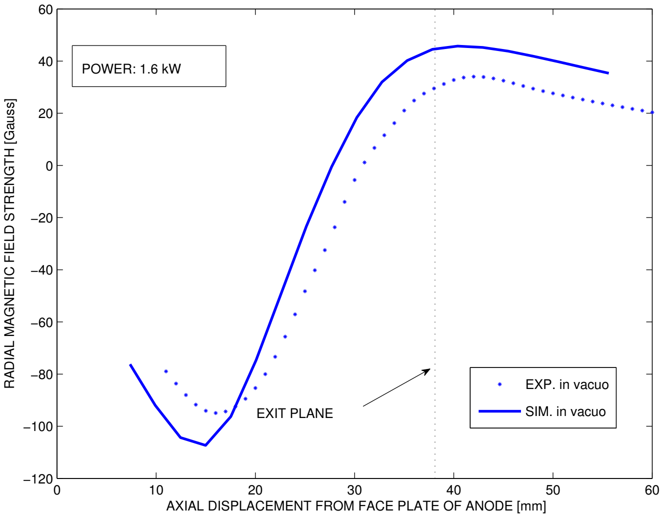

(a) 1.6 kW

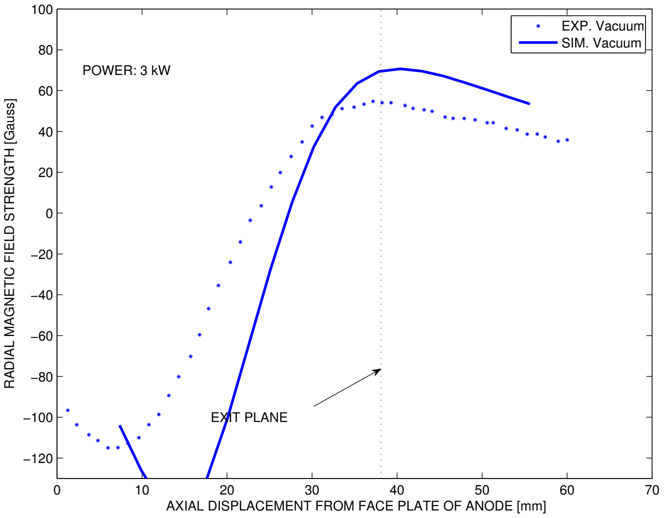

(b) 3.0 kW

Fig. A.7: Validation of MagNet 6 simulation of the axial component of the P5's magnetic field strength at 2.5 mm from the inner wall at 1.6 kW and 3 kW

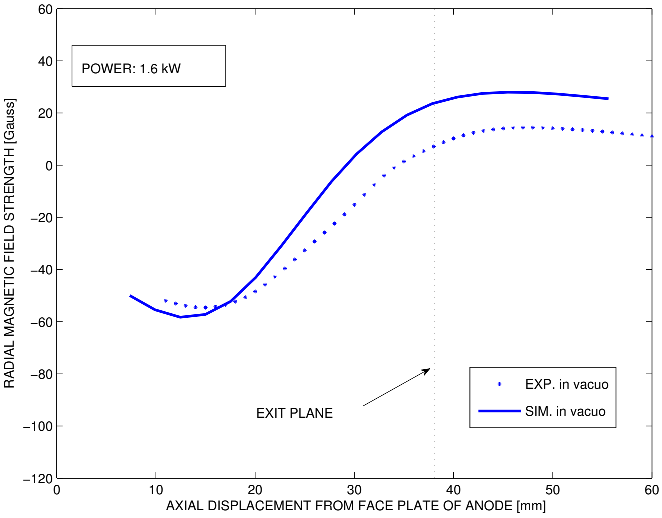

(a) 1.6 kW

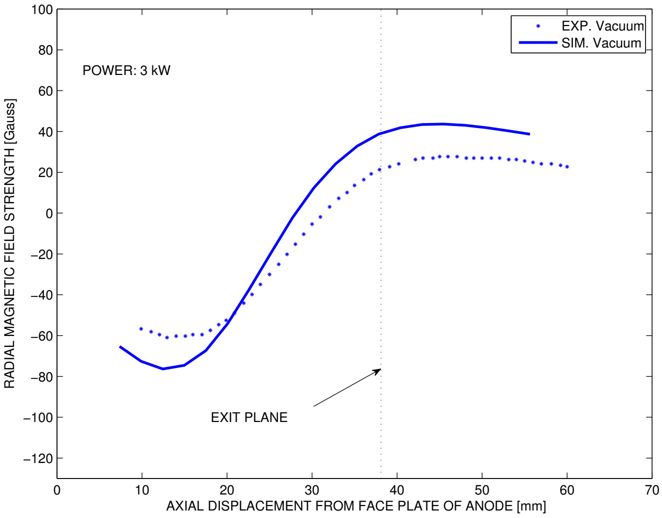

(b) 3.0 kW

Fig. A.8: Validation of MagNet 6 simulation of the axial component of the P5's magnetic field strength at 7.5 mm from the inner wall at 1.6 kW and 3 kW

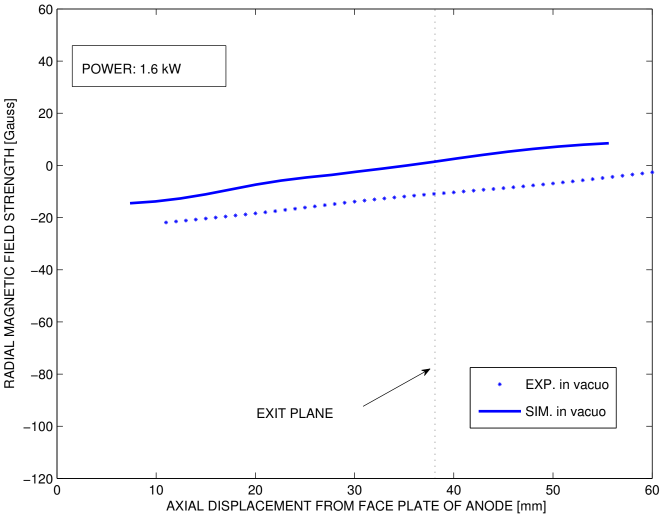

(a) 1.6 kW

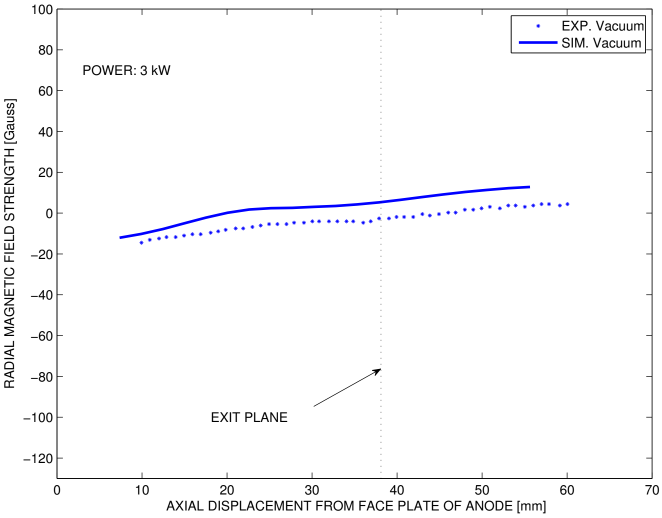

(b) 3.0 kW

Fig. A.9: Validation of MagNet 6 simulation of the axial component of the P5's magnetic field strength at 17.5 mm from the inner wall at 1.6 kW and 3 kW

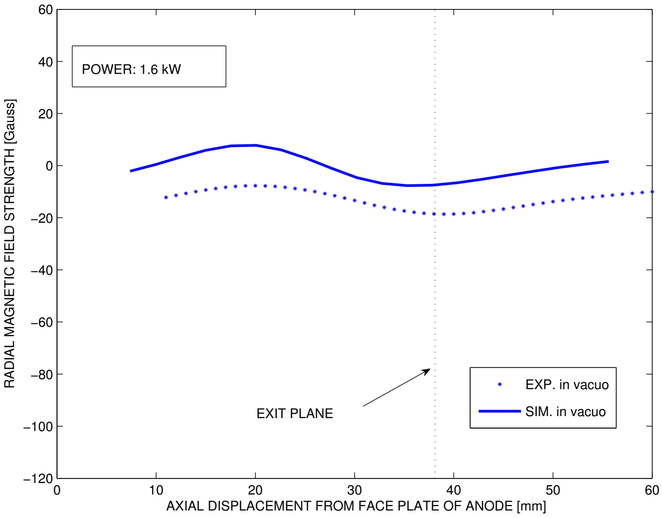

(a) 1.6 kW

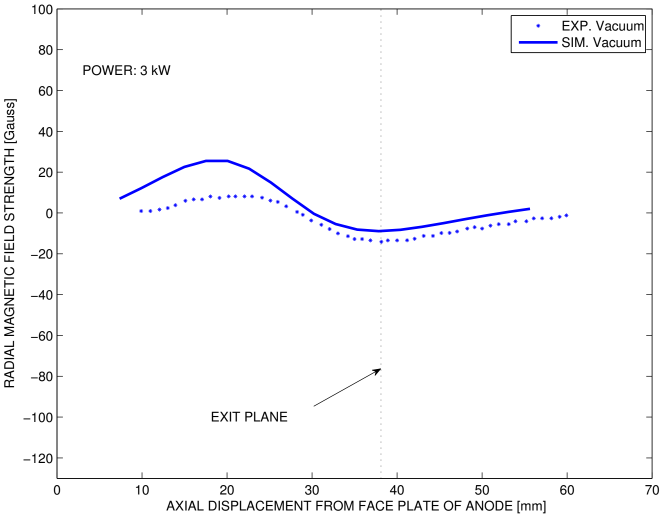

(b) 3.0 kW

Fig. A.10: Validation of MagNet 6 simulation of the axial component of the P5's magnetic field strength at 22.5 mm from the inner wall at 1.6 kW and 3 kW

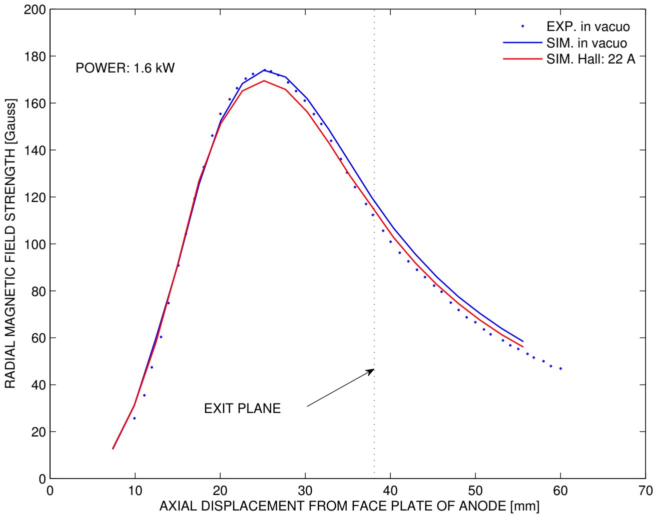

(a) 1.6 kW

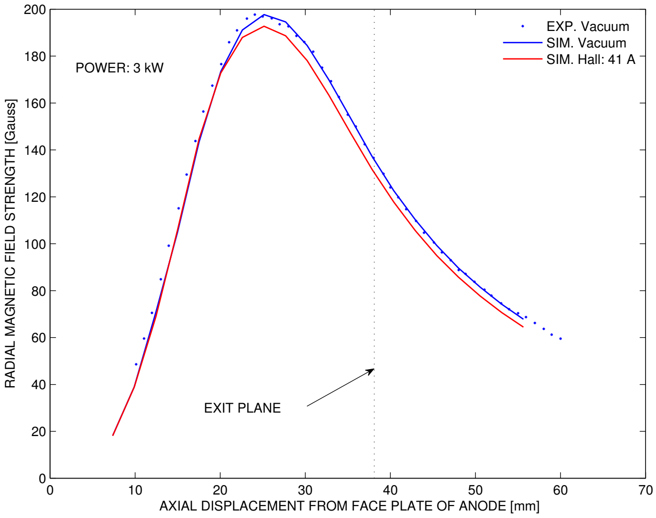

(b) 3.0 kW

Fig. A.11: Effect of the Hall current on the variation of in vacuo radial magnetic field strength in the discharge channel of the P5 at 2.5 mm from the inner wall. The variations are normalized by the maxima of experimental field strengths. The '22 A' and '41 A' labels refer to the integral of the Hall current distributions at 1.6 kW and 3.0 kW, respectively, in the area where its profile has been simulated. Experimental distributions in vacuo [1] are displayed in the figures for the sake of completeness.

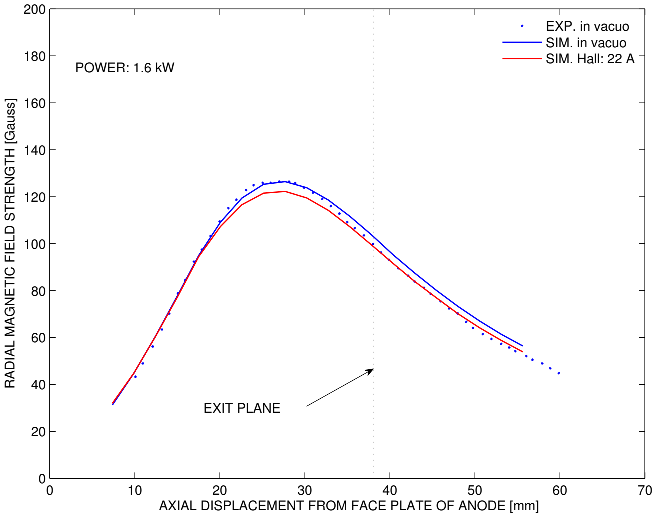

(a) 1.6 kW

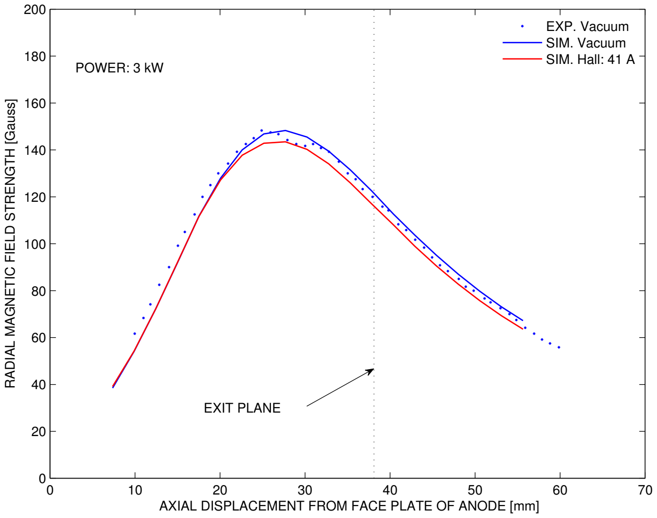

(b) 3.0 kW

Fig. A.12: Effect of the Hall current on the variation of in vacuo radial magnetic field strength in the discharge channel of the P5 at 7.5 mm from the inner wall. The variations are normalized by the maxima of experimental field strengths. The '22 A' and '41 A' labels refer to the integral of the Hall current distributions at 1.6 kW and 3.0 kW, respectively, in the area where its profile has been simulated. Experimental distributions in vacuo [1] are displayed in the figures for the sake of completeness.

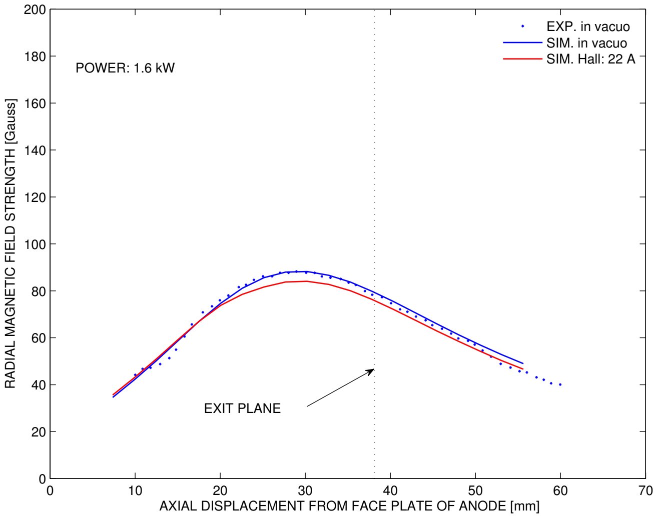

(a) 1.6 kW

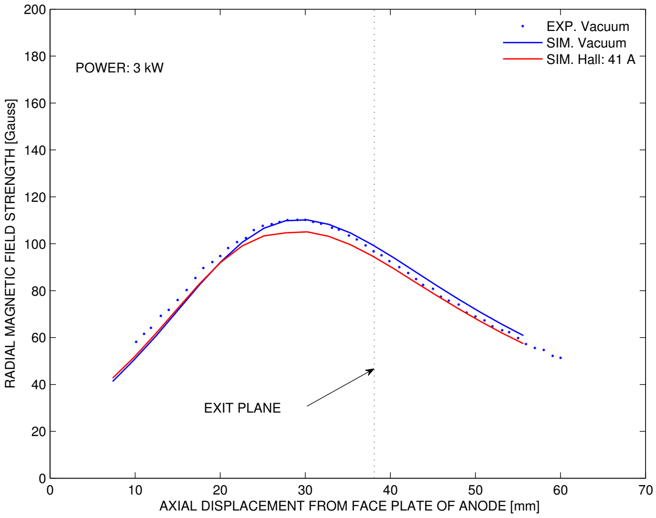

(b) 3.0 kW

Fig. A.13: Effect of the Hall current on the variation of in vacuo radial magnetic field strength in the discharge channel of the P5 at 17.5 mm from the inner wall. The variations are normalized by the maxima of experimental field strengths. The '22 A' and '41 A' labels refer to the integral of the Hall current distributions at 1.6 kW and 3.0 kW, respectively, in the area where its profile has been simulated. Experimental distributions in vacuo [1] are displayed in the figures for the sake of completeness.

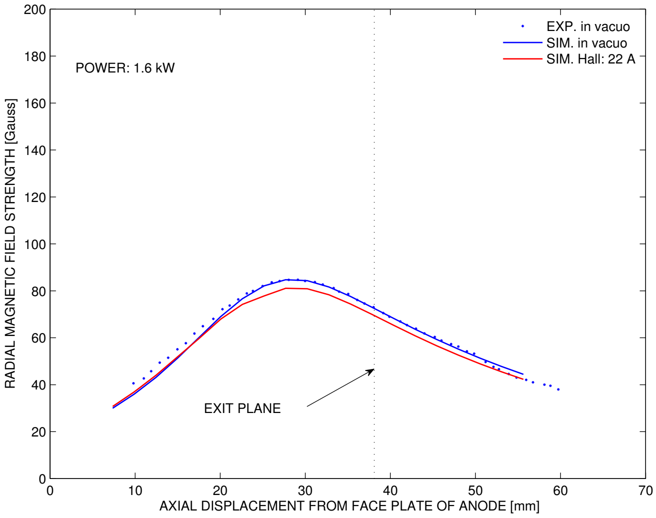

(a) 1.6 kW

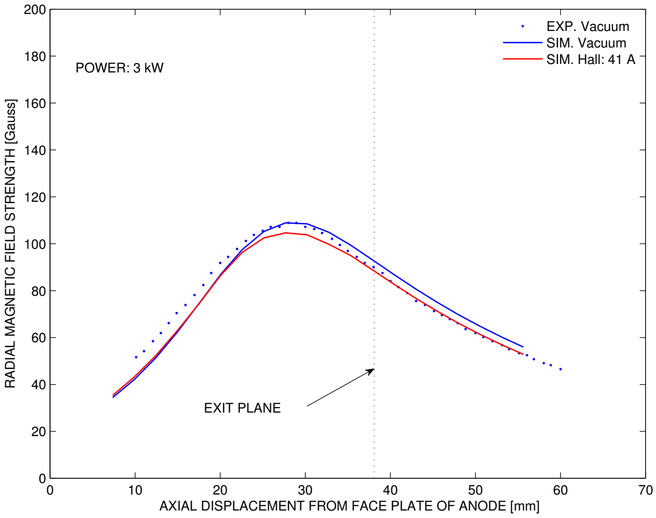

(b) 3.0 kW

Fig. A.14: Effect of the Hall current on the variation of in vacuo radial magnetic field strength in the discharge channel of the P5 at 22.5 mm from the inner wall. The variations are normalized by the maxima of experimental field strengths. The '22 A' and '41 A' labels refer to the integral of the Hall current distributions at 1.6 kW and 3.0 kW, respectively, in the area where its profile has been simulated. Experimental distributions in vacuo [1] are displayed in the figures for the sake of completeness.

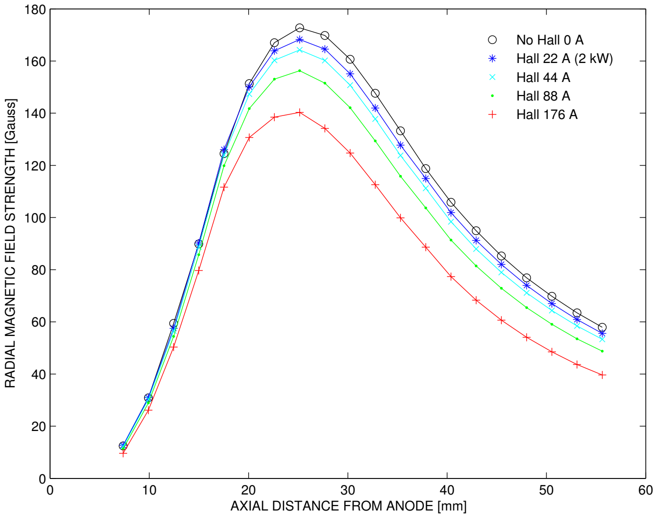

(a) 1.6 kW

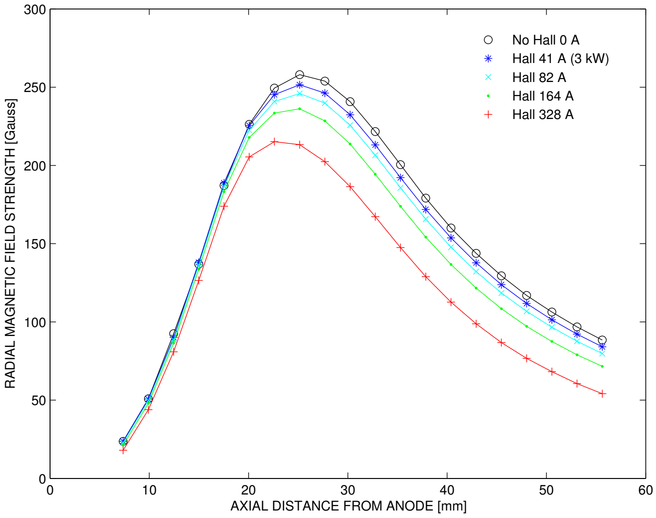

(b) 3.0 kW

Fig. A.15: Effect of the Hall current on the variation of in vacuo radial magnetic field strength in the discharge channel of the P5 at 2.5 mm from the inner wall. The variations are normalized by the maxima of experimental field strengths. Five different Hall current settings are considered: each results from scaling the Hall current distribution associated with the 1.6 kW (22 A) and 3 kW (41 A) power settings by 1, 2, 3, and 4. Experimental distributions in vacuo [1] are displayed on the figure for the sake of completeness.

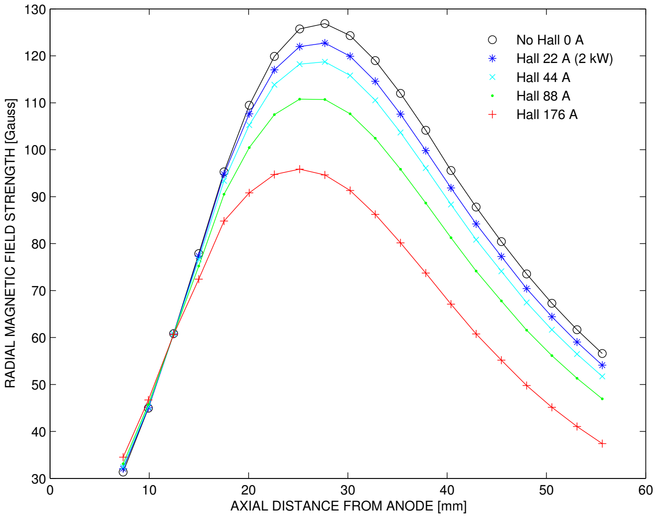

(a) 1.6 kW

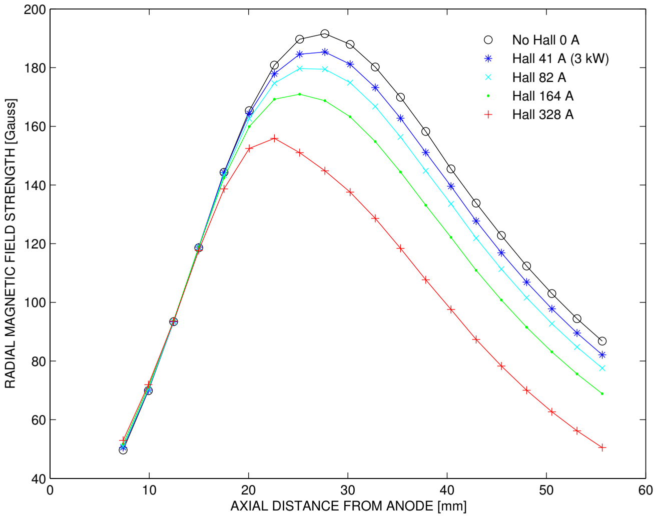

(b) 3.0 kW

Fig. A.16: Effect of the Hall current on the variation of in vacuo radial magnetic field strength in the discharge channel of the P5 at 7.5 mm from the inner wall. The variations are normalized by the maxima of experimental field strengths. Five different Hall current settings are considered: each results from scaling the Hall current distribution associated with the 1.6 kW (22 A) and 3 kW (41 A) power settings by 1, 2, 3, and 4. Experimental distributions in vacuo [1] are displayed on the figure for the sake of completeness.

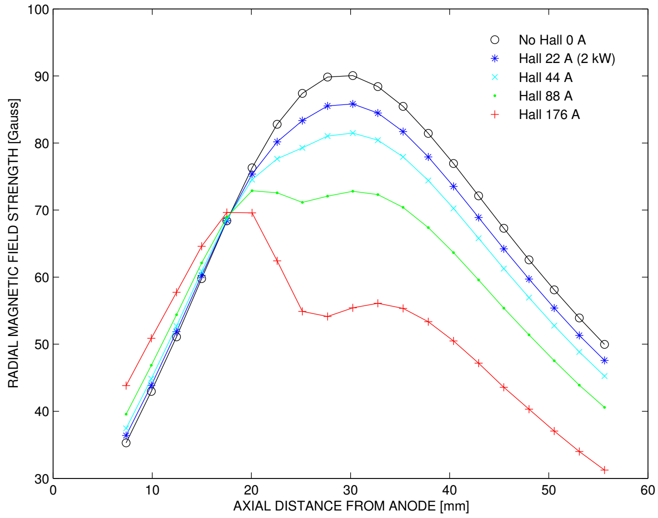

(a) 1.6 kW

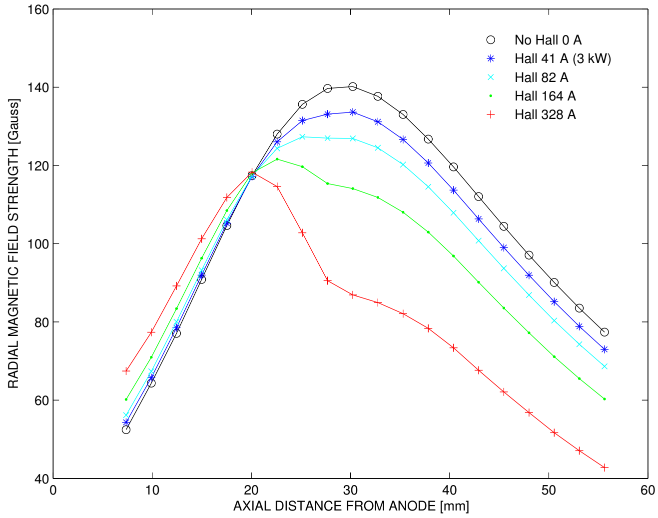

(b) 3.0 kW

Fig. A.17: Effect of the Hall current on the variation of in vacuo radial magnetic field strength in the discharge channel of the P5 at 17.5 mm from the inner wall. The variations are normalized by the maxima of experimental field strengths. Five different Hall current settings are considered: each results from scaling the Hall current distribution associated with the 1.6 kW (22 A) and 3 kW (41 A) power settings by 1, 2, 3, and 4. Experimental distributions in vacuo [1] are displayed on the figure for the sake of completeness.

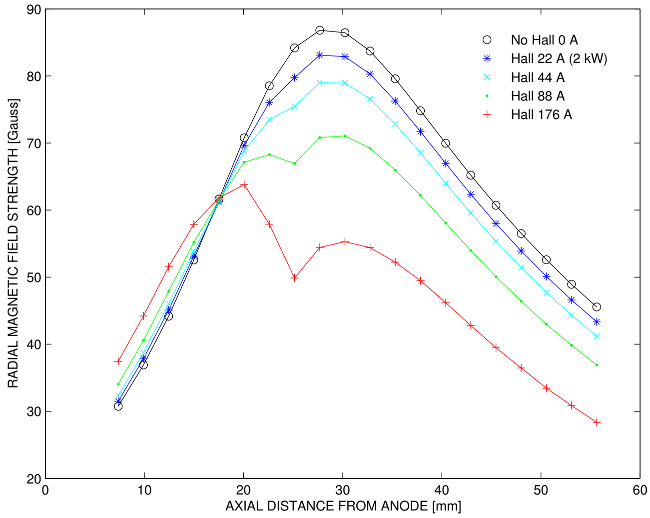

(a) 1.6 kW

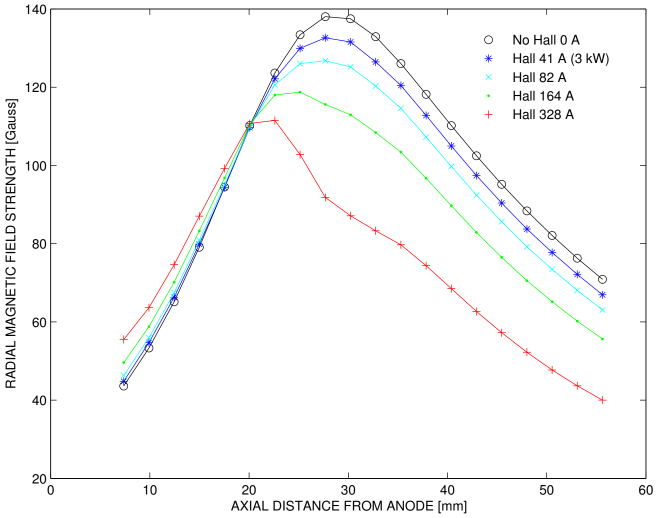

(b) 3.0 kW

Fig. A.18: Effect of the Hall current on the variation of in vacuo radial magnetic field strength in the discharge channel of the P5 at 22.5 mm from the inner wall. The variations are normalized by the maxima of experimental field strengths. Five different Hall current settings are considered: each results from scaling the Hall current distribution associated with the 1.6 kW (22 A) and 3 kW (41 A) power settings by 1, 2, 3, and 4. Experimental distributions in vacuo [1] are displayed on the figure for the sake of completeness.

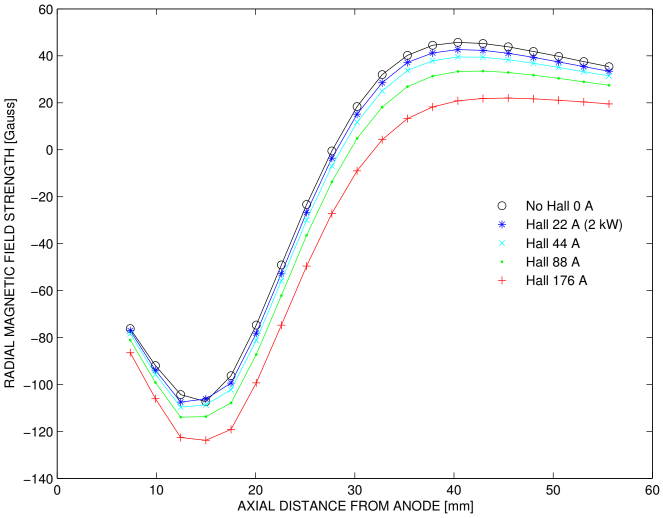

(a) 1.6 kW

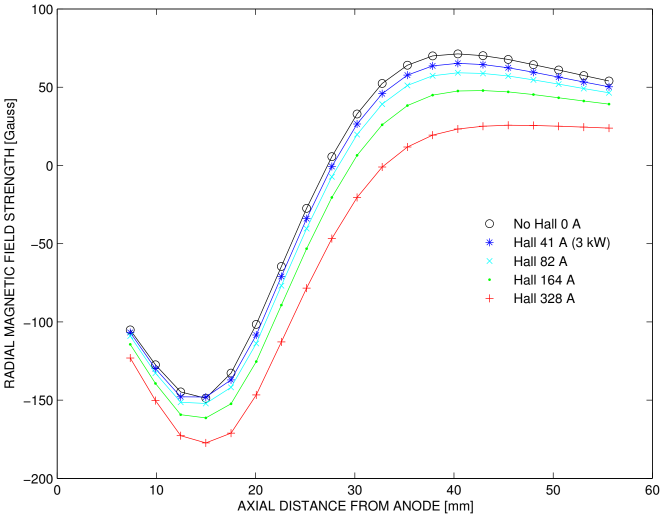

(b) 3.0 kW

Fig. A.19: Effect of the Hall current on the variation of in vacuo axial magnetic field strength in the discharge channel of the P5 at 2.5 mm from the inner wall. The variations are normalized by the maxima of experimental field strengths. Five different Hall current settings are considered: each results from scaling the Hall current distribution associated with the 1.6 kW (22 A) and 3 kW (41 A) power settings by 1, 2, 3, and 4. Experimental distributions in vacuo [1] are displayed on the figure for the sake of completeness.

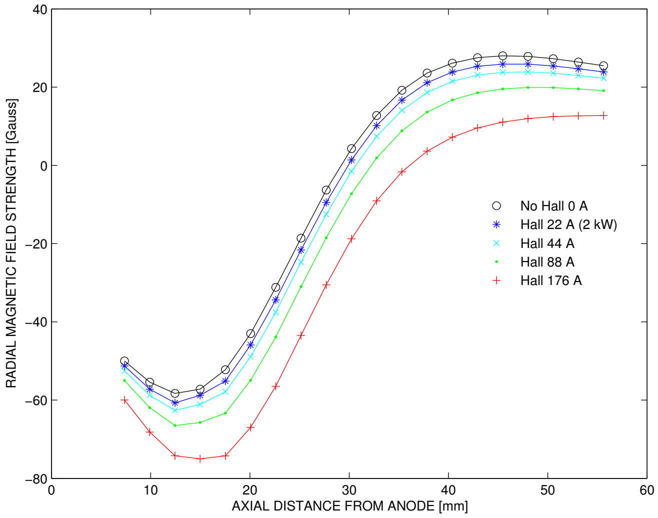

(a) 1.6 kW

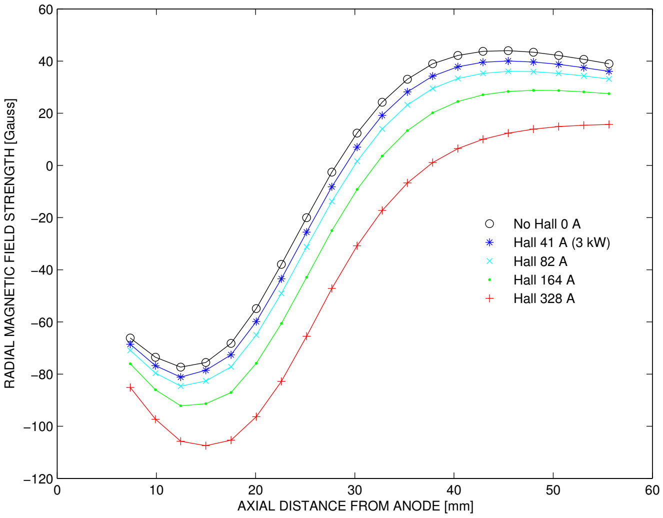

(b) 3.0 kW

Fig. A.20: Effect of the Hall current on the variation of in vacuo axial magnetic field strength in the discharge channel of the P5 at 7.5 mm from the inner wall. The variations are normalized by the maxima of experimental field strengths. Five different Hall current settings are considered: each results from scaling the Hall current distribution associated with the 1.6 kW (22 A) and 3 kW (41 A) power settings by 1, 2, 3, and 4. Experimental distributions in vacuo [1] are displayed on the figure for the sake of completeness.

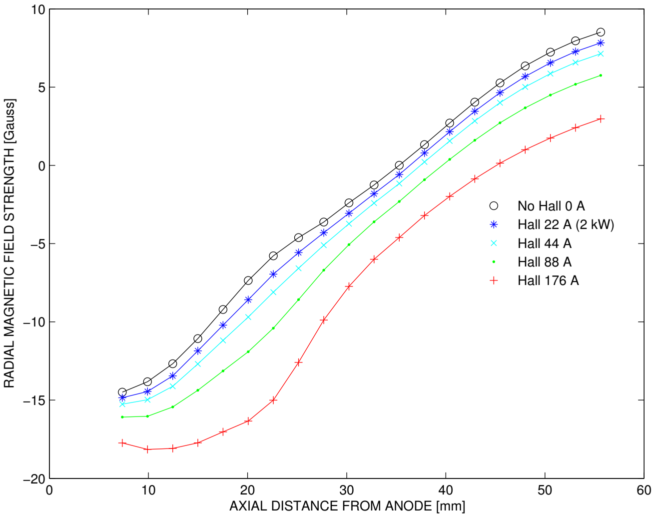

(a) 1.6 kW

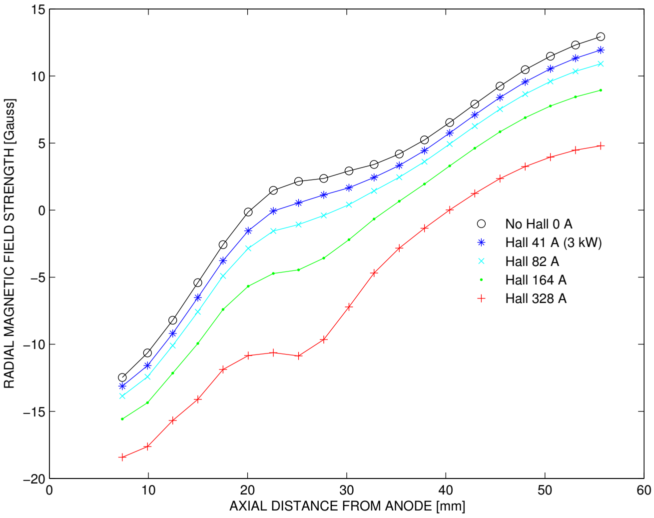

(b) 3.0 kW

Fig. A.21: Effect of the Hall current on the variation of in vacuo axial magnetic field strength in the discharge channel of the P5 at 17.5 mm from the inner wall. The variations are normalized by the maxima of experimental field strengths. Five different Hall current settings are considered: each results from scaling the Hall current distribution associated with the 1.6 kW (22 A) and 3 kW (41 A) power settings by 1, 2, 3, and 4. Experimental distributions in vacuo [1] are displayed on the figure for the sake of completeness.

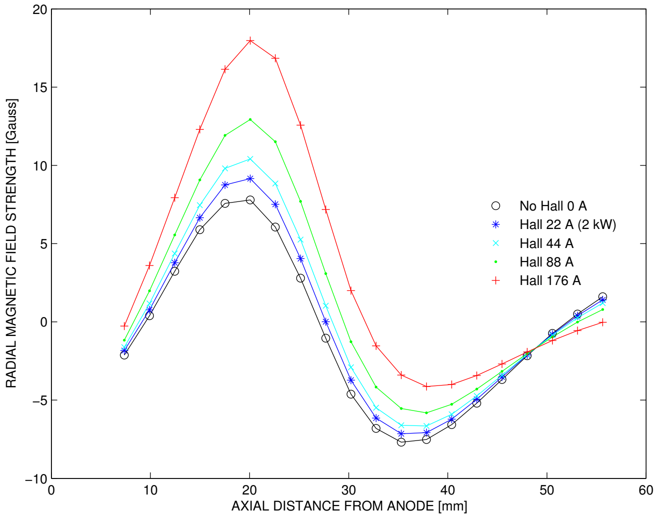

(a) 1.6 kW

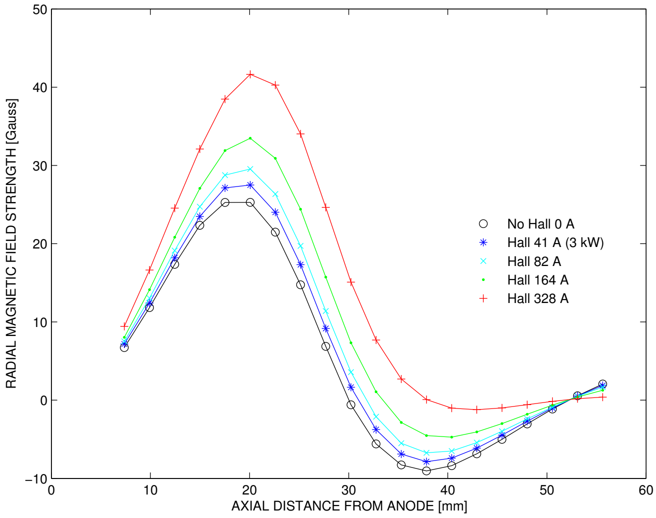

(b) 3.0 kW

Fig. A.22: Effect of the Hall current on the variation of in vacuo axial magnetic field strength in the discharge channel of the P5 at 22.5 mm from the inner wall. The variations are normalized by the maxima of experimental field strengths. Five different Hall current settings are considered: each results from scaling the Hall current distribution associated with the 1.6 kW (22 A) and 3 kW (41 A) power settings by 0, 1/2, 3, and 4. Experimental distributions in vacuo [1] are displayed on the figure for the sake of completeness.

APPENDIX B

High resolution measurement of the detuning of the laser frequency from the center-wavelength of an absorption spectrum

In this appendix, we describe the Fabry-Perot interferometer and illustrate how it can be used to resolve with high precision an absorption spectrum on the frequency scale instead of relying on a traditional low-resolution (1 pm) wavemeter (WA-1000 from Burleigh) for measuring the wavelength of a diode-laser.

A Confocal Fabry-Perot interferometer (FPI) is a simple and high-precision device when used for accurately resolving spectra on a frequency-scale. An SA^{PLUS} FPI (from Burleigh Instruments, Inc.) was used for generating all spectra reported in this thesis.

- an upstream four-axis mount with translation and tilt stages that houses a small disk with an input aperture and a converging lens
- a set of two spherical partially transmitting mirrors set up in a variable length cavity configuration
- a photodiode sensor at the downstream end of the system

In what follows, we summarize the FPI's principle of operation based on descriptions in presented in the model's operating manual [2] and in Hernandez [67] and The device operates based on the well-known interference property of light. When a light beam is aligned with the instrument's axis of symmetry, it propagates through a focusing lens located immediately downstream of its input aperture, gets transmitted through the upstream concave

$$2nd\cos\theta = m\lambda. \tag{B.1}$$

Constructive interference (or resonnance) is necessary for transmission of the standing wave through the downstream mirror. At resonnance, a standing wave gets transmitted accross the downstream mirror and reaches a photodiode sensor (Figure 2.1(b) (8)). When the intensity of the transmitted light exceeds the detection threshold of the sensor, the optical signal gets converted to an electrical signal, whose voltage is subsequently amplified and noise-filtered by a detector amplifier (DA).

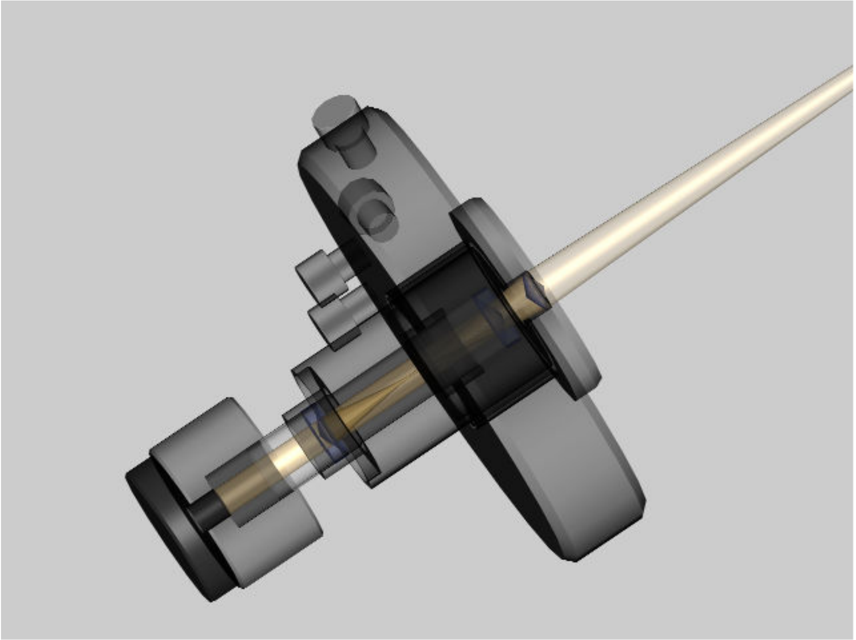

(a) Isometric view

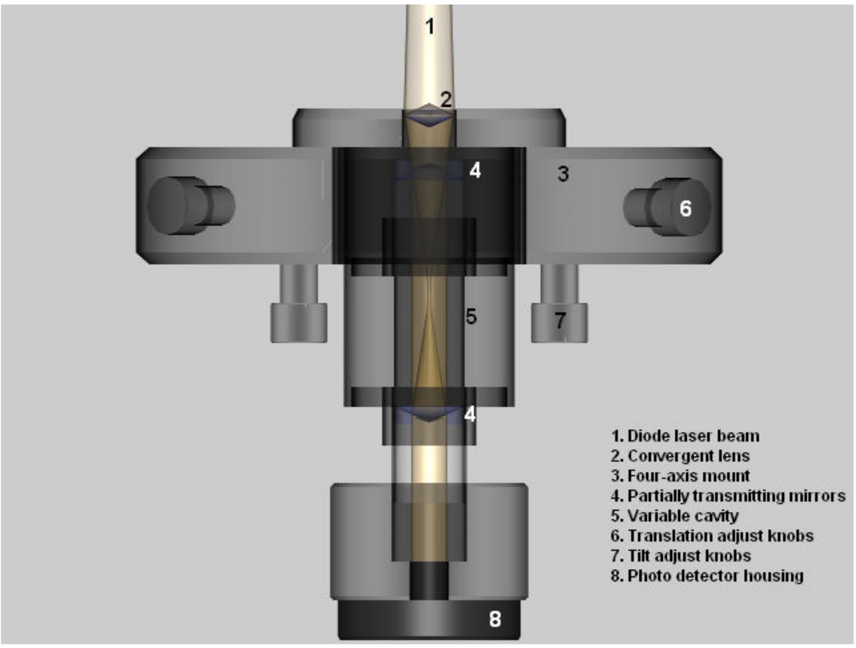

(b) Top view

Fig. B.1: Sketch of a confocal Fabry-Perot Interferometer

The laser frequency is varied by passing light from a diode through a diffraction grating element reposing on a rotational stage (Figure B.2). By applying a voltage to a piezo-electric transducer (PZT) that presses against the grating's stand, remote control of the laser wavelength is achievable via a ramp-voltage generator or Scan Controller (SC) unit encased within the main DL controller box. The SC can apply up to 40-Volt-magnitude voltage ramps to the PZT. Figure B.3 illustrates the voltage output of the PFI as function of SC voltage.

To help better appreciate the advantage of using the FPI, we introduce the following few key terms. We will use Figure B.3 as an illustration. Each peak on the figure corresponds to a principal interference mode m. The thinner the peaks and the longer the frequency difference between them, the better the rating or performance of the interferometer in matching the linewidth of laser operating at its maximal Mode-hop-free range (MHFR). More specifically, the following three parameters [67] serve to evaluate how well a single-mode laser spectrum has been rendered:

- The finesse (F), which is dependent on the reflectivity of the mirrors. The mirrors used in this experiment have a finesse exceeding 300.
- The free-spectral range (frequency separation between consecutive peaks) depends on the radius of the mirrors making up the cavity. When properly spaced and aligned, the FSR matches that of the DL (2 GHz).
- The resolution, which combines the above parameters through the ratio: $R = FSR/F$. Based on FSR and F values associated with the SA^{PLUS}, the FPI is able to resolve a spectrum to within 6.7 MHz (or 0.016 pm)—roughly corresponding to $1/50^{th}$ of the WA-1000 wavemeter's resolution.

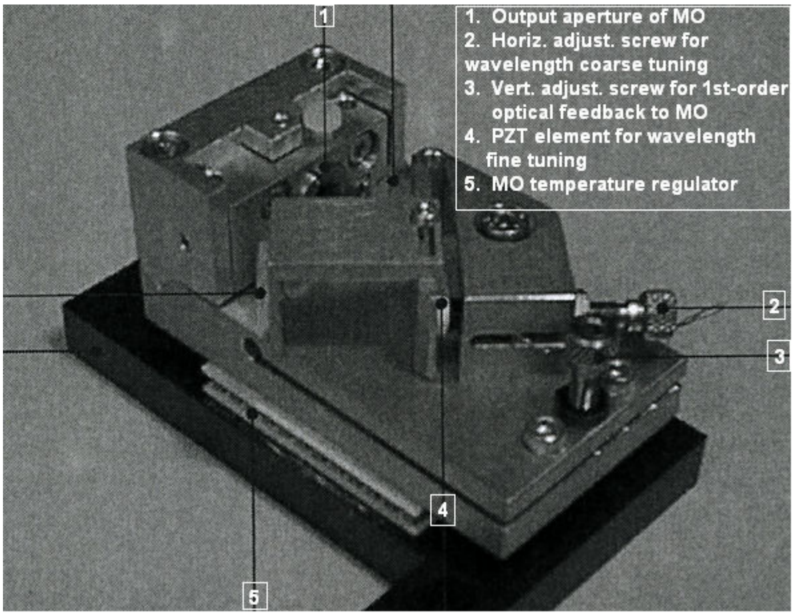

Fig. B.2: Description of the Master Oscillator component in the Diode Laser system [2]

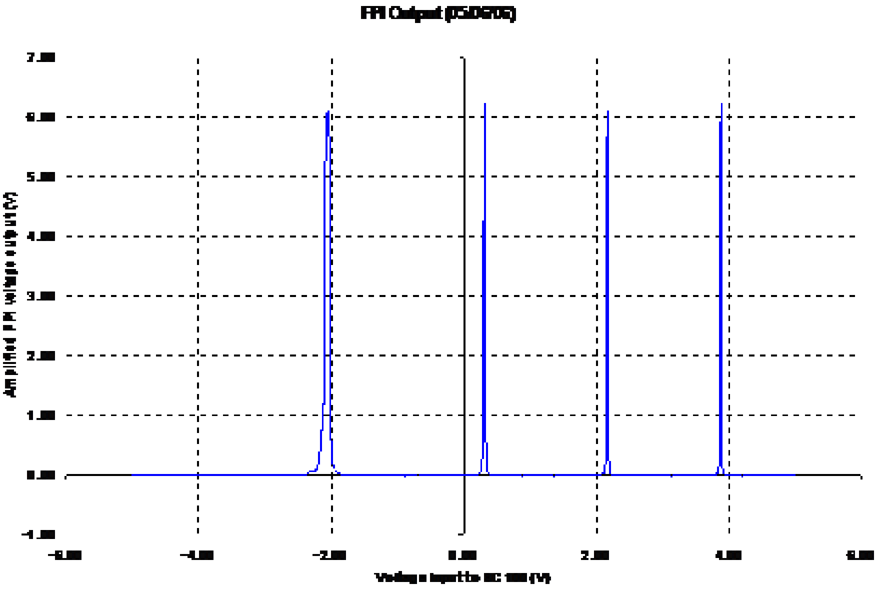

Fig. B.3: Variation of FPI voltage output of the laser's linewidth with PZT voltage

The next Based on the FPI's resolution reported above, one deduces that full-mode matching of the DL's FSR is possible to within 0.33 %. Such accuracy permits the use of outputted interference peaks as high-resolution frequency markers for absorption or emission spectra. Figure B.4 illustrates the procedure for frequency scaling from on a third-order polynomial fit of the laser lineshape over PZT voltage of frequencies associated with interference fringes' maxima; the reduced lineshape is reported in

- the laser power is higher at lower frequencies
- the high-gain setting of the DA-100 leads to clipping of any signal whose amplification leads to voltage outputs exceeding 6 V
- the non-linearity of the PZT response is more pronounced in the low voltage regime; hence the laser frequency changes over a broader voltage range in this regime

The clipping can be remedied to by reducing the gain setting on the DA-100. However, its monitoring during fine-tuning of the cavity-spacing is a great way to optimize its spacing; which, in turn, permits better monitoring and control of the laser's MHFR by varying the master oscillator's temperature and current, changing the DC current offset on the PZT, and feeding the grating forward (recall Figure B.2). Figure B.4 summarizes the result of these efforts as the number of interference fringes increased from 4 to 6; quantitatively, this corresponds to an increase of the MHFR from about 8 GHz to 12 GHz—an almost perfect match with the DL's specifications for optimal "grating fine tuning" [68].

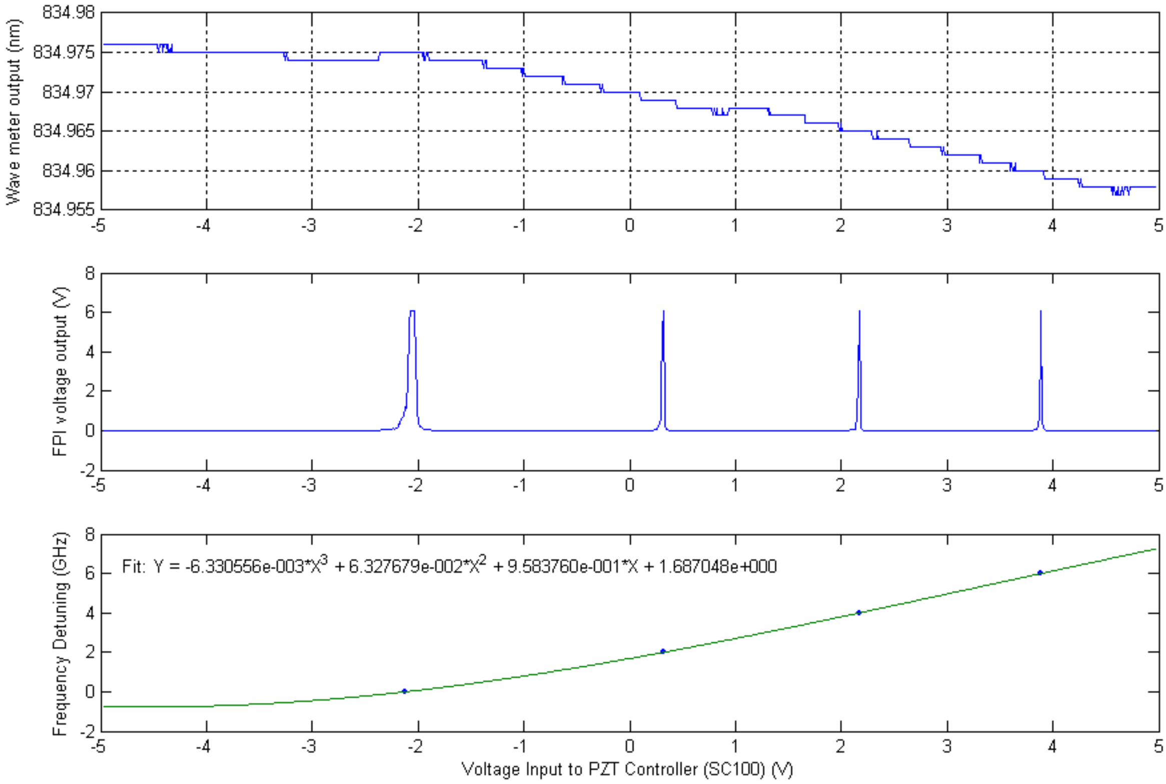

Fig. B.4: Procedure for relating the diode-laser's piezo electric transducer's voltage to its frequency detuning from some center-value at which a resonnant atomic transition of interest occurs. The sub-figures respectively illustrate the wavemeter's output (top), FPI voltage output of the laser linewidth (middle), and the analytical approach for converting PZT voltage to laser frequency (bottom)

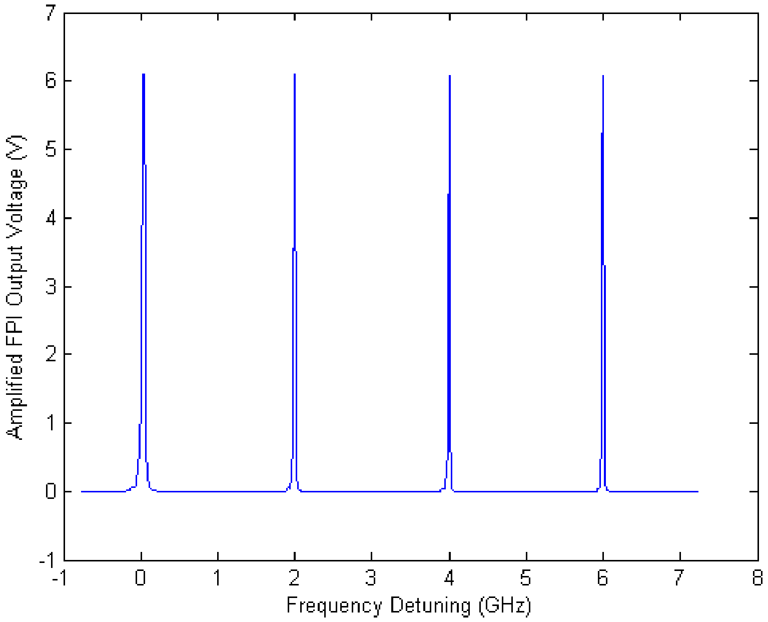

(a) 4 fringes

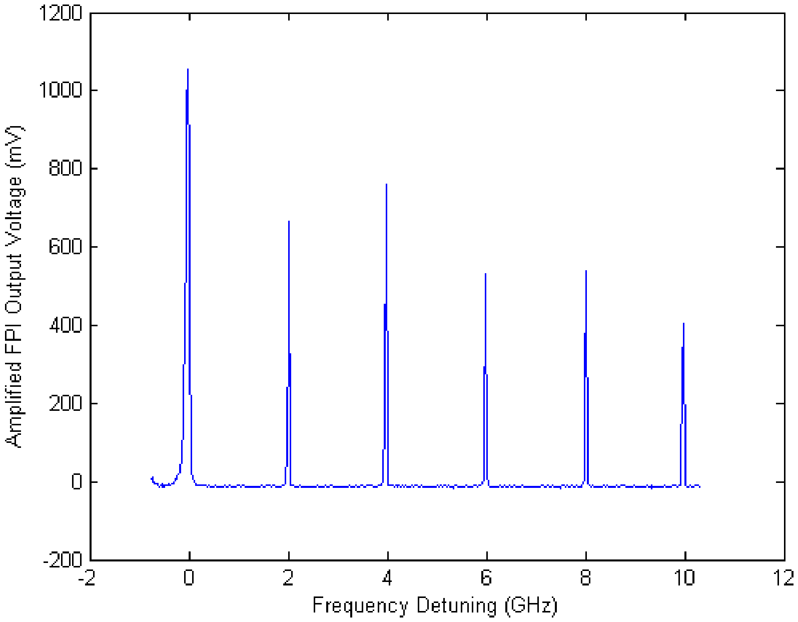

(b) 6 fringes

Fig. B.5: Comparison of laser spectra resolved on the frequency scale illustrating the effect of optimizing the laser's Master Oscillator to extend its mode-hop-free range

APPENDIX C

Motivation for relying on the 834.911 nm line in computing magnetic field strengths

Based on the high-resolving power of the FPI and on the method reported in Appendix B for converting absorption spectra from PZT voltage scale to frequency scale, we patch successive spectra, to show in Figure C.2 why the 834.911 nm was chosen in the place of neighboring lines in the narrow NIR range of the diode-laser.

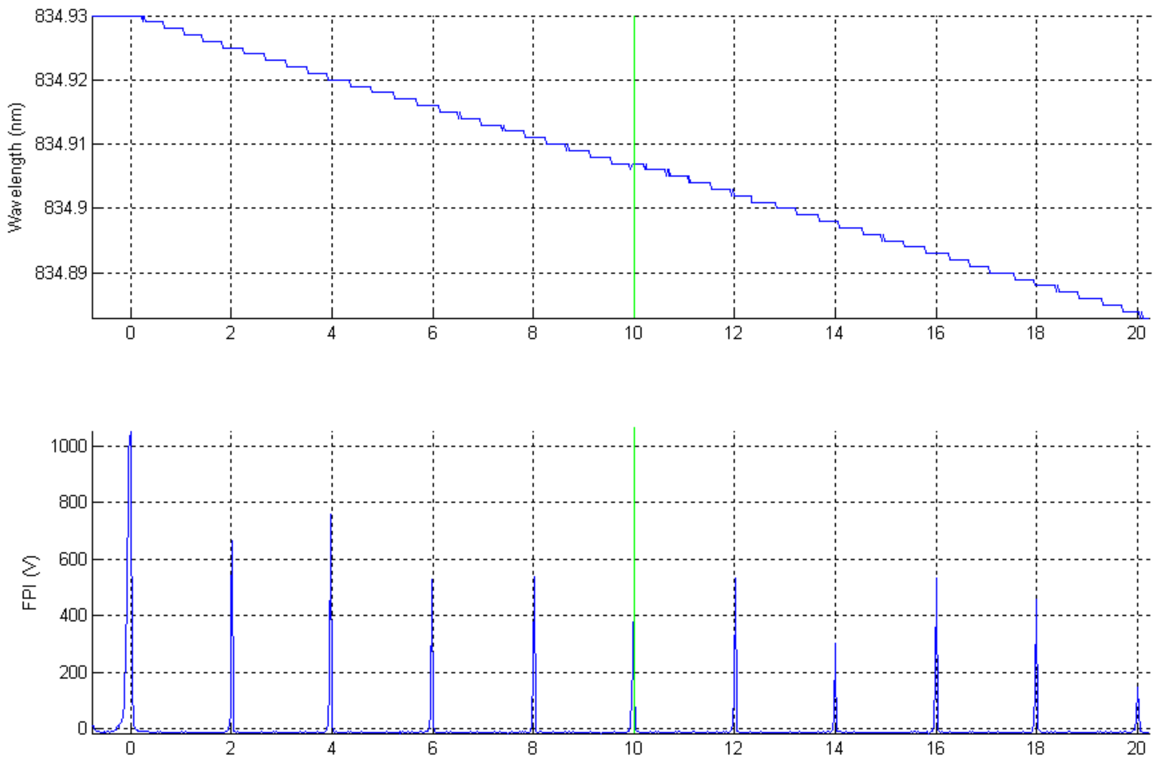

Fig. C.1: Spectral patching between two consecutive mode-hop-free ranges

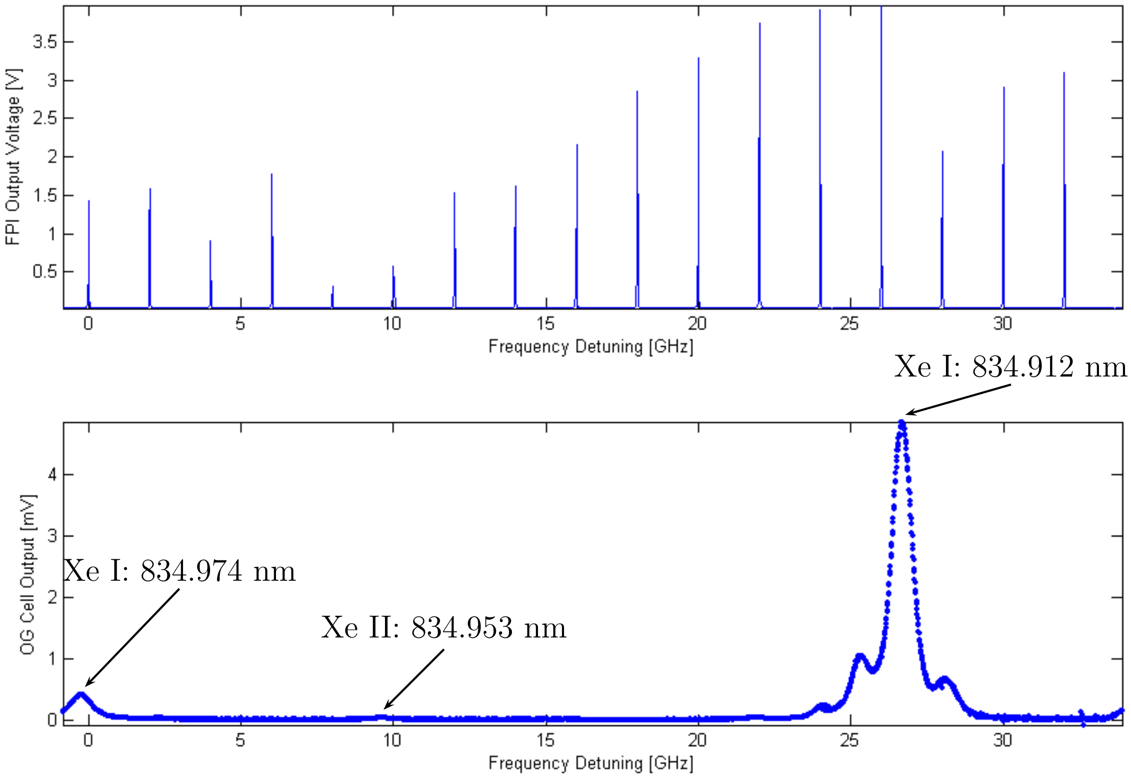

Fig. C.2: Illustration of the relative strength of the 834.912 nm (in vacuum) of the absorption of neutral xenon compared to other neighboring lines in the NIR

APPENDIX D

Non-linear Least-squares Fitting of Spectra of Xe I Plasma Particles by Solving for External Magnetic Field Strength and Plasma Kinetic Temperature - header files

Magnetic field strength (H) and kinetic temperature (T) solver - header files

Main solver for H and T
‘BTsolverZHFS.m’

```
clear all
close all

% DATA LOADING
Drive = input('Select drive, H or M: ');
MainDIR = [Drive ':\ThesisWork\H6BTsolver\'];
DataFolder = 'LIFdata\sigma';
ResultsFolder = 'LaTeXoutput';

% Add LIF data path
  DataPath = [MainDIR DataFolder];
  addpath(DataPath);

% Add output path
  OutputPath = [MainDIR ResultsFolder];
  addpath(OutputPath);
  Format = ['-' input('Enter output file format: ')];

% Extract files
  FileNames = dir([MainDIR DataFolder '\S*.txt']);
  NumFiles = length(FileNames); %NumFiles = 1;
```

```

% Load averaged optimized physical parameters
  %load Xopt; % solutions from pre-optimization
  Skip = [];
  run PhysicalConstantsOptimAvg;
  run Level1_InputsOptimAvg;
  run Level2_InputsOptimAvg;
  run IsotopesParametersOptimAvg;

% SOLVING FOR MAGNETIC FIELD STRENGTH AND TEMPERATURE-------------
  % Pick initial values and upper and lower bound values for
  % solver input
    % Kinetic temperature
      Tmin = 75; To = 150; Tmax = 300;
    % Magnetic field strengths
      Hmin = 100 ; Ho = 175; Hmax = 300;
    % Set solver inputs
      Xo = [Ho To]; Xup   = [Hmax Tmax]; Xlow = [Hmin Tmin];

 % Initializations
  f = 0; % Figure numbering
  Hsol_Arr = zeros(1,NumFiles); % Field strength solutions
  Tsol_Arr = zeros(1,NumFiles); % Temparature solution
 % Loop through LIF data files
for i=1:NumFiles
    MyId = i; % Variable name change for convenience
    % Plot experimental data

        % Extract frequency detuning data, opto-galvanic and LIF
        % spectra, and at each radial location
          [R, NUexp0, NUexp, I_lif, In_lif, I_og, In_og] = ...
          FunDATAreduction(FileNames, i, MainDIR, DataFolder);

    f = f + 1;
    figure(f)
    LIF = plot(NUexp0, I_lif); hold on
    OG =  plot(NUexp0, I_og, ':');

    xlabel('Frequency detuning [GHz]')
    ylabel('Intensities (scaled by maxima)')
    title(['LIF spectrum at exit plane at R = ' ...
           sprintf('%1.0f', R)...
           'mm from thruster centerline'])
    legend('LIF', 'OG')

    % Solve for kinetic temperatures and magnetic field strengths
      % Set solver option: to show output
        options = optimset('Display','iter');
      % Variable name change for convenience
        IexpN = In_lif;
      % Call solver
        [Xsol,Resnorm,FVAL,EXITFLAG,OUTPUT,LAMBDA,JACOB] = ...
            lsqnonlin...
        (@FUN_ZHFSforBT, Xo, Xlow, Xup, options, IexpN, NUexp,...
```

```
         MyId, Skip);
      % Extract solutions and store them
        H = Xsol(1); Hsol_Arr(MyId) = H; % magnetic field strength
        T = Xsol(2); Tsol_Arr(MyId) = T; % kinetic temperature

% COMPARE EXPERIMENTAL SPECTRA WITH SIMULATED SPECTRA BASED ON
% SOLVER'S OUTPUT OF SOLUTIONS

% Simulate line spectra of isotopes with no nuclear spin
  run NoHFsLines;

% Simulate line spectra of isotopes with no nuclear spin
  [Dummy,N1] = size(WithHFS);
  II = WithHFS(2,:); % nuclear spin quantum numbers
  gI = WithHFS(9,:); % Lande-g factor of nucleus

  run SigmaZHFS;

  % shift frequency of lines about weighted mean and combine line
  % spectra of all isotopes
    center = sum(dEhz_sig .* IntenHZiso_sig)/ sum(IntenHZiso_sig);
    x_lines  = FunCmtoGHz([dENoHFSiso_sig; dEhzIso_sig - center]);
    y_lines  = [IntenNoHFSiso_sig; IntenHZiso_sig]; ...
        N = length(x_lines);

 % Apply Voigt profile
   run Lorentzian;
   run Doppler;
   run Convolution;

 % Compare simulated and experimental spectra
   f = f + 1;
   figure(f)
   plot(NUexp, Warm,'LineWidth', 1.5, 'color', 'r'), hold on
   plot(NUexp, IexpN, '*','MarkerSize', 1, 'color', 'k') ;
   axis tight;

   % Display solutions on graphs
     StringH = ['H^{*} = ' sprintf('%1.0f', H) ' G'];
     StringT = ['T^{*} = ' sprintf('%1.0f', T) ' K'];
     Ceiling = max(IexpN);
     text(-4.9, .75*Ceiling, ...
         ['SOLUTIONS AT R = ' num2str(R) 'mm'] )
     text(-4.9, .7*Ceiling, StringH);
     text(-4.9, .65*Ceiling, StringT);

   % Labeling of axes and legend
     xlabel ('FREQUENCY DETUNING (GHz)');
     ylabel ('NORMALIZED SPECTRA');
     title(...
    'LIF FITTING OF XeI ABOUT 834.682 nm AT EXIT PLANE OF THE H6')
     legend('Z-HFS Model','Experiment');

  %  LaTeX output
```

```
    switch Format
        case '-dtiff'
            Ext = 'tiff';
        case '-depsc'
            Ext = 'eps';
    end
    File = [OutputPath '\LIFsigma' num2str(R) 'mm.' Ext];
    print(gcf, Format, File);
end
```

Experimental data loader and reducer ‘FunDATAreduction.m’

```matlab
function [R, NUexp0, NUexp, I_lif, In_lif, I_og, In_og] = ...
         FunDATAreduction(FileNames, i, MainDIR, DataFolder)

% Load data file
FileName = [FileNames(i).name];
Data = load(FileName);

% Identify radial location
R = str2double(FileName(7:8));

% Extract frequency and intensity values of spectra
NUexp0 = (1.e-9)*Data(:,1); % convert to GHz
I_lif = Data(:,2);          % LIF signal strength
I_og = Data(:,3);           % OG signal strength

% Normalize intensities
In_lif = FunNormTrap(NUexp0, I_lif);
In_og = FunNormTrap(NUexp0, I_og);

% Shift frequencies about weighted mean frequency
NUmean = FunTrapIntegral(NUexp0, NUexp0.*In_lif)...
        /FunTrapIntegral(NUexp0, In_lif);
NUexp = NUexp0 - NUmean;
```

Initialization scripts:

- 'Level1InputsOptimAvg.m'

```
%—————————————————Level 1 (upper Level) quantum constants——————————————

% Angular monentum quantum number.
  J1 = 1;

% Lande—g value.
  % Loading Lande—g value from pre—optimization program
  load gj1avg
  % Storing loaded vaue
  gj1 = gj1avg;
```

- ‘Level2InputsOptimAvg.m’

```
%------------Constants of Quantum state 2 (lower Level)----------

% Angular monentum quantum number.
  J2 = 2;

% Lande-g value.
  % Loading Lande-g value from pre-optimization program
    load gj2avg
  % Storing loaded vaue
    gj2 = gj2avg;
```

- ‘PhysicalConstantsOptimAvg.m’

```
%% Computing larmor precession ratio
AlphaInv = 137.035999679;          % Fine structure constant
m = 9.10938215 * 1.e-28;           % electron mass (grams)
c = 2.99792458*1.e10;              % vacuum speed of light (cm/s)
h = 6.62606896 * 1.e-27;           % Planck's constant erg s

den = (4*pi*c^2)*m;

e = sqrt((h*c/(2*pi)) / AlphaInv);

o = e/den; % cm^-1               % Larmor precession

%% Computing nuclear moment
    % Bohr magneton  [http://physics.nist.gov/constants]
        % Conversion from (m T)^(-1) to (cm G)^(-1)
        MuBinvmbyT = 46.6864515; % m^-1 / T
        MuB = MuBinvmbyT / (10000*100); % (PerCm)/G  1T = 10000G
        % Proton-to-electron mass ratio
        MassRatio = 1836.15267247;
    % Nuclear moment
        MuN = MuB / MassRatio; % SI

%% Einstein's spontaneous emission
load A_ijavg
A_ij = A_ijavg;
%% constants in SI units
    % speed of light
      cSI = c/100.;            % (m/sec)
    % Stephan-Boltzman constant NIST
      kSI = 1.3806504e-23;     % (J/(Kg.K)
    % Electron mass
      MSI = 131.29*1.6605e-27; % Kg
    % Some constant
      AlphSI = MSI/(2*kSI);
%% Transition center-wavelength of Xe I
l_oSI = 834.91157e-9;                  % SI
```

- ‘IsotopesParametersOptimAvg.m’

```
 % All variables ending with 'avg' are being loaded from a
 % database of variables saved after a run of the pre-
 % optimization program

 % Parameters associated with all Xe isotopes
    % Masses
      Masses    = [124  126  128  129  130  131  132  134  136];

    % Isotope shifts
      load ISOavg
      IsoShifts =  FunMHztoCm([ISOavg 0]);
    % Natural abundances (fraction)
      IsoAbunds=[0.1 0.09 1.91 26.4 4.1 21.2  26.9 10.4 8.9]/100;

 % Parameters associated with Xe isotopes with non-zero
 % nuclear spin
    % Nuclear spins
      NukeSpins = [0    0    0    1/2  0    3/2  0    0    0  ];
    % Nuclear moments
      load MuN129avg
      load MuN131avg
      gi=(1/MassRatio)*...
      [0 0 0 MuN129avg/NukeSpins(4) 0 MuN131avg/NukeSpins(6)...
      0 0 0];
    % Electric quadrupole interaction constants
      load A1_129avg
      load A1_131avg
      load A2_129avg
      load A2_131avg

      % Upper level values
        a1 = [0  0  0  A1_129avg  0  A1_131avg  0  0  0];
        a1 = FunMHztoCm(a1); % Convert from MHz to cm^-1

      % Lower level values
        a2 = [0  0  0  A2_129avg  0  A2_131avg  0  0  0];
        a2 = FunMHztoCm(a2);

     % Magnetic quadrupole interaction constants
     % (not relevant to this thesis)
        b1 = [0  0  0  0  0  24.5  0  0  0];
        b1 = FunMHztoCm(b1);

        b2 = [0  0  0  0  0  22.4  0  0  0];
        b2 = FunMHztoCm(b2);
% Grouping isotope parameters based on nuclear spin
% (depending on wether zero or non-zero)
[dum, N] = size(NukeSpins);
% Looping through number of isotopes
    c1 = 0; c2 = 0; % Initializations
    for i=1:N
```

```
        if (NukeSpins(i) == 0)
            c1 = c1 + 1;  % counter
            NoHFS(:,c1)=[Masses(i) NukeSpins(i) IsoShifts(i)...
                           IsoAbunds(i)]';
        else
            c2 = c2 + 1;  % counter
            WithHFS(:,c2)=[Masses(i) NukeSpins(i) IsoShifts(i)...
                    IsoAbunds(i) a1(i) b1(i) a2(i) b2(i) gi(i)]';
        end
    end
```

Lineshape simulator based on dependent variables: H and T ‘FunZHFSforBT.m’

```
function Diff = FUNZHFSforBT(X, Iexp, NUexp, MyId)

% This function computes the error between experimental and
% simulated spectra to be minimized later by the solver
% 'lsqnonlin'

% Extract magnetic field strength and kinetic temperature from
% previous iteration
H = X(1); T = X(2);

%load Xopt;

run PhysicalConstantsOptimAvg;
run Level1InputsOptimAvg;
run Level2InputsOptimAvg;
run IsotopesParametersOptimAvg;

[dum, N] = size(NukeSpins);

% Compute transition lines associated with isotopes with zero
% nuclear spin
run NoHFsLines;

[Dummy,N1] = size(WithHFS);
II = WithHFS(2,:); % Extract nuclear spin associated with the
% isotopes
gI = WithHFS(9,:); % extract nuclear lande-g factor

% Compute transition lines associated with isotopes with non-zero
% nuclear spin
run SigmaZHFS;

% Compute mean frequency from weight averagings
center = sum(dEhz_sig .* Ihz_sig)/ sum(Ihz_sig);

% Compute the relative displacement of energy levels (associated
% with non-zero spin isotopes) about mean frequency then convert
% to GHz and combine with those associated with other isotopes
  x_lines   = FunCmtoGHz([dENoHFSiso_sig; dEhzIso_sig - center]);
  N = length(x_lines);

% Combine intensities of all isotopes
  y_lines   = [IntenNoHFSiso_sig; IntenHZiso_sig];

% Apply Lorentz broadening
run Lorentzian;

% Apply Doppler broadening
run Doppler;
```

```

% Convolve cold and Doppler function
run Convolution;

% Exclude any imaginary numbers that might have resulted from the
% convolution process
Warm = real(Warm);

% Compute error between experimental and simulated spectra
Diff = Iexp — Warm;
```

APPENDIX E

Simulation of Zeeman-split spectra - generic files

Simulation of the lineshape of xenon isotopes with zero nuclear-spin
‘NoHFSLines.m’

```
 % A. Compute zeeman splittings for each shifted line -
 % assuming weak magnetic field - Anomalous Zeeman effect
   % a.1 Possible Mj states
         Mj1 = [J1:-1:-J1];   % upper-state values
         Mj2 = [J2:-1:-J2];   % lower-state values
   % a.2 Corresponding magnetic moments
         Muj1 = - Mj1 * gj1 * MuB;
         Muj2 = - Mj2 * gj2 * MuB;
   %  a.3 Corresponding magnetic energies relative to
   % isotopic shifts
          EMj1 =  -Muj1 * H;
          EMj2 =  -Muj2 * H;
% B. Compute Zeeman energy shifts for each allowed transition
%    for each isotope with I different of 0
   %  b.1 Count number of Zeeman-split states
      NumMj1 = length(Mj1);
      NumMj2 = length(Mj2);
   %  b.2 Finding all possible Mj-->Mj' transitions and
   % corresponding Zeeman energy shifts
           n1 = 0; n2 = 0; n3 = 0;
          %Norm = (2*J1 -1)*(2*J1 + 1)
 switch J2 - J1;
     case -1 ;
         error('J2 must be greater than J1')
     case 0        ;
         error('J2 must be greater than J1')
  %  J --> J+1
     case 1
```

```
        for i=1:NumMj1
            for j=1:NumMj2
                switch Mj2(j)-Mj1(i);
                    % Mj --> Mj-1
                       case -1;
                           n1=n1+1;  % counter
                           % compute intensities
                           Im = (J1-Mj1(i)+1)*(J1-Mj1(i)+2);
                           % store upper and lower quantum
                           % numbers by transitions along
                           % with their corresponding energy
                           % separations and intensities
                           MjtoMjmdEMj(n1,:)=...
                               [Mj1(i) i Mj2(j) j ...
                               (EMj2(j)-EMj1(i)) Im];
                     % Mj --> Mj
                     % not needed for this thesis
                     % their inclusion is for sake of
                     % completeness
                       case 0  ;
                           n2 = n2 + 1;
                           I = 4*((J1 +1)^2 - Mj1(i)^2);
                           MjtoMjdEMj(n2,:)=...
                               [Mj1(i) i Mj2(j) j ...
                               (EMj2(j)-EMj1(i)) I];
                     % Mj --> Mj+1
                       case 1 ;
                           n3 = n3 + 1;
                           Ip = (J1 + Mj1(i)+1)*(J1+Mj1(i)+2);
                           MjtoMjpdEMj(n3,:)=...
                               [Mj1(i) i Mj2(j) j ...
                               (EMj2(j)-EMj1(i)) Ip];
                end
            end
        end
end

        % Group all line shape components into one array
         Isig = [MjtoMjmdEMj(:,6); MjtoMjpdEMj(:,6)];

% B.3 Apply isotopic parameters to each set of isotopes
%      (depending on wether or not their nuclear-spin
%       is zero or non-zero)
       N1 = length(NoHFS);  % counter

       % loop initialization
       dENoHFSiso_sig = [];
       IntenNoHFSiso_sig = [];
       IntenNoHFS_sig = []; dENoHFS_sig = [];

         % Loop through each type of isotope
         for  k=1:N1
              % Apply isotopic shift to each set of
              % transition energies
```

```
             dENoHFSiso_sig = [dENoHFSiso_sig;...
             [[MjtoMjmdEMj(:,5); ...
             MjtoMjpdEMj(:,5)] + NoHFS(3,k)]];
             % Scale the intensity of each line according
             % to natural abundance; then normalize by sum
             IntenNoHFSiso_sig = [IntenNoHFSiso_sig;...
             [(Isig/sum(Isig)) * NoHFS(4,k)]];
        end

        % Storing transition energies without any isotope
        % shifting -- for later use
        dENoHFS_sig = [[MjtoMjmdEMj(:,5); MjtoMjpdEMj(:,5)] ];
```

Simulation of the lineshape of xenon isotopes with non-zero nuclear-spin
‘SigmaZHFS.m’

```

% Extract electric quadrupole interaction constants
% (or hyperfine structure  (hfs) contants)
AA1 = WithHFS(5,:);  % associated with upper state
AA2 = WithHFS(7,:);  % associated with lower state

% Loop initialization
dEhz_sig = [];
dEhzIso_pi = [];
IntenHZiso_pi = [];
dEhzIso_sig = [];
Ihz_sig = [];
IntenHZiso_sig = [];
% For each isotope with non-zero nuclear spin
for k=1:2
    % nuclear spin and lande-g
      I = II(k);  gi = gI(k);
    % conveniently store nuclear spin and angular
    % momentum quantums numbers into upper and lower-
    % state arrays
      IJ1 = [I J1]; IJ2 = [I J2];
    % Collect hyperfine structure constants
      A1 = AA1(k); % upper-state value
      A2 = AA2(k); % lower-state value
    % Generate arrays of quantum numbers [Mj Mi M F J]
    % and arrays of physical constants [a gj gi o]
    % associated with:
        % upper-state:
          [MjMiMFJ1, agjgio1] = FunMMjMi(IJ1, A1, o, gj1, gi);
        % lower-state:
          [MjMiMFJ2, agjgio2] = FunMMjMi(IJ2, A2, o, gj2, gi);

    % For each set of quantum numbers [Mj Mi M F J], generate
    % `coefficient-matrix' of eigenvalue-eigenvector problem
    % for later determination of energy level (eigenvalues) and
    % correponding mode-shape (eigenvector)
      % upper-state parameters
        [MjMi_MjmMip1,MjMi_MjpMim1,MjmMipM1,MjMioM1,MjpMimM1,...
            Coef1] ...
         = FunCoef(MjMiMFJ1,agjgio1,H,I);
      % lower-state parameters
        [MjMi_MjmMip2,MjMi_MjpMim2,MjmMipM2,MjMioM2,MjpMimM2,...
            Coef2] ...
        = FunCoef(MjMiMFJ2,agjgio2,H,I);

    % Determination of energy level (eigenvalues) and
    % correponding mode-shape (eigenvector) from `coefficient-
```

```
48      % matrix. Then, ensure that each subset of eigenvalues
49      % and mode shapes possessing an equal sum Mj+Mi are assigned
50      % to the proper sets of quantum numbers; note: these are
51      % associated to states whose degeneracies are lifted.
52        % upper-state parameters
53         [Shapes1, States_ok1]=FunEtoMjMi(MjMiMFJ1, Coef1);
54        % lower-state parameters
55         [Shapes2, States_ok2]=FunEtoMjMi(MjMiMFJ2, Coef2);
56
57        % extract energy levels
58         E1 = States_ok1(:,end); % upper levels
59         E2 = States_ok2(:,end); % lower levels
60
61        % Update array-variables of QNs and energy levels
62        % based on possible reassociations performed on from
63        % lines 47 to 56
64         MjMiMFJfjEzh1 = States_ok1; % upper-state parameters
65         MjMiMFJfjEzh2 = States_ok2; % lower-state parameters
66
67        % Define new array-variables of energy levels based on
68        % updated sorting
69         % energy levels
70          Ezh_cg1 = MjMiMFJfjEzh1(:,8) ; % upper state
71          Ezh_cg2 = MjMiMFJfjEzh2(:,8) ; % lower state
72         % quantum numbers
73          MjMiMFJ1 = MjMiMFJfjEzh1(:,[1:5]); % upper state
74          MjMiMFJ2 = MjMiMFJfjEzh2(:,[1:5]); % lower state
75
76        % Compute energy and intensity of each lineshape component
77         % Energy of each component:
78          % Generate sets of upper and lower-state QNs
79          % {[F J Mj Mi]_1  [F J Mj Mi]_2} for each possible
80          % transition and associate each to its energy separation
81          % (or energy of the corresponding lineshape component)
82          [MtoMmdEMjMi,MtoMdEMjMi,MtoMpdEMjMi]=...
83           FunMjMi1toMjMi2All...
84           (MjMiMFJ1,Ezh_cg1,MjMiMFJ2,Ezh_cg2);
85         % Intensity of each component:
86          % Mj-->Mj-1 transitions
87           [MtoMmInten, Xn1, Xmn2]= ...
88           FunIntensitiesJtoJp ...
89               (IJ1, IJ2, Shapes1, Shapes2, MtoMmdEMjMi);
90          % Mj-->Mj+1 transitions
91           [MtoMpInten, Xn1, Xpn2] = ...
92           FunIntensitiesJtoJp...
93           (IJ1, IJ2, Shapes1, Shapes2, MtoMpdEMjMi);
94          % Ensure equal number of sigma+ and sigma- transitions
95           Sizes1 = size(MtoMmInten);
96           Sizes2 = size(MtoMpInten);
97           if Sizes1(1) ≠ Sizes2(1);
98               error('Mismatch num states Sig')
99           end
100
101         % Group all transition energies (sigma+ and sigma-)
```

```
              dEhz_sig = [dEhz_sig; ...
                  [MtoMmInten(:,13); MtoMpInten(:,13)]];
            % Apply isotope shift
              dEhzIso_sig = [dEhzIso_sig; ...
                  [MtoMmInten(:,13); ...
                  MtoMpInten(:,13)] + WithHFS(3,k)];

            % Group all transition intensities
              Vals2 = [MtoMmInten(:,14); MtoMpInten(:,14)];
              Ihz_sig = [Ihz_sig; Vals2];
            % Scale intensities by natural abundance
              IntenHZiso_sig = [IntenHZiso_sig; ...
                  (Vals2/sum(Vals2))*WithHFS(4,k)];
end
```

Determination of the quantum number sets $\left|JFM_JM_I\right\rangle$ associated with each energy-level

‘FunMMjMi.m’

```
function [MjMiMFJ, agjgio]=FunMMjMi(IJ, a, o, gj, gi)
% This function computes quantum numbers Mj, Mi, J, F, and J and
% stores physical parameters

  I = IJ(1); % nuclear spin quantum number
  J = IJ(2); % angular momentum quantum number

% Determine possible Mi values from I such that |Mi| ≤ I
  Mi_Poss = I:-1:-I;

% Determine possible resultant angular momentum QNs
  Fspan = (I+J) :-1: abs(J-I);

% Determine possible Mj values from J such that |Mj| ≤ J
  Mj_Poss =  J:-1:-J;
  [Var, NumMj_Poss] = size(Mj_Poss);

  M = [];
  for i=1:length(Fspan)
    M = [M Fspan(i):-1:-Fspan(i)];
  end
  M = M'; % take transpose

  % Create arrays of F and J quantum numbers arranged
  % according to the distribution of M and Mi arrays
   Js=J; F=[]; J=[];
  for i=1:length(Fspan)
      Mspan = Fspan(i):-1:-Fspan(i);
      % Create column of J values
        DegenM = length(Mspan);
        Ones = ones(1,DegenM);
        J = [J Js*Ones];
      % Create column of F values
        F = [F Fspan(i)*Ones];
  end
  J = J'; F = F'; % take transpose

  % Find number of times each possible value of F occurs within
  % array
  N = length(F);
  for f=1:N
      IndxF(f) = find(Fspan == F(f));
  end
  IndxF = IndxF';

  % Arrange Mj and Mi quantum numbers into m sets of (Mj, Mi)
  % values forming an mx2 matrix (m being number of states) such
  % that the sum rule (M=Mj+Mi) is obeyed and no two quantum
```

```
  % states have the same is satisfied and no two states have the
  m = length(M);             % Count number of Zeeman-split states
  States = 100*ones(m,2);    % Initialize matrix of states
  for k = 1:length(M)
      for j=1:NumMj_Poss
          for i=1:length(Mi_Poss)
              % Apply sum rule
              if (Mj_Poss(j) + Mi_Poss(i) == M(k))
                Mj(k) = Mj_Poss(j);  % build array of Mj values
                Mi(k) = Mi_Poss(i);  % build array of Mi values
                Test=ismember...
               ([Mj(k)*ones(m,1) Mi(k)*ones(m,1)],States,'rows');
                if Test
                    % If [Mj Mi] has already been accounted for
                    % in the matrix of states skip the next step
                    % and perform the next test.
                else
                    % Build matrix of states
                    States(k,:)=[Mj(k) Mi(k)];
                end
              end
          end
       end
  end

Mj = States(:,1); % store Mj values
Mi = States(:,2); % store corresponding Mi values

  % Find number of times each possible value of Mj occurs within
  % array
    for j=1:length(Mj)
        IndxMj(j) = find(Mj_Poss == Mj(j));
    end
    IndxMj = IndxMj';

  % Conveniently store Mj and Mi values into some `MjMi' matrix
    MjMi = [Mj Mi];
  % Conveniently store sets [Mj Mi M F J] values into state
  % some state matrix `MjMiMFJ'
    MjMiMFJ = [MjMi M F J IndxF IndxMj];

 % Sort quantum number sets according to increasing M values
 [Dum,IndxM] = sort(-MjMiMFJ(:,3));
 MjMiMFJsort = MjMiMFJ(IndxM,:);
 MjMiMFJ = MjMiMFJsort;

% Build array of physical constants:
% Hyperfine interval unit--Lande g-factors--Larmor precession
agjgio = [a gj gi o];
```

Determination of the coefficient-matrix in the eigenvalue-eigenvector problem
‘FunCoef.m’

```
function [MjMi_MjmMip,MjMi_MjpMim,MjmMipM,MjMioM,MjpMimM,Coef]=...
    FunCoef(MjMiMFJ,agjgio,H,I)

% Extract physical parameters
% (hyperfine constants, lande-g factors, and Larmor precession)
a = agjgio(1); gj = agjgio(2); gi = agjgio(3); o = agjgio(4);

% Extract quantum numbers (Mj, Mi, and J) needed to build a
% 'coefficient matrix' whose eigenvalues and eigenvectors
% correspond to energy levels and mode-shapes respectively
MjMi  = MjMiMFJ(:,1:2);
J = MjMiMFJ(1,5);

% Start building coefficient matrix.
  % initializations
    m = length(MjMi); n = m;
    Coef  = zeros(m,n);
    MjmMipM  = zeros(m,n);
    MjpMimM  = zeros(m,n);
    MjMioM  = zeros(m,n);

    MjMi_MjmMip = [];
    MjMi_MjpMim = [];

    % Loop through states
      for r=1:m
      % compute coefficient of mode-shapes carrying Mj and Mi
      % indices
        Coef(r,r)  = FMjMi(MjMi(r,1),MjMi(r,2),a,gj,gi,o,H);

        % loop through states again to identify states whose
        % quantum numbers Mj and Mi that either:
        % - differ by plus or minus unity from the outer-loop
        %   quantum numbers
        % - or do not differ at all
          for c=1:n
            Diff  = (MjMi(r,:)-MjMi(c,:));
            % build a matrix of QN-state IDs associated with
             % (Mj-1, Mi+1) numbers
                if (Diff == [1 -1]);
                    MjmMip = MjMi(c,:);
                    MjMi_MjmMip = [MjMi_MjmMip; MjMi(r,:) MjmMip];

                    % compute coefficient of mode-shapes carrying
                    % 'Mj-1' and 'Mi+1' indices
                    Coef(r,c)  = FMjminusMiplus...
                      (MjmMip(1,1),MjmMip(1,2),a,J,I);

```

```
                   % build a matrix of state IDs associated with
                   % (Mj-1, Mi+1) numbers
                   MjmMipM(r,c) = c;
              end

        % build a matrix of QN-state IDs associated with
        % (Mj,Mi) numbers
        if (Diff == [0 0]);
            MjMioM(r,r) = r;
        end

        if (Diff == [-1 1]);
            MjpMim = MjMi(c,:);
            MjMi_MjpMim = [MjMi_MjpMim; MjMi(r,:) MjpMim];

            % compute coefficient of mode-shapes carrying
            % 'Mj+1' and 'Mi-1' indices
              Coef(r,c) = FMjplusMiminus...
                  (MjpMim(1,1),MjpMim(1,2),a,J,I);

            % build a matrix of QN-state IDs associated with
            % (Mj+1, Mi-1) numbers
              MjpMimM(r,c) = c;
        end
  end
end

   % Compute eigenvalues and eigenvectors from Coefficient
   % matrix
   [Shapes, Energ] = eig(Coef,'nobalance');
   DelE = diag(Energ);  % Zeeman-HFS energy shifts

   % Store (Mj, Mi, M, F, J) associated with each state as well
   % as corresponding energies
   MjMiMFJbyEzh = [MjMiMFJ DelE];
```

Sub-functions used in ‘FunCoef.m’:

- ‘FMjMi.m’

```
function F = FMjMi(Mj,Mi,aa,g,gi,o,H)

% Function FMjMi computes coefficient of mode-shapes
% carrying Mj and Mi indices

F=(H*(o*((Mj*g) + (Mi*gi)))) + (Mj*Mi)*aa ;
```

- ‘FMjminusMiplus.m’

```
function F = FMjminusMiplus(Mjminus,Miplus,aa,J,I)

% Function FMjminusMiplus computes coefficient of mode-shapes
% carrying 'Mj-1' and 'Mi+1' indices

F = [-[-(aa/2)*((J-Mjminus)*(I+Miplus))]];
```

- ‘FMjplusMiminus.m’

```
function F = FMjplusMiminus(Mjplus,Miminus,aa,J,I)

% Function FMjplusMiminus computes coefficient of mode-shapes
% associated with 'Mj+1' and 'Mi-1' states

F = [-[-(aa/2)*((J+Mjplus)*(I-Miminus))]];
```

Determination of energy levels and mode-shapes associated with each $\left|JFM_JM_I\right\rangle$ state

‘FunEtoMjMi.m’

```
function [Shapes, MjMiMFJbyEzh] = FunEtoMjMi(MjMiMFJ, Coef)

% This function ensures that the association between sets
% (Mj, Mi, M, F, J) and energy levels is correct; if not
% reassociates energy levels and mode shapes with the proper sets
% (Mj, Mi, M, F, J)

[U, MyTri] = schur(Coef);

Energ = diag(MyTri);

[Shapes_unsort, D] = eig(Coef, 'nobalance');
Energ_unsort = diag(D);

n = 0;
m=length(Energ);
length(Energ_unsort);
Precis = 7; MyNum = num2str(Precis);

Indx = [];
for i=1:length(Energ)
    for k=1:length(Energ_unsort)
        sign(Energ(i));
        switch sign(Energ(i));
            case −1;
                ESch = sprintf(['%1.' MyNum 'f'], Energ(i));
            case 1;
                MyVal = sprintf(['%1.' MyNum 'f'], Energ(i));
                ESch = ['+' MyVal];
        end

        switch sign(Energ_unsort(k));
            case −1;
                Eeig = sprintf(['%1.' MyNum 'f'], Energ_unsort(k));
            case 1;
                Eeig = ['+' sprintf(['%1.' MyNum 'f'], ...
                    Energ_unsort(k))];
        end
        if ESch == Eeig;
            n = n + 1      ;
            Indx(i) = k    ;
        else
            n = n        ;
        end

    end
end

```

```
DelEo = Energ_unsort(Indx',:); NumEngs = length(DelEo);

if n<length(NumEngs);
    error('Bad Match');
end

Shapes = Shapes_unsort(:,Indx);

Out = [];
i2 = 1;
i1 = 1;

M = MjMiMFJ(:,3);
while (i2≤m)
        M1 = M(i1); M2 = M(i2);
       while (M2 == M1 & i2≤m)
            i2 = i2 + 1;
            try
                M2 = M(i2);
            end
        end
        i2 = i2 - 1;
        Out = [Out; [i1 i2]];
       i1 = i2+1;
       i2 = i1;
end

    % Need to distinguish between energies of same M since
    % they 'equally' satisfy the characteristic equation
    TransfE = eye(m,m);
    for i=1:length(Out)
        Indx = []; % Empty contents
        Indx = [Out(i,1):Out(i,2)]'; a = length(Indx); A = eye(a);

        if length(Indx)>1

            [E_seg0, IndxE] = sort(Energ(Indx,:));
            Transfe = A(IndxE,:);  TransfE(Indx,Indx) = Transfe;

            [Mj_seg, IndxMj] = sort(MjMiMFJ(Indx,1));

            E_seg1 = E_seg0(IndxMj,:);
            DelEo(Indx,:) = E_seg1;

            Shapes0 = Shapes(Indx,Indx);
            Shapes1 = Shapes0(IndxMj,IndxE);
            Shapes(Indx,Indx) = Shapes1;
        end
    end

MjMiMFJbyEzh = [MjMiMFJ DelEo];
```

Determination of all sets of $|JFM_JM_I\rangle_1$ and $|JFM_JM_I\rangle_2$ quantum numbers involved in each possible transition as well as the energy associated with each corresponding lineshape component 'FunMjMi1toMjMi2All.m'

```
function [MtoMm, MtoM, MtoMp] ...
    = FunMjMi1toMjMi2All(MjMiMFJ1, Ezh_cg1,  MjMiMFJ2, Ezh_cg2)

% This function determines all possible {(Mj,Mi)_1 and (Mj,Mi)_2}
% sets for M_1-->M_2 transitions along with corresponding shape
% factors (X and Y values)
% Note 1:
% '1' and '2' indices refer to upper and lower states,
% respectively
% Note 2:
% X and Y designate mode shapes associated with upper and lower
% states respectively

M1    = MjMiMFJ1(:,3);              M2    = MjMiMFJ2(:,3);
MjMi1 = MjMiMFJ1(:,[1:2]);          MjMi2 = MjMiMFJ2(:,[1:2]);
FJ1   = MjMiMFJ1(:,[4:5]);          FJ2   = MjMiMFJ2(:,[4:5]);

mn1 = size(MjMiMFJ1); m1 = mn1(1);
mn2 = size(MjMiMFJ2); m2 = mn2(1);

% Initializations to loop
k1 = 0;
k2 = 0;
k3 = 0;
% Loop through upper and lower states
for i=1:m1 % upper states loop
      for j=1:m2 % lower states loop

          % If M-->M-1 transition found perform following tasks
          if (M2(j) - M1(i)) == -1;
                k1 = k1 + 1;  % increment counter
                % Compute energy of transition component
                  dEm = (Ezh_cg2(j) - Ezh_cg1(i));
                % Sort QNs and energy associated with
                % transition
                  MtoMm(k1,:) = [ FJ1(i,:) M1(i) MjMi1(i,:) i...
                    FJ2(j,:) M2(j) MjMi2(j,:) j dEm];
            % If M-->M transition found perform similar
            % tasks to above steps
            elseif (M2(j) - M1(i)) == 0;
                k2 = k2 + 1;  % and column-indices to final states.
                dE = (Ezh_cg2(j) - Ezh_cg1(i));
                MtoM(k2,:) = [ FJ1(i,:) M1(i) MjMi1(i,:) i...
                    FJ2(j,:) M2(j) MjMi2(j,:) j dE];
            % If M-->M+1 transition found perform similar
            % tasks to above steps
            elseif (M2(j) - M1(i)) == 1;
```

```
                k3 = k3 + 1;
                dEp = Ezh_cg2(j) - Ezh_cg1(i);
                MtoMp(k3,:) = [ FJ1(i,:) M1(i) MjMi1(i,:) i...
                    FJ2(j,:) M2(j) MjMi2(j,:) j dEp];
            % If no possible transition print error
            elseif (k1 == 0 & k2 == 0 & k3 == 0);
                error('no possible transition')
            end
        end
    end
```

Determination of the intensity associated with each lineshape component in a $\left|JFM_JM_I\right\rangle_1$ to $\left|JFM_JM_I\right\rangle_2$ transition such that $J_2 - J_1 = 1$ ‘FunIntensitiesJtoJp.m’

```
function [M1toM2Inten, Xn1, Xn2] = ...
    FunIntensitiesJtoJp(IJ1, IJ2, Shapes1, Shapes2, M1toM2)

% This function computes all transitions intensities
% for the specific case of J−−>J+1 transitions

% Nuclear spin quantum number
I = IJ1(1);

% angular momentum quantum numbers
J1 = IJ1(2); % upper state value
J2 = IJ2(2); % lower state value

% Removing transition components such that Mi1 different from Mi2
% Define the following M1toM2 array:
% [F1 J1 M1 Mj1 Mi1 i F2 J2 M2 Mj2 Mi2 j];

mn = size(M1toM2); m1 = mn(1);

DelM = M1toM2(:,9) − M1toM2(:,3);

% Intensity formula was derived for J−−>J−1 transitions. The same
% formula applies to J−−>J+1 by switching initial and final states

  % initialize matrices of normalized mode−shapes
  Xn2 = zeros(size(Shapes2));
  Xn1 = zeros(size(Shapes1));

  % Rename matrices of mode−shape vectors
  Y = Shapes2;     % Upper state's eigenvectors
  X = Shapes1;     % Lower state's eigenvectors

  % Collecting indices corresponding to shape coefficients
  % involved in allowed transitions for which Mi does not
  % change
  Indx_CompYms = M1toM2(:,12);
  Indx_CompXs = M1toM2(:,6);

  % Extract quantum numbers from matrix of transitions
  M = M1toM2(:,3);

  Mj1 = M1toM2(:,4); Mi1 = M1toM2(:,5);
  Mj2 = M1toM2(:,10); Mi2 = M1toM2(:,11);

  F1  = M1toM2(:, 1); MF1 = [M F1]; f = length(F1);

  % Looping through the transitons
  for k=1:m1
```

```
    xk =  Indx_CompXs(k); yk =  Indx_CompYms(k);

    Indx = find(M == M(k));

    Sumxy = 0; N1 = []; N2 = [];
    for i = 1:length(Indx)
            j = Indx(i);
            xj =  Indx_CompXs(j);
            yj = Indx_CompYms(j);
            if (Mi1(j) == Mi2(j));
                 switch DelM(j);
                     case 1;
                        Coeff = factorial(I+Mi2(j)) *...
                                factorial(I-Mi2(j)) *...
                                factorial(J2+Mj2(j)) *...
                                factorial(J2-Mj2(j));
                     case 0;
                        Coeff=  2 * factorial(I+Mi2(j)) *...
                                    factorial(I-Mi2(j)) *...
                                    factorial(J2+Mj2(j)) *...
                                    factorial(J2-Mj2(j));
                     case -1;
                        Coeff = factorial(I+Mi2(j)) *...
                                factorial(I-Mi2(j)) *...
                                factorial(J2+Mj2(j)) *...
                                factorial(J2-Mj2(j));
                 end
                 P = X(xj,xk) * Y(yj,yk);
                 Sumxy = (Sumxy + Coeff * P);

                 K2 = factorial(I+Mi2(j))*factorial(I-Mi2(j))...
                 *factorial(J2+Mj2(j))*factorial(J2-Mj2(j));
                 K1 = factorial(I+Mi1(j))*factorial(I-Mi1(j))...
                 *factorial(J1+Mj1(j))*factorial(J1-Mj1(j));

                 N1(i)= K1*(X(xj,xk)^2);
                 N2(i)= K2*(Y(yj,yk)^2);
            end
    end

     Ns1 = sum(N1);
     Ns2 = sum(N2);
                  XY(k)  = Sumxy / sqrt(Ns1 * Ns2);
                  Xn1(:,xk) = X(:, Indx_CompXs(k)) / sqrt(Ns1);
                  Xn2(:,yk) = Y(:, Indx_CompYms(k)) / sqrt(Ns2);
end

I_M1toM2 = transpose(XY.^2);
M1toM2Inten = [M1toM2 I_M1toM2];
```

Simulation of lineshape broadening

Lorentz broadening
‘Lorentzian.m’

```
% Lorentzian broading of lines: outputs c_nu


%center = 1.e-3 * NUmean;
%center = 0;
x_lines0 = x_lines;

[x_lines I]=sort(x_lines0);
y_linesOLD = y_lines;

for i=1:N
    y_lines(i)=y_linesOLD(I(i));
end

nu_l = A_ij/(2*pi);

NumPts = length(NUexp);
y = [];
for i=1:NumPts
    y(i)   = 0;
end

nu = NUexp;
y = y';
for i=1:N
   y = y_lines(i)*nu_l./(pi*( (nu-x_lines(i)).^2 + nu_l^2)) + y;
end

c_nu = FunNormTrap(nu, y);
%c_nu = y / sum(y);
```

Doppler broadening
‘Doppler.m’

```
% Doppler broadening function
nu0 = nu;
nu = 1000*nu0;
d_nu0 = exp(-((1.e6*l_oSI*nu).^2)*AlphSI/T);
%d_nu = d_nu/(75*sum(d_nu));

d_nu = FunNormTrap((1.e-3)*nu, d_nu0);
%d_nu = d_nu / sum(d_nu);
```

Convolution
'Convolution.m'

```
C_tau = fft(c_nu);
[NuShift, zero_loc] = min(abs(nu));
Shift = round(zero_loc);
d_nu_shifted=circshift(d_nu,-(Shift)); %d_nu_shifted=d_nu_shifted';
c_nu_shifted=circshift(c_nu,-(Shift));

%d_nu_shifted = FunNormTrap(1.e-3*nu, c_nu_shifted0);
D_tau = fft(d_nu_shifted);
W_tau = C_tau .* D_tau;
w_nu  = real(ifft(W_tau));

Warm = FunNormTrap(1.e-3*nu, w_nu);
%Warm = w_nu / sum( w_nu );
```

Subprograms used to simulate broadening:

- 'FunNormTrap.m' - Integrator based on trapezoid method then normalizer:

```
function yn = FunNormTrap(x, y)

for i = 2:length(x)
    Dx = x(i) - x(i-1);
    Dy = y(i) - y(i-1);
    Da(i) = Dx * (y(i) + y(i-1)) / 2;
end

Area = sum(Da);
yn = y / Area;
```

- 'FunTrapIntegral.m' - Integrator based on trapezoid method:

```
function Area = FunTrapIntegral(x, y)

for i = 2:length(x)
    Dx = x(i) - x(i-1);
    Da(i) = Dx * (y(i) + y(i-1)) / 2;
end

Area = sum(Da);
```

- 'FunMHztoCm.m' - Energy converter (from MHz to cm^{-1}):

```
function ValuePerCm = FunMHztoCm(ValueMHz)
% This function converts energy in cm^-1 units to MHz

ValuePerCm = ValueMHz ./ (2.99792458 *10^4);
% 1MHz --> 10^6 Hz f=c/lamda --> lamda = c/f
% so 1MHz --> 3*10^10 / 10^6
```

APPENDIX F

Determination of physical parameters within their respective uncertainty bounds based on fitting of spectra of an optogalvanic cell exposed to an external magnetic field - header files

Preliminary notes:

1. This process is optional and not necessary if the intervals of confidences associated with the physical parameters are reasonable.
2. The physical parameters to be optimized are:

   Spontaneous emission coefficient

   All isotope shifts except those associated with ^{136}Xe (reference isotope: with zero shift)

   Landé-g factors

   Electric quadrupole interaction constants

   Nuclear moments associated with ^{129}Xe and ^{131}Xe
3. The magnetic field strength (H) and kinetic temperature (T) are included in the optimization process only to 'help' the solver. Running the optimization program without including H and T has been found to lead to a poor convergence process due to fact that the error function is more sensitive to the latter two variables.
4. This optional program-header is to be used in conjunction with the generic codes described in Appendix E.

Main solver for H, T, and optimal physical parameters ‘BISOAgjgiTAijSolver.m’

```
clear all; close all;

% Inputs----------------------------------
MainDIR = ...
'H:\AE UM Bailo Bah Ngom Thesis 2009\Appendices';
DataFolder = '\OGdata';
FileNames = dir([MainDIR DataFolder '\*.txt']);
NumFiles = length(FileNames);

DataPath = [MainDIR DataFolder];
addpath(DataPath);

% Add output path
ResultsFolder = '\OGoptim';
  OutputPath = [MainDIR ResultsFolder];
  addpath(OutputPath);
 % Graphic: encapsulated post-script format
Format = input...
      ('Enter output file-format. 1 for tiff or 2 for eps: ');

Skip = 0;
f = 0;
Range = [1:NumFiles];
for MyId = 1:NumFiles
    FileId = Skip+MyId;
    [Int, Dec, Hout, IexpN, NUmean, NUexp]=...
        FunDATAloader(FileNames, FileId);

run PhysicalParamINIT2;

options = optimset('Display','iter');
[Xsol,Resnorm,FVAL,EXITFLAG,OUTPUT,LAMBDA,JACOB] = ...
   lsqnonlin(@FUNfromBISOAgjgiTAij, Xo, Xlow, Xup,...
   options, IexpN, NUexp);

% Declareariables to be optimized-------------------------------------------
H       = Xsol(1) ;
T       = Xsol(2) ;
T_Arr(MyId) = T  ;

I124   = Xsol(3); I126   = Xsol(4) ; I128   = Xsol(5);
I129   = Xsol(6); I130   = Xsol(7) ; I131   = Xsol(8);
I132   = Xsol(9); I134   = Xsol(10);

A1_129 = Xsol(11); A2_129 = Xsol(12);
A1_131 = Xsol(13); A2_131 = Xsol(14);

gj1 = Xsol(15); gj2 = Xsol(16);
```

```

MuN129 = Xsol(17); MuN131 = Xsol(18);

A_ij = Xsol(19);

ISO = [I124  I126  I128  I129  I130  I131  I132  I134];
A1 = [A1_129 A1_131];  A2 = [A2_129 A2_131];
gj = [gj1 gj2];
NukeMom = [MuN129 MuN131];


run Level1inputsBISOAgjgi;
run Level2inputsBISOAgjgi;
run PhysicalConstants;
run IsotopesParametersISOAgjgi;

run NoHFsLines;

% 2. Consider each isotope with hyperfine structure
% (I ≠(not equal) 0)
[Dummy,N1] = size(WithHFS);
II = WithHFS(2,:);
gI = WithHFS(9,:);
run SigmaHFS;

run Lorentzian;
run Doppler;
run Convolution;

f = f + 1;
figure(f)
plot(NUexp, Warm,'LineWidth', 2), hold on
plot(NUexp, IexpN, '*','MarkerSize', 1)
axis tight

legend(['Z-HFS Model: ' sprintf('%5.1f', H) ], ...
    ['   Experiment: ' sprintf('%5.1f', Ho)])
xlabel ('Detuning (GHz)')
ylabel ('Normalized intensity')
hold off

Xopt(MyId,:) = [Xsol];

switch Format
    case 1
        Ext = 'tiff';
    case 2
        Ext = 'eps';
 end
File = [OutputPath  num2str(Int) 'G.' Ext];
print(gcf, ['-d' Ext], File);

H_Arr(MyId,:)     = H ;
Hcent_Arr(MyId,:) = Ho;
```

```
Xcent(MyId,:)     = Xo;

% Table of optimal variables and averaged optimal variables
% at bottom (B-field of last row matches that of previous row)

%--Error function evaluation using optimal values at each b-field
% setting-
Xopt1 = Xopt(MyId,:);
Error_Opt(MyId,:) = ...
    sum((FUNfromBISOAgjgiTAij(Xopt1,IexpN,NUexp)).^2);

    % ---------------Error function evaluation at center bounds---
    % using effective B-field into Xcent
    Xopt2 = Xcent(MyId,:);
    ErrorCent(MyId,:) = ...
        sum(FUNfromBISOAgjgiTAij(Xopt2 , IexpN, NUexp).^2);

    Err(MyId,:) = 100 * (Error_Opt(MyId,:) - ErrorCent(MyId,:))...
        / Error_Opt(MyId,:);

    close all
end
%-----------------------------------------------------------------------
save 'Hoptim' H_Arr;
save 'Toptim' T_Arr;
save 'Xopt' Xopt;

% -------------Compare optimal Error with center-bound error-------
Opt_wrt_Cent_err = Err;

Table_Opt_wrt_Cent = [Hcent_Arr Xopt Opt_wrt_Cent_err];

%-----------------------------------------------------------------------
if NumFiles > 1
    OptVarsAvg = mean(Xopt(:,(2:end)));
else
    OptVarsAvg = Xopt(:,(2:end));
end

% Saving averaged variables
Tavg      = OptVarsAvg(1);  save 'T' Tavg;
I124avg   = OptVarsAvg(2);  save 'I124avg'   I124avg;
I126avg   = OptVarsAvg(3);  save 'I126avg'   I126avg;
I128avg   = OptVarsAvg(4);  save 'I128avg'   I128avg;
I129avg   = OptVarsAvg(5);  save 'I129avg'   I129avg;
I130avg   = OptVarsAvg(6);  save 'I130avg'   I130avg;
I131avg   = OptVarsAvg(7);  save 'I131avg'   I131avg;
I132avg   = OptVarsAvg(8);  save 'I132avg'   I132avg;
I134avg   = OptVarsAvg(9);  save 'I134avg'   I134avg;
A1_129avg = OptVarsAvg(10); save 'A1_129avg' A1_129avg;
A2_129avg = OptVarsAvg(11); save 'A2_129avg' A2_129avg;
A1_131avg = OptVarsAvg(12); save 'A1_131avg' A1_131avg;
A2_131avg = OptVarsAvg(13); save 'A2_131avg' A2_131avg;
gj1avg    = OptVarsAvg(14); save 'gj1avg'    gj1avg;
```

```
gj2avg    = OptVarsAvg(15); save 'gj2avg'    gj2avg;
MuN129avg = OptVarsAvg(16); save 'MuN129avg' MuN129avg;
MuN131avg = OptVarsAvg(17); save 'MuN131avg' MuN131avg;
A_ijavg   = OptVarsAvg(18); save 'A_ijavg'   A_ijavg;

ISOavg = [I124avg  I126avg  I128avg  I129avg  I130avg  I131avg...
    I132avg   I134avg];
save 'ISOavg' ISOavg;

% Grouping averaged optimal variables
X_Optavg = [H_Arr(end) Tavg ...
    I124avg I126avg I128avg I129avg I130avg I131avg I132avg...
    I134avg  A1_129avg A2_129avg A1_131avg A2_131avg ...
    gj1avg gj2avg MuN129avg MuN131avg A_ijavg];

Error_Avg = sum(FUNfromBISOAgjgiTAij(X_Optavg, IexpN, NUexp).^2);
Avg_Cent_err = 100 * (Error_Avg - ErrorCent(end,:)) ./ Error_Avg;

% Generating table to summarize optimizing process
Table_Opt_Mean = [Table_Opt_wrt_Cent; ...
    [Hcent_Arr(end) X_Optavg Avg_Cent_err]];

save 'T_Arr' T_Arr;
save 'H_Arr' H_Arr;
```

‘FUNfromBISOAgjgiTAij.m’

```
function [Diff] = FUNfromBISOAgjgiTAij(Xsol, Iexp, NUexp, NUmean)

H      = Xsol(1);

T      = Xsol(2);

I124   = Xsol(3);
I126   = Xsol(4);
I128   = Xsol(5);
I129   = Xsol(6);
I130   = Xsol(7);
I131   = Xsol(8);
I132   = Xsol(9);
I134   = Xsol(10);

A1_129 = Xsol(11);
A2_129 = Xsol(12);

A1_131 = Xsol(13);
A2_131 = Xsol(14);

gj1    = Xsol(15);
gj2    = Xsol(16);

MuN129 = Xsol(17);
MuN131 = Xsol(18);

A_ij    = Xsol(19);

% Function body
%
% This program applies to the 834.682 nm-air or 834.911 nm-vacuum
run PhysicalConstantsAij
run Level1InputsBISOAgjgi
run Level2InputsBISOAgjgi
%run Input_MagField

% Separate isotopes according hyperfine structure

run IsotopesParametersISOAgjgi
[dum, N] = size(NukeSpins);

%%---------------------------------------------------------
c1 = 0; c2 = 0;
for i=1:N
    if (NukeSpins(i) == 0)
        c1 = c1 + 1;
        NoHFS(:,c1) = ...
            [Masses(i) NukeSpins(i) IsoShifts(i) IsoAbunds(i)]';
    else
```

```
        c2 = c2 + 1;
        WithHFS(:,c2) = [Masses(i) NukeSpins(i) IsoShifts(i) ...
            IsoAbunds(i) a1(i) b1(i) a2(i) b2(i) gi(i)]';
    end
end

run NoHFsLines;

[Dummy,N1] = size(WithHFS);
II = WithHFS(2,:);
gI = WithHFS(9,:);
run SigmaHFS;

run Lorentzian
run Doppler
run Convolution

Warm = real(Warm);

Diff = Iexp - Warm;
```

Initialization scripts:

- ‘PhysicalParamINIT2.’ -Definition of mean values and error intervals associated with physical parameters to be optimized within published error intervals

```
% Initialization of magnetic field strength, kinetic temperature,
% and physical parameters to be optimized within their respective
% uncertainty bounds as reported in various sources
% (reported on the sides).
%% Isotope shifts (mean values and error bounds)
  % Published mean values
    ISOo = −[−201 −213.4 −154 −189.7 −116.9 −78;...% SuzukiIso
        −173.9 −213.4 −134.9 −189.7 −103.4 −68.9]; % JacksonIso
  % corresponding errors
    ErrISO = [26.0   4.7   19    6.1   4.5   7.0;...
               6.0   4.7   4.5   6.1   4.5   6.0];
  % resultant mean values and global error intervals
    [ISOout, ErrISOout] = FunISOshift(ISOo, ErrISO);
    % convenient redefinition of variables for later use
    ISOo = ISOout;
    ErrISO = ErrISOout;
  % Resulting lower and upper bounds
    ISOlow = ISOo − ErrISO ; ISOup = ISOo + ErrISO;
%% Electric quadrupole interaction constants (hfs constants)
% upper−state values
    %  per isotope: 129,     131
       A1 = [−5801.1  1713.7;  %  Suzuki
             −5808.0  1709.3;  %  D'amico
             −5795.0  1714.8;  %  Fisher
             −5805.5  1712.4]; % Jackson
       ErrA1 = [4.7     2.8;
                0.2     0.7;
                9.0     3.0;
                6.0     6.0];
       [A1o ErrA1] = FunErrorMean(A1, ErrA1);
       A1_129o = A1o(1)       ;  ErrA1_129 = ErrA1(1)   ;
       A1_131o = A1o(2)       ;  ErrA1_131 = ErrA1(2)   ;
%
% lower−state values
   % per isotope: 129 (Jackson),  131 (Suzuki)
       A2 = [−2894.6  858.9;
             −2891.5  858.9];
       ErrA2 = [4.7     3.1 ;
                6.0     3.1];
       [A2o ErrA2] = FunErrorMean(A2, ErrA2);
       % convenient variable redefinition for later use
       A2_129o = A2o(1)       ;  ErrA2_129 = ErrA2(1)   ;
       A2_131o = A2o(2)       ;  ErrA2_131 = ErrA2(2)   ;
       %
       Ao = [A1_129o  A2_129o  A1_131o A2_131o];
       ErrA = [ErrA1_129  ErrA2_129  ErrA1_131 ErrA2_131];
       %
```

```
48        Alow = Ao - ErrA;
49        Aup  = Ao + ErrA;
50  %% Parameters that are intrinsic to nucleus
51      % Lande factors
52        gj1o = 1.321   ; gj2o = 1.190;
53        Errgj1 = 0.0001; Errgj2 = 0.001;
54
55        gjo  = [gj1o gj2o];
56        Errgj  = [Errgj1  Errgj2];
57
58        gjlow = gjo  - Errgj ; gjup  = gjo  + Errgj ;
59      % Nuclear moments
60        MuN129o = -0.7768;       % Emsley
61        MuN131o = -MuN129o/1.11; % NIST
62
63        MuNo = [MuN129o MuN131o];
64          % According to Bacher, the errors on the nuclear moments
65          % should on the same order as the ones associated with
66          % the hyperfine constants
67            ErrMuN129 = .0001;
68            ErrMuN131 = .05; % this error computed based on the
69                             % ratio (1.11) given on line 61
70
71        ErrMuN = [ErrMuN129 ErrMuN131];
72
73        MuNlow = MuNo - ErrMuN ; MuNup = MuNo + ErrMuN;
74  %% Spontaneous emission coefficient
75  A_ijo = 0.636; ErrA_ij = 0.4 * A_ijo;
76
77  A_ijlow = A_ijo - ErrA_ij ; A_ijup = A_ijo + ErrA_ij;
78  %% Magnetic field and temperature
79  Ho = Hout/0.91; ErrH  = (.5) * (Ho);
80  Hlow = Ho   - ErrH; Hup   = Ho + ErrH   ;
81
82  To = 600; ErrT   = 300;
83  Tlow = To - (.5)*ErrT; Tup = To + ErrT  ;
84  %% OVERALL ARRAY OF PHYSICAL PARAMETERS
85      % mean values
86        Xo   = [Ho  To  ISOo  Ao gjo MuNo A_ijo];
87
88      % bounds
89        Xlow = [Hlow  Tlow ISOlow  Alow gjlow MuNlow A_ijlow];
90        Xup  = [Hup   Tup  ISOup   Aup  gjup  MuNup A_ijup] ;
```

Sub-function called by ‘PhysicalParamINIT2.m’:

- ‘FunISOshift.m’ - Averager of isotopic shifts

```
function [ISOout, ErrISOout] = FunISOshift(ISOo, ErrISO)

% This function computes mean isotope shifts
% (relative to isotope shift of 136) as well as errors
% associated on with each based on published data for
% isotopes 128 through 134.

% The function also estimates mean isotope shifts and errors
% associated with isotopes 124 and 126 based on known shifts
% associated with other isotopes.

% Known isotope shifts=======================================
% Xenon isotopes with non-zero spin (129 and 131)
  % mean values
    ISO129o = ISOo(1,2);
    ISO131o = ISOo(1,4);
  % errors
    ErrISO129 = ErrISO(2,2);
    ErrISO131 = ErrISO(2,4);

  % Computing effective mean values and errors from reported
  % values
   [ISOo ErrISO] = FunErrorMean(ISOo, ErrISO);

% Considering isotopes with zero nuclear spin
    % mean values
      ISOxo   = [ISOo(1) ISOo(3) ISOo(5) ISOo(6)];
      N = length(ISOxo);
    % errors
      ErrISOx = [ErrISO(1) ErrISO(3) ErrISO(5) ErrISO(6)];

  % Redefining upper and lower bounds of isotope shifts
    ISOxup  = ISOxo + ErrISOx; % upper bounds
    ISOxlow = ISOxo - ErrISOx; % lower bounds

% Unknown isotope shifts =====================================
  % Estimating unknown isotope shifts of 124 and 126 from
  % known ones using linear relation between isotopes to
  % find initial guesses on unknown shifts associated with
  % isotopes 124 and 126
    for i=1:N-1
      Dup(i)  = (ISOxup(i)  - ISOxup(i+1)) / 2 ;
      Dlow(i) = (ISOxlow(i) - ISOxlow(i+1)) / 2;
    end

    DupMean = mean(Dup)  ;
    DlowMean = mean(Dlow);

    DMean = mean([DupMean DlowMean]);
```

```

    ISO126o = 2* DMean + ISOxo(1);
    ISO124o = 2* DMean + ISO126o ;

    % Estimating error-bounds on isotope shifts of Xe124 and
    % Xe126 based on widest bounds
      ErrISO126 = max(ErrISOx);
      ErrISO124 = ErrISO126  ;

%===========================================================
% Outputted mean values and errors associated with all
% isotopes
ISOout = [ISO124o ISO126o ...
    ISOxo(1) ISOo(2) ISOxo(2) ISOo(4) ISOxo(3) ISOxo(4)];
ErrISOout = [ErrISO124 ErrISO126 ...
    ErrISOx(1) ErrISO(2) ErrISOx(2) ErrISO(4) ErrISOx(3)...
    ErrISOx(4)];
```

- ‘FunErrorMean.m’ - Averager of all other parameters (excluding isotopic shifts)

```
function [Xmean, dXmean]=FunErrorMean(XX, dXX)
% This function computes mean values and errors associated
% with physical parameters as published in several sources

[Dummy, NumVariables] = size(XX);

N = NumVariables;

for i = 1:N
    X  = XX(:,i);
    dX = dXX(:,i);

    XR = X + dX;
    XL = X - dX;

    Xmean(i) = (min(XL) + max(XR)) / 2;

    dXmean(i) = Xmean(i) - min(XL);
end
```

- ‘Level1inputsBISOAgjgi.m’

```
%--------------Level 1 (upper Level) quantum constants-----------

% Angular monentum quantum number.
J1 = 1;
```

- ‘Level2inputsBISOAgjgi.m’

```
%--------------Level 1 (upper Level) quantum constants-----------

% Angular monentum quantum number.
J2 = 2;
```

- ‘PhysicalConstants.m’

```
%% Computing larmor precession ratio
AlphaInv = 137.035999679;          % Fine structure constant
m = 9.10938215 * 1.e-28;           % electron mass (grams)
c = 2.99792458*1.e10;              % vacuum speed of light (cm/s)
h = 6.62606896 * 1.e-27;           % Planck's constant erg s

den = (4*pi*c^2)*m;
e = sqrt((h*c/(2*pi)) / AlphaInv);
o = e/den; % cm^-1               % Larmor precession
%% Computing nuclear moment
    % Bohr magneton  [http://physics.nist.gov/constants]
        % Conversion from (m T)^(-1) to (cm G)^(-1)
        MuBinvmbyT = 46.6864515; % m^-1 / T
        MuB = MuBinvmbyT / (10000*100); % (PerCm)/G  1T = 10000G
        % Proton-to-electron mass ratio
        MassRatio = 1836.15267247;
    % Nuclear moment
        MuN = MuB / MassRatio; % SI

%% constants in SI units
    % speed of light
      cSI = c/100.;            %  (m/sec)
    % Stephan-Boltzman constant NIST
      kSI = 1.3806504e-23;     %  (J/(Kg.K)
    % Electron mass
      MSI = 131.29*1.6605e-27; % Kg
    % Some constant
      AlphSI = MSI/(2*kSI);
%% Transition center-wavelength of Xe I
l_oSI = 834.91157e-9;
```

- ‘IsotopesParametersISOAgjgi.m’

```
%%%%%%%%%%%%%%%%%%%%%%%%%%%%%%%%%%%%%%%%%%%%%%%%%%%%%%%%%%%%%%%%%%%
% Script: IsotopesParametersISOAgjgi
% This script stores mean values (computed from Initialization
% process abouve) of all physical parameters associated with the
% 834.682 nm transition of xenon for each isotope based on
%%%%%%%%%%%%%%%%%%%%%%%%%%%%%%%%%%%%%%%%%%%%%%%%%%%%%%%%%%%%%%%%%%%

% masses
Masses = [124  126  128  129  130  131  132  134  136];
%
% nuclear spins
NukeSpins = [0  0  0 1/2  0 3/2  0  0   0];

% isotope shifts
IsoShifts =  FunMHztoCm...
    ([I124 I126 I128  I129  I130  I131 I132 I134 0]);

% natural abundances associated with each isotope
IsoAbunds  = [0.1 0.09  1.91  26.4  4.1  21.2  26.9  10.4 ...
              8.9]/100;  % percent

% nuclear lande-g factors estimated from nuclear moments and
% nuclear spins
gi = (1/MassRatio)*...
    [0  0  0 MuN129/NukeSpins(4)  0 MuN131/NukeSpins(6)  0  0  0];

      % electric quadrupole interaction constants
      a1       =      [0  0  0 A1_129  0 A1_131  0  0  0];
      a1 = FunMHztoCm(a1); % convert from MHz to Cm^-1

      b1       =      [0  0  0  0  0 -24  0  0  0];
      b1 = FunMHztoCm(b1); % convert from MHz to Cm^-1

      a2       =      [0  0  0 A2_129  0 A2_131  0  0  0];
      a2 = FunMHztoCm(a2); % convert from MHz to Cm^-1

      b2       =      [0  0  0  0  0 14  0  0];
      b2 = FunMHztoCm(b2); % convert from MHz to Cm^-1

 [dum, N] = size(NukeSpins);

% Grouping all physical parameters based according to isotopes
% with zero and non-zero spins
c1 = 0; c2 = 0;
for i=1:N
    if (NukeSpins(i) == 0);
        c1 = c1 + 1;        % counter
        % Isotopes zero nuclear spin; that is, exhibiting no
        % hyperfine structure
        NoHFS(:,c1) = [Masses(i) NukeSpins(i) IsoShifts(i) ...
            IsoAbunds(i)]';
```

```
    else;
        c2 = c2 + 1;        % counter
        % Isotopes zero nuclear spin; that is, exhibiting no
        % hyperfine structure
        WithHFS(:,c2)=[Masses(i) NukeSpins(i) IsoShifts(i) ...
            IsoAbunds(i) a1(i) b1(i) a2(i) b2(i) gi(i)]';
    end
end
```

BIBLIOGRAPHY

BIBLIOGRAPHY

[1] James M. Haas. *Low-perturbation Interrogation of the Internal and Near-field Plasma Structure of a Hall Thruster using a High-speed Probe Positioning System.* PhD thesis, University of Michigan, Ann Arbor, MI, 2001. (document), I, 3.1, 1, 3, 3.2.2, 4.1, 4.1, 4.1, 4.2, 4.2, 4.2.1, 4.2.2, 4.2.3, 4, 4.7, 4.2.3, 4.12, 4.13, 4.16, 4.17, 4.18, 4.19, V, VII, A.11, A.12, A.13, A.14, A.15, A.16, A.17, A.18, A.19, A.20, A.21, A.22

[2] Burleigh Instruments, Inc. *SA^{PLUS} Laser Spectrum Analyzer System Operating Manual.* (document), B, B.2

[3] George P. Sutton and Oscar Biblarz. *Rocket Propulsion Elements.* John Wiley and Sons, Inc., New York, 7th edition, 2001. (document), 2.2.2.2, 2.2.2.2, 2.2.2.2, 2.1

[4] Richard R. Hofer. *Development and Characterization of High-Efficiency, High-specific Impulse Xenon Hall Thrusters.* PhD thesis, University of Michigan, Ann Arbor, MI, 2004. (document), 2.2.2.2, 2.1, 3.3, 4.1, 4.2.1

[5] Douglas Fiehler and Steve Oleson. A Comparison of Electric Propulsion Systems for Mars Exploration. In *37^{th} Joint Propulsion Conference and Exhibit*, Huntsville, AL, 2003. (document), 2.1.2, 2.2.2.2, 2.1

[6] M. Suzuki, K. Katoh, and N. Nishimiya. Saturated Absorption Spectroscopy of Xe using a GaAs Semiconductor Laser. *Spectrochimica Acta Part A*, 58:2519–2531, 2002. (document), 5.3.1, 5.3.1, 5.2, 5.3.1, 5.3.2, 5.8

[7] R. B. Firestone and C. M. Baglin. *Table of Isotopes.* Wiley, New York, 1999. (document), 5.2, 5.3.1, 5.3.2, 5.8

[8] Martin J. L. Turner. *Rocket and Spacecraft Propulsion: Principles, Practice and New Developments.* Springer-Verlag, New York, 2nd edition, 2005. I, 2.1.1, 2.2.2, 2.2.2.2, 2.2.2.2, 2.2.2.2, 7, 8, 3.2.3

[9] H. R. Kaufman V. V. Zhurin and R. S. Robinson. Physics of Closed Drift Thrusters. *plasma sources science and technology*, 8:R1–R20, 1998. I, 4.2.4, 4.4

[10] Richard R. Hofer, Peter Y. Peterson, and Alec D. Gallimore. A High Specific Impulse Two-state Hall Thruster with Plasma Lens Focusing. IEPC-01-036, Cleveland, OH, 2001. I, 2.2.2.2, 4.2

[11] Richard R. Hofer et al. Optimization of Hall Thruster Magnetic Field Topology. 27th IEEE International Conference on Plasma Science, New Orleans, LA, 2000. I, 2.2.2.2

[12] Vladimir Kim. Main Physical Features and Processes Determining the Performance of Stationary Plasma Thrusters. *Journal of Propulsion and Power*, 8:R1–R20, 1998. I

[13] James M. Haas and Alec D. Gallimore. Considerations on the Role of the Hall Current in a Laboratory. 37^{th} Joint Propulsion Conference and Exhibit, Salt Lake City, UT, 2001. I, 2.2.2.2, 4.1, VII

[14] Peter Y. Peterson, Alec D. Gallimore, and James M. Haas. Experimental Investigation of a Hall Thruster Internal Magnetic Field Topography. 27^{th} International Electric Propulsion Conference, Pasadena, CA, 2001. I, 2.2.2.2, 4.1, 4.2

[15] Baïlo B. Ngom et al. Numerical Simulation of the Zeeman Effect in Neutral Xenon from NIR Diode-laser Spectroscopy. *Journal of Applied Physics*, 104:023303–14, 2008. I

[16] James E. A. John. *Gas Dynamics.* Prentice Hall, New Jersey, 2nd edition, 1984. 2.1.1, 2.2.1

[17] Roger R. Bate, Donald D. Mueller, and Jerry E. White. *Fundamentals of Astrodynamics.* Dover Publications, New York, 1971. 2.1.2

[18] Robert G. Jahn and Edgar Y. Choueiri. *Encyclopedia of Physical Science and Technology*, volume 5, chapter Electric Propulsion, pages 125–141. Academic Press, New Jersey, 2002. `http://nobelprize.org/nobel_prizes/physics/laureates/1902/zeeman-bio.html`. 2.2.2.1

[19] Dan M. Goebel and Ira Katz. *Fundamentals of Electric Propulsion: Ion and Hall Thrusters.* JPL Space Science and Technology Series. John Wiley and Sons, 2008. `http://descanso.jpl.nasa.gov/SciTechBook/st`$_{s}eries1_{c}hapter.cfm, ., , , , ,$

[20] Michael A. Lieberman and Allan J. Lichtenberg. *Principles of Plasma Discharges and Materials Processing.* John Wiley and Sons, Inc., New York, 2nd edition, 1994. 2.2.2.2, 2.2.2.2, 1, 3.2.3, 6.3

[21] `http://www.grc.nasa.gov/WWW/ion/past/90s/nstar.htm`. 4

[22] Frank S. Gulczinski III. *Examination of the Structure and Evolution of Ion Energy Properties of a 5 kW Class Laboratory Hall Effect Thruster at Various Operational Conditions.* PhD thesis, University of Michigan, Ann Arbor, MI, 1999. 3.1, 3.2.2, 4.2

[23] Francis F. Chen. *Introduction to Plasma Physics and Controlled Fusion.* Plenum Press, New York, 1974. 3.2.1, 1, 3.2.2, 3.2.3

[24] T. I. Gombosi. *Gas Kinetics Theory.* Cambridge University Press, 1994. 3.2.3

[25] A. I. Morozov et al. Plasma Accelerator with Closed Electron Drift and Extended Acceleration Zone. *Soviet Physics–Technical Physics*, 17:38–45, 1972. 3.3, 3.3, 4.2.4, 4.3.1, 4.4

[26] A. I. Morozov et al. Effect of the Magnetic Field on a Closed-electron-drift Accelerator. *Soviet Physics–Technical Physics*, 17:482–487, 1972. 3.3

[27] James M. Haas and Alec D. Gallimore. Considerations on the Role of the Hall Current in a Laboratory-model Thruster. 37^{th} Joint Propulsion Conference and Exhibit, Salt Lake City, UT, 2001. 4.1, 4.1, 4.2, 4.2

[28] `http://info.ee.surrey.ac.uk/Workshop/advice/coils/mu/#bhcurve`. 1

[29] C. A. Baldan et al. Design Studies of the Magnetic Properties of Structural Materials Affecting the Magnetic Field of High-homogeneity Superconducting Magnets. *Journal of Magnetism and Magnetic Materials*, 226–230:2104–2106, 2001. 4.2

[30] Richard R. Hofer and Alec D. Gallimore. The Role of Magnetic Field Topography in Improving the Performance of High-voltage Hall Thrusters. 38^{th} Joint AIAA Propulsion Conference, Indianapolis, IN, 2002. V

[31] `http://nobelprize.org/nobel_prizes/physics/laureates/1902/zeeman-bio.html`. V

[32] Timothy B. Smith et al. Optogalvanic and Absorption Spectroscopy of the Zeeman Effect in Xenon. 30^{th} International Electric Propulsion Conference, Florence, Italy, 2007. 5.1

[33] `sales.hamamatsu.com/assets/pdf/parts_L/L2783_TAPP1070E01.pdf`. 5.1

[34] T. B. Smith et al. Diode Laser-induced Fluorescence of Xenon Ion Velocity Distributions. 41^{th} Joint AIAA Propulsion Conference, Tucson, AZ, 2005. 5.1

[35] Hermann Haken and Hans C. Wolf. *The Physics of Atoms and Quanta.* Springer-Verlag, Verlag Berlin Heidelberg, 7th edition, 1997. 5.2.1, 5.2.2.1, 5.2.2.1, 5.3.1, 5.3.3

[36] Sune Svanberg. *Atomic and Molecular Spectroscopy: Basic Aspects and Practical Applications.* Springer-Verlag, New York, 3rd edition, 2001. 5.2.2, 5.3.1, 5.3.1, 6.1.3.1, 6.1.3.1, 10, 6.1.4.1, 6.1.4.3

[37] Charles G. Darwin. The Zeeman Effect and Spherical Harmonics. volume 115 of *Proceedings of the Royal Society of London. Series A, Containing Papers of a Mathematical and Physical Character*, pages 1–19, 1927. 5.2.2, 5.2.2.2

[38] K. Darwin. Examples of the Zeeman Effect at Intermediate Strengths of Magnetic Field. volume 118 of *Proceedings of the Royal Society of London. Series A, Containing Papers of a Mathematical and Physical Character*, pages 264–285, 1928. 5.2.2, 5.2.2.2

[39] R. F. Bacher. *The Zeeman Effect of Hyperfine Structure*. PhD thesis, University of Michigan, Ann Arbor, MI, 1930. 5.2.2, 5.2.2.1, 5.2.2.2, 5.2.2.2, 5.2.2.2, 5.2.2.2, 4

[40] I. I. Sobelman. *Atomic Spectra and Radiative Transitions*. Springer-Verlag, New York, 2 edition, 1992. 5.2.2.1, 5.2.2.1

[41] R. H. Garstang. Atoms in High Magnetic Fields (White Dwarfs). *Reports on Progress in Physics*, 40, 1977. 5.2.2.2, 5.4.5

[42] `http://physics.nist.gov/Pubs/AtSpec/node09.html#node095`. 5.3.1

[43] E. B. Saloman. Energy Levels and Observed Spectral Lines of Xenon, Xe I through Xe LIV. *Review of Modern Physics*, 8, 2004. 5.3.1, 5.2

[44] J. Emsley. *The Elements*. Oxford University Press, New York, NY, 1995. 5.3.1, 5.2

[45] D. A. Jackson and M. C. Coulombe. Hyperfine Structure in the Arc Spectrum of Xenon. 327(1569):137–145, 1972. 5.3.1, 5.2

[46] `http://physics.nist.gov/PhysRefData/ASD/lines_form.html`. 5.3.1

[47] D. A. Bethe and R. R. Bacher. Nuclear Physics A. Stationary States of Nuclei. *Review of Modern Physics*, 8, 1936. 5.2

[48] Timothy B. Smith et al. Deconvolution of Axial Velocity Distributions from Hall Thruster LIF Spectra. 27th International Electric Propulsion Conference, Pasadena, CA, 2001. 5.3.3, 5.4.4

[49] W. A. Hargus and M. A. Capelli. Laser-induced Fluorescence Measurements of Velocity within a Hall Discharge. *Applied Physics B*, 72, 2000. 5.3.3

[50] M. H. Miller, R. A. Roig, and R. D. Bengtson. Transition Probabilities of Xe I and Xe II. *Physical Review A*, 8(1), 1973. 5.3.3

[51] T. F. Coleman and Y. Li. On the Convergence of Interior-reflective Newton Methods for Nonlinear Minimization Subject to Bounds. *Mathematical Programming*, 67:189–224, 1994. 5.4.1, 7

[52] G. J. Williams. *The Use of Laser-Induced Fluorescence to Characterize Discharge Cathode Erosion in a 30cm Ring-Cusp Ion Thruster*. PhD thesis, University of Michigan, Ann Arbor, MI, 2000. 5.4.3.1

[53] Harvey E. White. *Introduction to Atomic Spectra.* McGraw-Hill Book Company, New York, 1st edition, 1934. 5.4.3.2, 6.1.3.1

[54] T. B. Smith. *Deconvolution of Ion Velocity Distributions from Laser-Induced Fluorescence Spectra of Xenon Electrostatic Thruster Plumes.* PhD thesis, University of Michigan, Ann Arbor, MI, 2003. 5.4.3.2, 6.1.4.2

[55] Wolfgang Demtröder. *Laser Spectroscopy: Basic Concepts and Instrumentation.* Springer-Verlag, New York, 1981. 6.1.1, 6.1.1.3, 5, 6, 6.1.2.3, 6.1.2.3, 6.1.3.1, 6.1.3.1, 6.1.3.1, 6.1.4.1, 6.1.4.2, 6.1.4.2, 6.1.4.2, 6.1.4.3, 6.1.4.3

[56] David Bohm. *Quantum Theory.* Dover Publications, New York, 1989. 6.1.1.3, 6.1.3.1

[57] Amnon Yariv. *Quantum Electronics.* John Wiley and Sons, New York, 1975. 6.1.1.3, 6.1.1.3, 6.1.2.2

[58] M. Mitchner and Charles H. Kruger. *Partially Ionized Gases.* John Wiley and Sons, New York, 1973. 6.1.2, 6.1.3.1, 6.1.4.1

[59] C. W. Allen. Broad Lines in the Arc Spectrum of Copper. *Physical Review*, 39:42–54, 1932. 6.1.3.1

[60] William A. Hargus. *Investigation of the Plasma Acceleration Mechanism within a Coaxial Hall Thruster.* PhD thesis, Stanford University, Stanford, CA, 2001. 6.1.4.2

[61] Wensheng Huang et al. Laser-induced Fluorescence of Singly-charged Xenon in a 6-kW Hall Thruster Plume. 44^{th} Joint Propulsion Conference and Exhibit, Hartford, CT, 2007. 6.1.4.2, 6.2.1

[62] Allan C. G. Mitchell and Mark W. Zemansky. *Resonnance Radiation and Excited Atoms.* The MacMillan Company, New York, 1934. 6.1.4.3, 6.1.4.3, 6.1.4.4

[63] Geoffrey V. Marr. *Plasma Spectroscopy.* Elsevier Publishing Company, New York, 1968. 6.1.4.3

[64] U. Litzén A. Thorne and S. Johansson. *Spectrophysics.* Springer, New York, 1999. 6.1.4.4

[65] Xenon. `http://periodic.lanl.gov/elements/54.html`. Accessed in September 2009. 6.3

[66] J. M. Goldfinch and D. C. Pack. *Dynamics of Ionized Gases*, chapter Expansion of a Plasma from a Spherical Source into a Vacuum, page 441. John Wiley and Sons, Inc., New York, 1973. 6.3, 6.3

[67] G. Hernandez. *Studies in Modern Optics: Fabry-Perot Interferometers*, volume 3. Cambridge University Press, 1986. B, B

[68] TOPTICA. *Diode Laser System DL 100 Manual.* B